DISSERTATION

submitted to the

Combined Faculties for the Natural Sciences and for Mathematics

of the Ruperto-Carola University of Heidelberg, Germany

for the degree of

Doctor of Natural Sciences

Put forward by

Ruomin Hu, M.Sc.
Born in Xining, China

Oral examination: February 5th 2020

Exploring Quadrupolar Interactions of ^{23}Na and ^{35}Cl with Triple-Quantum MRS/MRI

Referees: Prof. Dr. Lothar Schad
Prof. Dr. Peter Bachert

Erforschung von Quadrupolinteraktionen von ^{23}Na und ^{35}Cl mit Tripelquanten-MRI/MRS

Mit Hilfe der Magnetresonanztomographie (MRT) und der Magnetresonanzspektroskopie (MRS) können die Quadrupolkerne ^{23}Na und ^{35}Cl jeweils mit einem Kernspin von 3/2 untersucht werden. Die Na^{+}-Kationen und Cl^{-}-Anionen sind an zellulären Funktionen beteiligt und können Quadrupol-Wechselwirkungen mit geladenen Makromolekülen eingehen, wodurch Tripelquanten (TQ) Signale entstehen. Beeinträchtigte Physiologie verändert die makromolekulare Zusammensetzung und den Ionengehalt, die mit TQ MRI/MRS untersucht werden können. Das Ziel war es, eine Sequenz zur Aufnahme von *in vivo* Singelquanten- (SQ) und TQ-Bildern sowie Relaxationsparameterkarten innerhalb einer Messung zu entwickeln.
Zuerst wurde eine dichteangepasste radiale MRT-Technik (DA-R) an einem $9.4\,\mathrm{T}$ präklinischen Scanner implementiert. Phantombilder zeigten eine ausgezeichnete Bildqualität und eine hervorragende Messzeiteffizienz. Hochauflösende ^{23}Na- und ^{35}Cl-Bilder ermöglichten die Unterscheidung verschiedener anatomischer Merkmale in Ratten.
Zweitens wurde mit einer TQ-Spektroskopiesequenz mit zeitproportionaler Phaseninkrementierung (TQ-TPPI) Daten in Zellen und im Rattenkopf aufgenommen. Die Ergebnisse zeigten spannende Diskrepanzen zwischen dem ^{23}Na- und den ^{35}Cl-TQ-Signal, die Unterschiede in der Quadrupol-Wechselwirkung von ^{23}Na und ^{35}Cl auf molekularer Ebene aufdecken.
Schließlich wurde TQ-TPPI mit DA-R kombiniert, um die TQ- und SQ-TPPI-Sequenz (TASTI) zu entwickeln. Die Sequenz wurde erfolgreich im Rattenkopf angewendet. Erstmals wurden lokalisierte TQ-zu-SQ-Signalverhältnisse in verschiedenen Kopfbereichen abgebildet. Darüber hinaus ermöglichte sie die Unterscheidung zwischen TQ-zu-SQ-Signalverhältnissen im intra- und extrazellulären Raum. Mit der Möglichkeit, lokale Veränderungen des Ionengehalts, der Relaxationszeiten und des TQ-Signals zu analysieren, hat die TASTI-Sequenz das Potenzial, das eine Werkzeug zu werden, das alle wichtigen Ansätze von ^{23}Na NMR kombiniert.

Exploring Quadrupolar Interactions of ^{23}Na and ^{35}Cl with Triple-Quantum MRI/MRS

Magnetic resonance imaging (MRI) and magnetic resonance spectroscopy (MRS) can be used to investigate the quadrupolar nuclei ^{23}Na and ^{35}Cl, each with a nuclear spin of $3/2$. The Na^{+} cations and Cl^{-} anions are involved in cellular functions and can undergo quadrupolar interactions with oppositely charged macromolecules. These interactions give rise to triple-quantum (TQ) signals. Compromised physiological functions change the macromolecular composition and ion content, which can be investigated with TQ MRI/MRS. The goal was to develop a sequence to acquire single-quantum (SQ) and TQ images and to map relaxation parameters *in vivo* within one measurement.
First, a **d**ensity-**a**dapted **r**adial MRI technique (DA-R) was implemented at a $9.4\,\mathrm{T}$ scanner. Phantom images demonstrated superior image quality and measurement time efficiency. High-resolution ^{23}Na and ^{35}Cl images allowed for distinction of anatomical features in rat.
Second, **TQ** spectroscopy with **t**ime-**p**roportional **p**hase **i**ncrementation (TQ-TPPI) was used to acquire data in cells and in rat head. The results revealed interesting discrepancies in ^{23}Na and ^{35}Cl TQ signals, uncovering differences in the quadrupolar interactions of Na^{+} and Cl^{-} on a molecular level.
Finally, TQ-TPPI was combined with DA-R to create **TQ** **a**nd **SQ** **T**PPI **i**maging (TASTI). The sequence was sucsessfully applied to rat head. For the first time, localized ratios between TQ and SQ signal were mapped in different head regions. Furthermore, it enabled the distinction between TQ signal fractions in the intra- and extracellular space. With its ability to analyze local changes in ion content, relaxation times and TQ signal, the TASTI sequence has the potential to become the one tool to combine all major approaches to address ^{23}Na NMR.

Acknowledgement

> Perhaps all the questions we ask of love, to measure, test, probe, and save it, have the additional effect of cutting it short. Perhaps the reason we are unable to love is that we yearn to be loved, that is, we demand something (love) from others instead of delivering ourselves up to them demand-free and asking for nothing but their company.
>
> *(Milan Kundera, The Unbearable Lightness of Being)*

First and foremost I would like to express my sincere gratitude towards my advisor Prof. Lothar Schad for the continuous support from the time of my Master's thesis and throughout the learning process during my Ph.D. studies. I especially appreciate his trust in my ability by offering me a topic at the forefront of one of the most exciting research areas in MRI especially in terms of its requirement for a deep understanding of the physical phenomenom. Moreover I would like to thank Prof. Peter Bachert for his willingness to evaluate my dissertation.

Additionally I gratefully acknowledge the cooperation with Prof. Eric Gottwald and Cordula Nies of Karlsruher Institute of Technology. They patiently offered guidance on the handling of all bioreactor- and cell-related topics and shouldered the responsibility of the preparation of the bioreactor setup.

Special thanks go to Felix Hörner of Zentralinstitut für Seelische Gesundheit, without whom there would have been no working scanner hardware environment. Moreover he offered continuous support in animal handling which was the foundation of all in vivo applications in this work.

Furthermore I would like to thank Andreas for his initial guidance on working at the scanner as well as for sharing his knowledge both in form of discussion and Matlab files. Moreover I express my gratitude towards Jorge who helped me with coil construction and provided much input in discussions throughout the entirety of my time at CKM.

My office mate, Nadia, has the sweetest heart. Despite having the top of my bobble head behind our wall of screens as your most thrilling scenery at work, I could always count on seeing you smile when I lengthened my neck to distract you with all my jabbering. I could not have hoped to have shared my creative chaos with a more supportive, responsible and hard-working person. I am immensely grateful to have made it through all the steps of the PhD journey with you from the start, and now finally, to the finish.

Matze, despite your outfits in the blackest blacks (delicately garnished by your red strawberry beanie), you were the source of light that guided me through the most difficult times. There was without a single exception always time in your schedule to hear me out on all the ups and downs of doing science. Thanks for the tea talk, the coils (obviously) and the (awfully bad) jokes. This dissertation would absolutely not have been here without you.

Dennis, who always says the opposite of what he thinks, is a develish Carolina Reaper: mind-numbingly sharp, mind-boggling bright, and if you learn to love the unique spiciness, is the greatest friend and colleague you could wish for. Thanks for always declining to give me 5 minutes and then to instead spend hours on end diving into the world of qulti-muantum what-have-you with me. I might have given up a long time ago, had you not always been there for me unconditionally.

Tom, a unique snowflake on a special flower, is a pure bundle of joy. I deeply appreciate your genuineness and introspection and the fact that I could always count on you. From all the hammers you lurked around to gather, all the awkward wall poses you managed to pull off, and all the queens of clubs you bid farewell at the sight of my shiny tens of diamonds, I gathered so much power of happiness that this final smash facing the dissertation became only a B-button away.

Many thanks go to Nadia, Tanja, Wiebke, Simon, Matze and Tom, who took time out of their busy schedule to proofread parts of this work. Special thanks go to Dennis, who proofread the entire thesis. This dissertation would be full of errors and ill argumentations had you not taken time out of your busy schedule to help me.

Special thanks go to the fellow X-nuclei group members Nadia, Matze, Michaela and Dennis. I received endless support from all of you over the years. It was a cozy experience with you, hurdled around the camp fire of the ever-so bright future of X-nuclei NMR.

The MRI lectures at the Hochschule were a great pleasure to give, especially in the constructive and efficient team with Tanja and Sebastian.[1] Thank you for letting me be your bad cop.

Furthermore, thank you to everybody who, during vacations, at conferences or just in plain everyday life, waited for me to eat up, to finish taking the N^{th} with $N \gg \infty$ photograph, and to catch up on their long-legged pacing. Thanks for driving me around and for walking with me on foot due to me religiously rejecting the ownership of a bike. All the boulders we climbed, the cards we played, the fingers we injured while rigorously smashing controllers, the air hockey pucks we sent flying, and even the plushie-bike tour on volcanic-rocky terrain we undertook, are memories I shared with you that I will dearly cherish. Special thanks go to Simon, Tanja, Sebastian and Nadja, who where a part of a lot of these memories.

Arwin, thank you for being there for me for the last ten years. From my first encounter with $\varepsilon_{\mathrm{ijk}}$ to the most recent frustration with $\hat{T}_{\mathrm{lm}}$ you supported me unconditionally. Superfluous as it may seem to mention, this dissertation amassed from the last five+ years of distributing flyers would not have been completed without you.

Last but not least, I would like to thank my parents, who provided me with a head-start in life and supported me in every way imaginable. Your love gave me wings that guided me to soar above and beyond all the obstacles, pitfalls and avalanches in life. This dissertation is dedicated to you.

---

[1] We also pulled off very convincing professor outfits. Mind you, not as convincingly as Dr. Hubertus Simon though, to whom this one and only footnote in the entire thesis is dedicated. I would have loved to make a stylish footnote to the side in a hand-carved, intricate italic font. Much to my regret though, my Lyx preamble included no such pre-made feature.

Table of Contents

1 Introduction **1**

2 Theoretical Background **3**
2.1 Nuclear Magnetic Resonance . . . 3
2.1.1 Nuclear Spin and Nuclear Zeeman Effect . . . 3
2.1.2 Macroscopic Magnetization . . . 5
2.1.3 Bloch Equation . . . 6
2.1.4 Sensitivity . . . 9
2.2 Quadrupole Nuclei . . . 10
2.2.1 Nuclear Spin Hamiltonian . . . 10
2.2.2 Electric-Quadrupole Coupling . . . 11
2.2.3 Static and Fluctuating Electric-Quadrupole Interaction . . . 14
2.2.4 Spin Density Operator . . . 16
2.2.5 Irreducible Tensor Operator . . . 17
2.2.6 Effects of Hard RF Pulses . . . 18
2.2.7 Effects of Quadrupole Thermal Relaxation . . . 19
2.2.8 Acquisition of Multi-Quantum Coherences . . . 22
2.3 Biological Background . . . 25

3 Materials and Methods **29**
3.1 Experimental Setup . . . 29
3.1.1 Scanner . . . 29
3.1.2 Coils . . . 29
3.1.3 Phantoms . . . 31
3.1.4 Bioreactor . . . 33
3.1.5 Animal . . . 35
3.2 MR Methods and Sequences . . . 36
3.2.1 Flip Angle Calibration . . . 36
3.2.2 Spatial Resolution Analysis . . . 36
3.2.3 Relaxation Time Measurement . . . 37
3.2.4 Radial Imaging . . . 38
3.2.5 Triple-Quantum Spectroscopy with TPPI (TQ-TPPI) . . . 41
3.3 Sequence Parameters . . . 44
3.3.1 Density-Adapted Radial Imaging (DA-R) . . . 44
3.3.2 Triple-Quantum Spectroscopy with TPPI (TQ-TPPI) . . . 47
3.3.3 Triple- and Single-Quantum TPPI Imaging (TASTI) . . . 50

4 Results **53**
4.1 Density-Adapted Radial Imaging (DA-R) . . . 53
4.1.1 SNR Improvement through Density-Adaption . . . 53
4.1.2 Spatial Resolution Analysis . . . 54

4.1.3 Bioreactor 59
4.1.4 Rat Head and Rat Torso 61
4.2 Triple-Quantum Spectroscopy with TPPI (TQ-TPPI) 67
4.2.1 Agarose Phantoms 67
4.2.2 Lecithin Phantoms 71
4.2.3 Bioreactor 73
4.2.4 Rat Head 73
4.3 Triple- and Single-Quantum TPPI Imaging (TASTI) 75
4.3.1 TASTI Sequence Development 75
4.3.2 Varying TE, Δt_{evo} and $t_{\mathrm{evo,max}}$ in Agarose Phantoms 78
4.3.3 Application in Rat Head 89

5 Discussion **93**
5.1 DA-R 93
5.2 TQ-TPPI 97
5.3 TASTI 101

6 Conclusion and Outlook **109**

1 Introduction

Magnetic resonance imaging (MRI) and magnetic resonance spectroscopy (MRS) are non-invasive medical diagnostic techniques based on nuclear magnetic resonance (NMR). In clinical routine, MR images and spectra are generated by the excitation of ^{1}H nuclei via radiofrequency (RF) pulses and spatially encoded with magnetic gradients. They contain detailed information on pathological expressions that have manifested on a macroscopic scale. Apart from the ^{1}H nuclei, MRI and MRS can also be used to investigate the quadrupolar nuclei ^{23}Na and ^{35}Cl, each with a nuclear spin of $3/2$.

The sodium cations Na$^+$ and the chlorine anions Cl$^-$ are involved in vital cellular functions. In mammals, Na$^+$ play key roles in processes relying on energy metabolism, while chloride ions Cl$^-$ are indispensable in signal transfer involving depolarization of the cell membrane. Metabolic mechanisms on the cellular level often require the sequential participation of many types of transport proteins. Malfunctioning of transport proteins or disturbed homeostasis might lead to a chain reaction resulting in unbalanced concentrations of various types of ions and metabolites. This unbalance is the pathological expression of any disease on the cellular level.

Given the vital importance of Na$^+$ and Cl$^-$, this thesis explores ^{23}Na and ^{35}Cl MRI and MRS techniques at a preclinical scanner with 9.4 T field strength. ^{23}Na has the second highest physical NMR sensivitiy of 9.3×10^{-2} relative to ^{1}H. Taking into account the low *in vivo* concentration, its *in vivo* NMR sensitivity is 8.3×10^{-5} relative to ^{1}H (Haacke et al., 1999). The chlorine ions Cl$^-$ are the most abundant anions in the human body and hence have the vital responsibility of counterbalancing cations such as Na$^+$. The relative physical NMR sensitivity of ^{35}Cl is 3.6×10^{-3} and thus 26 times lower than that of ^{23}Na.

The physics of the quadrupolar nuclei ^{23}Na and ^{35}Cl has interesting properties that can be explored with NMR. They have an electric quadrupole moment which interacts with the surrounding electric field gradient. This electric-quadrupole interaction is the dominant relaxation mechanism for ^{23}Na and ^{35}Cl. It is much stronger than the magnetic dipole-dipole interaction and result in very short relaxation times. Additionally, ^{23}Na and ^{35}Cl have four Zeeman energy levels in an external magnetic field. Two kinds of multiple-quantum (MQ) coherences are of interest in this thesis: the transition between two neighboring energy levels, referred to as single-quantum (SQ) coherence, and that between the highest and the lowest energy level, referred to as triple-quantum (TQ) coherence.

One particularly exciting ^{23}Na and ^{35}Cl MRS approach is the MQ spectroscopy, which selectively detect MQ coherences. The original approach dates back to 1986 (Pekar and Leigh, 1986). This approach is based on the fact that interactions of different physical nature between the nuclei and the environment pertain to different MQ coherences. Single-quantum signal arises from the total pool of nuclei, while TQ signal results from very brief electric-quadrupole interactions between the nuclei and the charged quadrupolaer interaction sites within marcromolecules (Burstein and Springer, 2019). The TQ signal intensity is, however, only a fraction of the SQ signal intensity. The relative fraction of the TQ signal to the SQ signal is $10\,\%$ assuming relaxation rates in the human brain (Hancu et al., 1999; Navon, 1993; Tsang et al., 2012).

Early efforts of TQ MRS were driven by the prospect of becoming an intracellular-sensitive and shift reagent-free method (Dizon et al., 1996; Schepkin et al., 1996, 1998). The intracellular-sensitivity of the TQ signal is motivated as follows. The extracellular Na^+ content is high, yet there are few proteins in the extracellular space. The intracellular space has lower Na^+ content and yet an abundance of macromolecules and proteins as quadrupolar interaction sites. If the extracellular condition is kept constant, i.e. in perfused organs, then changes in the ^{23}Na TQ signal can be assigned to changes of the intracellular TQ signal. In diseased tissue, the TQ signal strength may be different due to changes in the molecular composition and ion content. Therefore, changes on the most fundamental level of a disease may be detected as changes in the strength and the correlation times of the ^{23}Na TQ signals (Griffey et al., 1990).

The TQ spectroscopy with time-proportional phase incrementation (TQ-TPPI) acquires SQ and TQ signals simultaneously. By time-proportional incrementation of the RF pulse phase, it separates SQ, double-quantum (DQ) and TQ signal contributions in frequency (Bodenhausen et al., 1980; Drobny et al., 1978; van der Maarel, 2003b,a). This sequence has been applied to investigate the competitive binding between Na^+ and potassium ions K^+ (Schepkin et al., 2017), the inhibition of the sodium-potassium-ATPase in cells in a bioreactor (Neubauer et al., 2017) and the characteristics of the TQ signal in liposomes (Hoesl et al., 2019).

Going one step further, the global MQ spectroscopy signal can be spatially encoded to obtain MQ images. TQ imaging based on the conventional TQ filter has been demonstrated in phantoms (Wimperis and Wood, 1991; Wimperis et al., 1992) and applied to the knee (Borthakur et al., 1999) and the brain (Hancu et al., 1999; Mirkes et al., 2016; Tsang et al., 2012). One preclinical study in the brain observed an increase in TQ signal despite unvarying SQ signal after ischemia (LaVerde et al., 2007). Fiege et al. (2013) developed the SISTINA sequence to acquire SQ signal in radial k-space readout and TQ signal in Cartesian readout in one measurement. However, SISTINA lacks comparability between the SQ and the TQ images. The images are not acquired at the same time point within the pulse sequence, nor are they encoded with the same readout gradient.

The main objective of this thesis was to develop a **t**riple- **a**nd **s**ingle-quantum **T**PPI **i**maging (TASTI) method. The TASTI sequence aims at acquiring SQ and TQ images as well as relaxation time and TQ-to-SQ-ratio maps under identical conditions in one single measurement.

In the first step of the thesis, a density-adapted radial (DA-R) imaging technique was implemented at the preclinical scanner. The aim was to establish a ^{23}Na and ^{35}Cl imaging routine with high efficiency in SNR on the one hand and to prepare the imaging unit for the localized MQ spectroscopy on the other hand. The DA-R sequence was validated in terms of SNR improvement and resolution capacity in ^{35}Cl phantom images. The SNRs in ^{23}Na and ^{35}Cl images in the bioreactor, rat head and rat torso were evaluated.

In the second step, the objective acquire TQ-TPPI data in phantoms and living systems, with the focus to differentiate between the quadrupolar interactions of Na^+ and Cl^-. A fit routine to determine the ratio between the TQ and the SQ signal fraction as well as the relaxation times was applied. In agarose phantoms, the fitted relaxation times were compared with those obtained from conventional spin echo measurements. Furthermore, the acquisition of global SQ and TQ signal was probed in rat head *in vivo* and in the bioreactor *in vitro*.

In the final step, the TASTI sequence was implemented by combining the RF pulse sequence and phase cycling scheme of TQ-TPPI with the DA-R imaging readout. This way, the SQ and the TQ image were acquired simultaneously under the same conditons. An offline reconstruction pipeline was written to perform voxel-wise fitting. It yields additional localized parameter maps of the transverse relaxation times as well as the ratio between the TQ and the SQ signal. The method was validated in phantoms for ^{23}Na and ^{35}Cl. Lastly, its applicability in rat head *in vivo* was probed.

2 Theoretical Background

This chapter covers the physics of NMR. The relaxation properties and the connections to the biological background of nuclei with $I = \frac{3}{2}$ are described. Extensive account on NMR and spin dynamics can be found in books such as Dubbers and Stoeckmann (2013), De Graaf (2007), Haacke et al. (1999), Levitt (2008) and Reiser et al. (2007).

2.1 Nuclear Magnetic Resonance

In the 1920s the concept of electron spin and magnetic moment was established by a number of studies including the infamous Stern-Gerlach experiment (Gerlach and Stern, 1924). Following that discovery, the nuclear spin and the nuclear magnetic moment of the hydron nucleus ^{1}H were detected by Rabi et al. (1938). In the next step, Purcell et al. (1946) and Bloch (1953)described the bulk magnetization of the nuclear magnetic moment in paraffin wax and water samples, respectively. This progress in basic physical research enabled extensive initial applications of NMR in spectrsocopy. Technical advances in super-conducting magnets helped paving the road to the independent development of NMR imaging by Lauterber (1974) and Damadian (1971).

Sections 2.1 and 2.2 follow the footsteps of the pioneers and treat the basics of NMRfrom the point of view of classical mechanics and quantum mechanics.

2.1.1 Nuclear Spin and Nuclear Zeeman Effect

Nuclei with a nuclear spin $I > 0$ are associated with a magnetic moment μ_{I} with

$$\boldsymbol{\mu}_{\mathrm{I}} = \gamma \boldsymbol{I} \; . \tag{2.1}$$

The proportionality factor γ is the nucleus-specific gyromagnetic ratio. It can assume positve or negative values and is expressed by

$$\gamma = g_{\mathrm{I}} \cdot \frac{\mu_{\mathrm{N}}}{\hbar} \; . \tag{2.2}$$

For $\gamma > 0$, the spin angular momentum $\boldsymbol{I}$, also refered to as the (nuclear) spin in short, is parallel to the magnetic moment $\boldsymbol{\mu}_{\mathrm{I}}$; for $\gamma < 0$, the spin angular momentum is antiparallel to the magnetic moment. The Planck constant is $\hbar = \frac{h}{2\pi} = 1.0545 \cdot 10^{-34}$ Js, and the Landé g-factor g_{I} is a nucleus-specific factor. The nuclear magneton μ_{N} is defined analogous to the Bohr magneton μ_{B} of the electron

$$\mu_{\mathrm{N}} = \frac{e\hbar}{2m_{\mathrm{p}}} = \frac{m_{\mathrm{e}}}{m_{\mathrm{p}}}\mu_{\mathrm{B}} \approx \frac{1}{1836}\mu_{\mathrm{B}} = 5.05 \cdot 10^{-27}\,\text{J/T} \; , \tag{2.3}$$

where e is the elementary charge and m_{p} is the mass of the proton.

The magnetic moment μ_{I} of a nucleus interacts with the magnetic field of the surrounding molecular environment as well as that of an external source. The Zeeman effect describes the splitting of energy levels in the presence of an external magnetic field.

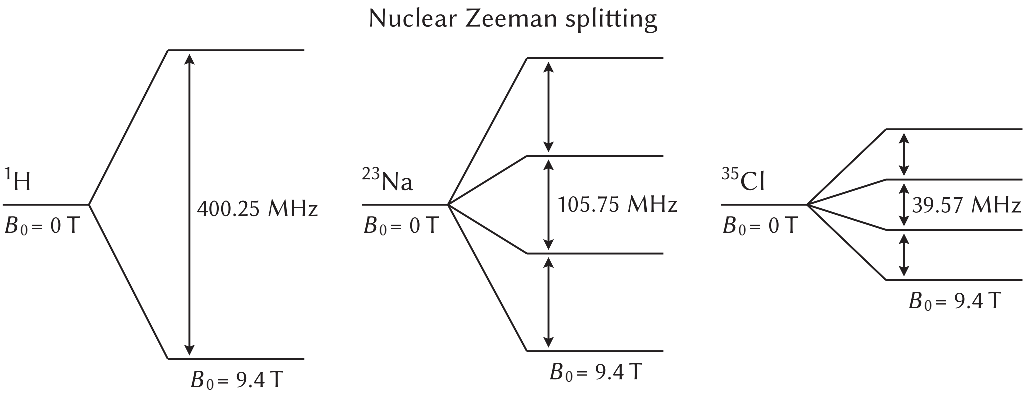

Figure 2.1: Scaled nuclear Zeeman effect at $B_0 = 9.4\,\mathrm{T}$ illustrated for the ^{1}H, the ^{23}Na and the ^{35}Cl nucleus. Th energy levels of the ^{23}Na and the ^{35}Cl nucleus are equidistant.

To deduct the energy difference between two Zeeman energy levels, first consider the spin angular momentum operator $\hat{\boldsymbol{I}} = \left(\hat{I}_{\mathrm{i}},\, \hat{I}_{\mathrm{j}}\,,\, \hat{I}_{\mathrm{k}}\right)$. The commutator identities of angular momentum operators state

$$[\hat{I}_{\mathrm{i}}, \hat{I}_{\mathrm{j}}] = i\hbar\varepsilon_{\mathrm{ijk}}\hat{I}_{\mathrm{k}} \quad \text{and} \quad [\hat{\boldsymbol{I}}^2, \hat{I}_{\mathrm{i}}] = 0 \ . \tag{2.4}$$

If the z-axis is chosen to be the axis of quantization, then the eigenvalue equations are

$$\hat{\boldsymbol{I}}^2|I,m\rangle = \hbar^2 I(I+1)|I,m\rangle \quad \text{and} \quad \hat{I}_z|I,m\rangle = \hbar m|I,m\rangle \ . \tag{2.5}$$

The magnetic quantum number m can assume values such that

$$m = -I, -I+1, \ldots, +I-1, +I \ . \tag{2.6}$$

Without an external magnetic field, the energy level is $(2I+1)$-fold degenerated. In the presence of an external magnetic field, the energy states of the nuclear spin are split into $2I+1$ individual states characterized by the magnetic quantum number m. If the external magnetic field $\boldsymbol{B}_0$ is applied in the z-direction, the external perturbation can be expressed by the Hamiltonian $\hat{\mathcal{H}}$ with

$$\hat{\mathcal{H}} = -\hat{\boldsymbol{\mu}}\boldsymbol{B}_0 = -\hat{\mu}_{\mathrm{z}}B_0 = -\gamma\hat{I}_{\mathrm{z}}B_0 \ . \tag{2.7}$$

The minus sign in Equation (2.7) indicates that the magnetic energy is at a minimum if the magnetic moment is parallel to the magnetic field. Solving Equation (2.7) with Equation (2.5) and the Schrödinger equation yields

$$\hat{\mathcal{H}}|I,m\rangle = E_{\mathrm{m}}|I,m\rangle \ , \tag{2.8}$$

with the eigenvalue E_{m} of each energy state

$$E_{\mathrm{m}} = -m\gamma\hbar B_0 \ . \tag{2.9}$$

For ^{1}H, ^{23}Na and ^{35}Cl, the Zeeman splitting is illustrated in Figure 2.1. The energy difference between two neighboring states depends on γ and B_0:

$$\Delta E = -m\gamma\hbar B_0 - (-m-1)\gamma\hbar B_0 = \hbar\gamma B_0 \tag{2.10}$$

The lower energy state is present if the nuclear magnetic moment μ_I is parallel to B_0, whereas the higher energie state is present if μ_I and B_0 are antiparallel. For nuclei with $\gamma > 0$, the nuclear spin and the magnetic moment point in the same direction, therefore $m = +I$ is the lowest possible energy level. For nuclei with $\gamma < 0$, the situation is reversed, and $m = -I$ is the lowest possible energy level.

In order for energy transition to occur, a photon with the energy $\hbar\omega_0$ needs to be emitted or absorbed. Equation (2.10) can be rewritten as

$$\Delta E = \hbar\omega_0 \tag{2.11}$$

with the nucleus-specific Larmor frequency ω_0 defined as

$$\omega_0 = \gamma B_0 \ . \tag{2.12}$$

By applying a radio-frequency (RF) pulse B_1 with the Larmor frequency ω_0 perpendicular to B_0, transitions from lower energy states to higher energy states are induced.

2.1.2 Macroscopic Magnetization

In the absence of an external magnetic field, the distribution of the spin polarization axes is isotropic. Consequently, the magnetic moments point in all directions. When an external magnetic field is turned on, each magnetic moment starts to precess around the axis of the magnetic field with the Larmor frequency. Thermal movements on the molecular level lead to a fluctuating local magnetic field, so that the spins assume precession cones with slightly different orientations and angles after some time. On a time scale much longer than the reciprocal of the Larmor frequency, a small, yet detectable bias of the orientation of the magnetic moment parallel to the external magnetic field emerges. The majority of the spins precess on a cone around the external magnetic field with a non-zero angle. Only a tiny fraction of spins are exactly parallel or anti-parallel to the external magnetic field. The time scale, on which thermal equilibrium is established, is described in Section 2.1.3.

At thermal equilibrium, the occupation probability p_m of an energy state due to Zeeman splitting is described by the normalized Boltzmann factor

$$p_m = \frac{1}{Z} \cdot \mathrm{e}^{-E_m/k_\mathrm{B}T} \tag{2.13}$$

where T stands for the temperature and $k_\mathrm{B} = 1.38 \cdot 10^{-23}$ J/K is the Boltzmann constant. The partition function Z is given by

$$Z = \sum_{m=-I}^{I} \mathrm{e}^{-E_m/k_\mathrm{B}T} \ . \tag{2.14}$$

Consider an imaging voxel of 1 mm^3 consisting of water only. Multiplying the hydrogen molarity of water ($0.11 \cdot 10^6\,\mathrm{mM} = 0.11 \cdot 10^{-3}\,\mathrm{mol/mm^3}$) with the Avogadro constant ($N_\mathrm{A} = 6.02 \cdot 10^{23}\,\mathrm{mol}^{-1}$) yields $6.62 \cdot 10^{19}$ hydrogen nuclei per voxel. The assumption of a macroscopic magnetization is justified given the vast amount of available nuclei. It can be expressed as a sum of the expected value of every single nuclear magnetic moment $\langle\hat{\boldsymbol{\mu}}_i\rangle$ over the volume:

$$\boldsymbol{M} = \sum_{i=1}^{N} \frac{\langle\hat{\boldsymbol{\mu}}_i\rangle}{V} = \sum_{i=1}^{N} \frac{\gamma\langle\hat{\boldsymbol{I}}_i\rangle}{V} = \frac{N}{V} \cdot \gamma\hbar \cdot \sum_{m=-I}^{I} p_m m \ . \tag{2.15}$$

At a body temperature of approximately $T = 310\,\mathrm{K}$, the ratio between the population of the higher energy state $N_{m=-1/2}$ and that of the lower energy state $N_{m=+1/2}$ is

$$\frac{N_{m=-1/2}}{N_{m=+1/2}} = \mathrm{e}^{-\Delta E/k_\mathrm{B}T} = \mathrm{e}^{-\gamma\hbar B_0/k_\mathrm{B}T} \ . \tag{2.16}$$

If an external magnetic field with the field strength of $B_0 = 3\,\mathrm{T}$ is applied, there will be approximately 3 nuclei per million that contribute to the macroscopic magnetization M_0 in thermal equilibrium. This small percentage contribution is made up by the vast number of $6.62 \cdot 10^{19}$ hydrogen nuclei per $1\,\mathrm{mm}^3$.

Using the high temperature approximation $E_m \ll k_\mathrm{B}T$ satisfied for room temperature and the Taylor expansion, the macroscopic magnetization M_0 can be simplified to

$$M_0 \approx \rho_0 \frac{\gamma^2\hbar^2 I(I+1)}{3k_\mathrm{B}T} B_0 \ , \tag{2.17}$$

with $\rho_0 = N/V$ as the spin density.

2.1.3 Bloch Equation

The time evolution of $\boldsymbol{M}$ of nuclei with $I = \frac{1}{2}$ can be described similarly to the torque equation in classical mechanics in a phenomenological approach by Bloch:

$$\frac{d}{dt}\boldsymbol{M} = \gamma\left(\boldsymbol{M} \times \boldsymbol{B}\right) \ . \tag{2.18}$$

It follows that as long as $\boldsymbol{M}$ has a component that is not parallel to $\boldsymbol{B}$, $\boldsymbol{M}$ will precess around $\boldsymbol{B}$. The thermal equilibrium can be perturbed by a time-dependent magnetic field $\boldsymbol{B}_1(t)$ that has the Larmor frequency ω_0 and is perpendicular to the static magnetic field $\boldsymbol{B}_0$. This way, transitions between the Zeeman energy states are induced. The $\boldsymbol{B}_1(t)$ field is also more commonly referred to as the RF pulse. Assume $\boldsymbol{B}_0 = (0,\, 0,\, B_0)^T$, then $\boldsymbol{B}_1(t)$ can be expressed by

$$\boldsymbol{B}_1(t) = \begin{pmatrix} B_1\cos(\omega_0 t) \\ B_1\sin(\omega_0 t) \\ 0 \end{pmatrix} \ , \tag{2.19}$$

resulting in an effective magnetic field of $\boldsymbol{B}_\mathrm{eff} = \boldsymbol{B}_0 + \boldsymbol{B}_1$. Equation (2.18) becomes

$$\frac{d}{dt}\boldsymbol{M} = \gamma\boldsymbol{M} \times \begin{pmatrix} B_1\cos(\omega_0 t) \\ B_1\sin(\omega_0 t) \\ B_0 \end{pmatrix} \ . \tag{2.20}$$

The transverse component of the magnetization in the xy-plane precesses with the Larmor frequency around the z-axis; the overall motion of $\boldsymbol{M}$ is overlapped by precession around the $\boldsymbol{B}_0$-axis and the $\boldsymbol{B}_1$-axis. The motion of precession around the $\boldsymbol{B}_0$-axis is discarded by transforming into a rotating frame of reference (superscript 'rot') around the $\boldsymbol{B}_0$-axis and rotating at the Larmor frequency. Let the $\boldsymbol{B}_1$ field point in x^rot-direction, then Equation 2.20 becomes

$$\frac{d}{dt}\boldsymbol{M}^\mathrm{rot} = \gamma\boldsymbol{M}^\mathrm{rot} \times \begin{pmatrix} B_1 \\ 0 \\ 0 \end{pmatrix} = \gamma\boldsymbol{M}^\mathrm{rot} \times \boldsymbol{B}_\mathrm{eff}^\mathrm{rot} \ . \tag{2.21}$$

In the rotating frame of reference, the RF pulse tips the net magnetization around $\boldsymbol{B}_{\text{eff}}^{\text{rot}}$.

The flip angle α between $\boldsymbol{B}_0$ and $\boldsymbol{M}^{\text{rot}}$ depends on the the duration τ_{p} and the amplitude B_1 of the RF pulse such that

$$\alpha = \gamma \int_{0}^{\tau_{\text{p}}} B_1(t)\text{d}t \ . \tag{2.22}$$

In case of a rectangular excitation pulse, Equation (2.22) can be simplified to

$$\alpha = \gamma \tau_{\text{p}} B_1 = \omega_1 \tau_{\text{p}} \ . \tag{2.23}$$

Assuming $\boldsymbol{B}_0 = (0,\, 0,\, B_0)^T$, $\boldsymbol{M}$ can be divided into a component parallel to $\boldsymbol{B}_0$, the longitudinal magnetization $\boldsymbol{M}_{\text{z}}$, and a component perpendicular to $\boldsymbol{B}_0$, the transverse magnetization $\boldsymbol{M}_{xy}$ (Equation 2.29).

After the application of an RF pulse, the magnetization returns to the state of thermal equilibrium by relaxation mechanisms depending on the nucleus and the environment (Section 2.2). The process of relaxation is described by the Bloch equations with the relaxation rates $1/T_1$ and $1/T_2$

$$\begin{aligned} \text{d}M_{\text{x}}/\text{dt} &= \gamma \left(\boldsymbol{M} \times \boldsymbol{B}\right)_{\text{x}} - M_x/T_2 \ , \\ \text{d}M_{\text{y}}/\text{dt} &= \gamma \left(\boldsymbol{M} \times \boldsymbol{B}\right)_{\text{y}} - M_y/T_2 \ , \\ \text{d}M_{\text{z}}/\text{dt} &= \gamma \left(\boldsymbol{M} \times \boldsymbol{B}\right)_{\text{z}} - \left(M_0 - M_{\text{z}}\right)/T_1 \ . \end{aligned} \tag{2.24}$$

Macroscopic Description of the Longitudinal Relaxation

The probability of spontaneous emission, postulated by Einstein, is proportional to f^3. For the visible part of the electromagnetic spectrum with $f \approx 10^{12}$ Hz, the probability is high. For the radiofrequency part of the spectrum with $f \approx 10^8$ Hz, spontaneous emission after an RF pulse is highly unlikely. Energy emission in NMR is therefore induced through interactions with the external environment. This relaxation process is called the longitudinal relaxation.

Solving the first order differential equation

$$\frac{d}{dt} M_{\text{z}} = \gamma \left(\boldsymbol{M} \times \boldsymbol{B}\right)_{\text{z}} - \frac{1}{T_1}\left(M_0 - M_{\text{z}}\right) \tag{2.25}$$

yields the solution

$$M_{\text{z}}(t) = M_{\text{z}}(0)\text{e}^{-t/T_1} + M_0\left(1 - \text{e}^{-t/T_1}\right) \ . \tag{2.26}$$

If a pulse with $\alpha = 90°$ is applied, then $M_{\text{z}}(0) = 0$ and Equation (2.26) becomes

$$M_{\text{z}}(t) = M_0\left(1 - \text{e}^{-t/T_1}\right) \ . \tag{2.27}$$

Macroscopic Description of Transverse Relaxation

The transverse relaxation does not involve energy transfer contrary to the longitudinal relaxation. For a spin ensemble to be coherent in phase, a consistent polarization direction must be ensured. In reality, however, each nucleus produces a local magnetic field due to its nuclear magnetic moment, and is in return influenced by the sum of the local magnetic fields of other nuclei in the vicinity. Due to Brownian motion, each nucleus experiences a different magnetic field $B_0 + B_{\mathrm{loc}}(t)$ depending on the local fluctuating magnetic field $B_{\mathrm{loc}}(t)$. The Larmor frequency of each nucleus is therefore also dependet on $B_{\mathrm{loc}}(t)$ such that $\omega(t) = \gamma\,(B_0 + B_{\mathrm{loc}}(t))$. This leads to an accumulation of phase differences among the nuclei and thus to a loss of phase coherence. This process increases the entropy and is irreversible.

In order to solve the set of Bloch equations

$$\begin{aligned} \mathrm{d}M_x/\mathrm{dt} &= \gamma\,(\boldsymbol{M} \times \boldsymbol{B})_{\mathrm{x}} - M_{\mathrm{x}}/T_2 \text{ and} \\ \mathrm{d}M_y/\mathrm{dt} &= \gamma\,(\boldsymbol{M} \times \boldsymbol{B})_{\mathrm{y}} - M_{\mathrm{y}}/T_2\,, \end{aligned} \tag{2.28}$$

it is helpful to rewrite the transverse magnetization M_{xy} as a complex entity. The x- and y-components are acquired simultaneously by RF coils and form the complex signal

$$M_{xy} = M_x + \mathrm{i}M_y = |M_{xy}| \cdot \mathrm{e}^{\mathrm{i}\phi}\ . \tag{2.29}$$

Assuming a homogeneous magnetic field B_0, Equation (2.28) is simplified to

$$\frac{d}{dt}M_{xy} = -\mathrm{i}\gamma B_0 M_{xy} - \frac{1}{T_2}M_{xy}\ . \tag{2.30}$$

The solution of this first order differential equation yields

$$M_{xy}(t) = M_{xy}(0)\mathrm{e}^{-\mathrm{i}\omega_0 t}\mathrm{e}^{-t/T_2}\ , \tag{2.31}$$

In the rotating frame of reference, the precession is not observed and Equation (2.31) becomes

$$M_{xy}^{\mathrm{rot}}(t) = M_{xy}(0)\mathrm{e}^{-t/T_2}\ . \tag{2.32}$$

In the laboratory frame of reference, the trajectory formed by the overlay of $M_{\mathrm{z}}(t)$ and $M_{xy}(t)$ is a three-dimensional helical spiral, which spirals from the x-y-plane towards the z-axis.

The longitudinal and the transverse relaxation processes are independent from each other in the sense that they are of intrinsically different physical nature. The practical upper limit of T_2 is set by T_1 (Levitt (2008))

$$T_2 \leq T_1\ . \tag{2.33}$$

T_2^* Relaxation

Additional to the local fluctuating magnetic fields $B_{\mathrm{loc}}(t)$, local static magnetic field inhomogeneities contribute to a reversible phase coherence loss depending on $T_2^{'}$. These inhomogeneities are caused by imperfect B_0 or susceptibility-induced field distortions caused by the measured object. The signal recorded for the transverse relaxation with the relaxation rate

$$\frac{1}{T_2^*} = \frac{1}{T_2} + \frac{1}{T_2^{'}} = R_2 + R_2^{'} \tag{2.34}$$

is referred to as the free induction decay (FID). It follows that $T_2 \geq T_2^*$. The effects of the static inhomogeneities can be reversed by a $180°$ RF pulse to determine the medically relevant T_2 values.

2.1.4 Sensitivity

The ^{1}H nucleus bound in water molecules is the only investigated nucleus in clinical NMR. The high gyromagnetic ratio and isotope percentage of ^{1}H leads to a high physical sensitivity. Furthermore, water molecules are abundant in the human body. X-nuclei, on the other hand, face the fundamental issue of low physical sensitivity and biological abundance, the former of which is explored in the following.

The physical NMR sensitivity S_{phy} of an isotope is proportional to the voltage induced in the receiver coil (Hoult and Richards, 1976). Using the expression for M_0 from Equation (2.17), S_{phy} of a nucleus with the spin quantum number I and the isotope abundance c can be estimated by Hancu et al. (1999)

$$S_{\text{phy}} \propto U_{\text{ind}} \propto c\gamma^3 I(I+1) \ . \tag{2.35}$$

The relevant sensitivity with regard to ^{1}H is listed in Table 2.1. The total sensitivity of a nucleus further includes the influence of the biological abundance c_{bio} and reads

$$S_{\text{total}} = S_{\text{phy}} \cdot c_{\text{bio}} \ .$$

Table 2.1: A selection of nuclei with their corresponding nuclear spin I, gyromagnetic ratio $\frac{\gamma}{2\pi}$, isotope abundance c, the physical NMR sensitivity S_{phy} relative to ^{1}H and the Larmor frequency ω_0 at 9.4 T (Harris et al., 2002).

element	I	$\frac{\gamma}{2\pi}$ $(\frac{\text{MHz}}{\text{T}})$	c (%)	relative S_{phy}	ω_0 at 9.4 T (MHz)
$^{1}_{1}$H	$\frac{1}{2}$	42.58	99.99	1	400.25
$^{23}_{11}$Na	$\frac{3}{2}$	11.25	100	9.3×10^{-2}	105.75
$^{35}_{17}$Cl	$\frac{3}{2}$	4.21	75.78	3.6×10^{-3}	39.57
$^{39}_{1}$K	$\frac{3}{2}$	1.99	93.26	4.8×10^{-4}	18.71
$^{17}_{8}$O	$\frac{5}{2}$	-5.77	0.037	1.1×10^{-5}	54.24

In general, the total sensitivity S_{total} cannot be enhanced unless additional substances are introduced into the imaging subject to increase the isotope or the biological abundance. However, technical strategies are available to increase the overall measured signal. To deduct strategies to combat the low signal strength in X-nuclei NMR, the dependencies of the macroscopic magnetiziaton M_0 and the signal-to-noise-ratio (SNR) can be consulted. The macroscopic magnetization is affected by the static magnetic field strength B_0 and the temperature T. It is given by Equation 2.17. The SNR further takes the effect of the relaxation constants T_1 and T_2 (see Subsection 2.1.3) and sequence parameters voxel volume $(\Delta x)^3$, readout time T_{RO} and total acquisition time T_{AQ} into account. It is proportional to

$$\text{SNR} \propto (\Delta x)^3 \cdot \sqrt{T_2/T_1} \cdot B_0^k \cdot \sqrt{T_{\text{RO}}} \cdot \sqrt{T_{\text{AQ}}} \ , \tag{2.36}$$

with static magnetic field strength B_0 to the power of k. The noise contribution may be dominated by the electrical components of the coil ($k = \frac{7}{4}$) or by the imaging subject ($k = 1$).

2.2 Quadrupole Nuclei

Quadrupole nuclei with $I > \frac{1}{2}$ have an electric-quadrupole moment caused by the deformation of the nucleus. The electric-quadrupole moment interacts with the electric field gradients. This relaxation mechanism is much stronger than the magnetic dipole-dipole interaction by which the relaxation of dipole nuclei with $I = \frac{1}{2}$ is goverened. Bloch equations can only be used in limited cases as a phenomenological approach to describe relaxation of quadrupole nuclei.

This section provides a discussion on the different relaxation mechanisms of quadrupole nuclei with a focus on electric-quadrupole interaction. Subsequently, the spin density operator expressed in the irreducible tensor basis is introduced along with solutions to differential equations under the effect of RF pulses or electric-quadrupole relaxation. Finally, concepts essential for the MQ spectroscopy such as coherence pathway transfer and phase cycling are explained. Detailed account on the dynamics of nuclei with $I = \frac{3}{2}$ can be found in Levitt (2008), Ernst et al. (1987), van der Maarel (2003b), van der Maarel (2003a) and Matthies (2010).

2.2.1 Nuclear Spin Hamiltonian

In general, the Hamilton operator $\hat{\mathcal{H}}_{\text{full}}$ covers all interactions between all electrons and nuclei inside the sample. The quantum state of the sample is given by the wave function $|\psi_{\text{full}}\rangle$. To describe the dynamics of nuclear spins, the time-dependent Schrödinger equation

$$\frac{d}{dt}|\psi_{\text{full}}(t)\rangle = -\mathrm{i}\hat{\mathcal{H}}_{\text{full}}|\psi_{\text{full}}(t)\rangle \tag{2.37}$$

has to be solved. The magnetic and electrical influences of the electrons can be expressed by a time-invariant average, assuming that they are on an entirely different timescale. The general Hamiltonian $\hat{\mathcal{H}}_{\text{full}}$ becomes the nuclear spin Hamiltonian $\hat{\mathcal{H}}_{\text{spin}}$ such that only the directions of the nuclear spin polarizations are taken into account. This *spin Hamiltonian hypothesis* allows the Schrödinger equation

$$\frac{d}{dt}|\psi_{\text{spin}}(t)\rangle \cong -\mathrm{i}\hat{\mathcal{H}}_{\text{spin}}|\psi_{\text{spin}}(t)\rangle \tag{2.38}$$

to be solved within the framework of NMR. The quantum states $|\psi_{\text{spin}}\rangle$ are now limited to the nuclear spin states.

In order to understand the dynamics of a spin ensemble, first consider the interactions between a single nucleus and its surrounding. The electric charge of a nucleus interacts with electric fields, and the nuclear magnetic moment interacts with magnetic fields. The energy of the nucleus depends on its orientation with respect to the surrounding electric and magnetic fields. For both dipole and quadrupole nuclei, the Hamiltonian $\hat{\mathcal{H}}_j$ of a nuclear spin I_j

$$\hat{\mathcal{H}}_j = \hat{\mathcal{H}}_j^{\text{elec}} + \hat{\mathcal{H}}_j^{\text{mag}} \ , \tag{2.39}$$

is a sum of the electric spin Hamiltonian $\hat{\mathcal{H}}_j^{\text{elec}}$ (Subsection 2.2.2) and the its magnetic spin Hamiltonian $\hat{\mathcal{H}}_j^{\text{mag}}$

$$\hat{\mathcal{H}}_j^{\text{mag}} = \hat{\boldsymbol{\mu}}_j \cdot \boldsymbol{B} \ . \tag{2.40}$$

Interactions can also be categorized as external and internal spin interactions. External spin interactions are between the nucleus and the electric or magnetic fields of an external source. They include interactions with the RF pulse, the gradient fields, and Zeeman interactions with the external magnetic field. Internal spin interactions are between the nucleus and the electric and magnetic fields from within the sample. They include chemical shift, dipole-dipole coupling, J-coupling and electric-quadrupole coupling. The types of interactions are illustrated in Figure 2.2.

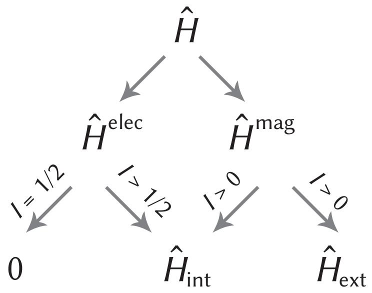

Figure 2.2: Types of spin interactions according to the nature (electric or magnetic) and the source of field (external and internal). Electric interactions are experienced by nuclei with $I > 1/2$ only, while all NMR-compatible nuclei are subject to magnetic interactions.

2.2.2 Electric-Quadrupole Coupling

The electric-quadrupole coupling between the electric quadrupole moment of the nucleus and the surrounding electric field gradients (EFG) is determined by the magnitude, orientation and temporal duration of the EFG. If the orientation of the EFG is equally distributed due to rapid motion on a timescale of the Larmor period, the electric-quadrupole coupling is averaged to zero. In anisotropic systems, however, the EFG is not averaged to zero. Such is the case in which the electric-quadrupole coupling causes a shift in the energy levels and frequency splitting in the spectrum.

In the following the energy difference caused by the electric-quadrupole coupling and the corresponding electric-quadrupole coupling frequency are deducted.

First consider the electric charge distribution $\rho(\boldsymbol{r})$ of a nucleus with the classical definition

$$\rho(\boldsymbol{r}) = Ze\Psi * (\boldsymbol{r})\Psi(\boldsymbol{r}) \tag{2.41}$$

with the atomic number Z and the elementary charge e. This electric charge distribution can be represented by a superposition of electric multipoles such that

$$\rho(\boldsymbol{r}) = \rho^{(0)}(\boldsymbol{r}) + \rho^{(1)}(\boldsymbol{r}) + \rho^{(2)}(\boldsymbol{r}) + \dots\ , \tag{2.42}$$

with spherical electric charge distribution $\rho^{(0)}(\boldsymbol{r})$, the electric-dipole charge distribution $\rho^{(1)}(\boldsymbol{r})$ and the electric-quadrupole charge distribution $\rho^{(2)}(\boldsymbol{r})$. The magnitude terms correspond to the total electric charge $\rho^{(0)}$, the electric-dipole moment $\rho^{(1)}$ and the electric-quadrupole moment $\rho^{(2)}$. Additionally, $\rho^{(n)} = 0$ for $n > 2I$. Therefore Equation (2.42) has a limited number of terms depending on the nucleus. For nuclei with $I = \frac{1}{2}$, the terms of the electric charge distribution terminates after $\rho^{1}(\boldsymbol{r})$; for nuclei with $I = \frac{3}{2}$, it terminates after $\rho^{3}(\boldsymbol{r})$.

Similarly, the electric potential $\phi(\boldsymbol{r})$ can be expressed by

$$\phi(\boldsymbol{r}) = \phi^{(0)}(\boldsymbol{r}) + \phi^{(1)}(\boldsymbol{r}) + \phi^{(2)}(\boldsymbol{r}) + \dots\ , \tag{2.43}$$

with the electric potential at the center of the nucleus $\phi^{(0)}$, the gradient of the electric potential i.e. the electric field $\phi^{(1)}$, and the gradient of the electric field $\phi^{(2)}$.

In general, the potential energy E_elec of the electric charge distribution $\rho(\boldsymbol{r})$ inside the electric potential $\phi(\boldsymbol{r})$ is

$$E_\text{elec} = \int \rho(\boldsymbol{r})\phi(\boldsymbol{r})\mathrm{d}^3r \ . \tag{2.44}$$

Taylor expansion at $\boldsymbol{r} = 0$ allows for interpretation of the individual superposition terms

$$E_\text{elec} = E^{(0)}_\text{elec} + E^{(1)}_\text{elec} + E^{(2)}_\text{elec} \cdots \tag{2.45}$$

with

$$E^{(0)}_\text{elec} = \phi_0 Ze \ , \tag{2.46}$$

$$E^{(1)}_\text{elec} = \sum_{i=1}^{3} \left(\frac{\partial\phi}{\partial x_i}\right)_0 \int \rho(\boldsymbol{r}) x_i \mathrm{d}^3r \ , \tag{2.47}$$

$$E^{(2)}_\text{elec} = \frac{1}{2}\sum_{i,j} \left(\frac{\partial^2\phi}{\partial x_i \partial x_j}\right)_0 \int \rho(\boldsymbol{r}) x_i x_j \mathrm{d}^3r \ . \tag{2.48}$$

- The term $E^{(0)}_\text{elec}$ describes the Coulomb energy of a point charge at $\boldsymbol{r} = 0$. This term is the same for all isotopes of the same element and determines the relative position of the nucleus to the electrons. For NMR, it is of no direct importance.
- The second term $E^{(1)}_\text{elec}$ corresponds to the interaction between the nuclear electric dipole moment with the electric field.
- The third term $E^{(2)}_\text{elec}$ represents the orientation-dependent interaction between the non-spherical electric-quadrupole charge distribution $\rho^{(2)}(\boldsymbol{r})$ of quadrupole nuclei and the electric field gradient $\phi^{(2)}(\boldsymbol{r})$.

Due to the symmetry property of parity conservation ($\rho(\boldsymbol{r}) = \rho(-\boldsymbol{r})$), the term $\rho^{(1)}$ becomes the integral over the product of an even and an odd function and therefore vanishes (see Equation (2.41) and (2.47)). Following a similar line of argumentation, other odd terms of the electric charge distribution in Equation (2.42) also vanishes.

For nuclei with $I = \frac{1}{2}$, it follows that $E_\text{elec} = E^{(0)}_\text{elec}$. This implies that the potential energy of dipole nuclei depends neither on the external electric potential nor on the orientation or structure of the nucleus. In the absence of the interaction between the nucleus and the surrounding electric potential, the Hamiltonian can be simplified to be

$$\hat{\mathcal{H}}^\text{elec} = 0 \quad \rightarrow \quad \hat{\mathcal{H}} = \hat{\mathcal{H}}^\text{elec} + \hat{\mathcal{H}}^\text{mag} = \hat{\mathcal{H}}^\text{mag} \ (\text{for } I = \frac{1}{2}) \ . \tag{2.49}$$

For quadrupole nuclei, on the other hand, both magnetic and electric interactions determine the behavior in the context of NMR. The tensor V_{ij} of the EFG is defined as

$$\left(\frac{\partial^2\phi}{\partial x_i \partial x_j}\right)_0 =: V_{ij} \ , \tag{2.50}$$

and the strength of the quadroplar coupling is given by the value of the EFG tensor at the location of the nucleus ($\boldsymbol{r} = 0$). The electric-quadrupole energy $E^{(2)}_\text{elec}$ can be written as

$$E^{(2)}_\text{elec} = \frac{1}{6}\sum_{i,j} \left(V_{ij} Q_{ij} + V_{ij}\delta_{ij} \int r^2 \rho(\boldsymbol{r}) \right) \ , \tag{2.51}$$

whereas

$$Q_{ij} = \int \left(3x_i x_j - r^2\delta_{ij}\right) \rho(\boldsymbol{r}) \mathrm{d}^3 r \tag{2.52}$$

is the electric-quadrupole tensor. The electric-quadrupole tensor is a measure for the deviation of the electric charge distribution from spherical symmetry. By diagonalizing the EFG tensor V_{ij} such that its trace $V_{xx} + V_{yy} + V_{zz}$ becomes zero by fulfilling the Laplace equation ($\boldsymbol{\nabla}^2 V$=0), the second term in Equation (2.51) vanishes. The EFG tensor can now be sufficiently described in terms of the largest principal value V_{zz} and the biaxiality parameter

$$\eta_Q = \frac{V_{xx} - V_{yy}}{V_{zz}} \ . \tag{2.53}$$

The quantum mechanical description of the electric-quadrupole tensor and the quadrupole Hamiltonian now read

$$\hat{Q}_{ij} = e \sum_{k=1}^{Z} \left(3\hat{x}_{ik}\hat{x}_{jk} - \delta_{ij}\hat{r}_k^2\right) \tag{2.54}$$

$$\hat{\mathcal{H}}_{\mathrm{Q}}^{\mathrm{elec}} = \frac{1}{6}\sum_{i,j} V_{ij}\hat{Q}_{ij} \tag{2.55}$$

In circumstances relevant to NMR, the quadrupole coupling can be viewed as a weak perturbation in comparison to the Zeeman splitting. Applying the perturbation theory of first order yields the quadrupole energy

$$\Delta E_Q = \hbar \cdot \frac{e^2 qQ}{4I(2I-1)\hbar} \left[\frac{1}{2}\left(3\cos^2\Theta - 1\right) + \frac{1}{2}\eta_Q \sin^2\Theta \cos 2\Phi\right] \left[3m^2 - I(I+1)\right] \equiv \hbar\omega_Q \ . \tag{2.56}$$

The Eular angles Θ and Φ indicate the direction of the external magnetic field B_0 with regard to the principal axes of the EFG tensor. By definition, ω_Q is the quadrupole interaction frequency. It indicates the spectral distance between the satellite and the central transition. The quadrupole energy ΔE_Q states by how much energy the spectral line is shifted against the central spectral line. In case of axial symmetry ($\eta_Q = 0$), the term $\frac{1}{2}\eta_Q \sin^2\Theta\cos 2\Phi = 0$ becomes irrelevant. At the magic angle of $\Theta = 54.7°$ the spectral shifting becomes zero. The central transition is an overlap of two Lorentz distributions, meaning that the relaxation process is bi-exponential. In general, the spectrum contains $2I$ resonance lines. In isotropic fluids and in most tissue types, however, ΔE_Q is zero overall, since the average $\langle \cos^2\Theta \rangle = 0$ is zero for an isotropic distribution of Θ.

In analogy to Equation (2.49), Equation (2.39) can now be rewritten for quadrupole nuclei

$$\hat{\mathcal{H}}^{\mathrm{elec}} = \hat{\mathcal{H}}_{\mathrm{Q}}^{\mathrm{elec}} \quad \rightarrow \quad \hat{\mathcal{H}} = \hat{\mathcal{H}}_{\mathrm{Q}}^{\mathrm{elec}} + \hat{\mathcal{H}}^{\mathrm{mag}} \ (\text{for } I > \frac{1}{2}) \ . \tag{2.57}$$

A summary of spin Hamiltonians with their relative magnitudes is shown in Figure 2.3. For quadrupole nuclei, the contribution by the quadrupole coupling is substantially stronger than that by the magnetic interactions, whereas dipole nuclei do not interact with the electric potential. Due to the strong electric-quadrupole coupling, the relaxation times of quadrupole nuclei are much smaller than those of dipole nuclei (Hubbard, 1970).

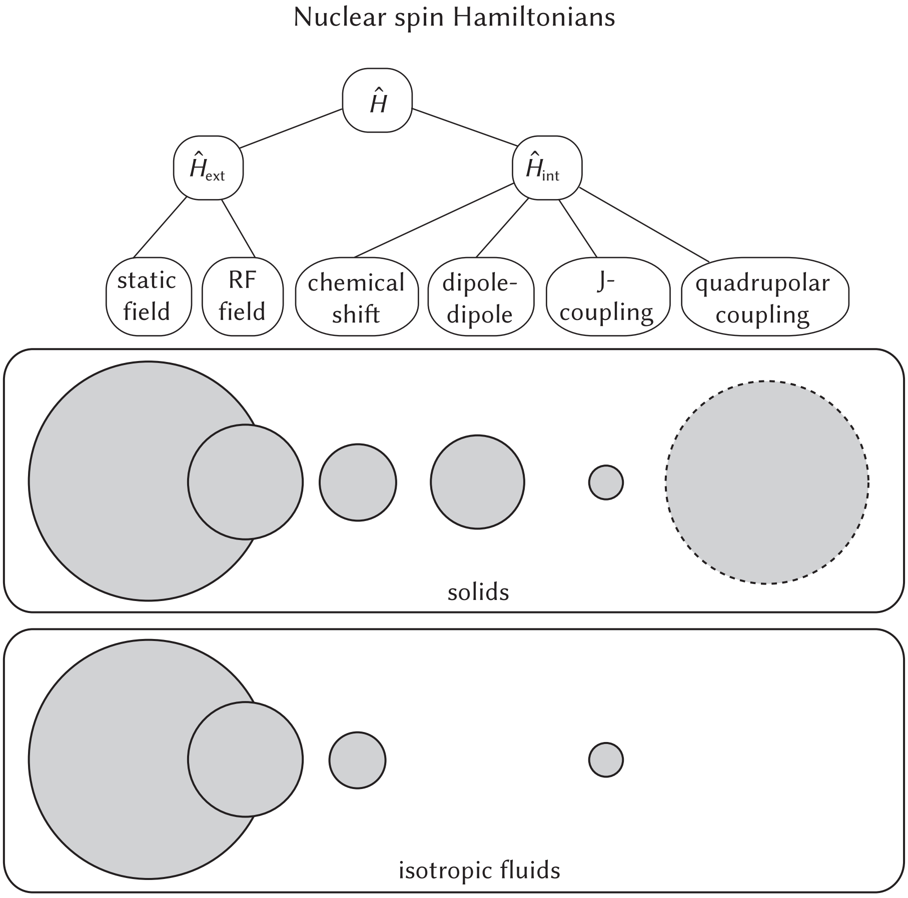

Figure 2.3: Summary of the nuclear spin Hamiltonians with their relative magnitudes for solids and isotropic liquids (adapted from Levitt (2008)). Electric-quadrupole coupling is only present for nuclei with $I > \frac{1}{2}$. It is marked by an dashed outline.

2.2.3 Static and Fluctuating Electric-Quadrupole Interaction

Two types of electric-quadrupole interactions on different time scales have to be differentiated. The local fluctuating electric-quadrupole interaction describes the interaction between the electric-quadrupole moment with the fluctuating EFG. The EFG fluctuates due to thermal motions. It is generated by the ion hydration shell or the charges of other atoms and (macro-)molecules. The macromolecules include proteins, DNA, RNA, amino acids, carbohydrates, proteoglycans, phospholipids and glycolipids Schepkin et al. (2017).The local fluctuating quadrupole interaction is averaged to zero in aqueous environment due to rapid movement. In soft tissue, on the other hand, it is the dominating relaxation mechanism on the microscopic scale Hubbard (1970). Relaxation is bi-exponential if the fluctuating electric-quadrupole interaction is not averaged to zero. In this case, both DQ and TQ coherences can be excited Rooney and Springer (1991); Jaccard et al. (1986); Pekar and Leigh (1986). The definition of MQ coherences is given in Subsection 2.2.4.

The static electric-quadrupole interaction is present in samples with global anisotropy. Anisotropic systems lacking global uniformity can be divided into domains in wich local anisotropy holds. Within each domain, static quadrupole interaction is a relevant relaxation mechanism and leads to splitting of the outer and the inner SQ transitions Madelin et al. (2014). In this case, DQ coherences can be excited in addition to TQ coherences.

In summary, TQ coherences reflect only the very brief interactions between the electric moment and the tissue EFG. DQ coherences, on the other hand, can result from either tissue anisotropy or interactions with the EFG van der Maarel (2003a). The magic angle method can be used to suppress signal from the latter origin, making the DQ signal specific to tissue anisotropy.

The SQ energy spectra of isolated systems of nuclei with $I = \frac{3}{2}$ depend on the environment. More specifically, they depend on the values of the averaged quadrupole interaction frequency $\bar{\omega}_Q$ and the product of the Larmor frequency and the correlation time $\omega_0\tau_c$ Rooney and Springer (1991). The (rotational) correlation time τ_c is the time a molecule or an ion takes to rotate 1 rad. It depends on both the size of the molecule or ion and the surrounding environment. The Larmor frequency ω_0 can also be expressed as the Larmor period ν_0 with $\nu_0 = \omega_0^{-1}$. Three types of spectra according to the classification of Rooney and Springer (1991).

Type d environment ("extreme narrow") In the case of up to moderate amount of NaCl solved in water, the fluctuations of the EFG are very rapid so that the correlation time τ_c is small compared with the Larmor period ν_0 ($\tau_c \ll \nu_0$, $\omega_0\tau_c \ll 1$). The value for ν_0 is in the order of nanosecond at 9.4 T, while τ_c is in the order of picosecond. The systematic isotropy results in a zero-average of the residual quadrupole coupling constant $\bar{\omega}_Q = 0$. It implies that the 'extreme narrow' spectrum has one resonance line only, consisting of three isochronous, degenerate spectral peaks of the three SQ coherences. T_1 and T_2 decay mono-exponentially with $T_1 = T_2$ (Jaccard et al., 1986). The relaxation rates (Subsection 2.2.7) are the same ($R_1^{(0)} = R_2^{(0)} = R_1^{(1)} = R_2^{(1)}$) and are therefore independent of ω_0 and B_0.

Type c environment ("bi-exponental/super-Lorentzian") In intra- as well as extracellular environment, (charged) macromolecules interact with sodium and chloride ions. The correlation time τ_c increases and is in the order of nanosecond. Therefore, it is in the range of the Larmor period ($\tau_c \approx \nu_0^{-1}$ and $\omega_0\tau_c \approx 1$). The rapid fluctuation of the hydration shells is overlayed by a slower modulation. This modulation is brought about by interactions between the nuclei of interest and the surrounding macromolecules and biological structures. The relaxation rates assume different values, and MQ coherences might occur (Jaccard et al., 1986). In this case the "extreme narrow" central resonance of the inner transition ($|-1/2\rangle \rightarrow |1/2\rangle$) is superimposed on the two broader Lorentzians of the outer satellite transitions ($|1/2\rangle \rightarrow |3/2\rangle$ and $|-3/2\rangle \rightarrow |-1/2\rangle$) with equal width. The inner transition pertains to the slower part of the bi-exponential relaxation with $T_{2\mathrm{s}}$, and the outer transitions to the faster part with $T_{2\mathrm{f}}$. The time period t, during which $\bar{\omega}_Q \neq 0$ is valid, is in the range of ν_0 such that $t \approx \nu_0$ and at the same time shorter than $\bar{\omega}_Q^{-1}$ such that $t < \bar{\omega}_Q^{-1}$.

Type a environment ("crystal") If the sample, typically a crystal and very unlikely a tissue sample, is anisotropic on a macroscopic scale, then $\bar{\omega}_Q > 0$ assumes one value for the entire sample on any time scale. In this case, three distinct spectral lines are observed as long as the quadrupole splitting exceeds the line width. The triplet with $2\bar{\omega}_Q$ splitting have an intensity ratio of $3 : 4 : 3$, whereby the central transition ($|-1/2\rangle \rightarrow |1/2\rangle$) makes up for 40%, and the combined satellite transitions ($|1/2\rangle \rightarrow |3/2\rangle$ and $|-3/2\rangle \rightarrow |-1/2\rangle$) make up for 60% of the total intensity. The intensity distribution is also reflected in the factors $\frac{2}{5}$ and $\frac{3}{5}$ for the slow and the fast relaxation component in the relaxation function $f_{11}^{(1)}(t)$, respectively (Equation (2.84)). The two outer energy levels are shifted up by $\bar{\omega}_Q$, while the two inner energy levels are shifted down by the same amount. The magnitude of $\bar{\omega}_Q$ is on the order of kilohertz, therefore the energy shift is relatively small compared to ω_0, which is on the order of megahertz Matthies (2010).

2.2.4 Spin Density Operator

In quantum mechanics, a quantum system in a pure state is represented by the Ket-notation of a single wavefunction $|\Psi_i\rangle$. A quantum system can also consist of many pure states, in which case it is referred to as a mixed state. The mixed state refers to an ensemble in thermal equilibrium, for which there exists no initial phase relationship between the elements of the ensemble. Unlike the case of a single wavefunction, quantum observables in a mixed state are obtained by performing statistical averaging. Given a quantum state $|\chi\rangle$, the probability of finding a particle in that state is given by $\langle\chi|\sigma|\chi\rangle$, with the density operator

$$\sigma(t) \equiv |\Psi(t)\rangle\langle\Psi(t)| \; . \tag{2.58}$$

The density operator describes the state of a quantum system and is the quantum mechanical equivalent to a classical probability density, hence the name. It can be applied to predict the probabalistic expected value of measurements on the system. In NMR, phyiscal systems are in a mixed state. The density operator is especially useful to characterize time-dependent events in a mixed state such as thermal relaxation.

Inside a spin ensemble, all individual particle ($i = 1$ to N) are found in the same internal basis states $|n\rangle$, though with varying occupation probability of these states. The wavefunction of a particle is then given by

$$|\Psi_i\rangle = \sum_n c_n^i |n\rangle \; , \tag{2.59}$$

where c_n^i is the complex time-dependent amplitude coefficient of the i-th particle for the occupation of the internal basis state $|n\rangle$, also referred to as the eigenstate coefficient. For a nucleus with $I = \frac{3}{2}$ it follows

$$|\Psi\rangle = c_{3/2}|\frac{3}{2}\rangle + c_{1/2}|\frac{1}{2}\rangle + c_{-1/2}|-\frac{1}{2}\rangle + c_{-3/2}|-\frac{3}{2}\rangle \; . \tag{2.60}$$

The density matrix is the matrix representation of the density operator. Its elements depend on the choice of the mathematical space. The elements of the density matrix are given by the averaged eigenstate coefficients, such that

$$\sigma_{\mu\nu} = \langle\mu|\sigma|\nu\rangle = \sum_i \langle\mu|\Psi_i\rangle\langle\Psi_i|\nu\rangle = \sum_i \sum_{\mu,\nu} c_\mu^i \left(c_\nu^i\right)^* = \overline{c_\mu c_\nu^*} \; . \tag{2.61}$$

They describe the strength of the superposition of the states $|\mu\rangle$ and $|\nu\rangle$, which is referred to as a coherence. A coherence between the states $|\mu\rangle$ and $|\nu\rangle$ exists if $\sigma_{\mu\nu}$ does not vanish. For diagonal elements $\sigma_{\mu\mu}$ ($\mu = \nu$), Equation (2.61) becomes

$$\sigma_{\mu\mu} = \overline{c_\mu c_\mu^*} = p_\mu \geq 0 \; , \tag{2.62}$$

where p_μ is the occupation probability of a quantum state $|\Psi_\mu\rangle$ with $\sum_\mu p_\mu = 1$.

The real diagonal elements of the density matrix constitute the occupation density and are thus referred to as *populations*. The total occupation density of all populations must be one. This corresponds to the fact that the trace of the diagonal elements is 1. The complex off-diagonal elements constitute the superposition of the quantum states $|\mu\rangle\langle\nu|$ and are referred to as *coherences*. The order $m = |\mu - \nu|$ of the coherence is given by the difference of the quantum numbers of the states $|\mu\rangle$ and $\langle\nu|$.

The energy levels and the density matrix for nuclei with $I = \frac{3}{2}$ are illustrated in Figure 2.4. In this figure, the black elements in the density matrix are the populations of the quantum states $|+3/2\rangle$, $|+1/2\rangle$, $|-1/2\rangle$ and $|-3/2\rangle$. They are also called zero-quantum "coherences" because they are of order $m = 0$. The red, green and blue elements are the SQ, DQ and TQ coherences, respectively. For instance, the superposition of the quantum states $|+3/2\rangle\langle-3/2|$ is a TQ coherence, as the order is $m = 3/2 - (-3/2) = 3$. In the diagram of the energy levels, the coherences are illustrated as transitions between quantum states represented by energy levels. Neglecting the energy shift by ω_Q caused by the quadrupole interaction (see Subsections 2.2.2 and 2.2.3), the spectral line of the TQ coherence is at threefold the resonance frequency as the spectral line of the SQ coherences.

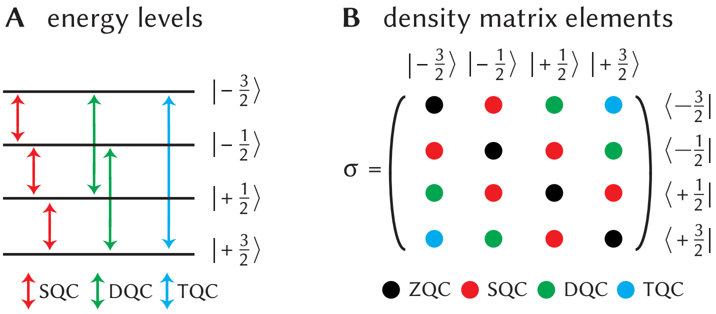

Figure 2.4: **A** Single-, DQ and TQ coherences illustrated as transitions between energy levels. **B** Density matrix elements. The real diagonal elements are the populations of the four quantum states. The complex off-diagonal elements are superpositions of two quantum states and per definition coherences.

2.2.5 Irreducible Tensor Operator

Coherences in a spin system is expressed by scalar elements of the density matrix σ (Subsection 2.2.4). This description is exact, yet its physical interpretation can be difficult (Bain, 1980). To study the time evolution of a mixed quantum system, an appropriate mathematical space is necessary to define the elements of the density matrix. This prompted the development of operator formalisms (Pyper, 1971; Wokaun and Ernst, 1977), in which the density matrix element is associated with a transition operator. This transition operator allows the coherences to be followed as it evolves in time. The irreducible tensor formalism provides such a mathematical space (for details refer to (van der Maarel, 2003b)). When it is applied to the spin density operator and the Hamiltonians, the rank l and the coherence order m of the density operator can be be followed under the influence of the RF pulses and thermal relaxation. This is the most important feature of the irreducile tensor formalism, and it allows for pulse sequence to excite specific coherences to be designed.

Due to the Hermitian nature ($\sigma^*_{lm} = \sigma_{ml}$) of the irreducible tensor operators, symmetric and antisymmetric combinations

$$\hat{T}_{lm}(s) = \frac{1}{\sqrt{2}}\left(\hat{T}_{l-m} + \hat{T}_{lm}\right) , \tag{2.63}$$

$$\hat{T}_{lm}(a) = \frac{1}{\sqrt{2}}\left(\hat{T}_{l-m} - \hat{T}_{lm}\right) , \tag{2.64}$$

can be formulated. As a result, the density operator can be expanded in 16 basis operators (Table 2.2).

Table 2.2: Basis operators using the symmetric and antisymmetric combinations of the irreducible tensor operators van der Maarel (2003a).

$\hat{T}_{00}$	identity
$\hat{T}_{10}$	proportional to the longitudinal magnetization
$\hat{T}_{11}(a)$ and $\hat{T}_{11}(s)$	proportional to the x- and the y-magnetization
$\hat{T}_{20}$	quadrupole spin polarization
$\hat{T}_{21}(s)$ and $\hat{T}_{21}(a)$	rank-two single quantum coherences
$\hat{T}_{22}(s)$ and $\hat{T}_{22}(a)$	rank-two double quantum coherences
$\hat{T}_{30}$	octupole spin polarization
$\hat{T}_{31}(s)$ and $\hat{T}_{31}(a)$	rank-three single quantum coherences
$\hat{T}_{32}(s)$ and $\hat{T}_{32}(a)$	rank-three double quantum coherences
$\hat{T}_{33}(s)$ and $\hat{T}_{33}(a)$	rank-three triple quantum coherences

In the rotating frame of reference, the Hamiltonian of a spin ensemble can be expressed by a combination of the Zeeman, RF, static quadrupole and fluctuating quadrupole Hamiltonians

$$\hat{\mathcal{H}}^{\mathrm{rot}}(t) = \hat{\mathcal{H}}^{\mathrm{rot}}_{\mathrm{Z}} + \hat{\mathcal{H}}^{\mathrm{rot}}_{\mathrm{RF}} + \hat{\mathcal{H}}^{\mathrm{rot}}_{\mathrm{QS}} + \hat{\mathcal{H}}^{\mathrm{rot}}_{\mathrm{QF}}(t) \ . \tag{2.65}$$

Consistent with van der Maarel (2003a), the representation of the discourse is chosen such that the Zeeman Hamiltonian, $\hat{\mathcal{H}}^{\mathrm{rot}}_{\mathrm{Z}} = \omega_0\sqrt{5}\hat{T}_{10}$, vanishes. The relevant components are furthermore

$$\hat{\mathcal{H}}^{\mathrm{rot}}_{\mathrm{RF}} = \sqrt{5}\omega_1\hat{T}_{11}(a) \text{ and} \tag{2.66}$$

$$\hat{\mathcal{H}}^{\mathrm{rot}}_{\mathrm{QS}} = \frac{e^2Q}{4}\overline{q\,(3\cos^2\Theta - 1)}\hat{T}_{20} = \bar{\omega}_Q\hat{T}_{20} \ , \tag{2.67}$$

with Q as the quadrupole moment. For $\bar{\omega}_Q \neq 0$ there is a residual static quadrupole interaction. This is the case if $\Theta \neq 54.7°$ (magic angle).

2.2.6 Effects of Hard RF Pulses

Hard pulses are very short, non-selective block pulses with a high bandwidth exceeding the spectral sweep width of the spectrum (Jaccard et al., 1986). In this section the effects of hard RF pulses on the time evolution of the spin density operator in biologically relevant samples are analyzed.

In soft-condensed matter, the long correlation times and the small quadrupole coupling constants justify the treatment of the fluctuating quadrupole Hamiltonian as a second-order pertubation. The Hamiltonian of the spin ensemble (Equation 2.65) is no longer time-dependet and becomes the static Hamiltonian

$$\hat{\mathcal{H}}^{\mathrm{rot}}_{\mathrm{S}} = \hat{\mathcal{H}}^{\mathrm{rot}}_{\mathrm{RF}} + \hat{\mathcal{H}}^{\mathrm{rot}}_{\mathrm{QS}} \ . \tag{2.68}$$

The time evolution of the density operator under a static Hamiltonian $\hat{\mathcal{H}}_{\mathsf{S}}^{\mathrm{rot}}$ is the Liouville equation

$$\frac{\mathrm{d}\sigma^{\mathrm{rot}}}{\mathrm{d}t} = -\mathrm{i}[\hat{\mathcal{H}}_{\mathsf{S}}^{\mathrm{rot}},\, \sigma^{\mathrm{rot}}]\ . \tag{2.69}$$

To determine the effect of hard RF pulses on the time evolution of the spin operator, it is assumed that both the static and the fluctuating quadrupole interactions can be neglected for the duration of the pulse. This assumption fails in the presence of long, soft RF pulses or large quadrupole splitting.

Consider an RF pulse that is applied in the x-direction with a frequency ω_1. Inserting Equation (2.66) in Equation (2.69) yields

$$\frac{\mathrm{d}\sigma^{\mathrm{rot}}}{\mathrm{d}t} = -\mathrm{i}[\hat{\mathcal{H}}_{\mathsf{RF}}^{\mathrm{rot}},\, \sigma^{\mathrm{rot}}] = -\mathrm{i}\omega_1[\sqrt{5}\hat{T}_{11}(a),\, \sigma^{\mathrm{rot}}]\ . \tag{2.70}$$

The solution are five sets of coupled, analytically solvable differential equations by means of commutation relations (Bowden et al., 1986). The message derived from this set of differential equations is that under a hard RF pulse, the rank of the tensor operators is conserved, while the order might change. This feature only holds true when the density operator is expressed in the irreducible spherical tensor basis (instead of, for example, the Cartesian basis).

A hard RF pulse with the pulse duration τ_p and the flip angle

$$\alpha = \omega_1\tau_p \tag{2.71}$$

rotates the frame of reference of the density matrix about the y-axis (Bain and Martin, 1978a). Changes in the coherence order from m_1 to m_2 are weighted by the Wigner matrix elements $d^{(l)}_{m_2 m_1}(\alpha)$, which depend on the flip angle α (Bain and Martin, 1978a; Jaccard et al., 1986; Mueller et al., 1987). In other words, the rotation of the density matrix in the basis of the spherical tensor operators can be described by the Wigner rotation matrix. Specifically, B_1-inhomogeneities and thus deviations in α affect the transfer between different coherences differently. The flip angle dependence of a particular coherence can be calculated by multiplication of the Wigner matrix elements of each pulse. As a rule of thumb, coherences of higher order are affected more by deviations in the flip angle. Additionally, the more pulses there are, the stronger the effects of B_1-inhomogeneities.

In the specific case of a π-pulse, all coherence orders are negated after the RF pulse. In this case, coherence transfer between spins is absent (Bain, 1980). This characteristic is utilized to refocus relative phase differences brought about by B_0-inhomogeneities.

Additional to the flip angle, RF pulses are commonly associated with a specific phase ϕ. This feature constitutes an integral part of any sophisticated pulse sequence using coherence pathway transfer and is detailed in Section 2.2.8. The reference coordinate system is rotated around the z-axis by angle of ϕ to align the pulse with the x-axis before the application of the RF pulse, and correspondingly rotated back by an angle of $-\phi$ afterwards.

2.2.7 Effects of Quadrupole Thermal Relaxation

Isotropic environments serve as the starting point to determine the quadrupole thermal relaxation effects on the time evolution of the density operator. In isotropic environments there is no macroscopic order ($\bar{\omega}_Q = 0 \ \rightarrow\ \hat{\mathcal{H}}_{\mathsf{QS}}^{\mathrm{rot}} = 0$), and the EFG is avarged to zero by molecular motion. In the absence of an RF pulse, the static Hamiltonians are zero ($\hat{\mathcal{H}}_{\mathsf{RF}}^{\mathrm{rot}} = 0\ ,\ \hat{\mathcal{H}}_{\mathsf{QS}}^{\mathrm{rot}} = 0$), and Equation (2.69) becomes

$$\frac{\mathrm{d}\sigma^{\mathrm{rot}}}{\mathrm{d}t} = -\int_0^{\infty} \langle [\hat{\mathcal{H}}_{\mathrm{QF}}^{\mathrm{rot}}(t),\, [\hat{\mathcal{H}}_{\mathrm{QF}}^{\mathrm{rot}}(t-\tau),\, \sigma^{\mathrm{rot}}(t)]] \rangle \mathrm{d}\tau \; . \tag{2.72}$$

Substituting the only contributing Hamiltonian $\hat{\mathcal{H}}_{\mathrm{QF}}^{\mathrm{rot}}(t)$ yields

$$\frac{\mathrm{d}\sigma^{\mathrm{rot}}}{\mathrm{d}t} = -\sum_{m=-2}^{2} [\hat{T}_{2m},\, [\hat{T}_{2m}^{\dagger},\, \sigma^{\mathrm{rot}}]]\, (J_m(\omega) + \mathrm{i}K_m(\omega)) \tag{2.73}$$

with the Hermitian adjoint $\hat{T}_{2m}^{\dagger} = (-1)^m \hat{T}_{2-m}$. The spectral density functions $J_m(m\omega_0)$ and $K_m(m\omega_0)$ are the real and the imaginary part of the Fourier transform of the EFG autocorrelation function, respectively. The solution of Equation (2.73) consists of a sum of exponential decay terms, the number of which depends on the number of coupled differential equations.

If the correlation function is assumed to be exponential with the correlation time τ_c, then the spectral density functions assume the Lorentzian form

$$J_m(\omega) = \omega_Q^2 \frac{2\tau_c}{1 + (m\omega\tau_c)^2} \; , \tag{2.74}$$

$$K_m(\omega) = \omega\tau_c J_m(\omega) \; , \tag{2.75}$$

the width of which is proportional to τ_c. The imaginary part $K_m(\omega)$ usually leads to a very small shift of the energy level and is thus neglected for most applications (van der Maarel, 2003b). The area under $J(\omega)$ is one. The spectral density can be understood as a probability function. It predicts the probability to find molecular rotational motion at a specific frequency ω and with the correlation time τ_c. This rotational motion is often referred to as "tumbling", hence the name "tumbling rate" for the reciprocal of the correlation time τ_c. The maximum of the real part $J_m(\omega)$ can be found at the Larmor frequency ω_0, indicating that relaxation is most effective in the vicinity of ω_0. In biological tissues, various processes independent of each other operate on different time scales. In that case, the overall spectral density function is the sum of many spectral density functions (Engstroem et al., 1984).

Opposite to the effect of an hard RF pulse, the coherence order is conserved under thermal relaxation, whereas the rank might change. Furthermore, the even- and odd-rank tensor operators are decoupled. It follows that in an isotropic environment, an even-rank coherence cannot be created from an odd-rank coherence by means of relaxation or coherence transfer, as the density matrix has an odd-rank in thermal equilibrium (Figure 2.5).

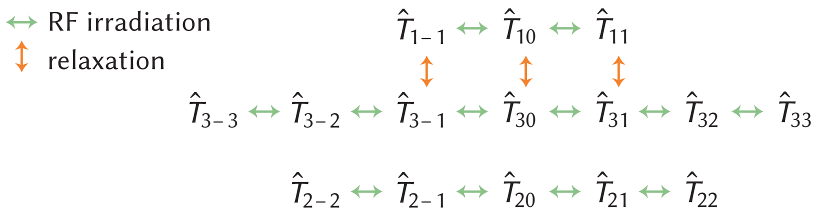
↔ RF irradiation
↕ relaxation
$\hat{T}_{1-1}$ ↔ $\hat{T}_{10}$ ↔ $\hat{T}_{11}$
$\hat{T}_{3-3}$ ↔ $\hat{T}_{3-2}$ ↔ $\hat{T}_{3-1}$ ↔ $\hat{T}_{30}$ ↔ $\hat{T}_{31}$ ↔ $\hat{T}_{32}$ ↔ $\hat{T}_{33}$
$\hat{T}_{2-2}$ ↔ $\hat{T}_{2-1}$ ↔ $\hat{T}_{20}$ ↔ $\hat{T}_{21}$ ↔ $\hat{T}_{22}$

Figure 2.5: Transformation of the spherical tensors $\hat{T}_{lm}$ in an isotropic environment with zero-average EFG. The rank might change upon the application of an hard RF pulse, whereas the order might change during relaxation. The even- and odd-rank tensors are decoupled in an isotropic environment, so that rank-two coherences cannot be created via relaxation.

For relaxation in an anisotropic environment with long-range order, however, the static quadrupole interaction has to be taken into account ($\hat{\mathcal{H}}_{\mathrm{RF}}^{\mathrm{rot}} = 0\,,\ \hat{\mathcal{H}}_{\mathrm{QS}}^{\mathrm{rot}} \neq 0$). In that case, the odd and even rank tensor operators are no longer decoupled. Therefore, rank-two coherences can be created via relaxation, and the detection thereof would be an indicator for long-range order in the probe.

Zero-Quantum Coherence (Spin Polarization)

The relaxation of the $\hat{T}_{10}$ spin polarization corresponds to that of the longitudinal magnetization. In general, the spin polarizations $\hat{T}_{10}$, $\hat{T}_{20}$ and $\hat{T}_{30}$ reflect on the eigenstate populations. The differential equations of $\hat{T}_{10}$ and $\hat{T}_{30}$ are coupled, while that of $\hat{T}_{20}$ stands on its own. The transformation matrix reads

$$\begin{pmatrix} \hat{T}_{10} \\ \hat{T}_{30} \end{pmatrix} \xrightarrow{R^{(0)}} \begin{pmatrix} f_{11}^{(0)} & f_{13}^{(0)} \\ f_{31}^{(0)} & f_{33}^{(0)} \end{pmatrix} \begin{pmatrix} \hat{T}_{10} \\ \hat{T}_{30} \end{pmatrix} \tag{2.76}$$

where the superscript (0) stands for the order and indicates “zero-quantum”. The relaxation functions $f_{l_2 l_1}^{(m)}$ are

$$f_{11}^{(0)} = \frac{1}{5}\left(\mathrm{e}^{-R_1^{(0)}t} + 4\mathrm{e}^{-R_2^{(0)}t}\right) \,, \tag{2.77}$$

$$f_{33}^{(0)} = \frac{1}{5}\left(4\mathrm{e}^{-R_1^{(0)}t} + \mathrm{e}^{-R_2^{(0)}t}\right) \,, \tag{2.78}$$

$$f_{31}^{(0)} = f_{13}^{(0)} = \frac{2}{5}\left(\mathrm{e}^{-R_1^{(0)}t} - \mathrm{e}^{-R_2^{(0)}t}\right) \,. \tag{2.79}$$

They indicate transfer of an m-order coherence (m-quantum coherences) from rank l_1 to l_2 during relaxation. Note that this notation is consistent with the notation of the Wigner matrix elements $d_{m_2 m_1}^{(l)}(\alpha)$ (Section 2.2.6) that describe the change of an l-rank coherence from order m_1 to m_2 under RF pulses (Jaccard et al., 1986).

In the one-compartment model, the relaxation rates R are expressed in terms of the spectral density function (Equation (2.74)) such that $J_1 = J_1(m = 1)$ and $J_2 = J_2(m = 2)$. In this model it is assumed that the spin ensemble consists of one comparment only, and that the fluctuations of the EFG can therefore be modeled with a mono-exponential correlation function with the same correlation time τ_c. The fast and the slow component of the longitudinal relaxation times can thus be given as

$$T_{1\mathrm{f}} = \frac{1}{R_1^{(0)}} = \frac{1}{2J_1} = \frac{1 + \omega_0^2\tau_c^2}{4\omega_Q^2\tau_c} \,, \tag{2.80}$$

$$T_{1\mathrm{s}} = \frac{1}{R_2^{(0)}} = \frac{1}{2J_2} = \frac{1 + 4\omega_0^2\tau_c^2}{4\omega_Q^2\tau_c} \,. \tag{2.81}$$

The longitudinal relaxation is bi-exponential with two relaxation times outside the extreme narrowing limit. The fast component $R_1^{(0)}$ contributes to $20\,\%$, and the slow component $R_2^{(0)}$ contributes to $80\,\%$ of the signal (Equation (2.77)). Within the extreme narrowing limit ($\omega_0\tau_c \ll 1$), it is $J_1 = J_2$, and the longitudinal relaxation is mono-exponential with one relaxation time

$$T_1 = \frac{1}{4\omega_Q^2\tau_c} \,. \tag{2.82}$$

Single-Quantum Coherence

The SQ coherences are $\hat{T}_{1\pm1}$, $\hat{T}_{2\pm1}$ and $\hat{T}_{3\pm1}$. The relaxation of $\hat{T}_{11}$ corresponds to that of the transverse relaxtion and transformation matrix reads

$$\begin{pmatrix} \hat{T}_{1\pm1} \\ \hat{T}_{3\pm1} \end{pmatrix} \xrightarrow{R^{(1)}} \begin{pmatrix} f_{11}^{(1)} & f_{13}^{(1)} \\ f_{31}^{(1)} & f_{33}^{(1)} \end{pmatrix} \begin{pmatrix} \hat{T}_{1\pm1} \\ \hat{T}_{3\pm1} \end{pmatrix} \tag{2.83}$$

with the relaxation functions

$$f_{11}^{(1)} = \frac{1}{5}\left(3\mathrm{e}^{-R_1^{(1)}t} + 2\mathrm{e}^{-R_2^{(1)}t}\right) , \tag{2.84}$$

$$f_{33}^{(1)} = \frac{1}{5}\left(2\mathrm{e}^{-R_1^{(1)}t} + 3\mathrm{e}^{-R_2^{(1)}t}\right) , \tag{2.85}$$

$$f_{31}^{(1)} = f_{13}^{(1)} = \frac{\sqrt{6}}{5}\left(\mathrm{e}^{-R_1^{(1)}t} - \mathrm{e}^{-R_2^{(1)}t}\right) , \tag{2.86}$$

and the fast and the slow components of the transverse relaxation times

$$T_{2\mathrm{f}} = \frac{1}{R_1^{(1)}} = \frac{1}{J_0 + J_1} = \frac{1 + \omega_0^2\tau_c^2}{2\omega_Q^2\tau_c\left(2 + \omega_0^2\tau_c^2\right)} , \tag{2.87}$$

$$T_{2\mathrm{s}} = \frac{1}{R_2^{(1)}} = \frac{1}{J_1 + J_2} = \frac{\left(1 + 4\omega_0^2\tau_c^2\right)\left(1 + \omega_0^2\tau_c^2\right)}{2\omega_Q^2\tau_c\left(2 + 5\omega_0^2\tau_c^2\right)} . \tag{2.88}$$

The fast component $R_1^{(1)}$ contributes to $60\,\%$, and the slow component $R_2^{(1)}$ contributes to $40\,\%$ of the signal (Equation (2.84)). This holds true only in one single pool of nuclei Burstein and Springer (2019). In tissue, the relaxation is a superposition of multiple bi-exponential curves. Fitting of the averaged transverse relaxation time in tissue will most likely not yield the theoretical percentages. Within the extreme narrowing limit ($\omega_0\tau_c \ll 1$), the relaxation times $T_{2\mathrm{f}}$ and $T_{2\mathrm{s}}$ are the same

$$T_2 = \frac{1}{4\omega_Q^2\tau_c} , \tag{2.89}$$

which is simultaneously the same as T_1 (Equation (2.82)). Additionally, the relaxation functions $f_{11}^{(1)}$ and $f_{31}^{(1)}$ become

$$f_{11}^{(1)} = \mathrm{e}^{-t/T_2} , \tag{2.90}$$

$$f_{31}^{(1)} = 0 . \tag{2.91}$$

In tissues, bi-exponential T_2 values are commonly measured with exceptions such as the cerebralspinal fluid. An increase of τ_c caused by the presence of comparatively small macromolecules is enough to expell the spectrum from the extreme narrowing limit. However, T_1 values in vivo are generally mono-exponential. In order for T_1 values to become bi-exponential, the presence of heavy proteins ($> 100\,\mathrm{kDa}$) is necessary. This would further increase τ_c such that $\tau_c > 60\,\mathrm{ns}$ (Andrasko, 1974; Monoi, 1985; Seo et al., 1990).

2.2.8 Acquisition of Multi-Quantum Coherences

MQ coherences can be excited in quadrupole spins even in the absence of nonvanishing quadrupole couplings (Jaccard et al., 1986). In type c environments as found in tissues (Section 2.2.3), the rotational correlation time τ_c is larger than or in the range of the Larmor period, resulting in bi-exponential relaxation times. Under this condition, MQ coherences can be excited and acquired using MQ spectroscopy.

The regular RF setup is only capable of detecting dipole radiation. This implies that only SQ coherences, which corresponds to the transverse magnetization, can be detected. Double- and TQ coherences have to be converted to rank-two or rank-three SQ coherences for detection, respectively. The MQ methods employed in this thesis acquire SQ and TQ coherences. Their relaxation functions acquired by the RF setup are described by Equations 2.84 and 2.86, respectively. Therefore, the mathematical solution for DQ and TQ coherences and their corresponding relaxation functions are not relevant (for completeness cf. van der Maarel (2003a)).

An MR sequence capable of recording MQ coherences consists of multiple phase cycles of a basic two-dimensional spectroscopy scheme. A phase cycle is a series of pulse sequences that are identical except for the relative phases of the RF pulses and the receiver (Bodenhausen, 2011). To specifically detect any MQ coherence, each pulse of the basic RF pulse scheme is assigned an angle and a phase, the latter of which might change with each phase cycle. By doing so, the coherences can be guided to follow certain coherence pathways (Bain, 1984; Bodenhausen et al., 1984). A coherence pathway describes the sequence of coherence orders m a signal passes through in the time span between the first RF pulse and its arrival in the receiver. During this time span, changes in the rank and the order under the influence of RF pulses and thermal relaxation occur. These changes are referred to as coherence transfer. To selectively detect certain coherences, the unwanted coherences have to be suppressed by manipulating the phases of the RF pulses over many phase cycles, a process referred to as phase cycling. The selective detection and suppression of coherences can also be referred to as constructive and destructive interference, respectively.

The first step in designing a MQ spectroscopy method is to construct the coherence pathway diagram that leads to the selecting of the desired coherence. The basic RF pulse scheme without specification of the angle and the phase of the RF pulses is illustrated in Figure 2.6A. Figure 2.6B depicts the coherence pathways followed by TQ, DQ and SQ coherences in a three-pulse experiment with hard pulses. Prior to the excitation pulse, the spin system is in thermal equilibrium. From this starting position, the excitation pulse creates SQ coherences ($m = \pm1$) of rank $l = 1$ only (Bain and Martin, 1978a,b). During the evolution time, they evolve under the influence of external and local fields into SQ coherences of rank $l > 1$. The conversion pulse converts them into MQ coherences ($m = \pm2$, $m = \pm3$) of rank $l > 1$. They cannot be directly detected and must be transfered to observable SQ coherences with rank $l > 1$ by the observation pulse in the last step (Bain, 1984). During the detection period, the SQ coherences with rank $l > 1$ undergo relaxation such that the rank becomes $l = 1$. SQ coherences with $m = 1$ and $m = -1$ correspond to clockwise and counter-clockwise rotating transverse magnetization of the Bloch equations in x- and y-directions. Therefore, they are equivalent, whereby the latter is chosen by definition of the polarization in the receiver (Bain, 1984). The rules concerning the conservation and evolution of the rank and the order of $\hat{T}_{lm}$ have been previously detailed in Subsections 2.2.6-2.2.7and Figure 2.5.

The second step in designing a MQ spectroscopy method is to determine the phase cycling scheme. If an RF pulse with a phase of ϕ changes the coherence by Δm , then its effect on the coherence is a multiplicatioin by the phase factor

$$\mathrm{e}^{\mathrm{i}\Delta m\phi}\ , \tag{2.92}$$

as shown by (Bain, 1980, 1984; Bodenhausen et al., 1984; Bodenhausen, 2011; Matthies, 2010).

Each coherence pathway is thus affected differently by the RF pulse phase. The total effect of the RF pulses on one coherence pathway is the multiplication of the phase factors from all RF pulses. Additionally, the signal arriving at the receiver is multiplied by the receiver phase. If the sum of the signals of one coherence pathway over all phase cycles is zero, then this pathway is canceled out.

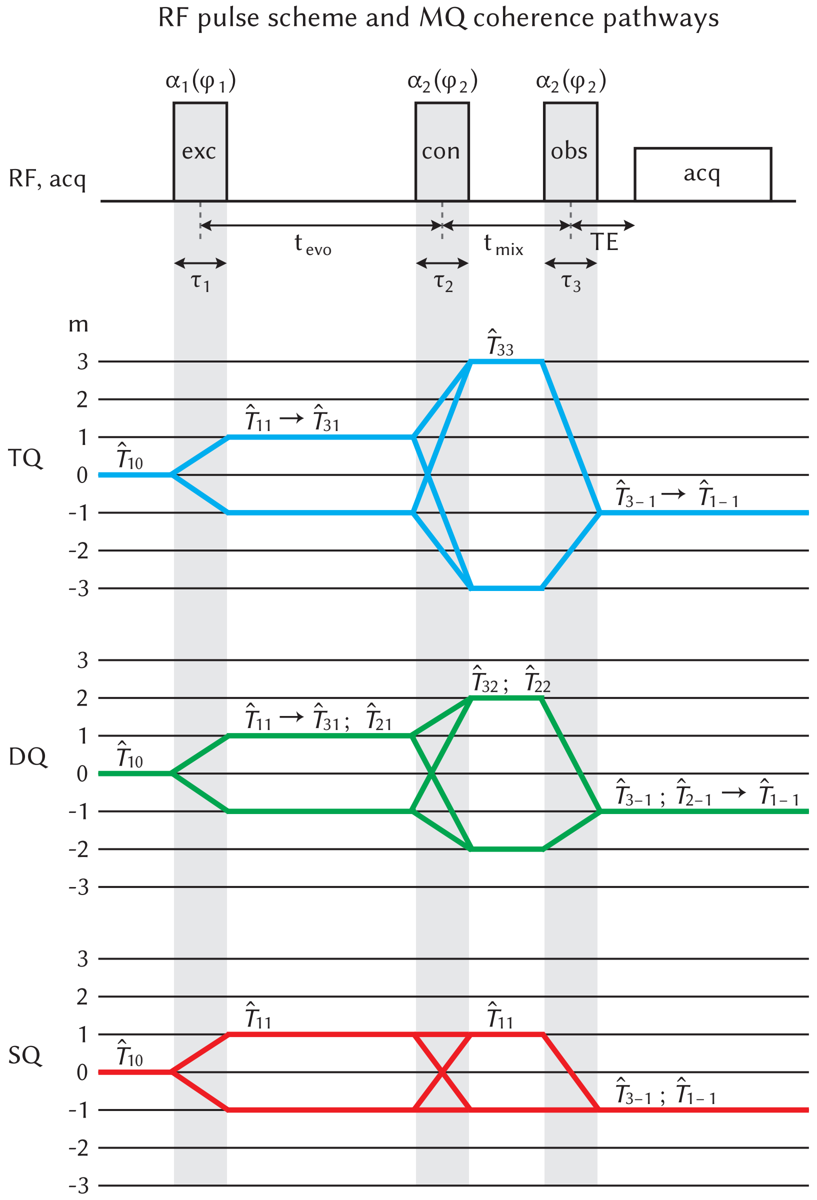
RF pulse scheme and MQ coherence pathways
$\alpha_1(\varphi_1)$
$\alpha_2(\varphi_2)$
$\alpha_2(\varphi_2)$
RF, acq
exc
con
obs
acq
t_{evo}
t_{mix}
TE
τ_1
τ_2
τ_3
m
3
2
1
0
-1
-2
-3
TQ
$\hat{T}_{10}$
$\hat{T}_{11} \rightarrow \hat{T}_{31}$
$\hat{T}_{33}$
$\hat{T}_{3-1} \rightarrow \hat{T}_{1-1}$
DQ
$\hat{T}_{10}$
$\hat{T}_{11} \rightarrow \hat{T}_{31}$; $\hat{T}_{21}$
$\hat{T}_{32}$; $\hat{T}_{22}$
$\hat{T}_{3-1}$; $\hat{T}_{2-1} \rightarrow \hat{T}_{1-1}$
SQ
$\hat{T}_{10}$
$\hat{T}_{11}$
$\hat{T}_{11}$
$\hat{T}_{3-1}$; $\hat{T}_{1-1}$

Figure 2.6: Basic RF pulse scheme to excite MQ coherences. TQ, DQ and SQ coherence pathways with matching time stamps are shown below.

2.3 Biological Background

This section has been adapted from Hu et al. (2019).

Roles of Na^+ and Cl^-in cell physiology

Cellular processes are regulated by the intricate interplay among ions such as Na^+, Cl^-, K^+, and Ca^{2+} (Stein and Litman, 2015). Depending on their polarity and concentration, they act as causal partners to each other or as counterparts to ions and charged macromolecules. Balanced concentrations of the ions are key to maintaining cellular functions. In this way, the chemical and electrical gradients across the cell membrane are maintained. Integral transport proteins are embedded in the cell membrane and control the uptake and efflux of ions. Among the transport proteins are active ion transporters and gated or passive ion channels. The study of transport proteins comprises a vast area of research in cell biology and physiology. In the following, a Na^+ transporter and Cl^- channels are highlighted to exemplify the fundamental importance of Na^+ and Cl^-.

The intracellular sodium concentration in healthy cells is $10 - 15\,\frac{mmol}{l}$ with an average volume fraction of 80%. It is much lower than the extracellular concentration of $140 - 150\,\frac{mmol}{l}$ with an average volume fraction of 20% Madelin and Regatte (2013). By means of ATP hydrolysis sodium is transported across the cell membrane against the electrochemical gradient. During this process, the Na^+/K^+-ATPase converts ATP into adenosine diphosphate (ADP) and “pumps” three sodium cations from and two potassium cations into the cell. In turn, ATP is generated by energy metabolism and O_2 is consumed. Unbalanced intra- and extracellular Na^+ concentrations might thus be an indication of metabolic deficits. Overall, Na^+ is involved in the sustainment of the pH level, the maintainance of the blood pressure, the propagation of nerve signals, the activation of muscle contraction and the regulation of the heartbeat. Disturbances in the energy metabolism or damage to the cell membrane might increase the intracellular sodium concentration and potentially bring about cell swelling/bursting.

Misconceptions persisted even into the 1990s that Cl^- was passively distributed across the membrane. The research interest was primarily in cation transporters inspite of the fact that Cl^- is the most abundant anion in mammals. The study of Cl^- channels was hindered by the low affinity and low specificity of Cl^- channel blockers and technical difficulties in measuring Cl^- fluxes (Hartzell, 2010). However, it has been understood in recent years that Cl^- is actively kept at non-equilibrium and that its concentrations are tightly regulated. The electrochemical gradient of Cl^- plays a central role in maintaing the electric potential necessary for the depolarization and hyperpolarization in muscle and neuronal cells. In general, the intracellular space is more negatively charged in relation to the extracellular space. Thus the membrane potential is negative, whereby the exact value depends on the type of cell. The active maintenance of the distribution of Cl^- in non-equilibrium is a prerequisite for the propagation of nerve signals meditated by neurotransmitters. During signal propagation, cation- and voltage-gated Cl^- ion channels subsequently dissipate the electrochemical gradient. This enables and controls the process of depolarization, hyperpolarization and pre- and post-synaptic inhibition. Disruption in the functionality of chloride carriers and channels underlie nervous system dysfunctions. Apart from its key role in signal progapation, Cl^- is essential to neuronal development, sensory transduction, salt balance, potassium recycling, and cell volume control (Alvarez-Leefmans, 2012). Disruption of chloride homeostasis can be pathological expression of brain edema, neurogenic inflammation and epilepsy. Research to comprehend the Cl^- transport mechanisms has great potential in treatment of especially neurological disorders. One area of application outside the spectrum of neurological disorders is the migration of primary brain tumor cells relying on Cl^- channels. Effective Cl^- channel blockers are studied to target primary brain tumor growth.

State-of-the-art diagnostic value of ^{23}Na and ^{35}Cl NMR techniques

This section was partially adapted from Hu et al. (2019).

^{23}Na MRI has been frequently applied to investigate diseases such as stroke, tumor, multiple sclerosis, and cartilage degradation (Madelin and Regatte, 2013; Thulborn, 2018).

During ischemic stroke, blood flow in the brain is reduced or blocked due to artery constriction or occlusion. Reduced oxygen inflow restricts energy supply for the Na^+/K^+-ATPase, causing cell death. To dissolve blockage in vessels and to avoid the risk of hemorrhage, treatment needs to be carried out 6 hours after onset at the latest (An et al., 2016). The exact onset time is often unknown, albeit being crucial for treatment decisions. A prospective biomarker to determine the onset time and to characterize tissue viability is the tissue sodium concentration (TSC) threshold (Boada et al., 2012; Thulborn, 2018).

Tumor tissue is characterized by disturbed homeostasis due to high cell division rates. Furthermore, the pH value is altered, and the interstitial space might be enlarged. Rapidly growing malignant cells have increased Na^+ concentrations that can be measured with ^{23}Na MRI (Bartha et al., 2008; Ouwerkerk et al., 2003). TSC was shown to increase in edema and necrotic tissue (Shah et al., 2016).

Multiple sclerosis is initially caused by inflammation and characterized by unpredictable, acute relapses. Over time, relapses become less frequent, accompanied by degenerative loss of cognitive function. The progressive demyelination of axons is coupled with overexpression of Na^+ channels and the redistribution thereof along axons Petracca et al. (2016a). Energy deprivation brought forth by such an adaptive mechanism leads to an increase in intracellular Na^+ and cell death. ^{23}Na MRI can support the evaluation of treatment response especially concerning the neurodegenerative component. Additionally, recent studies indicate that ^{23}Na MRI could be used to monitor inflammatory processes (Eisele et al., 2016, 2019).

Osteoarthritis causes progressive and irreversible cartilage degradation (Guermazi et al., 2015). The articular cartilage contains fluid and extracellular matrix. The extracellular matrix consists of collagen and proteoglycan molecules attached to glycosaminoglycans. Glycosaminoglycans are negatively charged and contribute to the fixed charge density of the extracellular matrix, which is balanced by Na^+. ^{23}Na signal was shown to correlate with the fixed charge density and might aid the detection of osteoarthritis before morphological manifestation (Lesperance et al., 1992). Apart from articular cartilage, ^{23}Na MRI of the intervertebral disc was also validated (Wang et al., 2010).

The first ^{35}Cl MR images were obtained in a combined study with ^{23}Na and ^{1}H at $9.4\,\mathrm{T}$ (Kirsch et al., 2010). In this study ^{23}Na and ^{35}Cl signal enhancement in infarcted region after a focal cerebral infarction in rat head was calculated. Na and ^{35}Cl chemical shift imaging was applied in a rat stroke model at different time points after the onset of stroke (Baier et al., 2014). It was found that the magnetization of ^{35}Cl in the infarcted region rose later and with a shallower slope than that of ^{23}Na. This findings supported the assumption that ^{35}Cl NMR offered complementary information on the disease progression. A combined ^{23}Na and ^{35}Cl study at $21.1\,\mathrm{T}$ revealed that ^{35}Cl concentration in glioma was $1,5$ times higher relative to normal brain tissue, therby investigating the involvement of Cl^- in the migration of glioma cells (Schepkin et al., 2014).

The clinical feasibility of ^{35}Cl MRI was first demonstrated in the brain at $7\,\mathrm{T}$ (Nagel et al., 2014). Changes of Na^+ and Cl^- homeostasis were visualized in the legs of patients suffering from periodic paralysis, a muscle disease induced by mutations in muscle ion channels (Weber et al., 2016). In vivo ^{23}Na, ^{35}Cl and ^{17}O T_2^* values in the brain was determined and improved upon using iterative partial volume correction based on ^{1}H MRI (Niesporek et al., 2017).

^{23}Na TQ imaging has been applied for the first time to a tumor rat model as early as 1990 (Griffey et al., 1990). It was shown that the TQ signal was $200 - 250\%$ greater in the growing margin of the tumor relative to that from surrounding tissue. TQ images of the human articular cartilage were shown to suppressed fluid signal in the knee joint (Borthakur et al., 1999). The authors argued that TQ images might be sensitive to structural changes in macromolecule composition in the extracellular matrix. Another study demonstrated the clinical feasibility of TQ images in the brain acquired in $20\,\mathrm{min}$ (Hancu et al., 1999). In a nonhuman primate stroke model, increased TQ signal in the ischemic hemisphere relative to the contralateral hemisphere was determined as early as $0.6\,\mathrm{hr}$ after ischemia onset (LaVerde et al., 2007). On the other hand, almost no change in the SQ signal was found. In combination with other imaging modules, TQ imaging was used to quantify intracellular sodium (Fleysher et al., 2013; Petracca et al., 2016b). Additional to intracellular sodium, parameter such as volume fractions, TSC and T_2^* in human brain *in vivo* were quantified using SISTINA (Worthoff et al., 2018). In contrast to the the publication base on ^{23}Na TQ imaging, there is no publication on ^{35}Cl TQ imaging up to date.

3 Materials and Methods

This chapter has three sections. Section 3.1 introduces the components of the experimental setup Section 3.2 describes the MR sequences DA-R and TQ-TPPI as well as additional evaluation methods. Section 3.3 lists sequence parameters for individual measurement series.

3.1 Experimental Setup

This section describes the scanner (Subsection 3.1.1), the coils (Subsection 3.1.2), the phantoms (Subsection 3.1.3), the bioreactor (Subsection 3.1.4) and animal handling (Subsection 3.1.5).

3.1.1 Scanner

Experiments were conducted at a $9.4\,\mathrm{T}$ preclinical MR system by Bruker (BioSpec, Bruker BioSpin MRI GmbH, Ettlingen, Germany). The scanner is equipped with active shielding and a superconducting magnet cooled down to $4.2\,\mathrm{K}$ (Figure 3.1). The maximum gradient strength is $706\,\frac{mT}{m}$ in all directions. The default gradient ramp time is $122\,\mathrm{\mu s}$ in y- and $110\,\mathrm{\mu s}$ in x- and z-direction. The scanner has multiple bandpass filters. In ^{23}Na and ^{35}Cl experiments ($\omega_0 = 105.75\,\mathrm{MHz}$ and $\omega_0 = 54.24\,\mathrm{MHz}$), the bandpass filters in the range of $70 - 125\,\mathrm{MHz}$ and $30 - 75\,\mathrm{MHz}$ are used, respectively.

3.1.2 Coils

All coils, unless specified otherwise, were built in-house. Surface coils were catered to the geometry of the bioreactor, saddle coils were adapted for the dimension of rodents, and all volume coils have an inner diameter of $72\,\mathrm{mm}$. All coils work in transmit-and-receive (TxRx) mode.

Volume coils have the advantage of a homogeneous transmit and receive field. However, this advantage is offset by two factors. First, the bigger the imaging volume covered by the coil, the longer the pulses are to achieve the same flip angle. A volume coil is thus expected to have longer pulses than surface coils. Second, the big distance between a volume coil and small imaging objects leads to reduced sensitivity. For experiments on the bioreactor (Subsection 3.1.4) and rodents (Subsection 3.1.5), surface and saddle coils are better suited, respectively.

If multiple-resonant coils are used, it is possible to perform NMR experiments at different frequencies without moving the imaging object. This way, ^{23}Na or ^{35}Cl images can be directly superimposed onto high-resolution ^{1}H images. Possible drawbacks include reduced sensitivity and prolonged pulses for each of the working frequencies.

The coils in use for measurements of this dissertation are not equipped with an electric matching and tuning procedure. Consequently, the working frequency has to be adjusted after having inserted both the coil and the imaging object into the scanner by manual adjustment of the matching and tuning capacitors via extension rods.

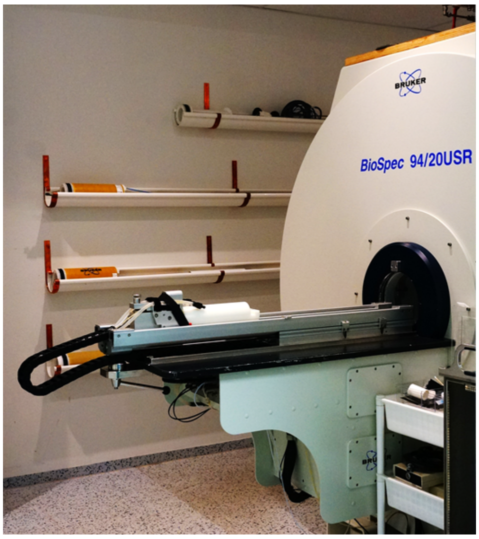

Figure 3.1: $9.4\,\mathrm{T}$ preclinical MR system by Bruker. Animal beds that can be heated with adjustable temperature are availabe. After the laser adjustment, the experimental setup is driven into the iso-center by a mechanical belt.

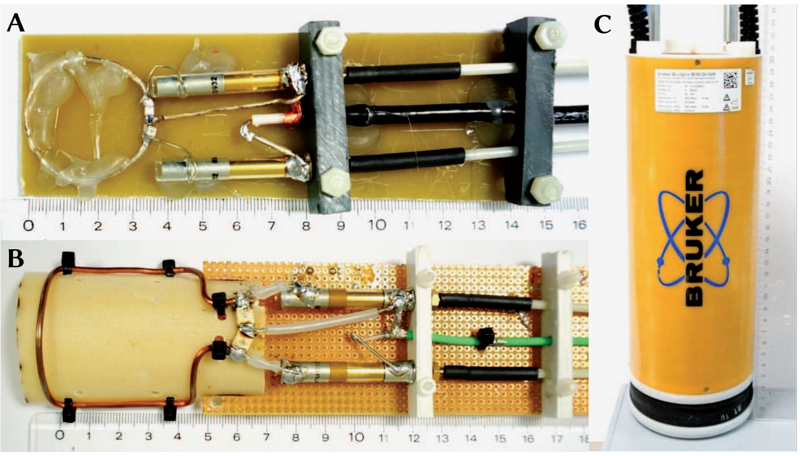

Figure 3.2: **A** ^{23}Na surface coil **B** ^{23}Na saddle coil **C** ^{1}H and ^{23}Na double-resonant volume coil (Bruker)

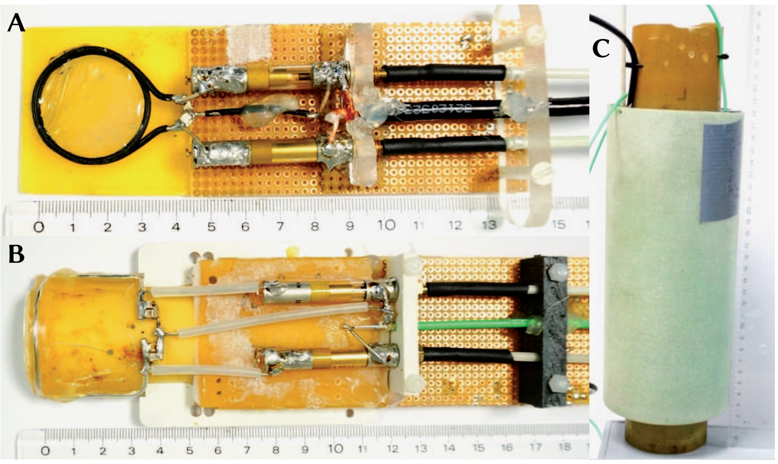

Figure 3.3: **A** ^{35}Cl surface coil **B** ^{35}Cl saddle coil **C** ^{35}Cl volume coil (Malzacher et al., 2018)

In all bioreactor experiments, the surface coils were used ($\tau^{\mathrm{Na}} = 80 - 120\,\mu\mathrm{s}$, $\tau^{\mathrm{Cl}} = 70 - 100\,\mu\mathrm{s}$). In all animal experiments and in some phantom experiments, the saddle coils were used ($\tau^{\mathrm{Na}} = 70 - 120\,\mu\mathrm{s}$, $\tau^{\mathrm{Cl}} = 60 - 90\,\mu\mathrm{s}$). The Bruker ^{1}H and ^{23}Na double-resonant volume coil and the ^{35}Cl volume coil were used in the remaining phantom experiments ($\tau^{\mathrm{Na}} = 130 - 150\,\mu\mathrm{s}$, $\tau^{\mathrm{Cl}} = 306\,\mu\mathrm{s}$).

3.1.3 Phantoms

In this section, the three types of phantoms used in the studies are described in terms of their purpose, production and properties.

Agarose Phantoms

Agarose gel has been shown to have bi-exponential relaxation times. Therefore it is used to minick tissue with bi-exponential relaxation properties (Andrasko, 1974). In this dissertation, the agarose phantoms were used in DA-R, TQ-TPPI and TASTI measurements to validate methods and to optimize sequence parameters. They were also used in animal experiments as reference phantoms for co-registration.

Agarose concentrations are given in $\%$, whereby $1\,\%$ agarose corresponds to 1 g per $100\,\mathrm{ml}$ water. Sodium chloride (NaCl) has a molecular weight of $58.443\,\frac{\mathrm{g}}{\mathrm{mol}}$ and its concentration is either given in weight per volume ($\%$) or in millimole per liter (mM). Clinical saline solutions have a concentration of $0.9\,\%$, corresponding to $154\,\mathrm{mM}$.

To produce agarose phantoms, both agarose powder and NaCl were solved in a measuring cup and heated by a heating plate. The solution was constantly stirred by a magnetic stirrer at $300 - 500\,\mathrm{rpm}$. The agarose dissolves at $88\,°\mathrm{C}$. When this temperature was reached, the heating was turned off, and evaporated water was added according to the difference in weight in regard to the solution before heating. Subsequently, the solution was filled in the container and set aside to cool.

The production of phantoms with an agarose concentration of approximately $5\,\%$ and higher faces difficulties due to the high viscocity of the fluid. Consequently, air bubbles escape slowly. At $90 - 95\,°\mathrm{C}$, the rate at which bubbles escape is similar to the rate at which bubbles emerge due to evaporation. If the fluid is left to cool under this condition, air bubbles are trapped.

This predicament is of concern especially for experiments which selectively detect TQ coherences and rely on a proper shim condition. A phantom filled with trapped air bubbles is the source of rapid susceptibility changes and has to be discarded due to difficulties in the shimming process. This leads to shortened T_2^* and reduced TQ signal amplitudes.

Resolution Phantoms

The resolution of an image with respect to the nominal pixel length can be assessed with the help of resolution phantoms. Such phantoms contain rows of structures. Each row contains structures of the same size, whereby the spacing between neighboring structures is the same as the diameter of the structure. Different rows contain structures of different sizes. In this thesis, resolution phantoms were used in imaging experiments to analyze the achieved image resolutions in different imaging methods.

Two types of resolution phantoms filled with $3.08\,\mathrm{M}$ NaCl were used (Figure 3.4). To produce Resolution Phantom MH, a polyvinyl chloride (PVC) layer was fixed inside a sphere. 36 holes in five groups of nine (diameter = $3.5 - 1.0\,\mathrm{mm}$) was drilled into the PVC layer. Here, the structures are filled with NaCl, whereas the spacing is solid. To produce Resolution phantom AG, 25 polystyrene rods in five groups of five (diameter = $2.50 - 0.75\,\mathrm{mm}$) were attached inside a vial. Here, the structures are solid, whereas the spacing is filled with NaCl. In that sense, the two resolution phantoms are inverted.

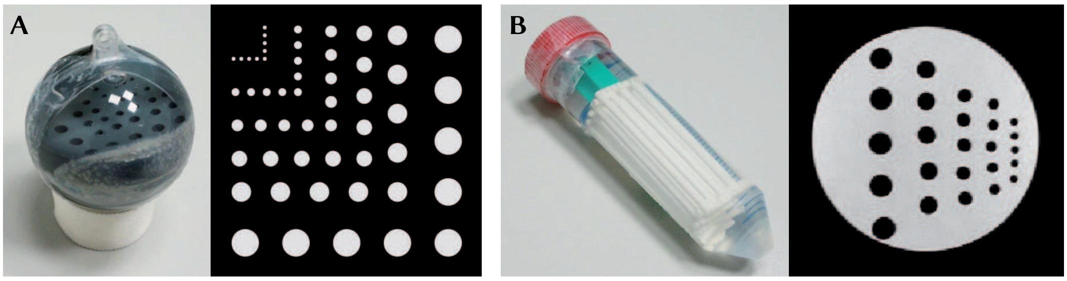

Figure 3.4: **A** Resolution phantom MH with its blueprint. White circles and black background indicate that the holes are filled with NaCl. **B** Resolution phantom AG with its ^{1}H MR image. Black circles and white background within the boundary of the cylindrical phantom indicate that the phantom is filled with NaCl while the rods are solid.

Lecithin Phantoms

Lecithin is the generic term for phospholipids, which consist of fatty acid, phosphoric acid, glycerol and choline. It can found as an integral part of the cell membrane of animals and plants. Its molecules are amphiphilic, meaning that they are hydrophilic on the one end and lipophilic on the other end. Therefore, lecithin allows for the emulsification of water and fat. When solved in aqueous solution, lecithin forms liposomes (Figure 3.5A), which is a lipid bilayer. This feature allows for the examination of structures imitating the cell membrane. Lecithin phantoms are therefore a candidate for cell-imitating phantoms. In this thesis, they were used in TQ-TPPI experiments to investigate whether they were a suitable alternative to agarose phantoms to mimick ^{23}Na and ^{35}Cl TQ relaxation properties.

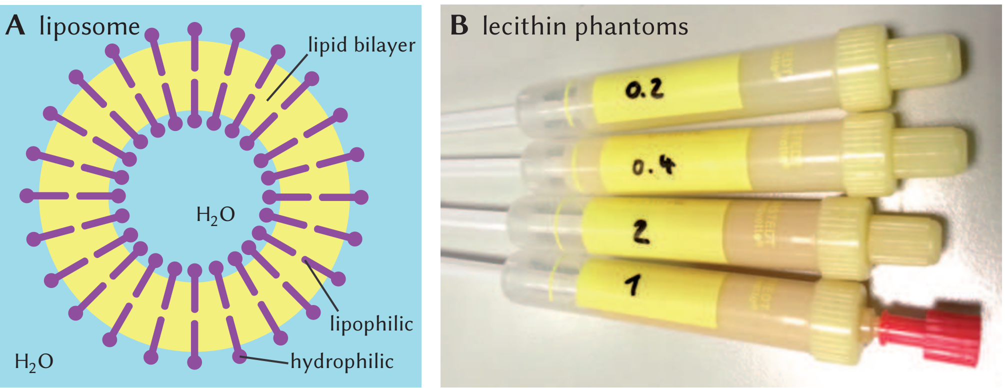

Figure 3.5: **A** Drawing of liposomes formed by lecithin solved in acqueous solution. Liposomes emulate cells as both share the feature of a lipid bilayer. **B** Lecithin phantoms with 2, 4, 10 and $20\,\%$ lecithin and $154\,\mathrm{mM}$ NaCl. Phantoms with a higher percentage of lecithin have a darker color.

Lecithin extracted from soy contains other types of phospholipids as emulsifier. We used soy lecithin from local pharmacy due to its easy accessibility for the initial study. Lecithin concentration is given in (weight/volume) $\%$, whereby 1% lecithin corresponds to 1 g per 100 ml water. Lecithin phantoms with $2/4/10/20\,\%$ lecithin and $154\,\text{mM}$ NaCl in water were thouroughly mixed using a rotary tool at $17000\,\text{rpm}$ for $10\,\text{min}$ (Figure 3.5B).

Phantoms with a lecithin concentration of $20\,\%$ and higher contained a high amount of air bubbles caused by the mixing process. Due to the high viscosity the air bubbles could not escape immediately, therefore lecithin phantoms should be left to rest before being used in experiments.

3.1.4 Bioreactor

NMR measurements are commonly done *in vivo* or on phantoms mimicking certain tissue characteristics. New methods can be tested on phantoms before they are applied *in vivo*. The middle ground between phantoms and *in vivo* measurements is the bioreactor. In this thesis, actively perfused 3D cell cultures in an MR-compatible bioreactor were measured *in vitro* (Gottwald et al., 2013). Conventional 2D cell cultures in petri dishes or cell culture flasks do not represent 3D tissue due, as cells are limited to in-plain growth. The bioreactor features microcavity arrays that act as a scaffold to facilitate 3D cell growth. The chip contained bowl-shaped cavities $500\,\mu\text{m}$ in diameter and $300\,\mu\text{m}$ in depth, with a spacing of $50\,\mu\text{m}$ between neighboring cavities. Figure 3.6 shows fluorescence images of cells on such a chip.

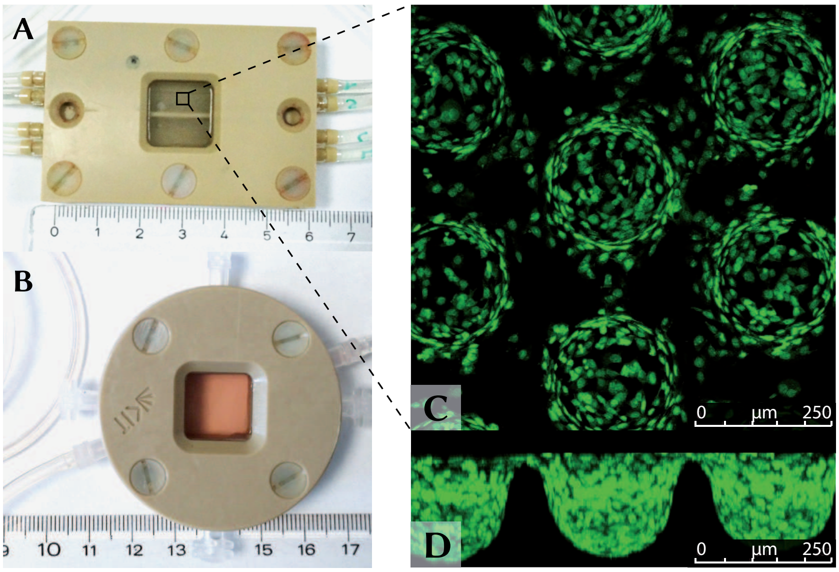

Figure 3.6: Fluorescence images of a microcavity array **A** from above and **B** in cross section (images courtesy of Cordula Nies). **C** Square bioreactor filled with isoproyl alcohol. **D** Round bioreactor filled with medium.

The robust and fast dividing hepatoma cell line HepG2 (ATCC, HB-8065, Manassas, VA, U.S.A.) was used in the experiments. The cells are cultured in Minimal Essential Medium (MEM) supplemented by $0.1\,\%\%$ phenol red, $10\,\%$ FBS, $1\,\%$ Penicillin-Streptomycin, $1\,\%$ Glutamine, $1\,\%$ non-essential amino acids and $1\,\%$ sodium pyruvate. Furthermore, the medium is by medical gasses comprised of $74\,\%$ N_2, $21\,\%$ O_2 and $5\,\%$ CO_2.

There are two models of the biorector housings (Figure 3.6). The square bioreactor is the commonly used model. Its dimensions are designed so that it can be passed through the passage in the wall separating the operator and the scanner room. Additionally, it fits onto the animal bed.

The animal bed heated the bioreactor from underneath by circulating water from a water reservoir with adjustable temperature. The square bioreactor contains 0.9 ml of liquid, whereas the round bioreactor contains 1.5 ml of liquid. However, the round bioreactor neither fitted through the passage in the wall nor onto the animal bed. The round bioreactor must be temporalily disconnected from the tubes to be put into the scanner room, possibly being contaminated in the process. A custom-made animal bed the round bioreactor was constructed using 3D printing.

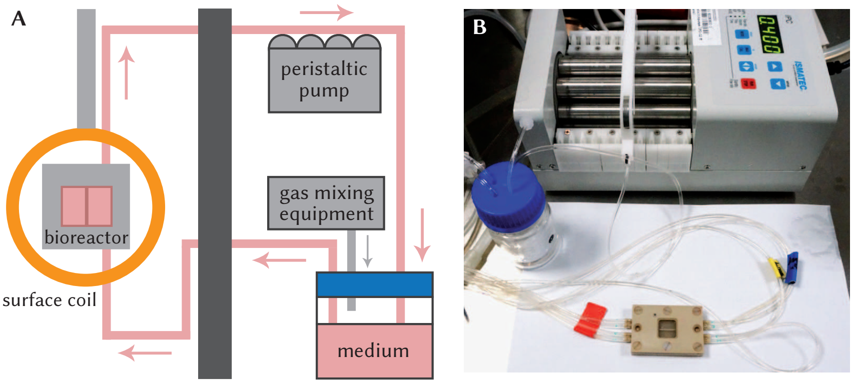

Figure 3.7: **A** Diagram and **B** photograph of the bioreactor setup. The scanner room is separated from the control room via a wall with a small hole to pass through the bioreactor and the medium tubes.

Additional life-sustaining equipments such as the gas mixing equipment, the peristaltic pump and the water bath were not MR-compatible and were thus set up in the operator room. The medium is pumped through the tubes connecting the bioreactor and the medium reservoir by means of a peristaltic pump. The flow rate of $400\,\frac{\mu l}{min}$ was set to emulate blood circulation. A diagram of the bioreactor setup is shown in Figure 3.7.

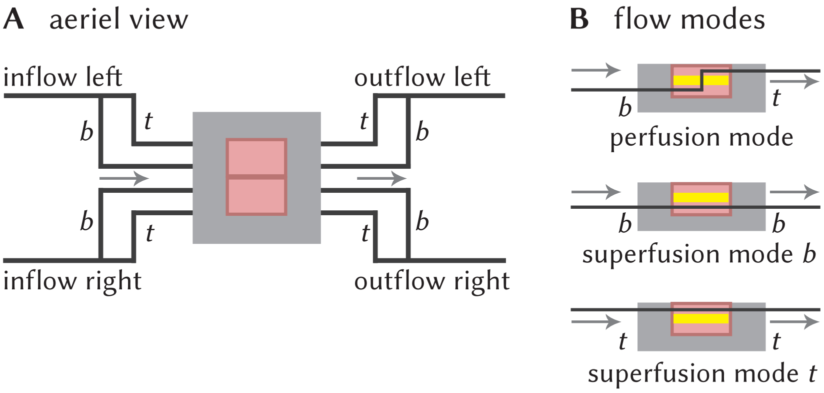

Figure 3.8: **A** Aeriel view of the flow system. In future models with densely sealed left and right compartments, either side could be operated independently through its inlets and outlets in bottom ('b') and top ('t') position. **B** Cross section of the flow system. In perfusion mode, the bottom inlets and the top outlets are open. This is the life-sustaining operation mode. In the superfusion modes, medium flows either entirely above or beneath the chip (yellow bar).

The bioreactor does not have two separate, densely sealed compartments yet. Nevertheless, each of the left and the right compartment within the bioreactor has its own independent tubes (Figure 3.8A). The bioreactor has two working modes, the perfusion and the superfusion modes (Figure 3.8B). Under normal condition, cells were perfused by medium inflow from beneath the chip in perfusion mode.

Commonly, microscopic pockets of air in the medium circulation system can accumulate and form macroscopic air bubbles. These air bubbles can be trapped in the bioreactor. Cells exposed to air bubbles will eventually die. In addition, air bubbles create abrupt susceptibility changes and destroy the shim. Especially for spectroscopic experiments or repeated measurements over time, the absence of air bubbles is crucial. Trapped air bubbles are flushed out in superfusion mode after taking the setup out of the scanner room.

3.1.5 Animal

Two healthy male Sprague Dawley rats with (weight 592 and $717\,\mathrm{g}$) were scanned (Figure 3.9).

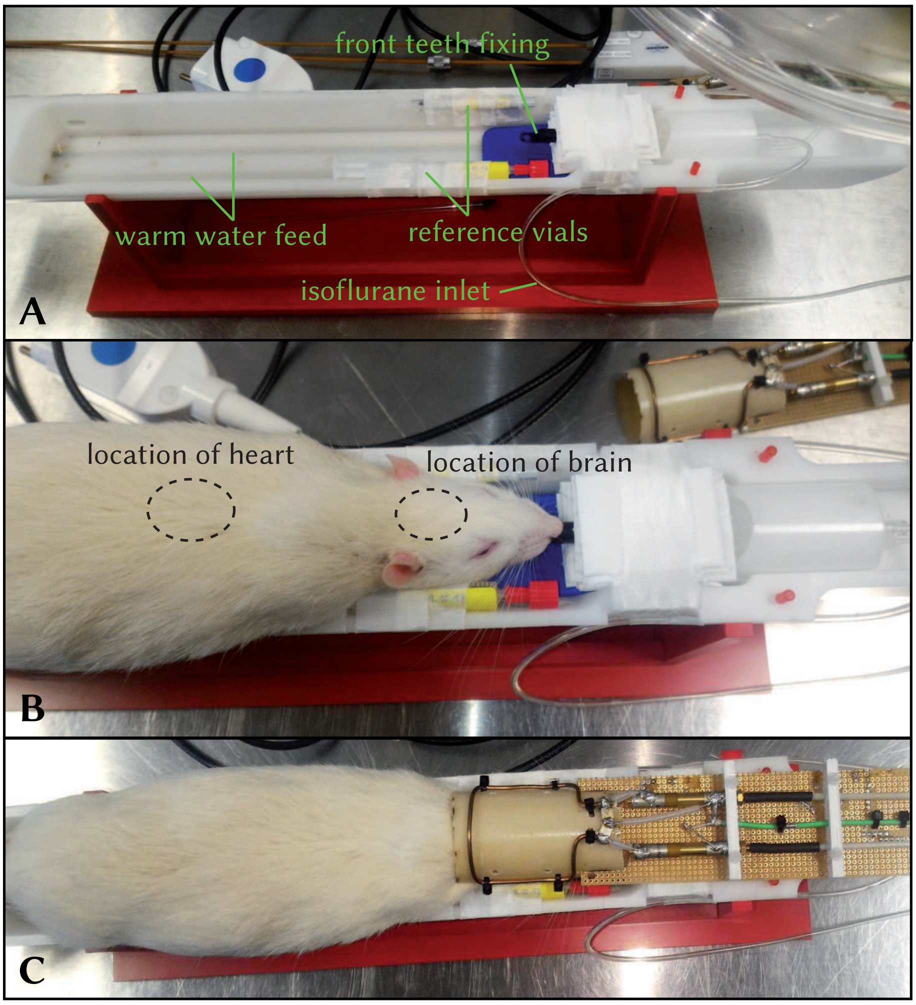

Figure 3.9: **A** The animal bed including the attached reference vials, the front teeth hold, and the isoflurane inlet. **B** Rat placed onto the bed with indication of the brain and the heart. **C** Setup for head measurement with ^{23}Na saddle coil.

In preparation, the rat was placed inside a box with isoflurane inlet. Reference vials were attached to the animal bed. The rat under anaesthesia was taped to the heated bed to avoid gross movement. To ensure continuous anaestasia intake, the front teeth of the rat was placed in a bite bar such that the nose was in the path of the isoflurane supply outlet. Excessive built-up of isuflorane was avoided by an extractor hood inside the scanner bore. The body temperature and the heart beat were monitored and kept at approximately $35\,^{\circ}\mathrm{C}$ and 40 beats per minute, respectively.

The reference vials were not attached directly onto the saddle coils due to a two-step process: First, a ^{1}H reference image was taken with the saddle coil being left out to avoid coil coupling. Afterwards, the animal bed was taken out to attach the saddle coil. The ^{1}H coil was then removed, and the ^{23}Na or ^{35}Cl measurements were done in the second step.

3.2 MR Methods and Sequences

In this section, methods to calibrate RF flip angles (Subsection 3.2.1), to analyze image resolution (Subsection 3.2.2) and to determine relaxation times by means of inversion recovery and spin echo (Subsection 3.2.3) are described. The DA-R sequence and the TQ-TPPI sequence are detailed in Subsection3.2.4 and Subsection 3.2.5, respectively.

3.2.1 Flip Angle Calibration

Flip angles depend on γ, the pulse duration τ_{p} and the strength of the RF field B_1 (Equation (2.23)). Since B_1 depends on the load, the flip angle was calibrated anew for each experimental setup. To achieve a certain flip angle, either τ_{p} or B_1 is varied. The strength of B_1 can be increased by increasing the RF power. In reality, the power is limited upwards by specifications of the coils. In practice, the power was set to maximum, and τ_{p} was adjusted to calibrate the flip angle. This was done by carrying out multiple FID readouts with varying τ_{p}. The maxima of the Fourier transform of the FID were fitted with $\sin(\tau_{\mathrm{p}})$, and the pulse length at $\sin(\tau_{\mathrm{opt}})$ was the pulse length for a 90° pulse (Figure 3.10).

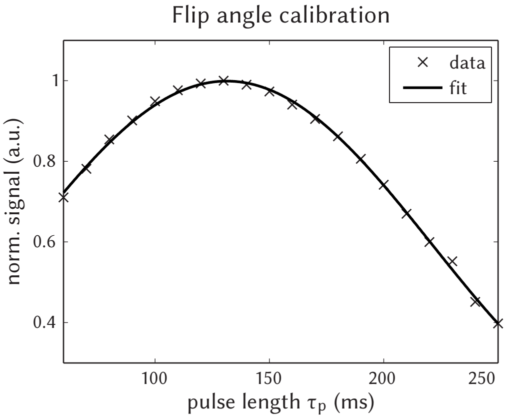

Figure 3.10: Example of a flip angle calibration fit.

3.2.2 Spatial Resolution Analysis

The true resolution of an image reflects on the ability of an imaging sequence to resolve small structures and it differs from the nominal voxel size. The resolutions were determined in images of resolution phantoms (Figure 3.4). First, the centers of structures of the same size are manually selected. The structure regions are then fitted by a 2D Gaussian to determine the coordinates of the centers. The centers of the structures of the same size are connected to form structure paths (Figure 3.11). To process the images of Resolution Phantom AG, in which the structures are solid and the background is filled with NaCl, the images are inverted so that the structures are represented by high gray values. Next, values of the line plots from the structure paths are determined. The mean values for both the high gray value data points (structure) and the low gray value data points (background) are calculated. The differences between the mean high and mean low gray values for each structure size constitute the data for the modulation transfer function (MTF) and are fitted by a logistic function. The threshold at which two structures are deemed distinguishable is 0.2 Davids et al. (2014).

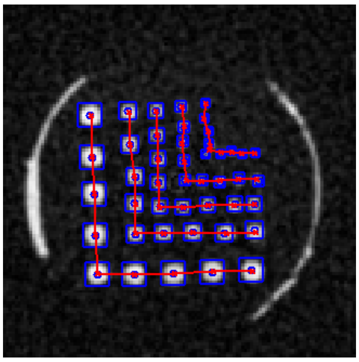

Figure 3.11: Example of structure paths in Resolution Phantom MH.

3.2.3 Relaxation Time Measurement

In this subsection, the conventional sequences to measure T_1 and T_2 are described. Both sequences do not use space encoding gradients and thus acquire signals from the entire object.

Inversion Recovery (IR): T_1

An IR sequence is used to measure T_1. After an initial $180°$ RF pulse, a $90°$ RF pulse is applied after the inversion time TI. The $90°$ pulse flips M_z into the transverse plane. The magnitude

$$M_z(t) = M_0 \left(1 - 2\mathrm{e}^{-t/T_1}\right) \tag{3.1}$$

is measured by incrementing $t = \mathrm{TI}$ for repeated IR experiments. The normalized value of M_z starts at -1 and ends at $+1$. The T_1 fit function is

$$S_{T_1}(\mathrm{TI}) = \mathrm{abs}\left[a \cdot \left(1 - b \cdot \mathrm{e}^{-\mathrm{TI}/T_1}\right) + h\right] \tag{3.2}$$

with the fitting paramters a, b, h and T_1.

Spin Echo (SE): T_2

The purpose of the SE sequence is to elimate effects of T_2^* relaxation and to therefore measure tissue-specific T_2. It is robust against susceptibility artifacts caused by inhomogeneities. The sequence consists of a 90° RF pulse followed by an $180°$ pulse at half the echo time $\mathrm{TE}/2$ to refocus the dephasing spins. At $t = \mathrm{TE}$ the spins are rephased, and a spin echo is formed. The acquired signal is described by mono-exponential decay

$$M_{xy}^{\text{mono}}(t) = M_0 \mathrm{e}^{-t/T_2} \tag{3.3}$$

or by bi-exponential decay

$$M_{xy}^{\text{bi}}(t) = M_0 \left(b \cdot \mathrm{e}^{-t/T_{2\mathrm{f}}} + (1-b) \cdot \mathrm{e}^{-t/T_{2\mathrm{s}}} \right) \; . \tag{3.4}$$

By repeating the SE experiment whlie incrementing TE, the T_2 relaxation curve can be recorded. The mono- and bi-exponential T_2 fit functions are

$$S_{T_2}^{\text{mono}}(\mathrm{TE}) = a \cdot \mathrm{e}^{-\mathrm{TE}/T_2} + c \; , \tag{3.5}$$

$$S_{T_2}^{\text{bi}}(\mathrm{TE}) = a \cdot \left(b \cdot \mathrm{e}^{-\mathrm{TE}/T_{2\mathrm{f}}} + (1-b)\mathrm{e}^{-\mathrm{TE}/T_{2\mathrm{s}}} \right) + c \; , \tag{3.6}$$

respectively, with the fitting parameters a, b, c, T_2, $T_{2\mathrm{f}}$ and $T_{2\mathrm{s}}$.

3.2.4 Radial Imaging

If Cartesian k-space readout is used, the gradients are straightforward, and the data points on a Cartesian grid allow discrete Fourier transform to be performed. Since the readout gradient covers k-space from $-k_{\max}$ to $+k_{\max}$, the center of k-space is reached after half the readout time. For X-nuclei with very short, possibly bi-exponential relaxation times, the disadvantage of signal loss before reaching k-space center outweighs the convenience of Cartesian sampling. Therefore, ultrashort echo time (UTE) techniques are preferred in X-nuclei imaging. In this thesis, two types of UTE techniques were used: conventional UTE sequence and DA-R sequence.

The conventional UTE imaging sequence is provided by Bruker (Figure 3.12A), and the images in form of Digital Imaging and Communications in Medicine (DICOM) file are reconstructed by the scanner. The frequency-encoding readout gradients of constant strength in all directions start at k-space center and acquire data towards k-space periphery. The gradients have constant strength, therefore the speed of data sampling along k-space trajectories is constant except in the ramp-up section. The resulting higher density of sampling points in k-space center is not SNR-efficient, as homogeneous k-space sampling minimizes noise (Liao et al., 1997).

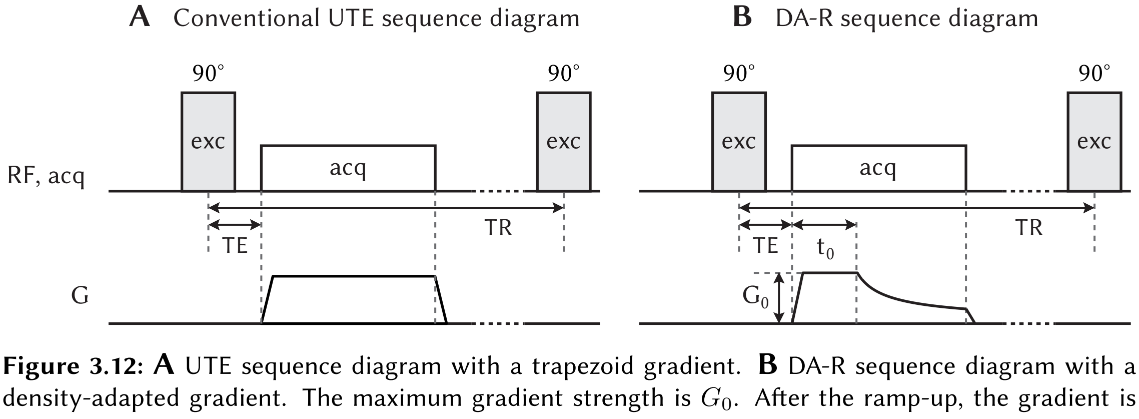

Figure 3.12: **A** UTE sequence diagram with a trapezoid gradient. **B** DA-R sequence diagram with a density-adapted gradient. The maximum gradient strength is G_0. After the ramp-up, the gradient is initially constant. The density-adapted part starts at t_0.

The DA-R technique (Nagel, 2009) has a higher degree of k-sapce sampling homogeneity (Figure 3.12B). This is achieved by adapting the sampling density of the sampling points along k-space trajectories. The density of data on the spherical k-space shells is constant from k_0 upwards. The gradient strenght is high in k-space center and decreases towards the periphery. With time-equidistant sampling rate, the distance between subsequent k-space points is larger in the center than in the periphery.

Ideally, the readout gradient would be entirely density-adapted. However, the gradient must first ramp up, and it cannot be immediately followed by density-adapted gradient due to slew rate limitation. For this reason, the sampling density

$$D(k) \propto \frac{1}{kG(k)} \text{ (2D)}, \tag{3.7}$$

$$D(k) \propto \frac{1}{k^2G(k)} \text{ (3D)}, \tag{3.8}$$

is uniform only after having reached a certain k-space radius $k_0 = k(t_0)$. The sampling density for the density-adapted part is therefore the same as that at time point t_0

$$\frac{1}{kG(k)} = \frac{1}{k_0G(k_0)} \text{ (2D)}, \tag{3.9}$$

$$\frac{1}{k^2G(k)} = \frac{1}{k_0^2G(k_0)} \text{ (3D)}, \tag{3.10}$$

Solving the differential equation

$$G(t) = \frac{1}{\gamma}\frac{\mathrm{d}k(t)}{\mathrm{d}t} \tag{3.11}$$

for $t \geq t_0$ yields the solution for the trajectory

$$k(t) = \sqrt{k_0^2 + 2\gamma k_0 G_0 (t - t_0)} \text{ (2D)}, \tag{3.12}$$

$$k(t) = \sqrt[3]{k_0^3 + 3\gamma k_0^2 G_0 (t - t_0)} \text{ (3D)}, \tag{3.13}$$

which is achieved by the gradient shape

$$G(t) = \frac{k_0 G_0}{\sqrt{k_0^2 + 2\gamma k_0 G_0 (t - t_0)}} \text{ (2D)}, \tag{3.14}$$

$$G(t) = \frac{k_0^2 G_0}{\sqrt[3]{\left(k_0^3 + 3\gamma k_0^2 G_0 (t - t_0)\right)^2}} \text{ (3D)}, \tag{3.15}$$

The distribution of the radial sampling spokes is determined by the polar angle φ and the azimuth angle θ in 3D (Figure 3.13). According to Rakhmanov et al. (1994), an isotropic distribution of N points on the surface of a sphere is given by

$$\theta_n = \arccos(h_n) \tag{3.16}$$

$$\varphi_n = \begin{cases} 0 & \text{for } n = 1 \\ \left(\varphi_{n-1} + \frac{C}{\sqrt{n}} \frac{1}{\sqrt{1-h_n^2}}\right) & \text{for } n > 1, \text{ with} \end{cases} \tag{3.17}$$

$$h_n = -1 + \frac{2(n-1)}{N-1} \text{ and } C = \sqrt{4\pi}. \tag{3.18}$$

The DA-R sequence can acquire 3D images, for which the spatial encoding gradients in all three axes are switched on. It can also acquire pseudo 2D images, which are 2D images containing all signals along the third dimension. To do so, the spatial enconding gradient is turned off along the dimension, along which the signals are added.

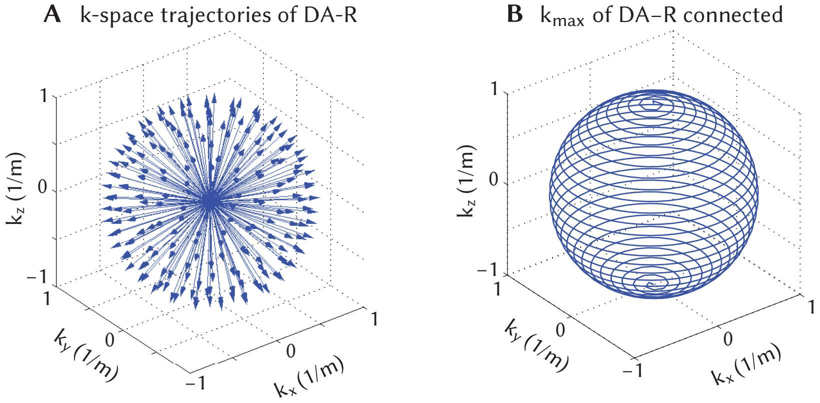

Figure 3.13: **A** Radial k-space spokes represented by arrows ($N_{\text{proj}} = 200$) **B** Connected path reached by the end points k_{max} of the spokes ($N_{\text{proj}} = 1000$)

The necessary number of discrete and equally spaced sampling points in k-space to unambiguously reconstruct a image is given by the Nyquist criterion (Nyquist, 1928). If the k-space is undersampled (FOV> Δk^{-1}), artifacts may occur. The appearence of the artifacts depends on the k-space trajectory. To calculate the Nyquist number of projections, first consider the distance Δk between two sampling points

$$\Delta k = \frac{\gamma}{2\pi} G \Delta t \text{ with FOV} = \frac{1}{\Delta k} \ . \tag{3.19}$$

The nominal resolution Δx in x-direction is

$$\Delta x = \frac{1}{2k_{\text{max},x}} = \frac{\text{FOV}}{N_x} = \frac{2\pi}{\gamma G_x \Delta t_x N_x} \, , \tag{3.20}$$

with N_x being the number of sampling points in x-direction.

In case of radial sampling, the Nyquist criteria read

$$N_{\text{proj}}^{(2D)} = \pi \frac{\text{FOV}}{\Delta x} \text{ (2D)} \, , \tag{3.21}$$

$$N_{\text{proj}}^{(3D)} = \pi \left(\frac{\text{FOV}}{\Delta x} \right)^2 \text{ (3D)} \, , \tag{3.22}$$

with N_{proj} being the number of equally spaced radial projections.

3.2.5 Triple-Quantum Spectroscopy with TPPI (TQ-TPPI)

This subsection introduces the TQ-TPPI sequence by building on the concepts of the measurement of MQ coherences detailed in Subsection 2.2.8. This method allows for simultaneously measurement of the SQ, DQ and TQ signal at distinct frequencies. This distinction among the coherences of different orders is achieved by time-proportional phase incrementation of the excitation and the conversion RF pulse (Drobny et al., 1978). The basic scheme of the TQ-TPPI sequence is shown in Figure 3.14.

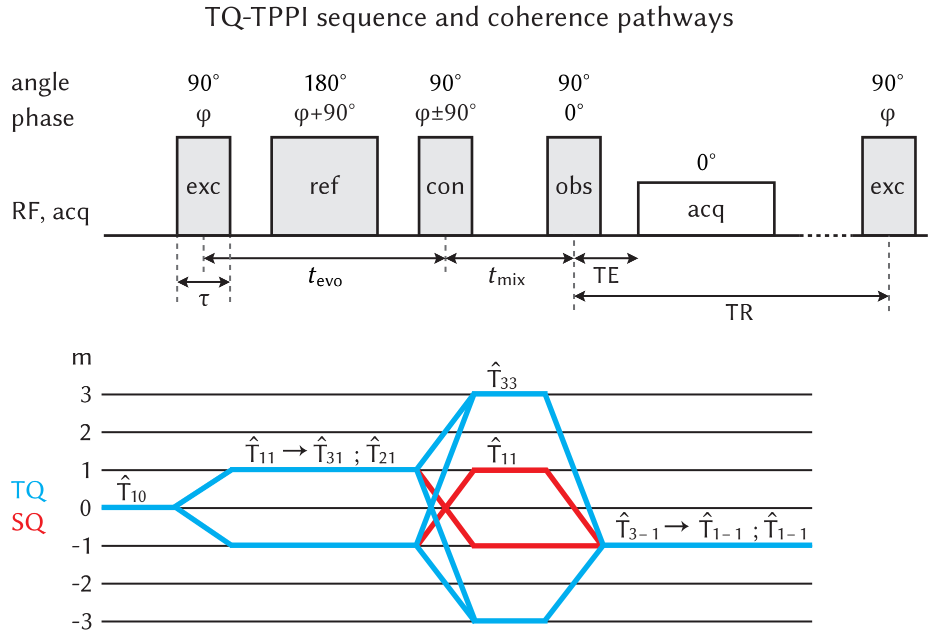
TQ-TPPI sequence and coherence pathways
angle
phase
RF, acq
90°
φ
180°
φ+90°
90°
φ±90°
90°
0°
0°
90°
φ
exc
ref
con
obs
acq
exc
τ
t_{evo}
t_{mix}
TE
TR
m
3
2
1
0
-1
-2
-3
TQ
SQ
$\hat{T}_{10}$
$\hat{T}_{11} \rightarrow \hat{T}_{31}$; $\hat{T}_{21}$
$\hat{T}_{33}$
$\hat{T}_{11}$
$\hat{T}_{3-1} \rightarrow \hat{T}_{1-1}$; $\hat{T}_{1-1}$

Figure 3.14: TQ-TPPI sequence diagram with coherence pathways.

In general, the TQ-TPPI sequence falls in the category of pseudo 2D spectroscopy(van der Maarel, 2003a), which is characterized by signal dependence on two frequency domains. The first frequency domain is the Fourier transform of the regular t-FID. The t-FID is sampled in the t-domain. In the second frequency domain f_{MQ}, the spectra of the SQ, DQ and TQ coherences are distinguished by frequencies. This frequency domain f_{MQ} is the Fourier transform of the t_{evo}-FID sampled in the t_{evo}-domain.

A scheme describing the TQ-TPPI phase steps and phase cycles is displayed in Figure 3.15. During the first phase step, the evolution time is minimal such that $t_{\mathrm{evo}} = t_{\mathrm{evo,min}}$, corresponding to the length of one $90°$ pulse if a refocussing pulse is not used. Each phase step is repeated twice with alternating conversion pulse phase to suppress the DQ signal. After each phase step, the phase φ is incremented by $\Delta\varphi = 45°$, so that a total of $n_{\mathrm{ps}} = 8$ phase steps completes 2π. In other words, the phase is incremented proportional to time (TPPI as in time-proportional phase increment) (van der Maarel, 2003a). It is exactly this phase incrementation scheme that results the separation between the SQ, DQ and TQ signal contributions.

After each phase step, t_{evo} is also incremented by Δt_{evo}. Its purpose is to sample the t_{evo}-FID. The incrementation of t_{evo} is not a necessary condition to separate between the MQ contributions in the f_{MQ} frequency domain, which is the Fourier transform of the t_{evo}-domain. The t_{evo}-FID in the t_{evo}-domain is sampled for each t_{evo} value. The number of phase cycle n_{pc} is the number, by which one cycle of $n_{\mathrm{ps}} = 8$ phase steps is repeated. In total, t_{evo} is incremented $n_{\mathrm{pc}} \cdot n_{\mathrm{ps}}$ times such that the maximum t_evo is $t_\text{evo,max} = t_\text{evo,min} + (n_\text{pc} \cdot n_\text{ps} - 1)\Delta t_\text{evo}$. The total number of spectral points in the f_MQ frequency domain is therefore also $n_\text{pc} \cdot n_\text{ps}$. The mixing time t_mix is kept constant and minimal at all times, equal to the length of one $90°$ pulse. The choice of n_pc and Δt_evo is a trade-off between the spectroscopic resolution in the second frequency domain and the measurement time.

Within each phase step, the phase relations between the RF pulses are fixed. The $90°$ excitation pulse has a phase of φ, while the $90°$ conversion pulse is phase-shifted by $+90°$ with regard to the excitation pulse. Both the observation pulse and the receiver have a phase of $0°$ throughout. The spectrum of the DQ coherence is $90°$ phase-shifted to both the SQ and the TQ coherence.

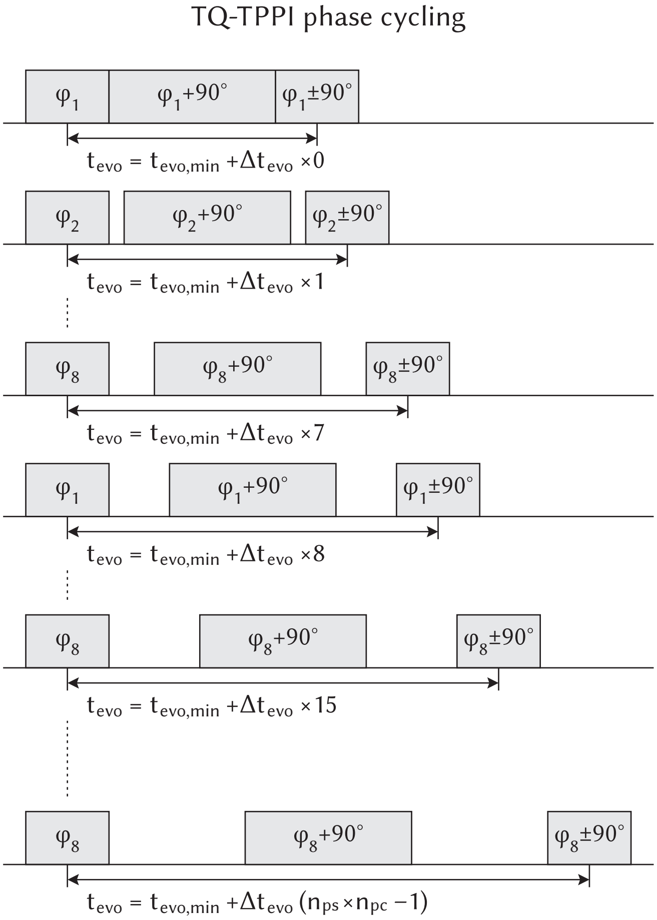
TQ-TPPI phase cycling
φ1
φ1+90°
φ1±90°
tevo = tevo,min +Δtevo ×0
φ2
φ2+90°
φ2±90°
tevo = tevo,min +Δtevo ×1
φ8
φ8+90°
φ8±90°
tevo = tevo,min +Δtevo ×7
φ1
φ1+90°
φ1±90°
tevo = tevo,min +Δtevo ×8
φ8
φ8+90°
φ8±90°
tevo = tevo,min +Δtevo ×15
φ8
φ8+90°
φ8±90°
tevo = tevo,min +Δtevo (nps×npc −1)

Figure 3.15: TQ-TPPI phase steps and phase cycles.

This leads to an overlap of the real part of the SQ and TQ spectral line with the broad imaginary part of the DQ spectral line. To suppress the DQ signal, the basic scheme can be repeated by alternating the phase of the conversion pulse $\varphi \pm 90°$. By adding the signal contributions acquired with alternating phases, contribution from the DQ coherence is eliminated by destructive interference. In additional to the necessary excitation, conversion and observation pulse, an $180°$ refocussing pulse with a phase of $\varphi + 90°$ can be implemented in the middle between the excitation and the conversion pulse to compensate for B_0 inhomogeneneities (Schepkin et al., 2017). The phases of the excitation, conversion and observation pulse are listed alongside the phases of all coherences for each phase step in Table 3.1.

The measured t_evo-FID can be a combination of signal contributions from coherences of different order. It can be fitted by equations containing different combinations of MQ coherences

$$f_{\mathrm{S}}(t_{\text{evo}}) = g_{\mathrm{S}}^{\text{mono}}(t_{\text{evo}}) + c\ , \tag{3.23}$$

$$f_{\mathrm{ST}}(t_{\text{evo}}) = g_{\mathrm{S}}^{\text{bi}}(t_{\text{evo}}) + g_{\mathrm{T}}(t_{\text{evo}}) + c \text{ and} \tag{3.24}$$

$$f_{\mathrm{SDT}}(t_{\text{evo}}) = g_{\mathrm{S}}^{\text{bi}}(t_{\text{evo}}) + g_{\mathrm{D}}(t_{\text{evo}}) + g_{\mathrm{T}}(t_{\text{evo}}) + c\ , \tag{3.25}$$

using an in-house routine in Matlab (MATLAB 2013a, The MathWorks, Natick, U.S.A.). The SQ, DQ and TQ signal contributions are described by

$$g_{\mathrm{S}}^{\text{mono}}(t_{\text{evo}}) = A_{\mathrm{S}} \cdot \sin(2\pi\alpha \cdot t_{\text{evo}} + \varphi) \cdot \mathrm{e}^{-t_{\text{evo}} R^{(1)}_{1=2}}\ , \tag{3.26}$$

$$g_{\mathrm{S}}^{\text{bi}}(t_{\text{evo}}) = A_{\mathrm{S},1} \cdot \sin(2\pi\alpha \cdot t_{\text{evo}} + \varphi) \cdot \mathrm{e}^{-t_{\text{evo}} R^{(1)}_{1}} + A_{\mathrm{S},2} \cdot \sin(2\pi\alpha \cdot t_{\text{evo}} + \varphi) \cdot \mathrm{e}^{-t_{\text{evo}} R^{(1)}_{2}}\ , \tag{3.27}$$

$$g_{\mathrm{D}}(t_{\text{evo}}) = A_{\mathrm{D}} \cdot \sin(2 \cdot 2\pi\alpha \cdot t_{\text{evo}} + \psi) \cdot \left(\mathrm{e}^{-t_{\text{evo}} R^{(1)}_{1}} - \mathrm{e}^{-t_{\text{evo}} R^{(1)}_{3}}\right) \text{ and} \tag{3.28}$$

$$g_{\mathrm{T}}(t_{\text{evo}}) = A_{\mathrm{T}} \cdot \sin(3 \cdot 2\pi\alpha \cdot t_{\text{evo}} + \theta) \cdot \left(\mathrm{e}^{-t_{\text{evo}} R^{(1)}_{1}} - \mathrm{e}^{-t_{\text{evo}} R^{(1)}_{2}}\right)\ , \tag{3.29}$$

respectively. The fit functions g_{S} and g_{T} pertaining to SQ and TQ coherences were derived from the relaxation functions $f^{(1)}_{11}$ and $f^{(1)}_{31}$ in isotropic environment, respectively. Even-ranked DQ coherences are decoupled from odd-ranked SQ and TQ coherences in isotropic environment and therefore cannot be measured if complete relaxation between subsequent repetitions is not granted for. The fit function g_{D} for DQ coherence were derived from the relaxation function $f^{(1)}_{21}$.

The choice of fit equation depended on the the presence of the DQ and/or TQ peak in the spectrum. The DQ and TQ signal are associated with twice and thrice the frequency as the SQ signal, respectively. Their frequency in the sine-term were therefore multiplied by the corresponding factor. A constant offset c was assumed for all fit equations. Fitting was done after manual substraction of the middle peak at zero frequency, which was caused by B_1 inhomogeneities and relaxation effects during the RF pulses.

Parameters such as $T_{2\mathrm{s,f}}$ and the ratio $S_{\mathrm{T/S}}$ between the TQ and the SQ signal

$$S_{\mathrm{T/S}} = A_{\mathrm{T}} / \left(A_{\mathrm{S},1} + A_{\mathrm{S},2}\right) \tag{3.30}$$

were obtained through fitting, with the TQ component scaling factor A_{T} and the SQ scaling factors $A_{\mathrm{S},1}$ and $A_{\mathrm{S},2}$. In a medium with given $T_{2\mathrm{s,f}}$, the optimal evolution time $t_{\text{evo,opt}}$ can be calculated. If t_{evo} is fixed such that $t_{\text{evo}} = t_{\text{evo,opt}}$, then the maximum TQ signal in the medium can be measured. It can be derived from the TQ relaxation function $f^{(1)}_{31}$ (Equation 2.86). In the presence of a refocussing pulse between the excitation and the conversion pulse, such as the case of TQ-TPPI, B_0 inhomogeneities were eliminated, and $t_{\text{evo,opt}}$ became

$$t_{\text{evo,opt}} = \frac{\ln\left(\frac{R^{(1)}_{1}}{R^{(1)}_{2}}\right)}{R^{(1)}_{2} - R^{(1)}_{1}} = \frac{\ln\left(\frac{T_{2\mathrm{s}}}{T_{2\mathrm{f}}}\right)}{\frac{1}{T_{2\mathrm{s}}} - \frac{1}{T_{2\mathrm{f}}}}\ , \tag{3.31}$$

with $T_{2\mathrm{f}} = \frac{1}{R^{(1)}_{1}}$ and $T_{2\mathrm{s}} = \frac{1}{R^{(1)}_{2}}$. In the absence of a refocussing pulse such as the case of conventional TQ filtering, the relaxation times are substitutede with $T^{*}_{2\mathrm{s,f}}$.

n_{ps}	φ in °	$\varphi + 90°$ in °	$\varphi \pm 90°$ in °	SQ phase in °	TQ phase in °	TQ phase in °
1	90	180	180	90	270	90
	90	180	0	90	90	90
2	135	225	225	135	0	225
	135	225	45	135	180	225
3	180	270	270	180	90	0
	180	270	90	180	270	0
4	225	315	315	225	180	135
	225	315	135	225	0	135
5	270	0	360	270	270	270
	270	0	180	270	90	270
6	315	45	45	315	0	45
	315	45	225	315	180	270
7	360	90	90	0	90	180
	360	90	270	0	270	180
8	45	135	135	45	180	315
	45	135	315	45	0	315

Table 3.1: Phases of each phase step of the SQ, DQ and TQ coherence within one phase cycle using TPPI with DQ suppression.

3.3 Sequence Parameters

This section lists the materials, methods and sequence parameters used in individual experiments. It is arranged in the same order as the results in Chapter 4.

3.3.1 Density-Adapted Radial Imaging (DA-R)

Four measurement series were conducted using the DA-R sequence. The degree of SNR improvement and the ability to resolve small structures were investigaed in ^{35}Cl phantom studies. ^{23}Na and ^{35}Cl images of the bioreactor and of rat head and rat torso were evaluated.

SNR Improvement through Density-Adaption

3D ^{35}Cl DA-R images of a bundle of three $50\,\mathrm{ml}$ phantoms containing $134.75\,\mathrm{mM}$ NaCl and 2, 4 and $6\,\%$ agarose were acquired using the volume coil. The benefit of density-adapted k-space sampling was examined. The results are found in Subsection 4.1.1, and the DA-R sequence parameters are summarized in Table 3.2.

The degree of density-adaption was adjusted by the parameter t_0 (Figure 3.12), the time between the beginning of the gradient and the beginning of the density-adapted readout. The maximum and the minimum degree of density-adaption ($\mathrm{DA}_{\mathrm{max}}$ and $\mathrm{DA}_{\mathrm{min}}$) for a readout time of $t_{\mathrm{ro}} = 8\,\mathrm{ms}$ were achieved by setting $t_0 = 0.2\,\mathrm{ms}$ and $t_0 = 8.0\,\mathrm{ms}$, respectively (Figure 3.16). The absolute maximum percentage of density-adaption ($\mathrm{DA}_{\mathrm{max,theo}}$) with $t_0 = 0\,\mathrm{ms}$ is unachievable due to limitation in gradient rise time. On the other hand, the gradient takes the conventional trapezoidal shape for $t_0 = t_{\mathrm{ro}}$ ($\mathrm{DA}_{\mathrm{min}}$), in which case the k-space sampling rate becomes constant. Images with a nominal voxel size of $2\,\mathrm{mm}$ were acquired with14 different t_0 values. By varying t_0, different degrees of density-adaption were achieved.

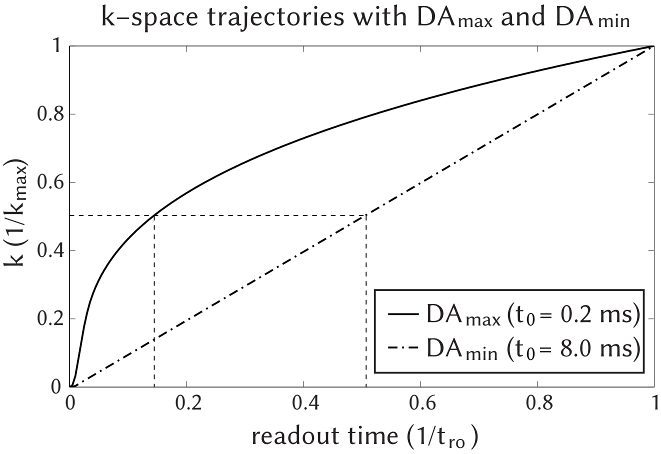

Figure 3.16: Exemplary k-space trajectories for $\mathrm{DA}_{\mathrm{max}}$ and $\mathrm{DA}_{\mathrm{min}}$ with a readout time of $8\,\mathrm{ms}$. The trajectory with a higher percentage of density-adapted readout has a lower sampling density at k-space center and reaches a given point in k-space along the trajectory faster. To reach $0.5k_{\mathrm{max}}$ in this example, the trajectory with $\mathrm{DA}_{\mathrm{min}}$ takes approximately 3.5-fold the readout time as that with $\mathrm{DA}_{\mathrm{max}}$.

Table 3.2: 3D DA-R sequence parameters to investigate SNR improvement through density-adaption. The flip angle was $\alpha = 90°$ and no spoiling was used.

	voxel (mm)	Fig.	TE (µs)	TR (ms)	n_{av}	n_{proj}	FOV (^{3} mm^3)	BW (kHz)	t_{ro} (ms)	t_{sc} (m:s)	t_0 (ms)
^{35}Cl	2	4.1	306	80	8	4000	64	25	8	$42:40$	$0.5-8.0$

Spatial Resolution Analysis

3D ^{35}Cl DA-R and UTE images of two resolution phantoms (Figure 3.4) containing $3.08\,\mathrm{M}$ NaCl were acquired with the volume coil. In this experiment series, the nominal resolution set as sequence parameter is termed voxel size to avoid confusion with the spatial resolution determined from fitting. In images acquired with the same sequence, the fitted resolution was compared with the nominal voxel size. Moreoever, the image quality and the ability to resolve small structures were compared between the DA-R and the UTE images. The results are found in Subsection 4.1.2, and the DA-R and UTE sequence parameters are summarized in Table 3.3.

In experiment series I and II, phantom AG (Figure 3.4B) was scanned; in series III and IV, phantom MH (Figure 3.4A) was scanned. Each phantom was scanned with a nominal voxel size of $0.49\,\mathrm{mm}$ (series I and III) and $0.33\,\mathrm{mm}$ (series II and IV). In each series, 3D images were acquired with both UTE and DA-R. Additionally, series I and III contained one extra DA-R measurement for which the FOV and the necessary number of projections were adjusted to fit the geometry of interest in the transverse plane.

In the UTE sequence, the readout bandwith and dwell time are fixed based on the readout time and image matrix size. In the DA-R sequence, they are chosen independently. All other parameters were identical within each series of experiment.

The DICOM images obtained from UTE measurements were reconstructed by the scanner. The UTE image data are spherical by Bruker default, in accordance with the shape of the spherical k-space volume. DA-R images were reconstructed by an offline Matlab routine using a Hamming filter and without zerofilling. Our offline algorithm returns 3D DA-R data in form of a cube.

The resolution of the images were subsequently assessed based on the methods described in Subsection 3.2.2.

Table 3.3: Parameters of the DA-R sequence and the UTE sequence. Identical parameters for all series are: $t_{\mathrm{ro}} = 8\,\mathrm{ms}$, $n_{\mathrm{av}} = 8$, $\alpha = 90°$, $\mathrm{TE} = 306\,\mu\mathrm{s}$ and $\mathrm{TR} = 80\,\mathrm{ms}$.

phantom	voxel (mm)	series	Fig.	sequence	n_{proj}	BW (kHz)	FOV (^{3} mm^3)	t_{sc} (h:m)
AG	0.49	I	4.3	UTE	19932	5	39.20	03 : 32
				DA-R	19932	25	39.20	03 : 32
				DA-R	12756	25	31.36	02 : 16
	0.33	II	4.2	UTE	39040	7.5	39.12	06 : 56
				DA-R	39040	25	39.12	06 : 56
MH	0.49	III	4.5	UTE	39040	7.5	58.80	06 : 56
				DA-R	39040	25	58.80	06 : 56
				DA-R	13284	25	34.30	02.21
	0.33	IV	4.4	UTE	69644	10	52.16	12.22
				DA-R	69644	25	52.16	12.22

Bioreactor

Pseudo 2D ^{23}Na and ^{35}Cl DA-R images of the square bioreactor were acquired using the surface coil. The goal was the demonstrate the potential of acquiring high resolution images in the bioreactor. The results are found in Subsection 4.1.3, and the DA-R sequence parameters are summarized in Table 3.4.

One high resolution and two low resolution images with an in-plane nominal voxel size of $0.15\,\mathrm{mm}$ and $0.40\,\mathrm{mm}$, respectively, were obtained. A pseudo 2D ^{35}Cl image of the square bioreactor with an in-plane nominal voxel size of $0.8\,\mathrm{mm}$ were acquired using the surface coil.

The maximum SNR was calculated by dividing the maximum value along the line by the standard deviation of the background. The range of the background was determined by visual judgement and contained only regions outside the bioreactor housing. In the ^{23}Na images, the background included the pixels within the region $2.8\,\mathrm{mm}$ on either side of the image border. In the ^{35}Cl image, the background included $4.8\mathrm{mm}$ to the left and to the right of the bioreactor.

Table 3.4: Pseudo 2D DA-R sequence parameters used to acquire ^{23}Na and ^{35}Cl images of the square bioreactor. Spoilers were not used, and the flip angle was $\alpha = 90°$.

	BR	Fig.	TE (µs)	TR (ms)	n_{av}	n_{proj}	voxel (mm)	FOV (^{2} mm^2)	t_{sc} (h:m)	BW (kHz)	t_{ro} (ms)
^{23}Na	square	4.6	75	160	64	400	0.15	28	01 : 08	25	8
			75	160	16	125	0.40	28	00 : 05	25	8
^{35}Cl	square	4.7	69	80	360	125	0.80	27	01 : 00	25	8

Rat Head and Rat Torso

3D DA-R ^{23}Na and ^{35}Cl DA-R images of the head and the torso of a healthy rat were acquired using the saddle coils. The images were evaluated in terms of SNR and signal ratios between different types of tissue. The results are found in Subsection 4.1.4, and the sequence parameters are listed in Table 3.5.

In the first step, two reference vials used to match the ^{23}Na images to the ^{1}H reference images were attached to the animal bed. The vials contained $1\,$ml and $2\,$ml of $50\,$mM NaCl and $4\,\%$ agarose. In all experiments, each vial was attached to the same side of the rat. The saddle coil was left out while the ^{1}H reference image was acquired with a quadrature volume coil. In the second step, the ^{1}H coil was taken out of the bore, and the ^{23}Na or the ^{35}Cl saddle coil was attached to the rat. The ^{1}H images were extracted from the scanner as DICOMs. The ^{23}Na and ^{35}Cl 3D images were reconstructed offline and subsequently matched to the ^{1}H images.

In the head imaging session, the rat was placed in prone position. In the torso imaging session, the rat was placed in supine position, which allowed the rat heart located closer to the anterior side to be closer to the coil. In both imaging sessions, the reference vials were attached directly to the bed, their respective position in the images was identical regardless of the rat placement.

SNRs were calculated by dividing the mean signal intensity in the respective tissue of interest by the standard deviation of the signal intensity of the background. The ROIs of the tissue were manually drawn on up to five coronal slices depending on the size of the organ and the extent of the coil sensitivity. Care was taken to omit border pixels affected by partial volume effects, though it was especially difficult in ^{35}Cl images with comparatively low resolution and SNR. To determine the pixels of the background, a rectangular ROI was drawn in the transverse slice. It was ensured that this ROI included only background signal in all transverse slices. The signal intensities within this ROI across all transverse slices were used to calculate the standard deviation of the background. The relative signal ratios between two tissues were calculated by division and Gaussian propgation of uncertainty.

Table 3.5: 3D DA-R sequence parameters used to acquire ^{23}Na and ^{35}Cl images of the rat brain and the rat heart. Spoilers were used to lower TR. Global *in vivo* T_1 measurements were done to esimate the optimal flip angle. The bandwidth was $25\,$kHz and identical for all measurements.

	region	Fig.	TE (µs)	TR (ms)	n_{av}	n_{proj}	voxel (mm)	FOV (^{3} mm^3)	α °	spoiling	t_{sc} (h:m)	t_{ro} (ms)
^{23}Na	brain	4.8	56	35	1	12000	1.0	56	67	yes	00 : 07	16
	heart	4.10	73	35	3	17000	1.0	64	60	yes	00 : 29	16
^{35}Cl	brain	4.9	86	17	128	1400	1.5	52	81	yes	00 : 50	8
	heart	4.11	96	17	84	5000	1.5	60	81	yes	01 : 59	8

3.3.2 Triple-Quantum Spectroscopy with TPPI (TQ-TPPI)

Inversion Recovery and Spin Echo Measurements

^{23}Na and ^{35}Cl T_1 and T_2 relaxation times were determined using the inversion recovery and the spin echo sequence, respectively. Four phantoms in $50\,$ml vials containing $134.75\,$mM NaCl and 0, 2, 4 and $6\,\%$ agarose were measured with the saddle coils. Parameters were adapted to the relaxation time and NMR sensitivity of each nucleus-phantom combination. The results are found in Subsection 4.2.1. Data were fitted with methods described in Subsection 3.2.3. The inversion recovery and spin ech sequence parameters are summarized in Table 3.6 and Table 3.7, respetively.

Table 3.6: Inversion recovery sequence parameters to measure T_1 in agarose phantoms.

	agarose (%)	TR (ms)	TI (ms)	#(TI)	n_{av}	t_{ro} (ms)	t_{sc} (m:s)
^{23}Na	0, 2, 4, 6	350	$2-350$	256	1	102.4	04 : 29
^{35}Cl	0	200	$3-200$	64	4	102.4	02 : 34
	2, 4, 6		$1-120$	128	8	51.2	08 : 52

Table 3.7: Spin echo sequence parameters to measure T_2 in agarose phantoms.

	agarose (%)	TR (ms)	TE (ms)	#(TE)	n_{av}	t_{ro} (ms)	t_{sc} (m:s)
^{23}Na	0	350	$1-255$	128	4	102.4	04 : 04
	2, 4, 6		$1-192$	192			05 : 42
^{35}Cl	0	200	$1-77$	128	4	102.4	02 : 02
	2, 4, 6		$1-39$		8	51.2	03 : 45

Agarose Phantoms

^{23}Na and ^{35}Cl TQ-TPPI experiments were performed using the saddle coil. Four phantoms in 50 ml vials with 134.75 mM NaCl and 0, 2, 4 and 6 % agarose were scanned. The first aim of the experiments was to examine the differences between the TQ-TPPI results of both nuclei. The second aim was to investigate whether the T_2 fitting results obtained through spin echo and TQ-TPPI experiments were in agreement. The sequence parameters are summarized in Table 3.9. The results of the TQ-TPPI fits with methods described in Section 3.2.5 are found in Section 4.2.1.

Depending on the T_1 of the nucleus-phantom combination, a list of TR values covering a wide range of relevant TR $/T_1$ ratios was composed. On the other hand, TR was limited downwards by the readout duration. For ^{23}Na, the TR range was$115-310$ ms with an increment of 15 ms for all phantoms. For ^{35}Cl, the TR range was $80-200$ ms with an increment of 15 ms for the phantom with 0 % agarose; for the remaining phantoms, it was $35-105$ ms with an increment of 10 ms. The ^{35}Cl T_1 and T_2 values in phantoms with > 0 % agarose were much smaller than those in the phantom without agarose. Therefore t_{ro} and TR were reduced to avoid acquiring noise.

Table 3.9: ^{23}Na and ^{35}Cl TQ-TPPI sequence parameters of agarose phantom experiments to investigate the effect of TR length on the qualitative and quantitative behavior of the TQ-TPPI spectrum. The scan time t_{sc} was in the range of $2-5$ min and $4-16$ min for ^{23}Na and ^{35}Cl experiments, respectively.

	agarose (%)	Fig.	TE (µs)	TR (ms)	#(TR)	n_{av}	BW (kHz)	t_{ro} (ms)	Δt_{evo} (µs)	n_{ps}	n_{pc}
^{23}Na	0, 2, 4, 6	4.12	143	$115-310$	14	1	10	102.4	500	8	50
^{35}Cl	0	4.13	82	$80-200$	9	4	7.5	68.3	320	8	32
	2, 4, 6		82	$35-105$	8	16	5	25.6	120	8	32

Lecithin Phantoms

^{23}Na and ^{35}Cl TQ-TPPI spectra of four phantoms with $154\,\mathrm{mM}$ NaCl and 2, 4, 10 and $20\,\%$ lecithin were obtained using the saddle coil. The experiments were conducted in an in-house collaboration. The aim of the experiments was to investigate whether lecithin phantoms could be an alternative to study TQ signals. Moreover, the differences in the ^{23}Na and the ^{35}Cl spectra were to be contrasted against the corresponding differences in agarose phantoms. The sequence parameters are summarized in Table 3.10. The results of the TQ-TPPI fits are found in Section 4.2.2.

Table 3.10: TQ-TPPI sequence parameters of lecithin phantom experiments to examine the difference in ^{23}Na and ^{35}Cl $S_{\mathrm{T/S}}$ ratios.

	Fig.	TE (µs)	TR (ms)	n_{av}	BW (kHz)	t_{ro} (ms)	t_{sc} (m:s)	Δt_{evo} (µs)	n_{ps}	n_{pc}
^{23}Na	4.15	170	120	3	20	102.4	15 : 59	200	8	100
^{35}Cl	4.16	76	120	4	5	51.2	17 : 46	5	8	512

Bioreactor

^{23}Na and ^{35}Cl TQ-TPPI spectra of the bioreactor were acquired using the surface coils. Initial ^{35}Cl experiments were conducted on the square bioreactor only due to the contamination risk associated with the round bioreactor. To obtain more conclusive findings on the feasibility of measuring cellular ^{35}Cl TQ signal, ^{35}Cl TQ-TPPI spectrum was acquired in the round bioreactor. The sequence parameters are shown in Table 3.11. The results of the TQ-TPPI fits are found in Section 4.2.3.

Table 3.11: ^{23}Na and ^{35}Cl TQ-TPPI sequence parameters of bioreactor experiments to probe the feasibility of acquiring TQ signal *in vitro*.

	BR	Fig.	TE (µs)	TR (ms)	n_{av}	BW (kHz)	t_{ro} (ms)	t_{sc} (m:s)	Δt_{evo} (µs)	n_{ps}	n_{pc}
^{23}Na	square	4.17	61	120	3	20	102.4	15 : 59	200	8	100
^{35}Cl	square, round	4.17	97	80	128	5	51.2	27 : 21	640	8	8

Rat Brain

^{23}Na and ^{35}Cl TQ-TPPI spectra in the brain of a healthy rat *in vivo* were acquired with the saddle coils. Reference vials were not included. To be able to detect TQ signal globally is a prerequisite of acquiring localized TQ images with TASTI. The extent to which this prerequisite was fulfilled for ^{23}Na and ^{35}Cl was studied. The sequence parameters are shown in Table 3.12. The results of the TQ-TPPI fits are found in Section 4.2.4.

Table 3.12: ^{23}Na and ^{35}Cl TQ-TPPI sequence parameters of measurements on the rat brain to investigate the difference in TQ/SQ signal ratio between ^{23}Na and ^{35}Cl *in vivo*.

Fig.	TE (µs)	Fig.	TR (ms)	n_{av}	BW (kHz)	t_{ro} (ms)	t_{sc} (m:s)	Δt_{evo} (µm)	n_{ps}	n_{pc}
^{23}Na	160	4.18	140	1	2048	51.6	06 : 31	100	8	128
^{35}Cl	52	4.18	100	16	128	12.8	14 : 15	35	8	32

3.3.3 Triple- and Single-Quantum TPPI Imaging (TASTI)

Varying TE, Δt_{evo} and $t_{\mathrm{evo,max}}$ in Agarose Phantoms

The TASTI sequence was developed to simultaneously acquire TQ and SQ images. Detailed description of the sequence and the reconstruction pipeline can be found in Subsection 4.3.1. In the reconstructed TASTI dataset, each image voxel corresponded to one t_{evo}-FID in the second time dimension, which could be fitted in the say way as the TQ-TPPI t_{evo}-FIDs. Voxel-wise fitting yielded parameter maps of the $S_{\mathrm{T/S}}$ ratio and the relaxation times $T_{2\mathrm{s,f}}$.

The feasibility of the TASTI sequence was probed in ^{23}Na measurements of a bundle of three phantoms in $50\,\mathrm{ml}$ vials containing $134.75\,\mathrm{mM}$ NaCl and 2, 4 and $6\,\%$ agarose. The measurements were conducted with the ^{1}H/^{23}Na double-resonant volume coil. Apart from the verification of the sequence feasibility, the goal was extended to the evaluation of the images and the parameter maps. To do so, sequence parameters TE, Δt_{evo} and $t_{\mathrm{evo,max}}$ were varied in two sets of experiments to investigate their influence on the images and the parameter maps. The insight served as the basis for *in vivo* studies, and the experimental results were compared with the theoretical predictions. The TASTI sequence parameters are shown in Table 3.13. The results are found in Subsection 4.3.2.

Table 3.13: TASTI sequence parameters in ^{23}Na agarose phantom studies. In the first set of measurements, TE was varied. In the second set of measurements, different combinations of Δt_{evo} and n_{pc} were set. The identical parameters for all measurements are: $n_{\mathrm{proj}} = 70, \mathrm{BW} = 25\,\mathrm{kHz}, t_{\mathrm{ro}} = 8\,\mathrm{ms}$ and $n_{\mathrm{ps}} = 8$.

Fig.	TE (ms)	TR (ms)	n_{av}	voxel (mm)	FOV (^{2} mm^2)	t_{sc} (h:m)	Δt_{evo} (µs)	n_{pc}
4.25	$1-19$	100	1	3.0	72	01 : 22	300	32
4.29, 4.32	10	150	1	3.0	72	00 : 21 − 03 : 44	150	$8-64$
	10	150	1	3.0	72	00 : 11 − 04 : 30	300	$4-64$

In the first set of experiments, TE was varied between $1-19\,\mathrm{ms}$ to probe its influence on $T_{2\mathrm{s,f}}$ and $S_{\mathrm{T/S}}$. This objective was motivated by two limiting factors. (1) Unlike spectroscopic experiments which may sample the entire FID, the time of the readout accompanied by spatial encoding gradients is limited upwards in imaging sequences. The length is a trade-off between acquiring insufficient amount of signal with a very short readout, and acquiring too much noise due to relaxation effects with a very long readout. (2) The relaxation function of the TQ signal has a maximum whose position depends on the relaxation times. If the maximum is during the later portion of the readout, then the TQ signal is weighted towards higher frequencies. It might be dephased by the readout gradient and therefore fall below noise level during readout. And if the readout is completed before the maximum has been reached, then a significant portion of the TQ signal will be missed. For the combination of these two reasons, the readout window, chosen by TE, will affect the outcome in terms of image quality and fitted parameters.

In the second set of experiments, results of measurements with different combinations of Δt_{evo} and n_{pc} were compared. This objective was motivated by the following. To compensate the low signal gain of especially the TQ signal, it may be necessary to spend the limited scan time on t-FID averaging while reducing the number of phase cycles n_{pc} and increasing the sampling step Δt_{evo}. This comes at the cost of lowered MQ spectral resolution, which may increase instability in fitting due to the reduced number of fitting points. It may be problematic especially in potentially noisy t_{evo}-FIDs *in vivo*.

Rat Head

TASTI ^{23}Na experiments in the rat head *in vivo* were performed on a healthy Sprague Dawley rat using the saddle coil. The first goal was to probe the feasibility of obtaining TQ and SQ images *in vivo*. Following this step, the second goal was to determine localized $S_{\text{T/S}}$ ratios and $T_{2\text{s,f}}$ values in rat head.The TASTI sequence parameters are shown in Table 3.14. The results are found in Subsection 4.3.3.

Identical to the procedure of rat brain imaging in Subsection 3.3.1, two reference vials to match the ^{23}Na SQ and TQ images to the ^{1}H reference images were attached to the animal bed. The vials contained $1\,\text{ml}$ and $2\,\text{ml}$ of $50\,\text{mM}$ NaCl and $4\,\%$ agarose. In all experiments, each vial was attached to the same side of the rat. The ^{23}Na coil was left out while the ^{1}H reference image was acquired with a quadrature volume coil. In the second step, the ^{1}H coil was taken out of the bore, and the ^{23}Na coil was attached to the rat.

The k-space was filtered by a $\cos^2$ function of factor 2 to reduce the influence of noise in the k-space on the reconstructed images. The images were reconstructed with a Hamming filter and without zerofilling.

Table 3.14: TASTI sequence parameters to acquire pseudo 2D ^{23}Na images in rat head.

Fig.	TE (ms)	TR (ms)	n_{av}	n_{proj}	voxel (mm)	FOV (^{2} mm^2)	t_{sc} (h:m)	BW (kHz)	t_{ro} (ms)	Δt_{evo} (µm)	n_{ps}	n_{pc}
4.34	1	100	3	200	1.0	54	01 : 11	25	16	800	8	4

4 Results

4.1 Density-Adapted Radial Imaging (DA-R)

This section presents the results obtained from the applications of ^{23}Na and ^{35}Cl DA-R imaging. The SNR benefits of the density-adapted sampling and the achived higher resolution are demonstrated in Subsection 4.1.1 and 4.1.2, respectively. Measurements in the bioreactor and rats are presented in Subsection 4.1.3 and 4.1.4, respectively.

Discourse of ultra-short imaging techniques was provided in Section 3.2.4. Descriptiuon of materials and sequence parameters can be found in Section 3.3.1.

4.1.1 SNR Improvement through Density-Adaption

To examine the benefit of density-adapted k-space sampling, ^{35}Cl DA-R images with varying t_0 were acquired. The maximum degree of density-adaption $\mathrm{DA_{max}}$ was achieved for minimal t_0, while $\mathrm{DA_{min}}$ was achieved for maximal t_0. The sequence parameters are listed in Table 3.2.

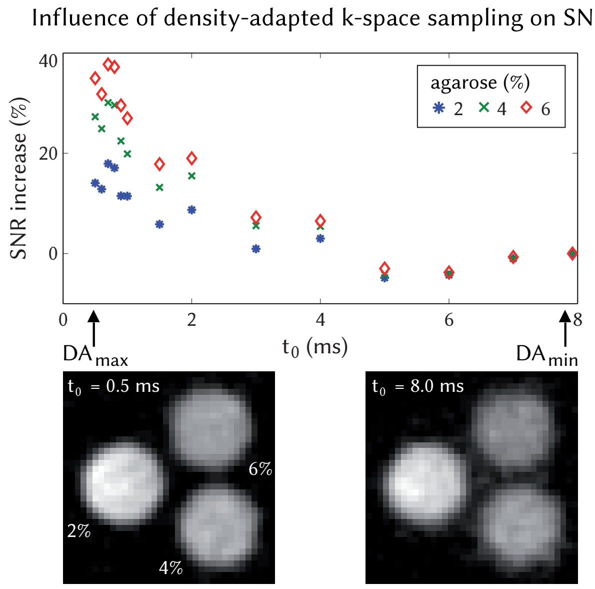

Figure 4.1: Percentage SNR increase in DA-R images acquired with different t_0 and thus varying degrees of density-adaption. The nominal resolution was 2 mm with a FOV of $(64\,\mathrm{mm})^2$.

The SNR values are plotted against t_0 and shown in Figure 4.1, with exemplary images acquired with $\mathrm{DA_{max}}$ and $\mathrm{DA_{min}}$ are shown beneath. In the $\mathrm{DA_{max}}$ image, phantoms had sharper edges, and the background was more homogeneous. In the $\mathrm{DA_{min}}$ image, border smearing was distinctive for the 4 % and 6 % phantoms. The SNR increase in each phantom was referenced to its SNR at $\mathrm{DA_{min}}$. For each phantom, the SNR was generally higher in images with a higher degree of density-adaption. Among the three phantoms, the benefit of density-adaption was more prominent in the phantoms with a higher agarose concentration. The maximum SNR increase was (18 ± 0.9) %, (30 ± 1.3) %, and (38 ± 2.4) % in the 2 %, 4 % and 6 % phantom, respectively.

4.1.2 Spatial Resolution Analysis

^{35}Cl images of two resolution phantoms with reverse construction principles (Subsection 3.1.3) were acquired with the Bruker UTE and the implemented DA-R sequence (Subsection 3.2.4). The aim was to demonstrate the superior spatial resolution capacity and the potential of measurement time reduction in DA-R imaging. The sequence parameters are listed in Table 3.3.

In each figure, the UTE results are shown in the top subfigure, and the DA-R results are shown in the bottom subfigure(s). Each subfigure contains three plots: (1) an image of the resolution phantom, (2) an exemplary bar plot showing the gray values structure paths of the biggest structure, and (3) the MTF obtained from the mean peak-valley differences in the bar plots of all five structures with, if applicable, the logistic fit and the fitted resolution.

Improvement in image quality over the UTE sequence was most prominent in the DA-R images with the smaller voxel size of 0.33 mm. Overall, the following was observed when comparing each figure. Every UTE image was considerably noisier than the respective DA-R image. This was also observed in the DA-R bar plot(s): the recurring alternation between high and low gray values was smoother, with more distinctive shapes of the hills. The minimum gray value was lower, while the maximum gray value was higher in the DA-R images.

Results of phantom AG with a voxel size of 0.33 mm are shown in Figure 4.2. The noisy UTE image texture was reflected in its gray value bar plots, which allow no interpretation of the underlying physical object without prior knowledge. A logistic fit of the MTF was not applicable in both the UTE and the DA-R image. Nonetheless, the peak-valley signal differences of each structure size was higher with a smaller standard deviation in **(B)** than in **(A)**.

Results of phantom AG with a voxel size of 0.49 mm are shown in Figure 4.3. Thinly spaced ringing was present in the center of the UTE image. Additionally, the UTE image was encircled by a prominent white signal ring along the image border. The minimum FOV of the UTE image was restricted downwards by this signal ring. Without this restriction, a minimalist FOV and consequently smaller image matrix can be chosen to reduce scan time. A second DA-R image shown in **(C)** was acquired with this minimalist FOV, which saved 48.8 % of measurement time compared with **(A)** and **(B)**. DA-R Images in **(B)** and **(C)** had similarly good quality, and the logistic fit yielded a comparable resolution of 0.68 mm and 0.72 mm, respectively. This corresponded to 1.39 and 1.47 times the nominal voxel size, respectively. A logistic fit was not applicable in **(A)** due to poor dispersion of the MTF data. The peak-valley signal difference of the two biggest structures was approximately 25 % lower in **(A)** than in **(B)** or **(C)**.

Results of phantom MM with a voxel size of 0.33 mm are shown in Figure 4.4. In the UTE bar plots, the peak values were > 0.5 for all structure sizes except for the smallest one. However, the registered high values along the structure paths were superimposed by false noise spikes and thus cannot be entirely attributed to pixel values inside the structures. In the DA-R bar plots in **(B)**, on the other hand, high values could be unambiguously attributed to pixel values inside the structures in the majority of cases. Logistic fit of the MTF was not applicable. For the same structure size, the peak-valley signal difference was higher in **(B)** than in **(A)**.

Results of phantom MM with a voxel size of 0.49 mm are shown in Figure 4.5. Similar to Figure **4.3**, a third measurement with minimalist FOV is shown in **(C)** with 80.2 % reduced measurement time. This high percentage comes from the fact that the object of interest was square-shaped, therefore it was able to efficiently make use of the cubic image volume of DA-R. Logistic fit in **(A)** was not applicable due to poor data dispersion. The peak-valley signal difference of the smallest structure was higher in **(A)** than in **(B)** or **(C)**, potentially a result of false noise spikes. The logistic fit determined a resolution of $0.77\,\mathrm{mm}$ and $0.82\,\mathrm{mm}$ in **(B)** and **(C)**, corresponding to 1.57 and 1.67 times the nominal voxel size, respectively.

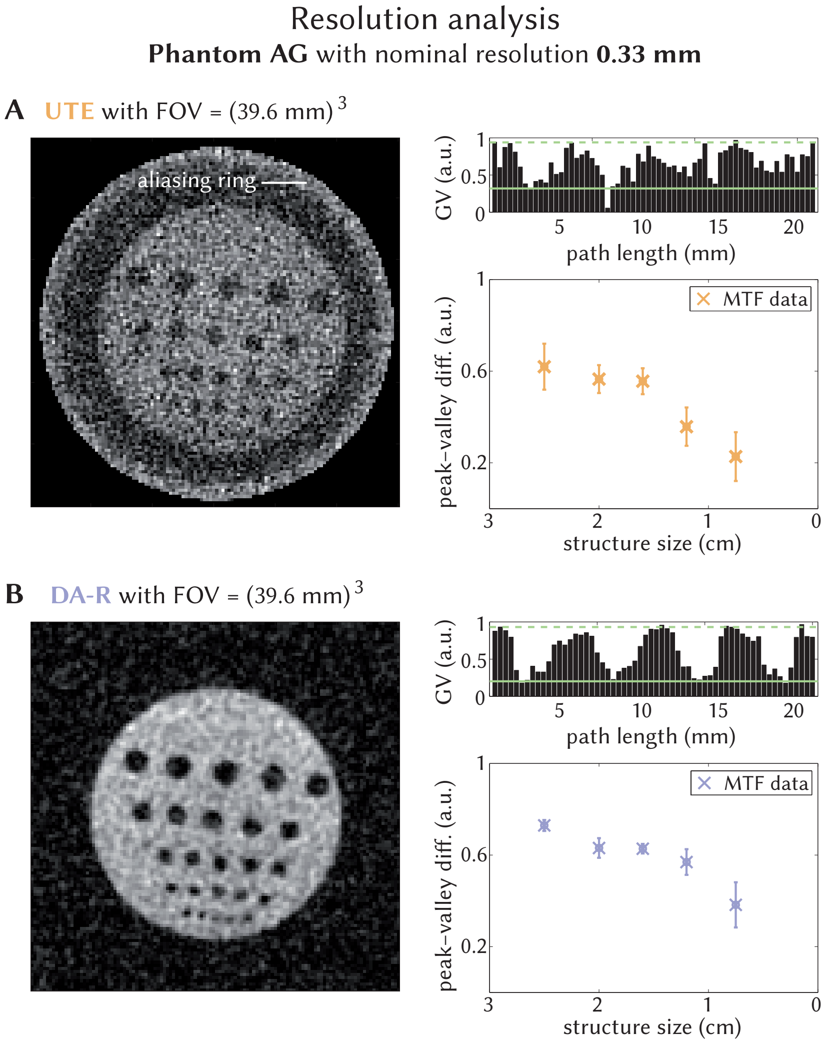

Figure 4.2: ^{35}Cl resolution phantom analysis with phantom AG and a nominal voxel size of $0.33\,\mathrm{mm}$. Gray values in the bar plots were reversed for this phantom. In **A** and **B** the same FOV with the same number of spokes were sampled. The high noise level of **A** was also reflected in the higher standard deviation of the MTF points. The GV along the structure paths shown in the bar plots in **A** also failed to clearly reveal the distribution of the structures, while those in **B** contained repetitive patterns of signal in- and decrease for all except the smallest structure size.

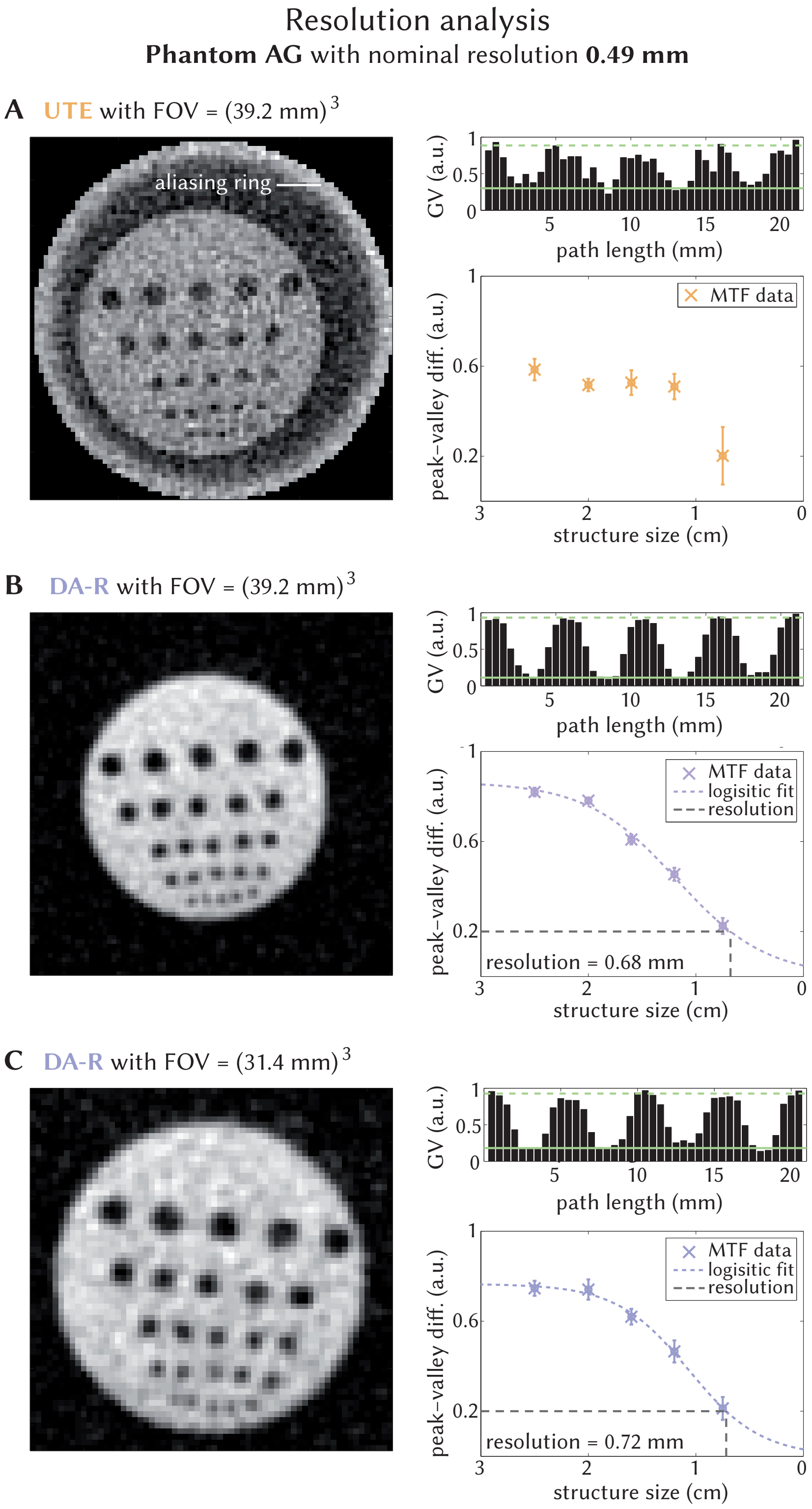

Figure 4.3: ^{35}Cl resolution phantom analysis with phantom AG and a nominal voxel size of 0.49 mm. Gray values in the bar plots were reversed for this phantom. In **A** and **B** the same FOV with the same number of spokes were sampled. In **A** fine ringing artefacts were visible in the center; gross ringing was found at the edge of the circular image. The image of the minimalist FOV chosen in **C** had comparable image quality and fitted spatial resolution as the image in **B**.

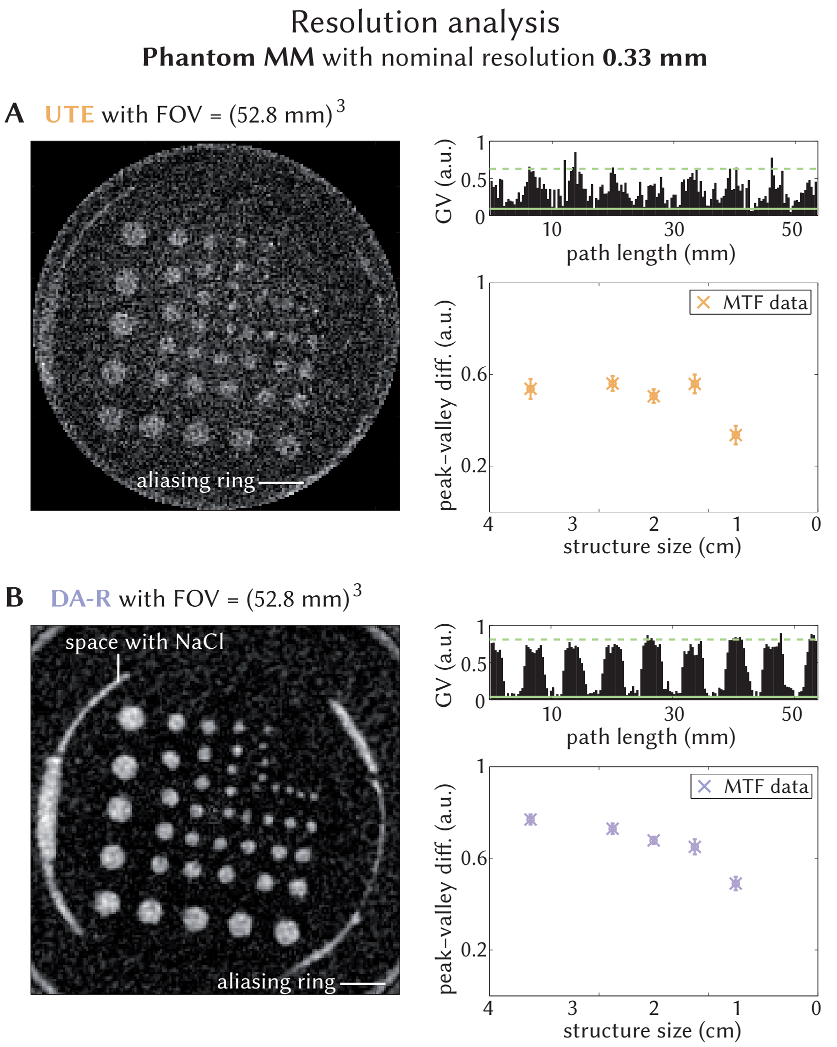

Figure 4.4: ^{35}Cl resolution phantom analysis with phantom MM and a nominal voxel size of 0.33 mm. Gray values in the bar plots in **A** are overlayed by noise, whereas the distinction between peaks and valleys were clear in **B**. Despite the fact that fitting was not applicable due to low dispersion of the MTF values, the higher peak-valley gray value differences in **B** was nevertheless an indicator for a better spatial resolution capacity.

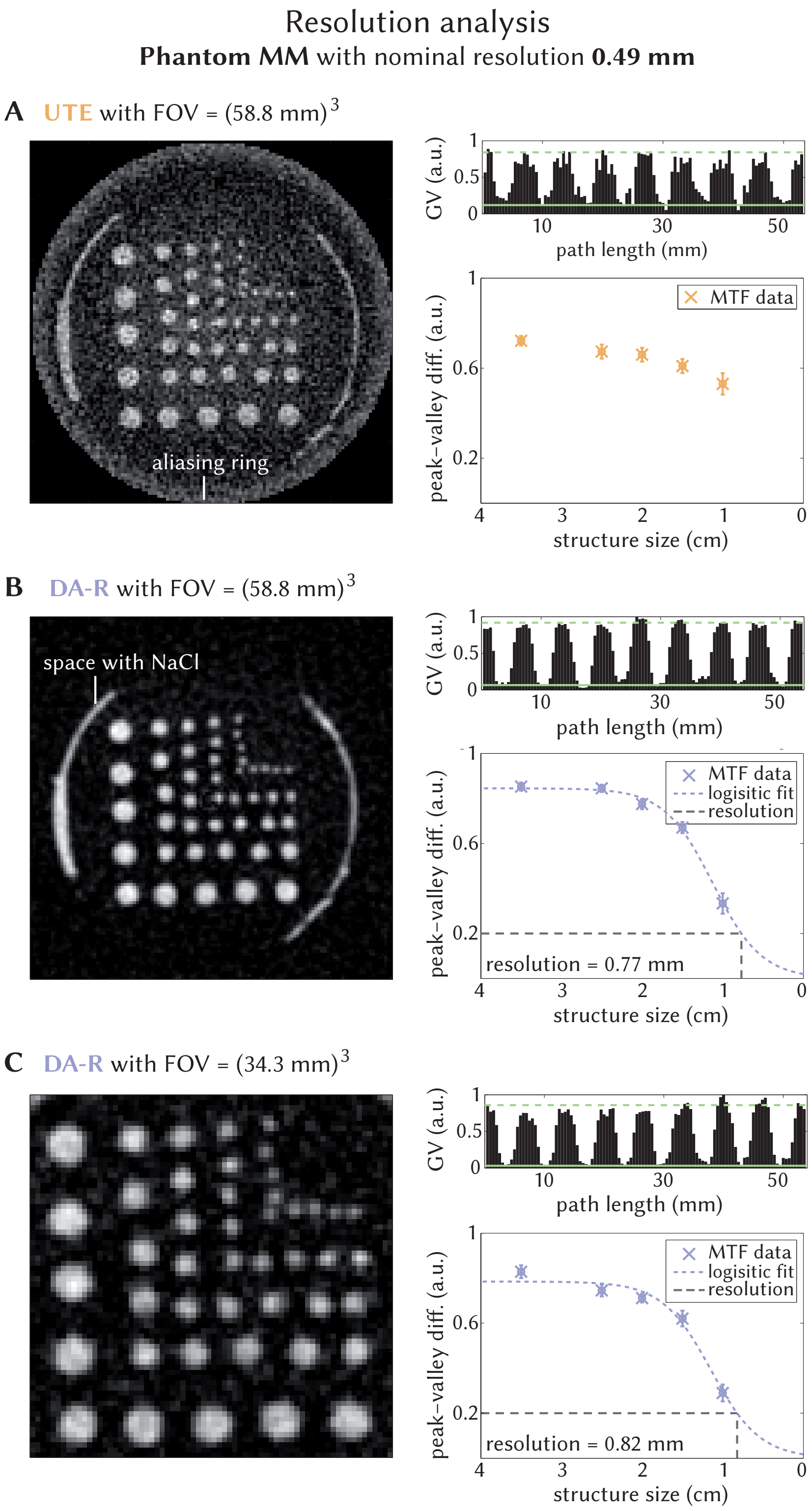

Figure 4.5: ^{35}Cl resolution phantom analysis with phantom MM and a nominal voxel size of 0.49 mm. In **A** and **B** the same FOV with the same number of spokes were sampled. Uncorrelated signal spikes due to the high noise level in **A** artificially increased the peak-valley signal differences especially for smaller structures. Imaging objects not compliying with the circular image edge of UTE benefited from the cubical FOV of DA-R in terms of drastically reduced measurement time. Comparable spatial resolutions in **B** and **C** were obtained through fitting of the MTF.

4.1.3 Bioreactor

Pseudo 2D DA-R images were acquired to demonstrate the imaging potential in the square bioreactor. ^{23}Na images were acquired with two isotropic voxel sizes (Figure 4.6). The sequence parameters are listed in Table 3.4.

The high resolution images had a nominal voxel size of $0.15\,\mathrm{mm}$ and were acquired in 1 hour and 8 minutes. Two low resolution images had an nominal voxel size of $0.40\,\mathrm{mm}$ and were obtained in 5 minutes. The low resolution images were acquired with a time gap of a few hours during which the bioreactor was perfused. The ^{35}Cl image had an isotropic nominal voxel of $0.8\,\mathrm{mm}$ and was acquired in 1 hour (Figure 4.7). In addition, a line plot crossing both chambers of the bioreactor is shown beneath each bioreactor image. The position of the line plot is indicated by the dashed line (bottom rows in Figure 4.6 and 4.7).

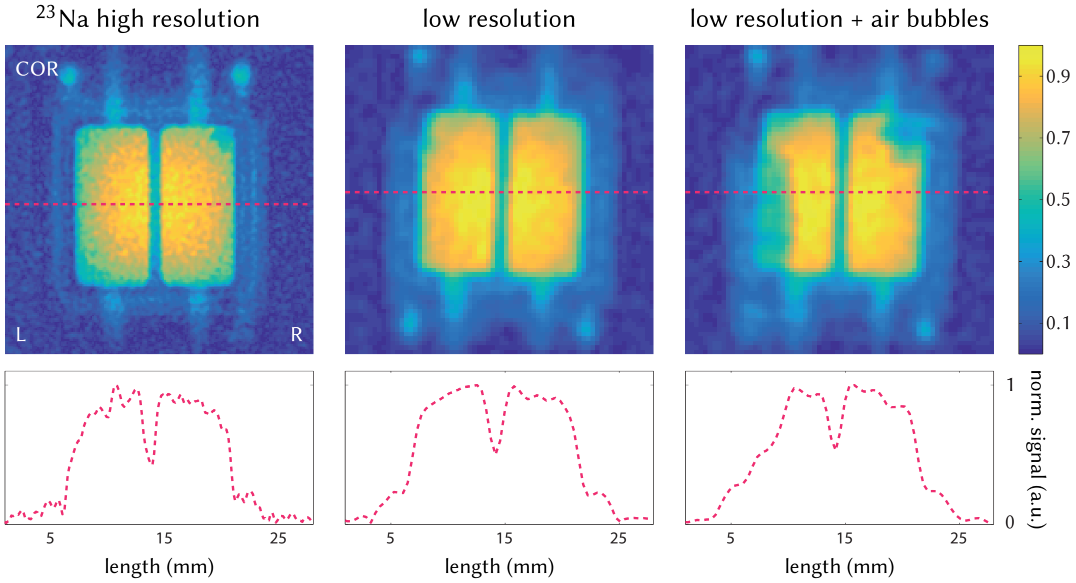

Figure 4.6: Normalized pseudo 2D ^{23}Na DA-R images of the square bioreactor in the coronal view with a FOV of $(28\,\mathrm{mm})^2$ and the corresponding line plots. The high resolution image and the low resolution image have an isotropic nominal voxel of $0.15\,\mathrm{mm}$ and $0.40\,\mathrm{mm}$, respectively. The positions of the line plots are indicated by the dashed lines across the images.

The radial symmetric coil profile of the surface coil was clearly visible in all ^{23}Na images, with the highest intensity observed in the center. Both chambers were distinguishable from the background as well as from each other in all images. In the high resolution image, the tubes that supply the bioreactor chambers with medium could be discerned. Apart from the two chambers filled with medium, medium residues were generally also present between the top and the bottom part of the housing. They were in form of stripes encircling the chambers. Moreoever, medium residues were also found in the spacings for the screws. In the top corners to both sides, the screw spacings were also visible. In the low resolution images, medium residues were also clearly distinguishable from the background, though they appeared more blurry than in the high resolution image. In the low resolution image to the right, regions of reduced signal attributed to air bubbles were found in both chambers.

The line plots derived from the ^{23}Na images had a similar shape, whereby the ones belonging to the low resolution images appeared smoother. The air bubble in the left chamber of the low resolution image was reflected in the dent in the corresponding section of the line plot.

The ratios between the maximum value along the line and the minimum value in the spacing between the two chambers were 2.30 ± 0.04 in the high resolution image and 1.97 ± 0.02 in the low resolution image. The SNRs in the high resolution and the low resolution image were 39.9 ± 0.7 and 83.1 ± 0.9, respectively. Assuming comparable sequence parameters, the SNR ratio between two can be estimated with

$$\sqrt{\frac{t_{\text{scan},1}}{t_{\text{scan},2}}} \cdot \left(\frac{\text{voxel}_1}{\text{voxel}_2}\right)^2 \cdot \left(\frac{\omega_1}{\omega_2}\right)^{\frac{7}{4}} \tag{4.1}$$

with the frequency-dependent sensitivity of $\omega_0^{7/4}$ (Hoult and Richards, 1976). It yielded an SNR ratio of 1.93 between the low resolution and the high resolution image. Multiplied with the SNR in the high resolution image yielded an expected SNR of 77.0 ± 1.4 in the low resolution image, corresponding to (7.3 ± 2.0) % deviation from the measured value of 83.1 ± 0.9.

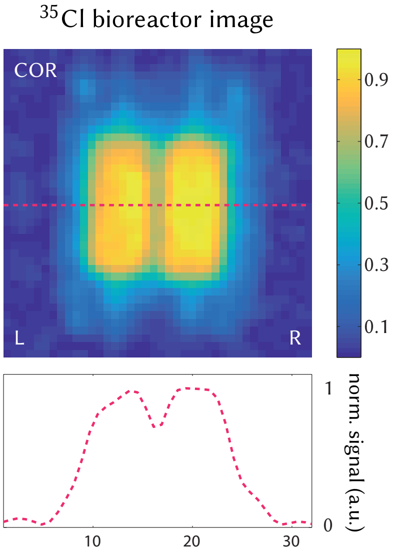

Figure 4.7: Normalized pseudo 2D ^{35}Cl DA-R image of the square bioreactor in the coronal view and the corresponding line plot. The image was normalized to its own maximum. The image has a FOV of $(32\,\text{mm})^2$ and an isotropic nominal voxel of $0.8\,\text{mm}$. The position of the line plot is indicated by the dashed lines across the image.

In the ^{35}Cl image of the bioreactor, the radial symmetric coil profile was not as distinctive as in the ^{23}Na images. The right chamber had a more homogeneous signal distribution than the left chamber, which was visible both in the image itself and the line plot. The chambers could be distinguished from each other despite the larger nominal voxel size of 0.8 mm. Signal originating in the medium residues in the bioreactor housing surrounding the chambers were above noise level and could be differentiated from the background.

The line plot derived from the ^{35}Cl image had a similar shape as those derived from the ^{23}Na images. The ratio between the maximum value along the line and the minimum value in the spacing between the two chambers was 1.37 ± 0.01. It was lower than the ones found in the line plots derived from ^{23}Na images due to the bigger voxel size and the therefore greater influence of the partial volume effect. Neverthelss, the ratio was sufficiently high to distinguish the two chambers. Furthermore, the SNR was 65.7 ± 0.5. Using Equation 4.1, the expected ratio between the ^{35}Cl image and the high resolution ^{23}Na image was 1.33. This resulted in an expected ^{35}Cl SNR of 52.6 ± 2.2, which is (20.0 ± 3.1) % lower than the measured value.

4.1.4 Rat Head and Rat Torso

In this subsection, the results of DA-R imaging in healthy rats in vivo are shown. ^{23}Na and ^{35}Cl images of the rat head and the rat heart were evaluated qualitatively. Furhtermore, the SNRs of various types of tissues as well as the signal ratios between different types of tissue were discussed quantitatively. The sequence parameters were listed in Table 3.5.

SNR values in different organs and types of tissues are summarized in Table 4.1. Relative SNR ratios between different organs were calculated from the SNR values and tabluated in Table 4.2.

^{23}Na rat head Two coronal slices of the ^{23}Na rat head image to include different anatomical features are shown in Figure 4.8. The slice in the top row included the nasal cavity, the eyes and the brain. These regions were labeled in the ^{1}H image. More specifically, the left eye was slightly lower and only its vitreous humor was seen in this slice, while both the lens and the vitreous humor of the right eye were seen in this slice. The most superior part of the brain included in this slice was the olfactory bulb, a structure more pronounced in rats than in humans. The olfactory bulb was connected to the cortex. To the inferior end of the cortex, part of the cerebellum was visible. In the corresponding ^{23}Na image the eyes had very high signal intensities and appeared prominent. The left eye had the shape of an egg, while the right eye had the shape of a crescent. The skin to either side of the head was very close to the coil and had a relatively high ^{23}Na signal intensity due to the high sodium concentration in the skin. Despite its relatively low signal intensity, the cheek tissue between the skin and the brain could be distinguished from the back-

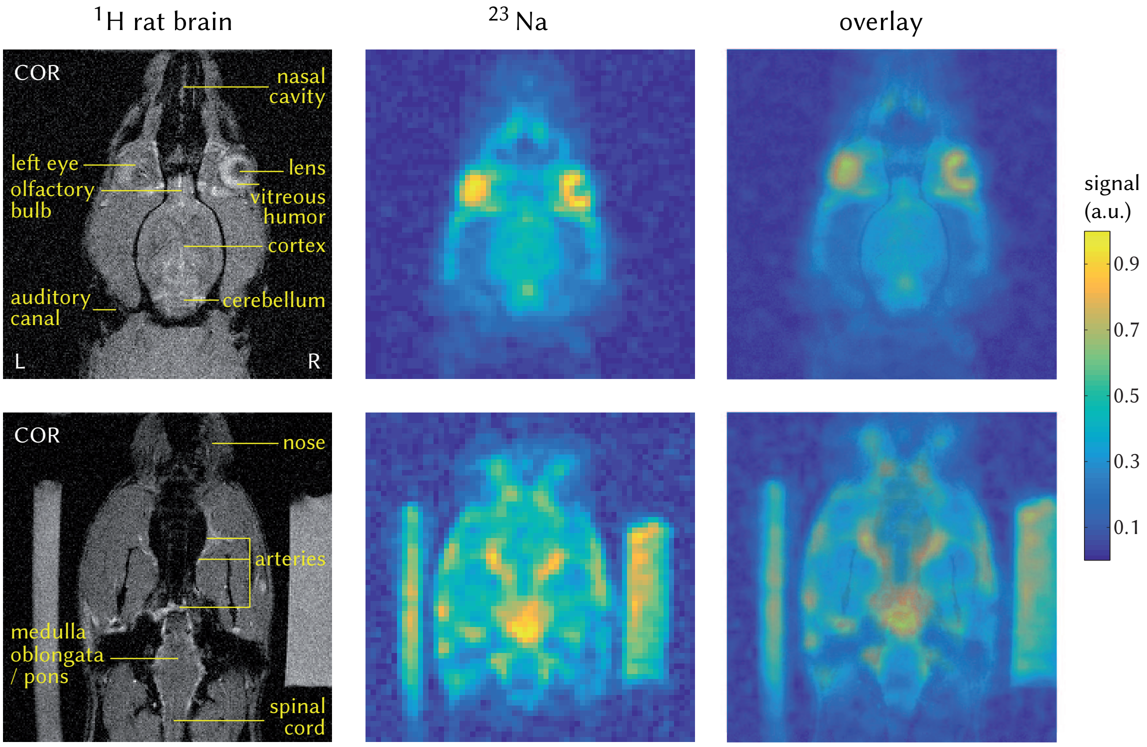

Figure 4.8: 3D *in vivo* ^{23}Na DA-R images of the rat head in prone position acquired in 7 minutes. The coronal slice in the top row is closer to the surface coil. Each image is normalized to its own maximum. The images have a FOV of $(64\,\mathrm{mm})^2$. The ^{1}H and the ^{23}Na images have an isotropic nominal voxel of $0.25\,\mathrm{mm}$ and $1\,\mathrm{mm}$, respectively.

ground. The olfactory bulb and the cerebellum located superior and inferior to the cortex, respectively, were seen with a narrower shape and could be differentiated from the cortex. In the overlay image, the egg- and crescent-shaped ^{23}Na signal distributions were matched to the virtreous humor in the left and the right eye, respectively. In comparison, the lens in the eye had much lower signal than the virtreous humor.

The slice in the bottom row depicts part of the medulla oblongata, the pons, the spinal cord, and the arteries in many instances. These regions were labeled in the ^{1}H image. The arteries had a similarly high ^{23}Na signal intensity as the reference vials. In comparison, the medulla oblongata and the pons had very low signal intensities and could not be well differentiated from the background. Their locations were inferred from the distribution of the surrounding arteries. The spacing between the reference vials and the rat was occupied by the surface coil and the plastic housing of the vials, therefore appearing as dark background. The signal intensity was relatively high in some areas close to the coil, such as the skin of the rat head and the vials. The part of the rat nose included in this slice appeared as two diverging structures. In the overlay image, the many instances of arteries in both images coincided well.

In the rat head, ^{23}Na SNRs were calculated in the virteous humor in the eyes, in the brain including the cortex and the cerebellum, in the cheek tissue, and in the blood in the arteries. The SNR was the highest in the eye with 67.7 ± 5.6. The SNR of 34.2 ± 5.2 in the cerebellum was not significantly higher than the SNR of 33.1 ± 3.4 in the cortex. On average, the brain had an SNR of 33.3 ± 3.6. In comparison, the relative SNR between the eye and the brain was 2.04 ± 0.28. The coil was attached to the rat head in a way that the brain was expected to fall into the region of the highest sensitivity. It follows that the SNR ratio between the eyes, which were further away from the center of the coil, and the brain, which was under the center of the coil, might be underestimated in comparison to values acquired by a coil with a homogeneous B_1. The SNR of the cheek tissue between the brain and the skin was 18.9 ± 1.6. It was extracted from the same slices as the eyes and the brain and had the lowest SNR. Nevertheless, the value was well over noise level. The relative SNR between the brain and the cheek tissue was 1.76 ± 0.24. The SNR in the arterial blood was 31.1 ± 4.3. However, as the value was extracted from slices further away from the coil with a lower coil sensitiviy, it was likely underestimated.

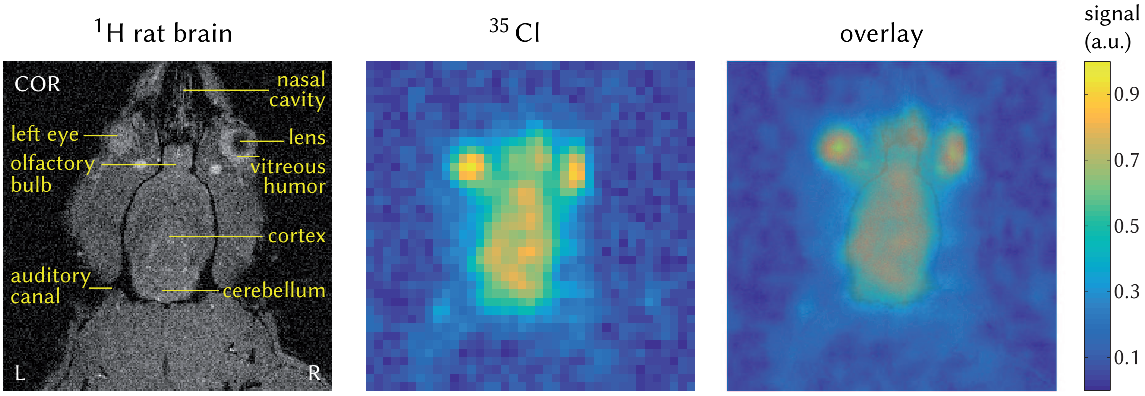

Figure 4.9: 3D *in vivo* ^{23}Na DA-R image of the rat head in prone position acquired in 50 minutes. One coronal slice is shown containing the same anatomical features as the first slice of the ^{23}Na image is shown. The ^{35}Cl image is normalized to its own maximum and has a FOV of $(60\,\mathrm{mm})^2$. The ^{1}H and the ^{35}Cl image have an isotropic nominal voxel of $0.25\,\mathrm{mm}$ and $1.5\,\mathrm{mm}$, respectively.

^{35}Cl rat head One coronal slice of the ^{35}Cl rat head image is shown in Figure 4.9. This slice contained the same anatomical features as the first slice of the ^{23}Na head images shown in Figure 4.8. The nasal cavity, the eyes and the brain were labeled in the ^{1}H image. Unlike the ^{23}Na image, in which the eyes exhibited a much higher signal intensity than the brain, the eyes had only slightly higher signal intensities than the brain in the ^{35}Cl image. The outline of the brain was distinguishable from surrounding tissues, yet the cerebellum could no be distinguished from the cortex. While the olfactory bulb had a similar signal intensity as the cortex in the ^{23}Na image, it appeared to have a reduced signal intensity in the ^{35}Cl image. ^{35}Cl signal intensities in tissues adjacent to the brain and the eyes did not rise above noise level. The extent of the eyes and the brain from the ^{35}Cl and the ^{1}H image matched well in the overlay.

In the rat head, ^{35}Cl SNR values were calculated in the eyes without distinguishing between the lens and the virteous humor, and in the brain without distinguishing between the cortex and the cerebellum. The SNRs in the eyes and the brain were 24.4 ± 3.5 and 20.4 ± 1.3, respectively. The relative SNR between the eyes and the brain was 1.20 ± 0.19. In ^{23}Na images, the eyes appeared much brighter in comparison to the brain, whereas in ^{35}Cl images, the eyes appeared similarly bright as the brain.

^{23}Na rat torso One transverse, one sagittal, and one coronal slice of the ^{23}Na image in the rat torso are shown in Figure 4.10. The transverse slice of the ^{1}H image included the left ventricle, the right ventricle, the inferior vena cava and the aorta. These anatomical regions were labeled in the ^{1}H image. In the ^{23}Na image, the blood vessels in front of the heart were visible, while the vena cava and aorta behind the heart could not be discerned. The left and the right ventricles were well separated by the myocardium with a lower ^{23}Na signal intensity. The penetration depth of the ^{23}Na saddle coil was estimated to be maximum $35\,\mathrm{mm}$ in rat measurements.

The sagittal slice of the ^{1}H image was chosen to include the cartilage in the frontal rib cage. Over all, the cartilage had high ^{23}Na signal intensities due to its very high sodium concentration. It could be distinguished from the surrounding tissue in five instances, whereby the cartilage located in the most inferior position had the highest signal intensity of the five. The skin of the front torso close to the coil could also be distinguished. It was separated from the cartilage by a layer of fat with a low ^{23}Na signal intensity. In the overlay image, the five instances of the costal cartilage as seen in the ^{23}Na image were matched onto the ^{1}H image.

In the coronal slice of the ^{23}Na image, the myocardium in the boundary between the right and the left ventricle was clearly delineated. The heart appeared very bright in both ventricles due to the high ^{23}Na signal intensity in the blood.

In the rat torso, ^{23}Na SNRs were calculated in the blood in the left and the right ventricles, in the myocardium, and in the cartilage of the rib cage. The SNR in the cartilage was the highest among the three regions with 70.1 ± 5.8. The SNRs of the myocardium and the blood in the heart were 47.4 ± 2.8 and 63.0 ± 6.2, respectively. The total sodium concentration in mammalian blood is $80\,\mathrm{mM}$. Using the SNR ratio of 0.68 ± 0.07 between the myocardium and the blood while neglecting B_1 inhomogeneities within the heart, the total sodium concentration in the myocardium could be estimated to be (54.4 ± 5.6) mM.

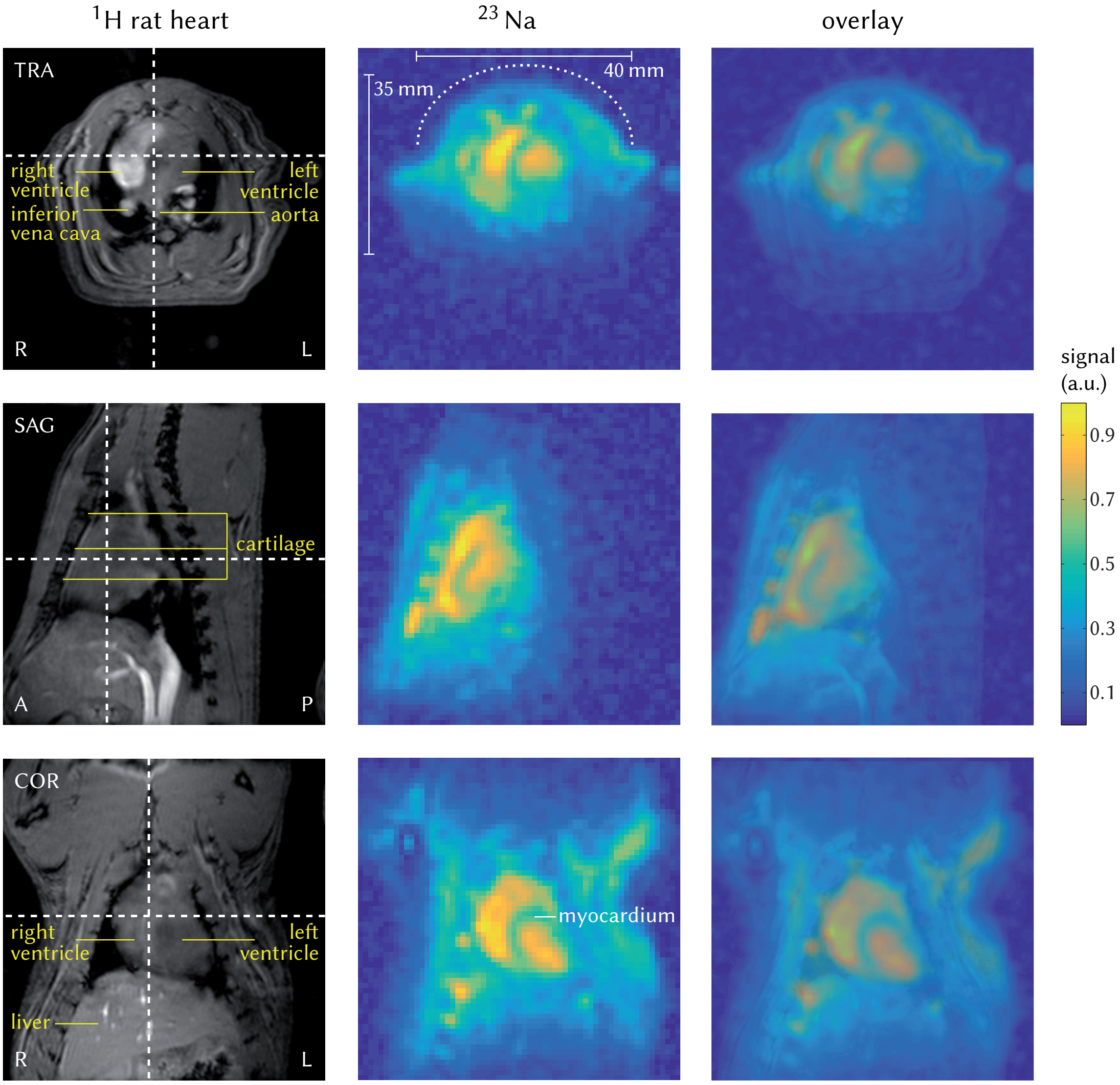
^{1}H rat heart
^{23}Na
overlay
TRA
right ventricle
inferior vena cava
left ventricle
aorta
R
L
35 mm
40 mm
signal (a.u.)
0.9
0.7
0.5
0.3
0.1
SAG
cartilage
A
P
COR
right ventricle
left ventricle
liver
R
L
myocardium

Figure 4.10: 3D *in vivo* ^{23}Na DA-R images of the rat torso in supine position acquired in 29 minutes. One transverse, one sagittal and one coronal slice with a FOV of $(64\,\text{mm})^2$ are shown. The locations of the other slices are indicated by dashed lines, and the coil position is indicated by the dotted line. Each image was normalized to its own maximum. The ^{1}H and the ^{23}Na images have an isotropic nominal voxel of $0.25\,\text{mm}$ and $1\,\text{mm}$, respectively. In the sagittal ^{1}H image, the anterior and the posterior direction are labeled with "A" and "P", respectively.

^{35}Cl rat torso One transverse, one sagittal, and one coronal slice of the ^{35}Cl image in the rat torso are shown in Figure 4.11. The transverse slice of the ^{35}Cl image included both reference vials. By using their positions to overlay the ^{1}H and the ^{35}Cl image, the area with the high signal intensity was matched to that of the heart. The space between the right and the left ventricle had a reduced ^{35}Cl signal intensity. It might be attributed to the myocardium, while contributions from other tissues could not be excluded due to partial volume effects. The ^{35}Cl coil was smaller and less bent than the ^{23}Na coil and had a smaller penetration depth of approximately $25\,\text{mm}$.

In the sagittal slice, the heart was recognized as the area with high ^{35}Cl signal intensity. Other anatomical structures with distinctive shapes and locations such as rib cartilage and skin were not visible. It would therefore require *a priori* knowledge from a ^{1}H image to locate them.

In the coronal slice of the ^{1}H image it was visible that the rat was attached to the animal bed with a twist around its spine. Therefore the coronal slices were twisted towards the sagittal view. With the help of the reference vials, the ^{35}Cl signal of the heart was matched well onto the extent of the heart in the ^{1}H image. In this view, the myocardium could not be distinguished from the ventricles, though the matching might have been hampered by the twisted view of the heart.

In the rat torso, ^{35}Cl SNR calculated in the heart was 28.4 ± 2.2. Contrary to the ^{23}Na images, signals from the blood in the ventricles and the myocardium could not be distinguished. Therefore the SNR presented a mean of both signal origins.

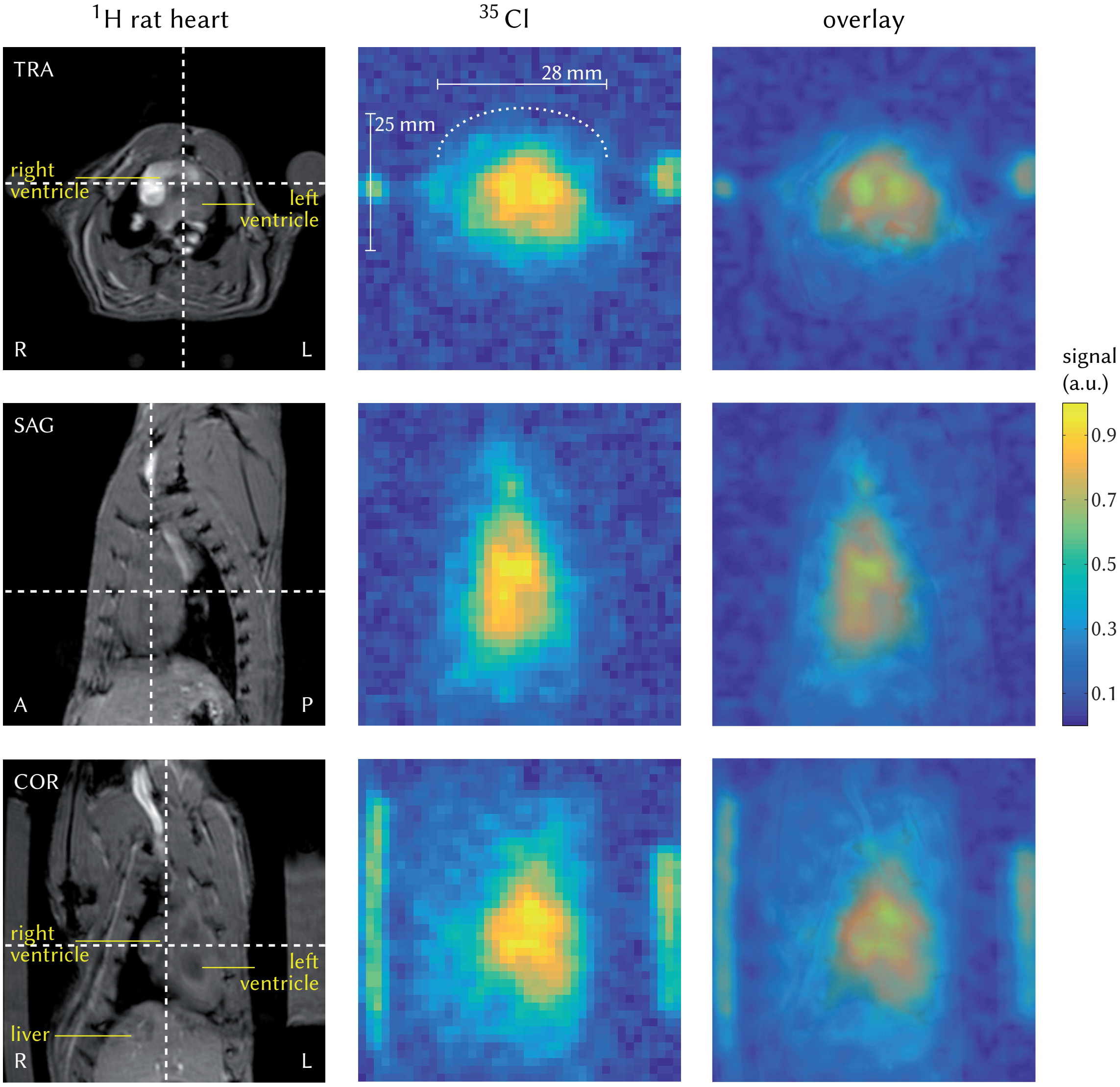
^{1}H rat heart
^{35}Cl
overlay
TRA
right ventricle
left ventricle
R
L
28 mm
25 mm
SAG
A
P
COR
right ventricle
left ventricle
liver
R
L
signal (a.u.)
0.9
0.7
0.5
0.3
0.1

Figure 4.11: 3D *in vivo* ^{35}Cl DA-R images of the rat torso in supine positiosn acquired in 1 hour and 59 minutes. One transverse, one sagittal and one coronal slice with a FOV of $(63\,\mathrm{mm})^2$ are shown. The slice locations of the other two slices are indicated by dashed lines, and the coil position is indicated by the dotted line. Each image was normalized to its own maximum. The ^{1}H and the ^{35}Cl images have an isotropic nominal voxel of $0.25\,\mathrm{mm}$ and $1.5\,\mathrm{mm}$, respectively. In the sagittal ^{1}H image, the anterior and the posterior direction are labeled with “A” and “P”, respectively.

Table 4.1: SNR values in different organs and tissues in rat head (upper section) and rat torso (lower section) extracted from ^{23}Na and ^{35}Cl *in vivo* images.

	SNR	
organ / tissue	^{23}Na	^{35}Cl
eye	67.7 ± 5.6	24.4 ± 3.5
brain	33.3 ± 3.6	20.4 ± 1.3
cortex	33.1 ± 3.4	–
cerebellum	34.2 ± 5.2	–
cheek tissue	18.9 ± 1.6	–
blood (arteries)	31.1 ± 4.3	–
blood (heart)	63.0 ± 6.2	28.4 ± 2.2
myocardium	47.4 ± 2.8	
cartilage	70.1 ± 5.8	–

Table 4.2: Signal ratios between organ regions in the column and those in the top row in ^{23}Na rat head, ^{35}Cl rat head and ^{23}Na rat torso images.

^{23}Na rat head	eye	brain	cortex	cerebellum	cheek tissue	arterial blood
eye	–	2.04 ± 0.28	2.04 ± 0.27	1.98 ± 0.36	3.59 ± 0.42	2.18 ± 0.35
brain	0.49 ± 0.07	–	1.00 ± 0.15	0.97 ± 0.18	1.76 ± 0.24	1.07 ± 0.19
cortex	0.49 ± 0.06	1.00 ± 0.15	–	0.97 ± 0.18	1.76 ± 0.23	1.07 ± 0.18
cerebellum	0.51 ± 0.09	1.03 ± 0.19	1.03 ± 0.19	–	1.81 ± 0.32	1.10 ± 0.23
cheek tissue	0.28 ± 0.03	0.57 ± 0.07	0.57 ± 0.07	0.55 ± 0.10	–	0.61 ± 0.10
arterial blood	0.46 ± 0.07	0.94 ± 0.17	0.94 ± 0.16	0.91 ± 0.19	1.65 ± 0.27	–

^{35}Cl rat head	eye	brain
eye	–	1.20 ± 0.19
brain	0.84 ± 0.13	–

^{23}Na rat torso	ventricular blood	myocardium	cartilage
ventricular blood	–	1.48 ± 0.15	1.11 ± 0.15
myocardium	0.68 ± 0.07	–	0.75 ± 0.09
cartilage	0.90 ± 0.12	1.33 ± 0.15	–

4.2 Triple-Quantum Spectroscopy with TPPI (TQ-TPPI)

This section presents the ^{23}Na and ^{35}Cl TQ-TPPI measurement results in agarose phantoms (Subsection 4.2.1), lecithin phantoms (Subsection 4.2.2), rodents *in vivo* (Subsection 4.2.4) and the bioreactor (Subsection 4.2.3).

Both the sequence and the fitting procedure were treated in Subsection 3.2.5. Description of materials and sequence parameters can be found in Subsection 3.3.2.

4.2.1 Agarose Phantoms

In this part the ^{23}Na and ^{35}Cl TQ-TPPI measurement results in phantoms containing 0%, 2%, 4% and 6% agarose and $134.75\,\mathrm{mM}$ NaCl are presented. The influence of the length of TR on the artificial creation of DQ and TQ coherences was looked into. Furthermore, the differences between the spin echo T_2 values and the TQ-TPPI T_2 values were examined.

To determine the range of TR for each nucleus-phantom combination, T_1 was determined using the inversion recovery sequence (Subsection 3.2.3). The T_1 fitting results are summarized in Table 4.3. The T_1 relaxation curves of all data sets were mono-exponential, with the values in the range of $T_1^{\mathrm{Na}} = 52.6 - 35.2\,\mathrm{ms}$ and $T_1^{\mathrm{Cl}} = 32.1 - 8.9\,\mathrm{ms}$. The TRs used in the TQ-TPPI measurements for each nucleus-phantom combination can be found in Subsection 3.3.2.

Table 4.3: ^{23}Na and ^{35}Cl inversion recovery T_1 fitting results with the fit function $S_{T_1}(\mathrm{TI}) = \mathrm{abs}\left[a \cdot \left(1 - b \cdot \mathrm{e}^{-\mathrm{TI}/T_1}\right)\right]$ for agarose phantoms with 0, 2, 4 and $6\,\%$ agarose and $134.75\,\mathrm{mM}$ NaCl. The RMSE was < 0.014 overall.

	^{23}Na		^{35}Cl	
agarose (%)	b	T_1 (ms)	b	T_1 (ms)
0	1.993 ± 0.002	52.6 ± 0.1	1.980 ± 0.003	32.1 ± 0.1
2	1.876 ± 0.002	45.3 ± 0.1	1.656 ± 0.010	16.0 ± 0.2
4	1.818 ± 0.001	39.3 ± 0.0	1.647 ± 0.013	11.3 ± 0.1
6	1.822 ± 0.003	35.2 ± 0.1	1.579 ± 0.017	9.0 ± 0.1

All TQ-TPPI t_{evo}-FIDs were fitted with Equation 3.25, except for the data of the 0% phantom at large TR, which were fitted with Equation 3.23. The RSME was < 0.004 and < 0.020 in the ^{23}Na and the ^{35}Cl fits, respectively. Examples of fitted ^{23}Na and ^{35}Cl t_{evo}-FIDs acquired with maximum TR are shown in Figure 4.12 and Figure 4.13, respectively.

In the same phantom, the ^{23}Na t_{evo}-FID was sampled longer than the ^{35}Cl t_{evo}-FID. Furthermore, the t_{evo}-FIDs in phantoms with higher agarose concentrations and hence shorter relaxation times reached noise level at smaller t_{evo}. In the TQ-TPPI spectra, the SQ peak had a higher FWHM in phantoms with $> 0\%$ agarose, attesting to shorter relaxation times. Its peak shape of the phantom with $> 0\%$ agarose with its wide base indicated that the peak is a superposition of two Lorentzians. The TQ peak shape with its downward side lobes indicated that the peak was a superposition of two Lorentzians substracted from each other.

The ratio $S_{\mathrm{T/S}}$ as a function of TR$/T_1$ is depicted in Figure 4.14. In the phantom with 0% agarose, the initially non-zero $S_{\mathrm{T/S}}^{\mathrm{Na}}$ droped to zero at TR$/T_1 \gtrsim 3.5$. In phantoms with $> 0\%$ agarose, the $S_{\mathrm{T/S}}^{\mathrm{Na}}$ is constant within the margin of error for TR$/T_1 \gtrsim 3$. The $S_{\mathrm{T/S}}^{\mathrm{Na}}$ was higher in phantoms with a higher agarose concentration. At TR $= 310$ ms, the $S_{\mathrm{T/S}}^{\mathrm{Na}}$ ratios were $(19.4 \pm 0.4)\%$, $(28.3 \pm 0.3)\%$ and $(30.4 \pm 0.4)\%$ in the phantoms containing 2%, 4% and 6% agrose, respectively.

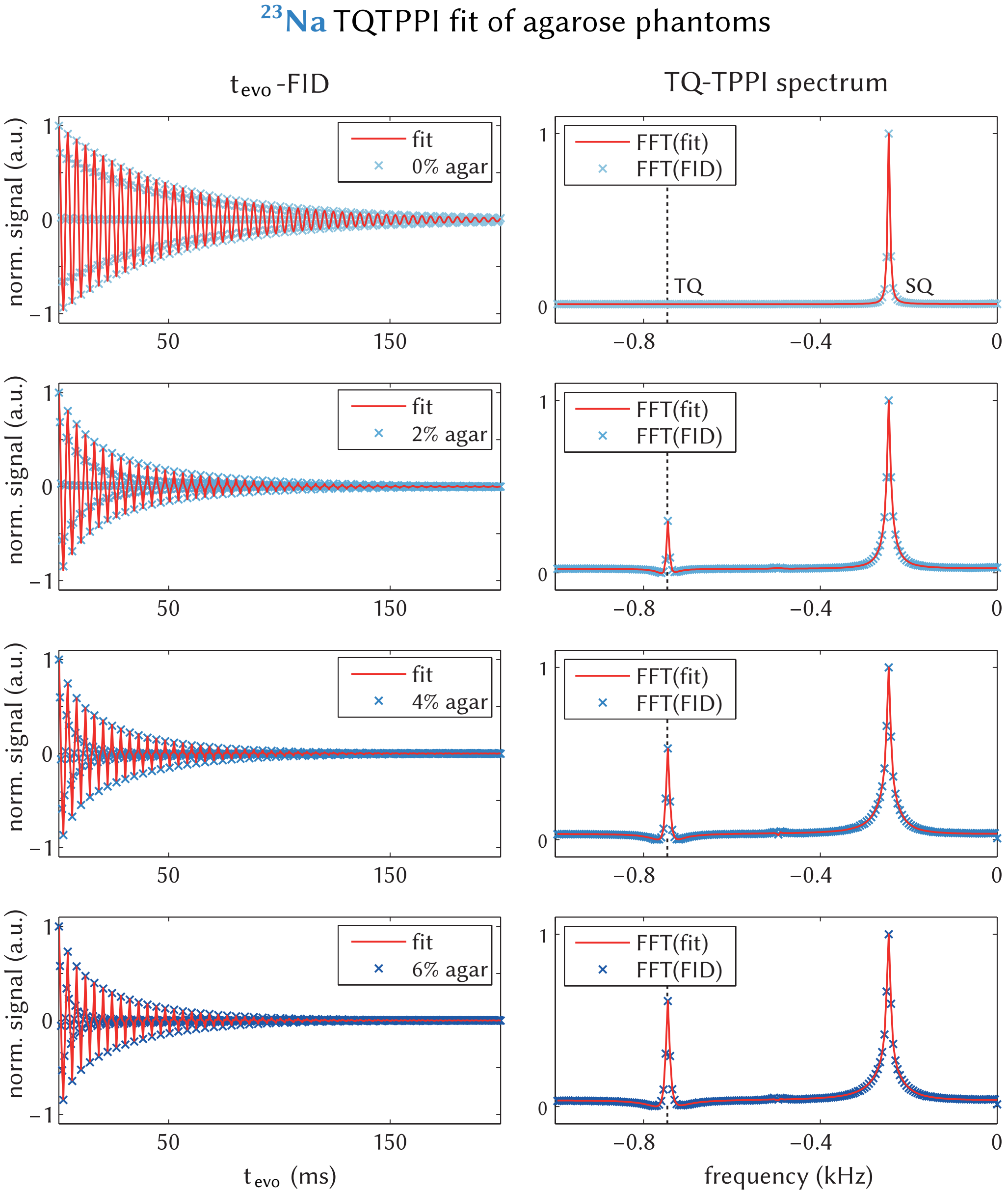

Figure 4.12: Fitted TQ-TPPI ^{23}Na t_{evo}-FIDs and the corresponding TQ-TPPI spectra along the acquired with maximum TR. The fit function was $f_{\text{SQDQTQ}}(t_{\text{evo}}) = g_{\text{S}}^{\text{bi}}(t_{\text{evo}}) + g_{\text{D}}(t_{\text{evo}}) + g_{\text{T}}(t_{\text{evo}}) + c$ unless the TQ component was absent, in which case the fit function was $f_{\text{S}}(t_{\text{evo}}) = g_{\text{S}}^{\text{mono}}(t_{\text{evo}}) + c$.

In the phantom with 0% agarose, the $S_{\text{T/S}}^{\text{Cl}}$ was zero in spectra acquired with any TR/T_1 ratio. In phantoms with $> 0\%$ agarose, both the margins of error of $S_{\text{T/S}}$ and the fluctuations in $S_{\text{T/S}}^{\text{Cl}}$ with varying TR/T_1 were higher compared to the ^{23}Na data points. Neverthelss, the data of each phantom appeared to fluctuate around a constant value. The phantom with 4% agarose had the highest $S_{\text{T/S}}^{\text{Cl}}$ value. At maximum TR, the $S_{\text{T/S}}^{\text{Cl}}$ ratios were $(23.9 \pm 1.0)\%$, $(27.0 \pm 1.2)\%$ and $(22.1 \pm 1.1)\%$ in the phantoms containing 2%, 4% and 6% agrose, respectively.

The parameters $T_{2\text{f}}$ and $T_{2\text{s}}$ were also obtained through fitting. They are plotted in Figure 4.14 as a function of TR/T_1. Mono-exponentially fitted T_2^{Na} values decreased continuously with increasing TR/T_1, the maximum difference being $0.8\,\text{ms}$. In phantoms with $> 0\%$ agarose, the $T_{2\text{f}}^{\text{Na}}$ and the $T_{2\text{s}}^{\text{Na}}$ were constant within the margin of error for TR/$T_1 \gtrsim 3$. The ^{35}Cl data showed that T_2^{Cl} was constant within the margin of error for all TR/T_1. The phantom with 6% agarose had both the shortest T_{2s}^{Cl} and the shortest T_{2f}^{Cl}. Despite the T_{2s}^{Cl} values deviating outside the margigns of error at different TR/T_1, they appeared to fluctuate around a constant value. The T_{2f}^{Cl} values, on the other hand, was constant within the margin of error for all TR/T_1.

To validate the TQ-TPPI T_2 fitting results, T_2 values were additionally determined with the spin echo sequence (Subsection 3.2.3). were comared with the spin echo T_2 results. Alongside the TQ-TPPI T_2 fitting results, the spin echo T_2 fitting results are summarized in Table 4.4. The differences in T_2^{Na} and T_2^{Cl} in the 0% phantom measured with both methods were $1.5\,\mathrm{ms}$ and $2.3\,\mathrm{ms}$, respectively. The majority of T_{2f} and T_{2s} values was the same within the margin of error for both nuclei. The fraction b of the fast relaxing component was in agreement in the majority of cases.

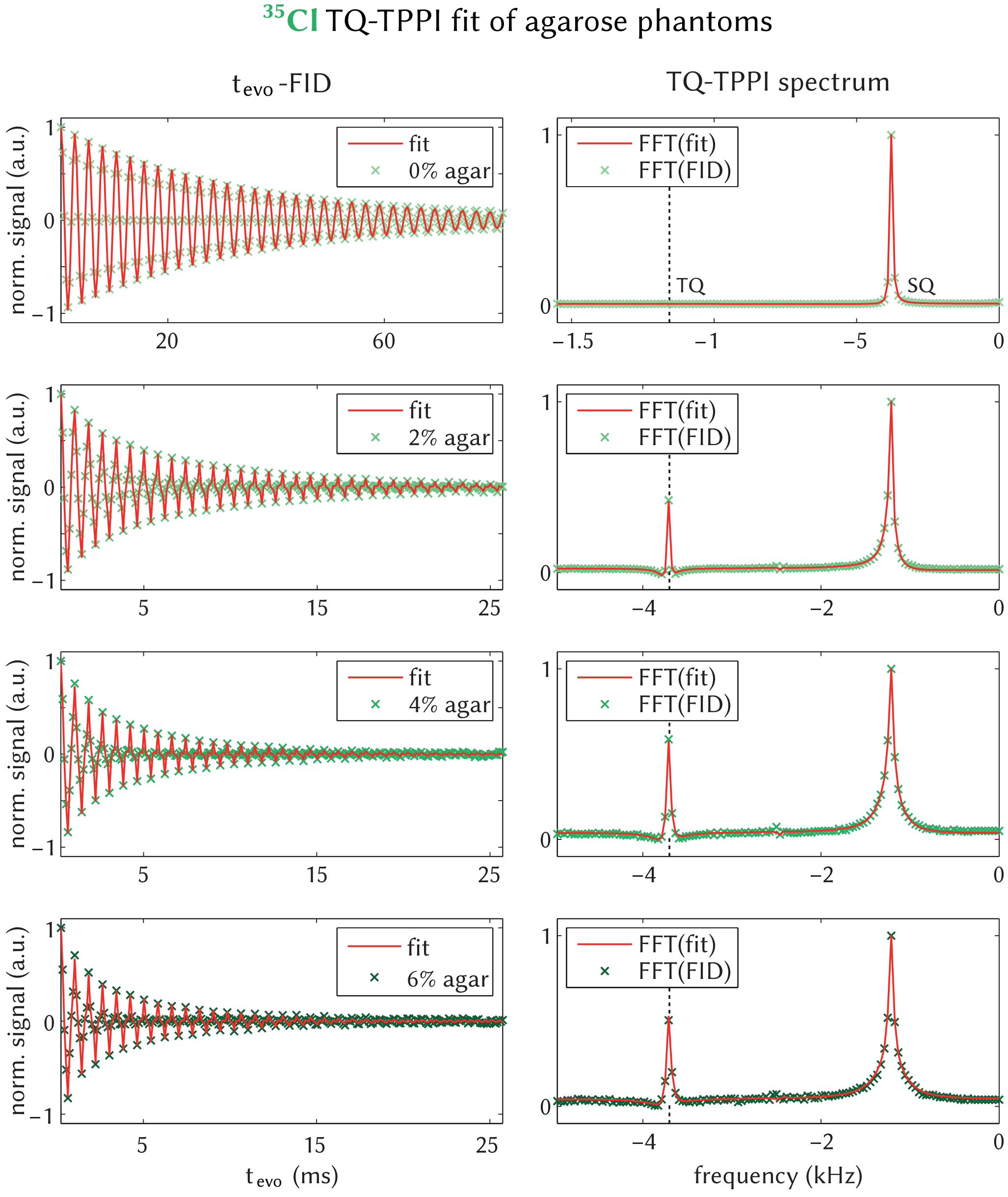

Figure 4.13: Fitted TQ-TPPI ^{35}Cl t_{evo}-FIDs and the corresponding TQ-TPPI spectra acquired with maximum TR. The fit function was $f_{\mathrm{SQDQTQ}}(t_{\mathrm{evo}}) = g_{\mathrm{S}}^{\mathrm{bi}}(t_{\mathrm{evo}}) + g_{\mathrm{D}}(t_{\mathrm{evo}}) + g_{\mathrm{T}}(t_{\mathrm{evo}}) + c$ unless the TQ component was absent, in which case the fit function was $f_{\mathrm{S}}(t_{\mathrm{evo}}) = g_{\mathrm{S}}^{\mathrm{mono}}(t_{\mathrm{evo}}) + c$.

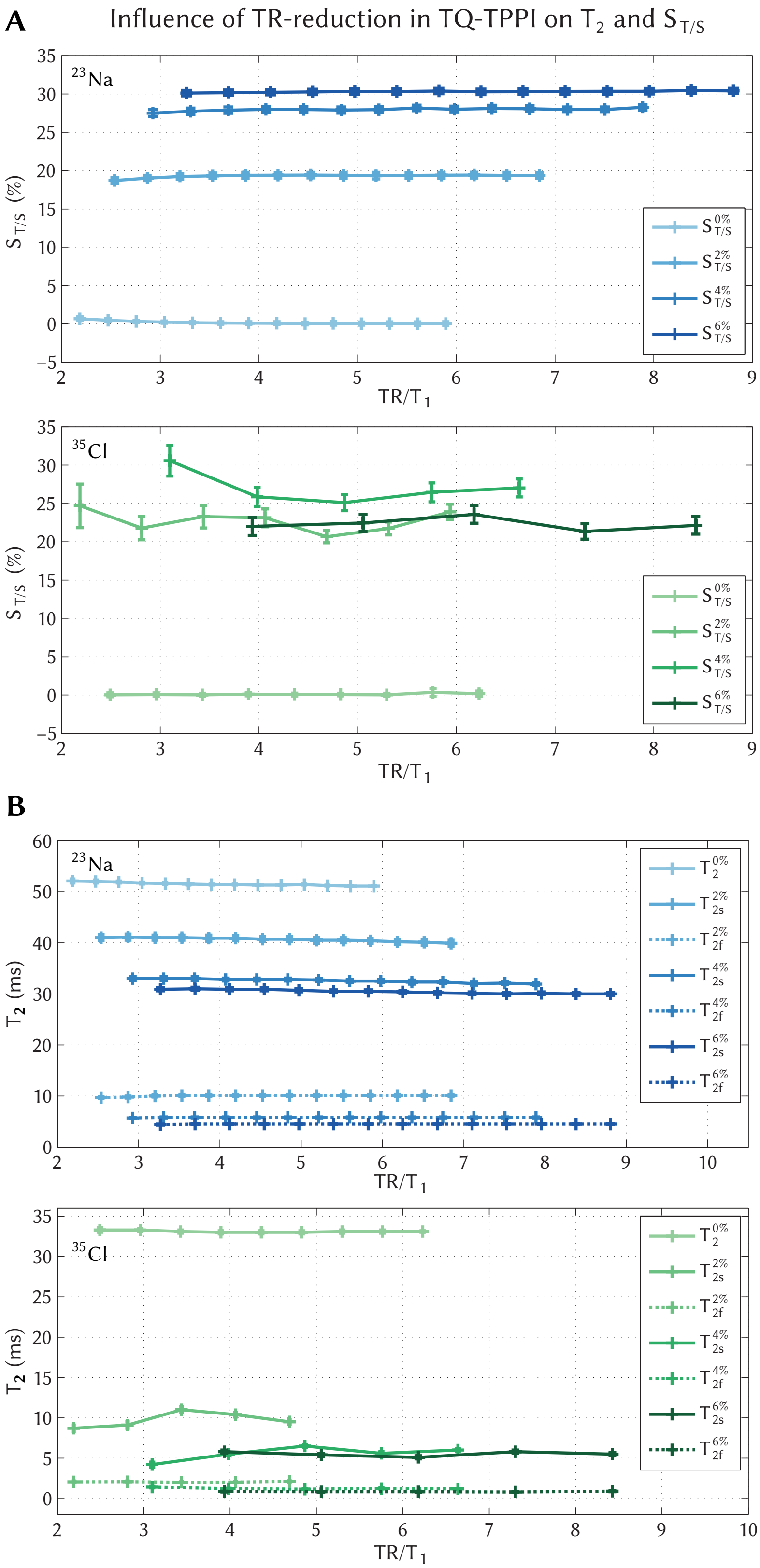

Figure 4.14: **A** ^{23}Na (in blue) and ^{35}Cl (in green) $S_{\text{T/S}}$ ratios plotted against TR/T_1. The $S^{\text{Na}}_{\text{T/S}}$ratios were constant in the range of TR/$T_1 \gtrsim 3.5$. The $S^{\text{Cl}}_{\text{T/S}}$ ratios were constant for all TR/T_1 in the 0% phantom. In the $> 0\%$ phantoms, the $S^{\text{Cl}}_{\text{T/S}}$ ratios fluctuated around a constant value. **B** ^{23}Na (in blue) and ^{35}Cl (in green) T_2 plotted against TR/T_1. In some cases, the confidence interval was too small to be discerned.

Table 4.4: Summary of ^{23}Na and ^{35}Cl T_2 values in agarose phantoms with 0, 2, 4 and $6\,\%$ agarose and $134.75\,\text{mM}$ NaCl. The TQ-TPPI results of each nucleus-phantom combination were from the respective measurement at maximum TR. The fraction of the fast component is given by b. The spin echo T_2 were determined with the fit functions $S^{\text{mono}}_{T_2}(\text{TE}) = a \cdot \mathrm{e}^{-\text{TE}/T_2} + c$ and $S^{\text{bi}}_{T_2}(\text{TE}) = a \cdot \left(b \cdot \mathrm{e}^{-\text{TE}/T_{2\text{f}}} + (1-b)\mathrm{e}^{-\text{TE}/T_{2\text{s}}}\right) + c$, with the overall RMSE < 0.019.

	experiment	agar. (%)	T_2 (ms)	b (%)	$T_{2\text{f}}$ (ms)	$T_{2\text{s}}$ (ms)	$S_{\text{T/S}}$ (%)
^{23}Na	spin echo	0	52.6 ± 0.1	-	-	-	-
		2	-	65.5 ± 1.9	10.5 ± 0.2	38.0 ± 0.9	-
		4	-	67.8 ± 0.8	6.1 ± 0.1	33.2 ± 0.4	-
		6	-	68.2 ± 7.9	4.7 ± 0.1	30.1 ± 0.4	-
	TQ-TPPI	0	51.1 ± 0.1	-	-	-	0.0 ± 0.2
		2	-	63.2 ± 1.0	10.0 ± 0.2	39.9 ± 0.6	19.4 ± 0.4
		4	-	65.5 ± 0.6	5.8 ± 0.1	31.9 ± 0.3	28.3 ± 0.3
		6	-	65.1 ± 0.6	4.5 ± 0.1	30.0 ± 0.3	30.4 ± 0.4
^{35}Cl	spin echo	0	30.8 ± 0.5	-	-	-	-
		2	-	67.6 ± 14.2	2.1 ± 0.3	7.9 ± 1.3	-
		4	-	69.6 ± 16.4	1.3 ± 0.2	4.9 ± 0.9	-
		6	-	71.9 ± 6.9	1.4 ± 0.5	4.1 ± 1.6	-
	TQ-TPPI	0	33.1 ± 0.1	-	-	-	0.0 ± 0.2
		2	-	67.6 ± 2.5	2.1 ± 0.1	9.5 ± 0.3	23.9 ± 1.0
		4	-	62.2 ± 2.5	1.2 ± 0.1	5.9 ± 0.2	27.0 ± 1.2
		6	-	71.1 ± 3.2	0.9 ± 0.1	5.5 ± 0.2	22.1 ± 1.1

4.2.2 Lecithin Phantoms

This subsection presents the results from TQ-TPPI measurements of lecithin phantoms. The fitted ^{23}Na and ^{35}Cl TQ-TPPI spectra of phantoms containing 2%, 4%, 10% and 20% lecithin

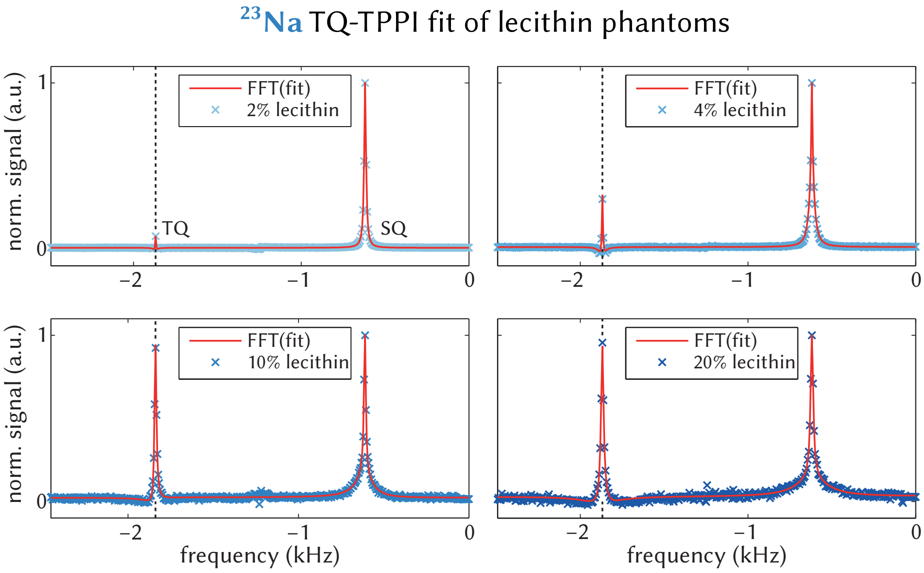

Figure 4.15: Fitted ^{23}Na TQ-TPPI spectra of lecithin phantoms with the fit function $f_{\text{SDT}}(t_{\text{evo}}) = g^{\text{bi}}_{\text{S}}(t_{\text{evo}}) + g_{\text{T}}(t_{\text{evo}}) + c$. In all four phantoms, a TQ peak was present, whereby its amplitude increases with increasing lecithin concentration.

and 154 mM NaCl are shown in Figure 4.15 and 4.16, respectively. The RMSE was < 0.0126 and < 0.0782 for the ^{35}Cl and the ^{23}Na fits, respectively. The fitted parameters such as $S_{\text{T/S}}$, $T_{2\text{f}}$ and $T_{2\text{s}}$ from this subsection are summarized in Table 4.5.

In the ^{23}Na spectra, a TQ peak is present in all phantoms. The $S_{\text{T/S}}$ ratio increases with increasing concentration of lecithin, with $S_{\text{T/S}}$ between $S_{\text{T/S}}^{2\%} = (10.0 \pm 1.1)\%$ and $S_{\text{T/S}}^{20\%} = (36.0 \pm 1.4)\%$. In the ^{35}Cl spectra, an additional zoomed view at the TQ peak location is shown. In the zoomed view, both the real and the imaginary part of the spectrum are included. In case of a conclusive TQ peak, the imaginary part, which is phase-shifted by $\pi/2$ relative to the real part, is expected to cross the zero line at the TQ peak position. The zoomed view helps answering the question of whether a TQ peak is present, especially if the fitting results are inconclusive. In phantoms with 2% and 4% lecithin, no discernable TQ peak is found, whereas in phantoms with 10% and 20% lecithin, a TQ peak with phase-shifted zero crossing of the imaginary part was distinctive. The $S_{\text{T/S}}$ ratios were $S_{\text{T/S}}^{2\%} = (2.9 \pm 0.5)\%$ and $S_{\text{T/S}}^{20\%} = (12.7 \pm 4.0)\%$.

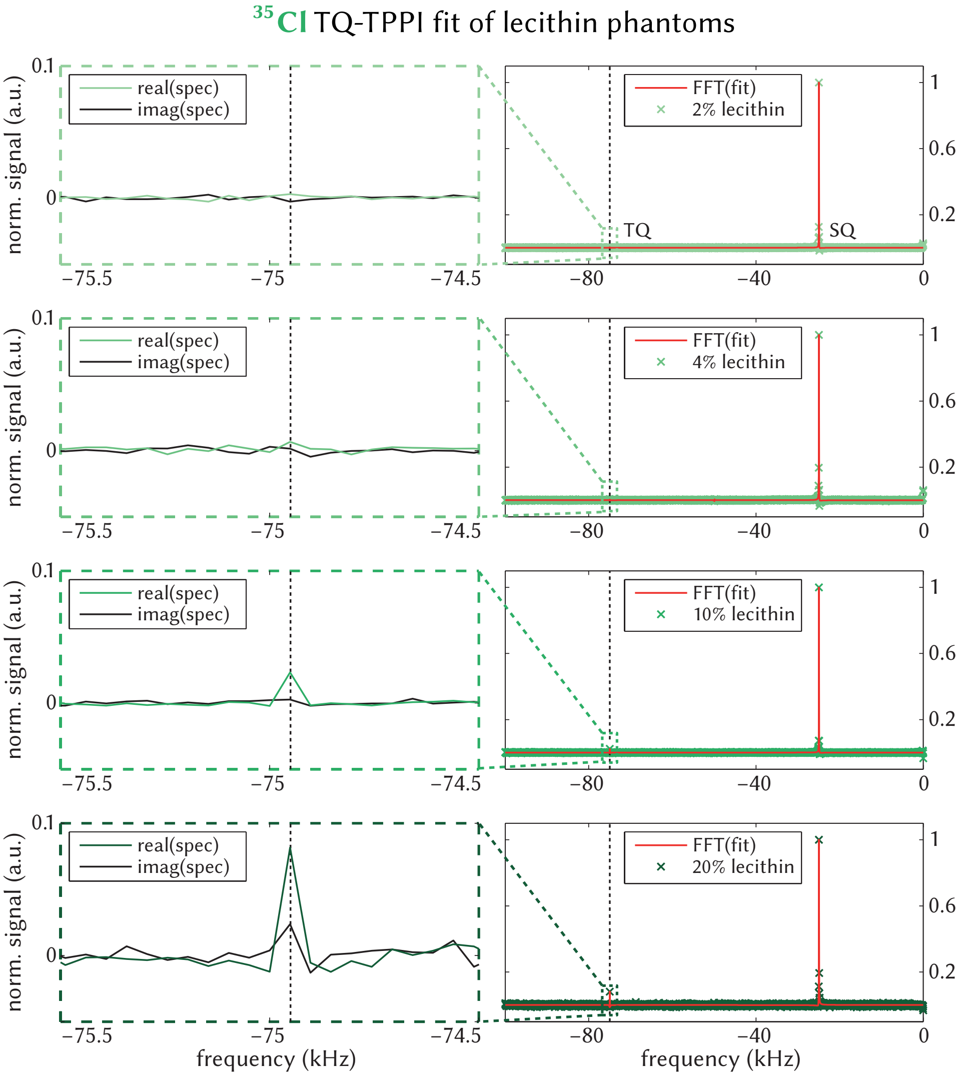

Figure 4.16: Fitted ^{35}Cl TQ-TPPI spectra of lecithin phantoms with the fit function $f_{\text{SDT}}(t_{\text{evo}}) = g_{\text{S}}^{\text{bi}}(t_{\text{evo}}) + g_{\text{T}}(t_{\text{evo}}) + c$. A zoomed view of the TQ peak is displayed in the left column. A TQ peak was present only in the phantoms with 10% and 20% lecithin.

4.2.3 Bioreactor

This subsection presents the results from *in vitro* TQ-TPPI measurements of cells in the bioreactor. The fitted ^{23}Na and ^{35}Cl spectra are displayed in Figure 4.17. The fitted parameters such as $S_{\mathrm{T/S}}$, $T_{2\mathrm{f}}$ and $T_{2\mathrm{s}}$ from this subsection are summarized in Table 4.5.

The ^{23}Na TQ-TPPI spectrum obtained from measurements of cells in the square bioreactor yielded a TQ peak with $S_{\mathrm{T/S}}^{\mathrm{Na,square}} = (0.4 \pm 0.1)\%$. The relaxation times were $T_{2\mathrm{f}}^{\mathrm{Na,square}} = (0.2 \pm 0.1)\,\mathrm{ms}$ and $T_{2\mathrm{s}}^{\mathrm{Na,square}} = (64.0 \pm 0.2)\,\mathrm{ms}$, the latter being in the range of the mono-exponential T_2 relaxation time in saline. In the ^{35}Cl TQ-TPPI spectra of experiments of cells in the square bioreactor, however, no TQ peak was identified. One such spectrum is shown as an example in Figure 4.17. Using a different setup, in which the cells are perfused in the round bioreactor (Subsection 3.1.4), a ^{35}Cl TQ peak with $S_{\mathrm{T/S}}^{\mathrm{Cl,round}} = (5.1 \pm 3.0)\%$ was measured. The relaxation times were $T_{2\mathrm{f}}^{\mathrm{Cl,round}} = (5.0 \pm 2.7)\,\mathrm{ms}$ and $T_{2\mathrm{s}}^{\mathrm{Cl,round}} = (16.9 \pm 3.8)\,\mathrm{ms}$.

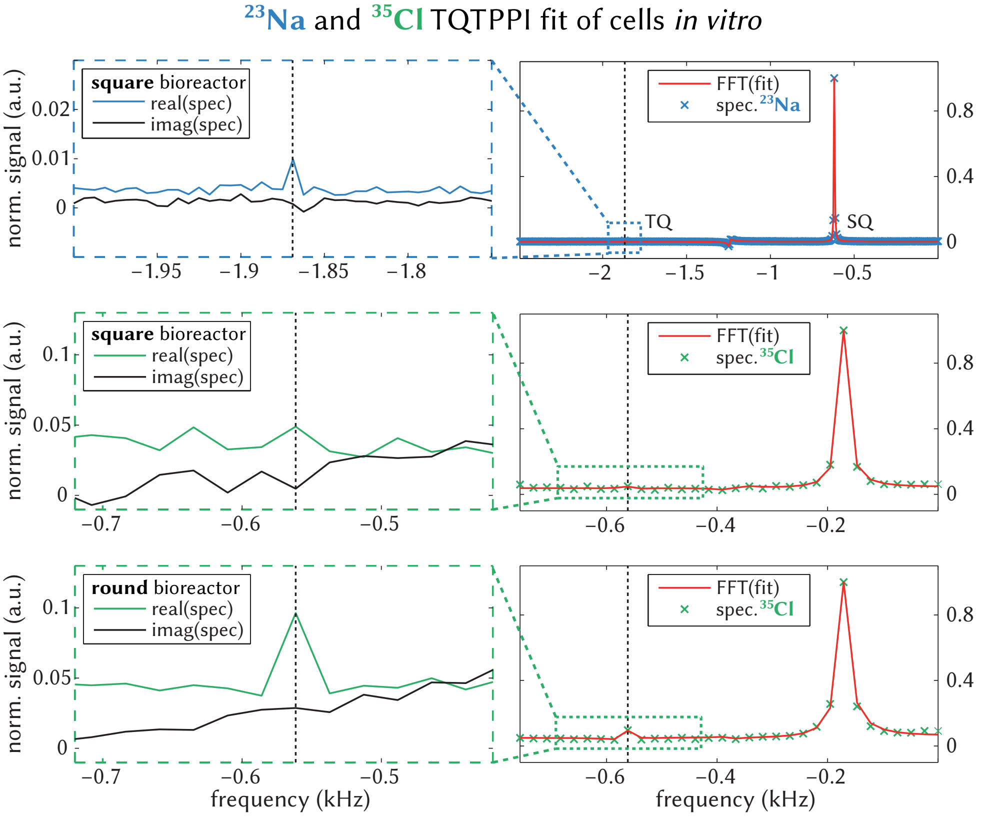

Figure 4.17: Fitted ^{23}Na and ^{35}Cl TQ-TPPI spectra of cells in the bioreactor. The ^{23}Na spectrum of the square bioreactor showed a TQ peak with $S_{\mathrm{T/S}}^{\mathrm{Na,square}} = (0.4\pm0.1)\%$. In the same setup, a ^{35}Cl TQ peak was not measured. The ^{35}Cl spectrum of the round bioreactor showed a TQ peak with $S_{\mathrm{T/S}}^{\mathrm{Cl,round}} = (5.1\pm3.0)\%$.

4.2.4 Rat Head

This subsection presents the results from TQ-TPPI measurements in rat head (Figure 4.18). The fitted parameters such as $S_{\mathrm{T/S}}$, $T_{2\mathrm{f}}$ and $T_{2\mathrm{s}}$ from this subsection are summarized in Table 4.5.

In the spectrum, the ^{23}Na TQ peak was very well defined. On the contrary, the ^{35}Cl peak was only just above the noise level. A ^{23}Na TQ peak with $S_{\mathrm{T/S}}^{\mathrm{Na}} = (8.9 \pm 0.5)\%$ was measured. This ratio is approximately eight times the ^{35}Cl TQ peak with $S_{\mathrm{T/S}}^{\mathrm{Cl}} = (1.1 \pm 0.7)\%$. The ^{23}Na relaxation times are $T_{2\mathrm{f}}^{\mathrm{Na}} = (2.2 \pm 0.2)$ ms and $T_{2\mathrm{s}}^{\mathrm{Na}} = (27.7 \pm 0.6)$ ms; the ^{35}Cl relaxation times are $T_{2\mathrm{f}}^{\mathrm{Cl}} = (1.1 \pm 0.4)$ ms and $T_{2\mathrm{s}}^{\mathrm{Cl}} = (30.0 \pm 5.8)$ ms. Therefore, the relaxation times $T_{2\mathrm{f}}$ and $T_{2\mathrm{s}}$ were in a similar range for both nuclei. However, the fraction b of the fast relaxing component was much higher for ^{23}Na than for ^{35}Cl.

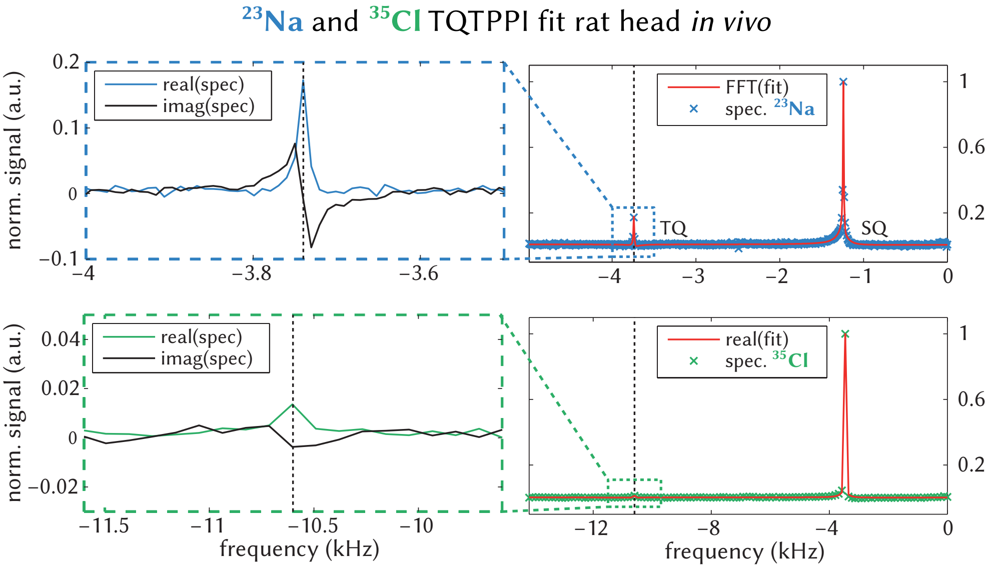

Figure 4.18: Fitted ^{23}Na and ^{35}Cl TQ-TPPI spectra of rat head *in vivo* with zoom on the TQ peak. The ^{23}Na TQ peak was very prominent, whereas the ^{35}Cl TQ peak was barely above noise level.

Table 4.5: Summary of ^{23}Na and ^{35}Cl TQ-TPPI fitting results in phantoms, rat head *in vivo* and cells in the bioreactor *in vitro*. The fraction of the fast relaxing component is given by b.

	experiment		b (%)	$T_{2\mathrm{f}}$ (ms)	$T_{2\mathrm{s}}$ (ms)	$S_{\mathrm{T/S}}$ (%)	$t_{\mathrm{evo,opt}}$ (ms)
^{23}Na	agarose (%)	0	–	–	–	0.0 ± 0.2	–
		2	63.2 ± 1.0	10.0 ± 0.2	39.9 ± 0.6	19.4 ± 0.4	18.5 ± 0.3
		4	65.5 ± 0.6	5.8 ± 0.1	31.9 ± 0.3	28.3 ± 0.3	12.1 ± 0.1
		6	65.1 ± 0.6	4.5 ± 0.1	30.0 ± 0.3	30.4 ± 0.4	10.1 ± 0.1
	lecithin (%)	2	77.8 ± 9.8	20.1 ± 0.5	37.1 ± 2.2	10.0 ± 1.1	26.9 ± 0.8
		4	20.1 ± 3.2	8.9 ± 0.2	41.6 ± 1.3	14.7 ± 0.5	17.5 ± 0.3
		10	81.7 ± 4.9	2.7 ± 0.1	24.0 ± 0.5	21.1 ± 1.3	6.6 ± 0.2
		20	67.8 ± 2.3	1.4 ± 0.1	16.7 ± 0.4	36.0 ± 1.3	3.8 ± 0.2
	rat	head	55.5 ± 1.6	2.2 ± 0.2	27.7 ± 0.6	8.9 ± 0.5	6.1 ± 0.4
	bioreactor	square	22.2 ± 2.8	0.2 ± 0.1	64.0 ± 0.2	0.4 ± 0.1	1.2 ± 0.5
^{35}Cl	agarose (%)	0	–	–	–	0.0 ± 0.2	–
		2	67.6 ± 2.5	2.1 ± 0.1	9.5 ± 0.3	23.9 ± 1.0	4.1 ± 0.1
		4	62.2 ± 2.5	1.2 ± 0.1	5.9 ± 0.2	27.0 ± 1.2	2.4 ± 0.1
		6	71.1 ± 3.2	0.9 ± 0.1	5.5 ± 0.2	22.1 ± 1.1	2.0 ± 0.1
	lecithin (%)	2	–	–	–	0.0 ± 0.0	–
		4	–	–	–	0.0 ± 0.0	–
		10	15.3 ± 0.6	3.4 ± 0.9	14.2 ± 0.6	2.9 ± 0.5	6.4 ± 1.0
		20	40.6 ± 8.9	4.5 ± 1.0	10.6 ± 1.5	12.7 ± 4.0	6.7 ± 0.9
	rat	head	22.6 ± 0.8	1.1 ± 0.4	30.0 ± 5.8	1.0 ± 0.5	3.8 ± 1.0
	bioreactor	square	–	–	–	1.9 ± 2.1	–
		round	37.2 ± 9.8	5.0 ± 2.7	16.9 ± 3.8	5.1 ± 3.0	8.6 ± 2.9

4.3 Triple- and Single-Quantum TPPI Imaging (TASTI)

This section presents the results related to the TASTI sequence. Subsection 4.3.1 describes the TASTI sequence as well as the data reconstruction pipeline. The overall sequence feasibility was demonstrated in ^{23}Na agarose phantom studies in Subsection 4.3.2. Finally, the results in ^{23}Na rat head *in vivo* are presented in Subsection 4.3.3. Materials and sequence parameters have been given in Subsection 3.3.3.

4.3.1 TASTI Sequence Development

The TASTI sequenceillustrated in Figure 4.19 was programmed by expanding on the TQ-TPPI sequence (Subsection 3.2.5). The RF pulse scheme and the phase cycling remained identical. Density-adapted radial readout gradients (Subsection 3.2.4) were added to acquire localized TQ-TPPI signals. TE was defined as the time between the middle of the observation pulse and the beginning of the ramp up section of the gradient. Both 3D and pseudo 2D images could be acquired with the TASTI sequence. In 3D mode, readout gradients in all three axes were switched on. In pseudo 2D mode, the readout gradient in the x-, the y- or the z-axis was switched off to obtain a sagittal, a coronal or a transverse image, respectively. The Nyquist numbers of probjections in pseudo 2D and 3D mode were given in Equation 3.21 and 3.22, respectively.

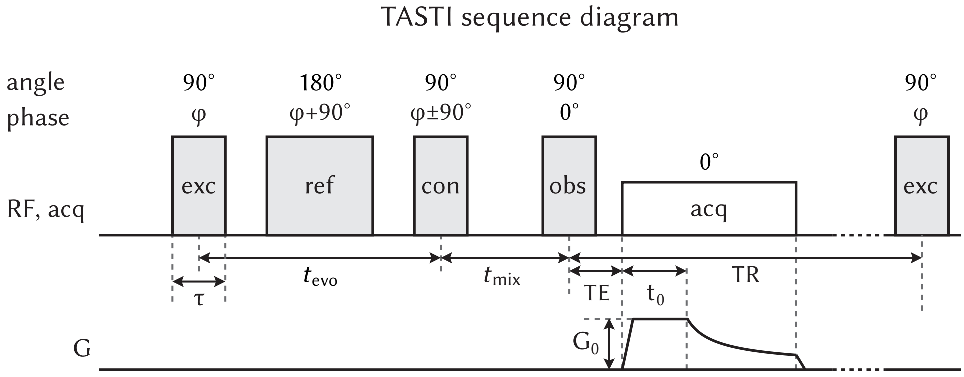
TASTI sequence diagram

Figure 4.19: TASTI sequence diagram. The RF pulse scheme and the density-adapted readout gradient were adopted from the TQ-TPPI and the DA-R sequence, respectively. TE was the time between the observation pulse and the readout gradients, which marks the beginning of signal acquisition. TR was defined as the time between the observation pulse and the next excitation pulse. This way, the time for signal decay after the observation pulse was constant in all phase steps with varying t_{evo}.

In the TASTI sequence, the TQ relaxation was relevant in two instances. In the first instance, the TQ relaxation in the t_{evo}-FID between the excitation and the conversion pulse was described by $f_{31}^{(1)}$ (Equation 2.86). The t_{evo} was not fixed, and t_{evo}-FID was fully sampled. In the second instance, the TQ relaxation in the t-FID after the observation pulse could also be described by the relaxation function $f_{31}^{(1)}$. In this case $f_{31}^{(1)}$ depended on $T_{2\text{f},s}^{*}$ due to the absence of a refocussing pulse. If the majority of the t -FID signal was assumed to be acquired at k-space center and therefore at $t = \text{TE}$, then the available TQ signal S_{TQ} at $t = \text{TE}$ was

$$S_{\text{TQ}} = a \left(\mathrm{e}^{-\frac{\text{TE}}{T_{2\text{f}}^{*}}} - \mathrm{e}^{-\frac{\text{TE}}{T_{2\text{s}}^{*}}} \right) + h \; , \tag{4.2}$$

with the signal amplitude a and the offset h. Derivation of Equation 4.2 yielded the optimal TE to obtain the maximum TQ signal

$$\mathrm{TE}_{\mathrm{opt}} = \frac{\ln\left(\frac{T_{2\mathrm{s}}^*}{T_{2\mathrm{f}}^*}\right)}{\frac{1}{T_{2\mathrm{s}}^*} - \frac{1}{T_{2\mathrm{f}}^*}} \,. \tag{4.3}$$

Similarly, the available SQ signal was

$$S_{\mathrm{SQ}} = b \cdot \mathrm{e}^{-\mathrm{TE}/T_{2\mathrm{f}}^*} + (b-1) \cdot \mathrm{e}^{-\mathrm{TE}/T_{2\mathrm{s}}^*} + h \tag{4.4}$$

with the b as the percentage of the fast relaxing component and h as the offset.

In order to acquire localized spectroscopic data, the RF pulse and readout scheme was repeated according to a loop hierarchy on four levels (Figure 4.20). Initially in the averaging loop ("n_{av} loop"), the t-FID signals from all n_{av} averages were added. Subsequently in the DQ signal suppression loop ("$\varphi \pm 90°$ loop"), the t-FID signals from two subsequent acquisitions with alternating conversion pulse phase were added. Afterwards in the phase cycling loop ("$n_{\mathrm{ps}} \cdot n_{\mathrm{pc}}$ loop"), the t_{evo}-FID was sampled in $n_{\mathrm{ps}} \cdot n_{\mathrm{pc}}$ steps in total. The loop hierarchy until this step can also be found in the TQ-TPPI sequence. The complex dataset acquired thus far was 2D, spanned by the t-dimension and the t_{evo}-dimension. Finally in the projection loop ("n_{proj} loop"), the k-space was sampled along a total of n_{proj} differently orientated radial projections. This loop added a third dimension to the dataset, which was now spanned by the t-dimension, the t_{evo}-dimension and the n_{proj}-dimension. This dataset was the raw input data in the reconstruction pipeline.

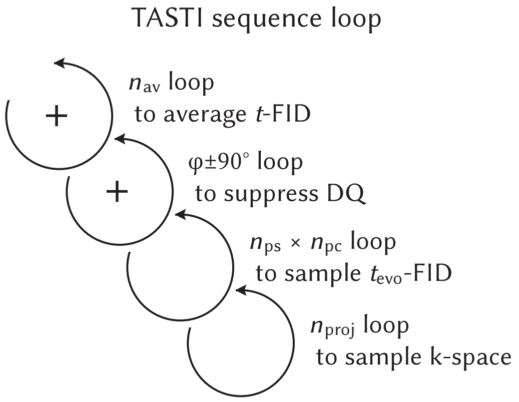

Figure 4.20: TASTI sequence loop hierarchy. First, the n_{av} loop averages the t-FIDs. Second, the $\varphi \pm 90°$ loop suppresses DQ signal contributions with opposite phase from two subsequent acquisitions. Third, the $n_{\mathrm{ps}} \cdot n_{\mathrm{pc}}$ loop acquires the t_{evo}-FID in $n_{\mathrm{ps}} \cdot n_{\mathrm{pc}}$ steps in total. Last, the n_{proj} loop records the k-space along different radial projections. Loops in which the acquired signals were added contain a plus sign.

An offline Matlab reconstruction pipeline, as illustrated in Figure 4.21, was written to reconstruct the final spectroscopic imaging data. The raw data were available in form of a 3D matrix with the axes t, t_{evo} and n_{proj}. The reconstruction pipeline was broken down into the following steps:

(1) Fourier transform was performed along the t_{evo}-axis. The 3D matrix was now spanned by the axes t, f_{MQ} and n_{proj}. The f_{MQ}-axis was the MQ frequency axis equivalent to the f_{MQ}-axis in TQ-TPPI. The SQ frequency was found at $f_{\mathrm{SQ}} = \pm\frac{1}{8\Delta t_{\mathrm{evo}}}$, and the TQ frequency was found at $f_{\mathrm{TQ}} = 3 f_{\mathrm{SQ}}$. The TQ and the SQ k-space were located at f_{SQ} and f_{TQ}, respectively. Each radial k-space was spanned by the t-axis and the n_{proj}-axis. The brightest part of the k-space was located along minimal t across all projections instead of the center of the 2D plane as is the case of Cartesian k-space. Correspondingly, the k-space periphery was located at maximal t.

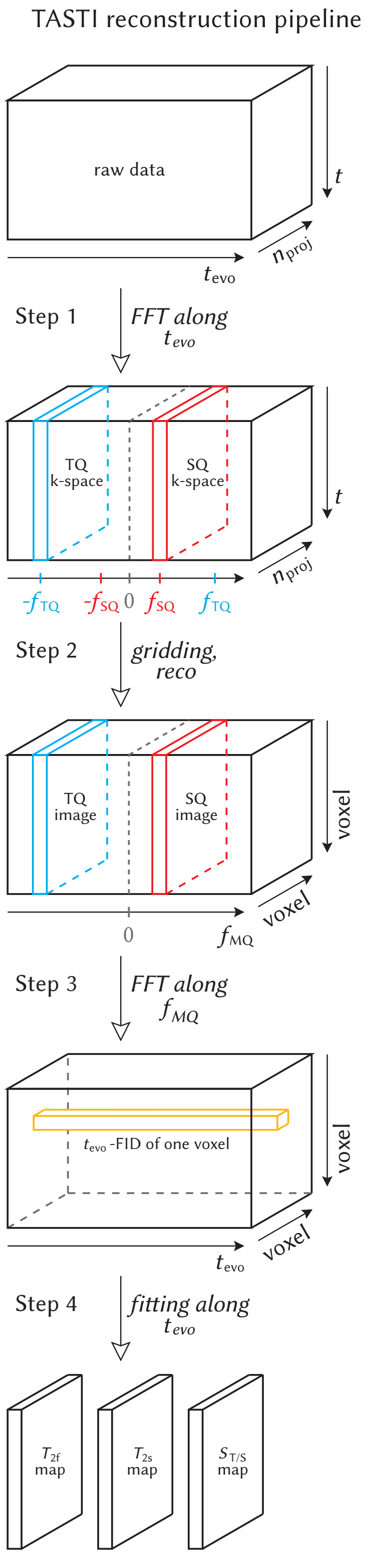
TASTI reconstruction pipeline
raw data
t
n_{proj}
t_{evo}
Step 1
FFT along t_{evo}
TQ k-space
SQ k-space
t
n_{proj}
$-f_{\text{TQ}}$
$-f_{\text{SQ}}$
0
f_{SQ}
f_{TQ}
Step 2
gridding, reco
TQ image
SQ image
voxel
voxel
0
f_{MQ}
Step 3
FFT along f_{MQ}
t_{evo}-FID of one voxel
voxel
voxel
t_{evo}
Step 4
fitting along t_{evo}
$T_{2\text{f}}$ map
$T_{2\text{s}}$ map
$S_{\text{T/S}}$ map

Figure 4.21: TASTI reconstruction pipeline. Fourier transform of the raw data along the t_{evo}-axis yielded a 3D matrix in which 2D radial k-space planes were aligned along the f_{MQ}-axis. Fourier transform of the k-space gridded onto a Cartesian grid yielded a 3D matrix with MQ images ligned up along the f_{MQ}-axis. To fit each voxel along the t_{evo}-domain, Fourier transform was performed along the f_{MQ}-axis. The t_{evo}-FIDs were fitted to obtain parameter maps such as the $T_{2\text{f}}$ map, the $T_{2\text{s}}$ map and the $S_{\text{T/S}}$.

(2) The radial k-space data were gridded onto a Cartesian grid. Fourier transform thereof yielded a 3D matrix spanned by the f_{MQ}-axis and two image dimension axes. In this stage, one image was allocated to one MQ frequency. The TQ and SQ images were now found at their respective frequencies. Potential thresholds were determined based on the images to speed up the fitting in the fourth step.

(3) Fourier transform of the 3D matrix was performed along the f_{MQ}-axis so that the t_{evo}-FIDs of individual voxels could be fitted in the next step The 3D matrix was now spanned by the t_{evo}-axis and two image dimension axes, and each voxel was associated with one t_{evo}-FID.

(4) Voxel-wise fitting of the t_{evo}-FIDs by Equation 3.24 yielded parameter maps such as the $T_{2\mathrm{f}}$ map, the $T_{2\mathrm{s}}$ map and the $S_{\mathrm{T/S}}$ map.

4.3.2 Varying TE, Δt_{evo} and $t_{\mathrm{evo,max}}$ in Agarose Phantoms

Results of the ^{23}Na TASTI experiments in phantoms are presented. The underlying goal was to verify the sequence and to probe the possibility of obtaining parameter maps from the reconstruction pipeline. On top of that, sequence parameters were varied to investigate their influence on the images and the parameter maps. The insight into the influences served as the basis for *in vivo* studies, and the experimental results were compared with the theoretical predictions.

Varying TE

In this part, TE was varied between $1\,\mathrm{ms}$ and $19\,\mathrm{ms}$. TASTI images were acquired in three phantoms containing $134.75\,\mathrm{mM}$ NaCl and 2, 4 and 6 % agarose. The influence of TE on the TQ and SQ relaxation was investigated, and TE$_{\mathrm{opt}}$ was determined. Furthermore, the T_2 and $S_{\mathrm{T/S}}$ maps obtained from voxel-wise t_{evo}-FID fitting at different TE were evaluated. The fitting results of $T_{2\mathrm{f}}$ and $T_{2\mathrm{s}}$ are summarized in Table 4.6. The fitting results of $S_{\mathrm{T/S}}$ are summarized in Table 4.7.

Table 4.6: Fitted $T_{2\mathrm{s}}$ and $T_{2\mathrm{f}}$ in phantoms with graphical presentation in Figure 4.22.

TE (ms)	$T_{2\mathrm{s}}$ (ms) in agarose of (%)			$T_{2\mathrm{f}}$ (ms) in agarose of (%)		
	2	4	6	2	4	6
1	49.0 ± 2.9	44.1 ± 0.7	36.8 ± 1.4	10.9 ± 0.5	6.3 ± 0.1	4.5 ± 0.2
2	54.8 ± 3.4	43.5 ± 0.7	37.2 ± 1.3	11.6 ± 0.5	6.3 ± 0.1	4.3 ± 0.2
3	45.4 ± 2.1	43.0 ± 0.6	36.6 ± 1.3	10.4 ± 0.5	6.2 ± 0.1	4.4 ± 0.3
4	50.3 ± 2.0	42.8 ± 0.5	37.3 ± 1.2	11.1 ± 0.4	6.2 ± 0.1	4.5 ± 0.2
5	48.4 ± 1.6	43.7 ± 0.5	37.7 ± 1.1	10.8 ± 0.4	6.2 ± 0.1	4.6 ± 0.2
7	48.8 ± 1.5	43.5 ± 0.4	$38.4 \pm 1,1$	10.8 ± 0.3	6.1 ± 0.1	4.6 ± 0.2
9	49.9 ± 1.2	43.8 ± 0.4	38.7 ± 1.0	11.0 ± 0.3	6.0 ± 0.1	4.6 ± 0.2
11	47.8 ± 1.1	42.9 ± 0.4	38.4 ± 1.0	10.7 ± 0.2	6.1 ± 0.1	4.6 ± 0.2
13	49.0 ± 1.2	42.9 ± 0.4	38.6 ± 1.0	10.8 ± 0.2	6.1 ± 0.1	4.6 ± 0.2
15	51.0 ± 1.1	43.6 ± 0.4	39.0 ± 0.9	11.0 ± 0.2	6.1 ± 0.1	4.8 ± 0.2
17	50.3 ± 1.1	43.2 ± 0.4	39.0 ± 0.9	11.0 ± 0.2	6.1 ± 0.1	4.7 ± 0.2
19	49.8 ± 1.2	43.4 ± 0.3	38.8 ± 0.8	11.0 ± 0.2	6.0 ± 0.1	4.8 ± 0.2

The $T_{2\mathrm{s,f}}$ values were grouped for each phantom and plotted as a function of TE in Figure 4.22. At smaller TEs, the margins of error of $T_{2\mathrm{s}}$ and $T_{2\mathrm{f}}$ were larger in all phantoms, and the variance of all $T_{2\mathrm{s}}$ data points were higher, with that of the $T_{2\mathrm{s}}^{2\%}$ values being the most prominent. Additionally, the $T_{2\text{s}}^{6\%}$ values trended towards smaller values at smaller TEs. The $T_{2\text{f}}$ values, on the other hand, showed neglectible variance across different TEs, and their absolute margins of error were very small in absolute terms.

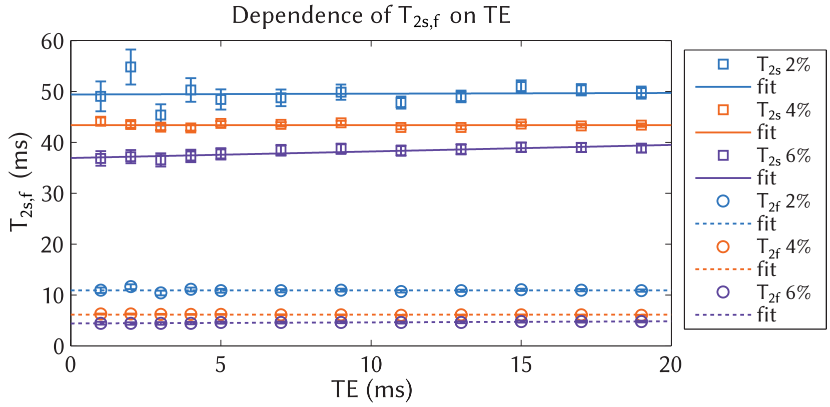

Figure 4.22: Dependence of fitted $T_{2\text{s,f}}$ on TE. The data points of each relaxation time component of each phantom was fitted by the linear fit function $T_{2\text{s,f}} = m \cdot \text{TE} + h$, whereby the constant offset h is approximately $T_{2\text{s,f}}$ if the slope m fulfills $|m| \ll 1$. In comparison with values from TQ-TPPI fits, the $T_{2\text{f}}$ values are in agreement, while the $T_{2\text{s}}$ values are larger by up to 36%.

Table 4.7: Fitted $S_{\text{T/S}}$ in phantoms with graphical presentation in Figure 4.23.

TE (ms)	$S_{\text{T/S}}$ (%) in agarose of (%)		
	2	4	6
1	2.2 ± 0.3	4.1 ± 0.1	6.0 ± 0.5
2	3.7 ± 0.3	6.9 ± 0.1	9.7 ± 0.5
3	5.8 ± 0.4	9.9 ± 0.2	13.9 ± 0.7
4	7.2 ± 0.4	12.7 ± 0.2	17.4 ± 0.7
5	8.7 ± 0.4	15.0 ± 0.2	20.6 ± 0.8
7	12.0 ± 0.4	20.3 ± 0.2	26.9 ± 0.9
9	14.9 ± 0.5	24.9 ± 0.2	32.2 ± 1.1
11	18.6 ± 0.5	29.8 ± 0.3	37.2 ± 1.3
13	21.3 ± 0.5	33.7 ± 0.3	40.7 ± 1.4
15	23.4 ± 0.5	36.5 ± 0.4	43.3 ± 1.4
17	26.6 ± 0.6	39.7 ± 0.4	45.7 ± 1.4
19	29.1 ± 0.8	41.8 ± 0.4	46.8 ± 1.4

To obtain the mean $T_{2\text{s,f}}$ values while taking account the variance of the $T_{2\text{s,f}}$ values in each phantom at each TE, the $T_{2\text{s,f}}$ data points were fitted by the linear fit function $T_{2\text{s,f}} = m \cdot \text{TE} + h$. The RSME was < 0.05, and the slope was $m < 0.02$ in all linear fits. The offset h was approximated as the fitted T_2 due to $|m| \ll 1$. The results were $h_{2\text{s}}^{2\%} = (49.4 \pm 2.7)\,\text{ms}$, $h_{2\text{s}}^{4\%} = (43.4 \pm 0.3)\,\text{ms}$, $h_{2\text{s}}^{6\%} = (36.9 \pm 0.5)\,\text{ms}$, $h_{2\text{f}}^{2\%} = (10.9 \pm 0.3)\,\text{ms}$, $h_{4\text{f}}^{2\%} = (6.1 \pm 0.1)\,\text{ms}$ and $h_{6\text{f}}^{2\%} = (4.4 \pm 0.1)\,\text{ms}$. The $h_{2\text{f}}$ values were in close proximity to those obtained from the TQ-TPPI fits (Table 4.4), whereas the $h_{2\text{s}}$ values are larger by up to 36%.

The voxel-wise fitted $S_{\text{T/S}}$ ratios in each phantom were plotted in Figure 4.23. They were highly dependent on TE. Comparing $S_{\text{T/S}}(\text{TE} = 19\,\text{ms})$ with $S_{\text{T/S}}(\text{TE} = 1\,\text{ms})$, the ratio increased from $(2.2 \pm 0.3)\%$ to $(29.1 \pm 0.8)\%$ in the 2% phantom, from $(4.1 \pm 0.1)\%$ to $(41.8 \pm 0.4)\%$ in the 4%

phantom, and from $(6.0 \pm 0.5)\%$ to $(46.8 \pm 1.4)\%$ in the 6% phantom (Table 4.5). The percentage increase was highest in the 2% phantom and lowest in the 6% phantom. An increase in the margin of error towards higher TEs was observed in the 6% phantom. The $S_{\text{T/S}}$ ratios obtained from TQ-TPPI fits were $S_{\text{T/S}}^{2\%} = (19.4 \pm 0.4)\%$, $S_{\text{T/S}}^{4\%} = (28.3 \pm 0.3)\%$ and $S_{\text{T/S}}^{6\%} = (30.4 \pm 0.4)\%$ (Table 4.7). Assuming these ratios as the ground truth, the TE to obtain the correct $S_{\text{T/S}}$ in TASTI would be in the range of $11 - 13$ ms, $9 - 11$ ms or $7 - 9$ ms for the 2%, the 4% and the 6%

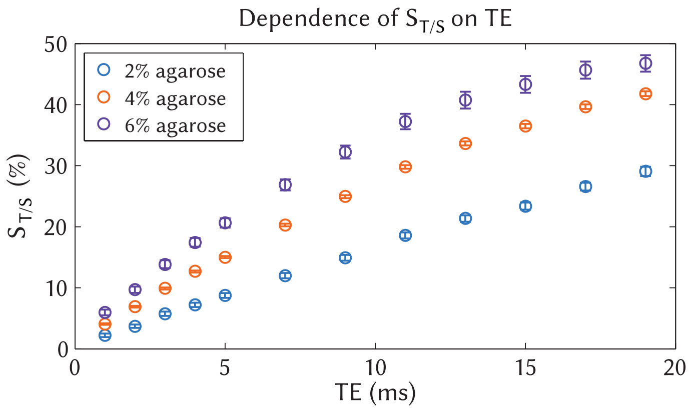

Figure 4.23: Dependence of fitted $S_{\text{T/S}}$ on TE. The choice of TE in TASTI influences $S_{\text{T/S}}$ The percentage increase was highest in the 2% phantom and lowest in the 6% phantom.

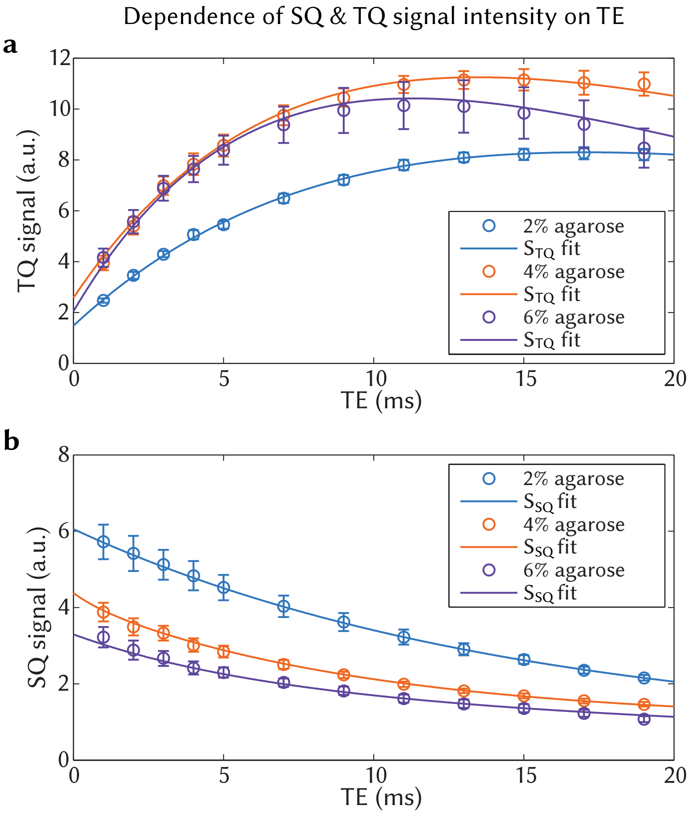

Figure 4.24: **a** The TQ signal intensities in each phantom obtained from TQ images acquired with different TEs, fitted by $S_{\text{TQ}} = a\left(\mathrm{e}^{-\text{TE}/T_{2f}^{*}} - \mathrm{e}^{-\text{TE}/T_{2s}^{*}}\right) + h$. **b** The SQ signal intensities in each phantom obtained from SQ images acquired with different TEs, fitted by $S_{\text{SQ}} = b \cdot \mathrm{e}^{-\text{TE}/T_{2f}^{*}} + (1-b) \cdot \mathrm{e}^{-\text{TE}/T_{2s}^{*}} + h$.

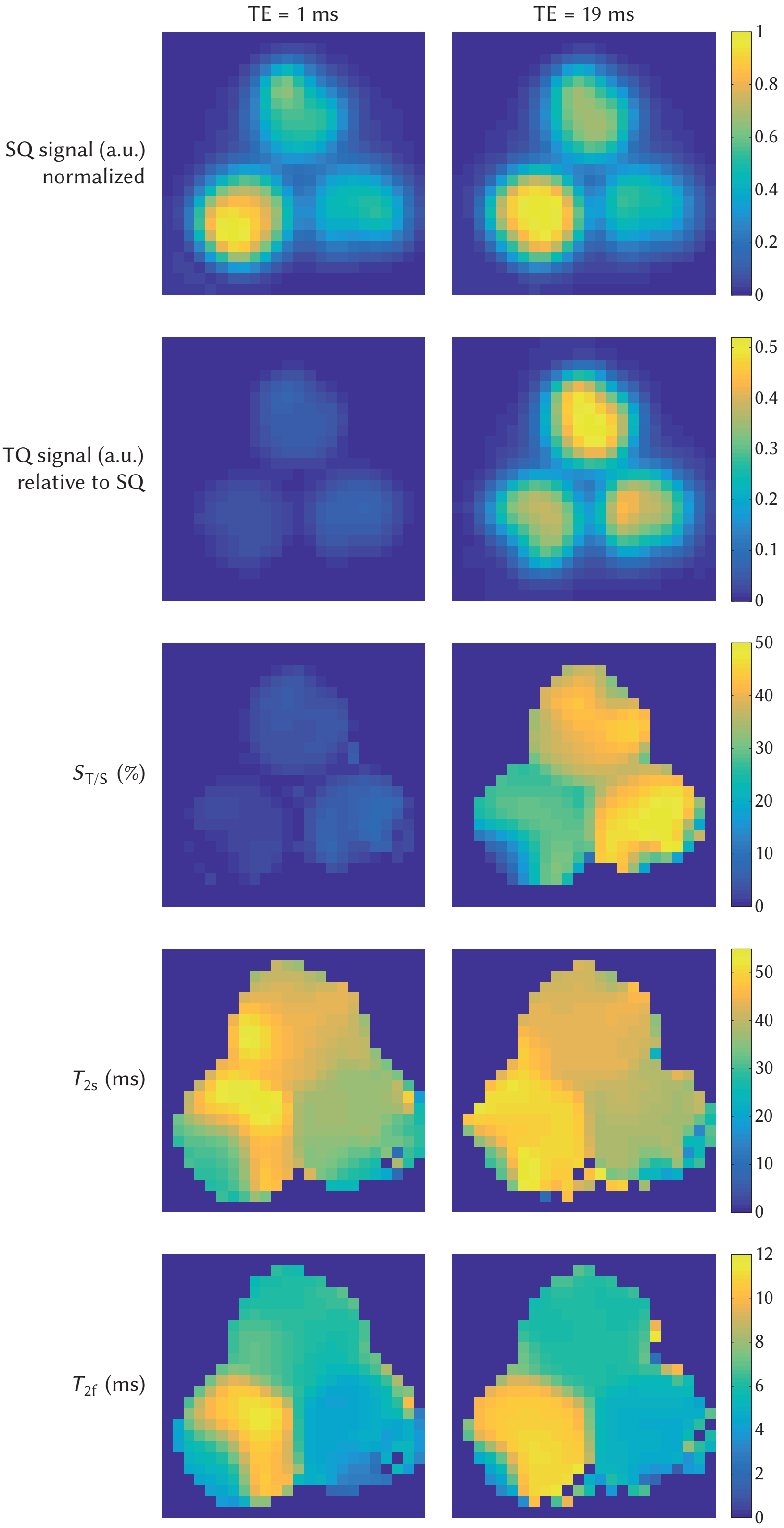
TE = 1 ms
TE = 19 ms
SQ signal (a.u.)
normalized
TQ signal (a.u.)
relative to SQ
$S_{T/S}$ (%)
T_{2s} (ms)
T_{2f} (ms)
1
0.8
0.6
0.4
0.2
0
0.5
0.4
0.3
0.2
0.1
0
50
40
30
20
10
0
50
40
30
20
10
0
12
10
8
6
4
2
0

Figure 4.25: Exemplary images and maps acquired with TE $= 1$ ms and TE $= 19$ ms. Images of the same row are scaled identically. All images and maps have a FOV of $(72\,\mathrm{mm})^2$ and a resolution of $(3\,\mathrm{mm})^2$. The phantoms have different relaxation properties and a different ratio between the TQ and the SQ component. These physical properties are reflected in the TQ image, the SQ image, the $S_{\mathrm{T/S}}$ map, the $T_{2\mathrm{s}}$ map and the $T_{2\mathrm{f}}$ map. Additionally, the relative TQ signal intensity, the absolute SQ signal intensity and the $S_{\mathrm{T/S}}$ ratios differ in the images acquired with different TEs. The relaxation times in all three phantoms are, however, largely the same regardless of TE.

phantom, respectively. Setting TE in the range of $9 - 11\,\text{ms}$ would, for instance, underestimate $S_{\text{T/S}}^{2\%}$, correctly estimate $S_{\text{T/S}}^{4\%}$, and overestimate $S_{\text{T/S}}^{6\%}$.

The TQ and SQ signal intensities in each phantom obtained from the TQ and SQ images, respectively, are displayed in Figure 4.24a as a function of TE. With increasing TE, the SQ signal intensity continuously decreased. On the other hand, the maximum TQ signal intensity was reached at a different TE depending on the phantom. At any TE, it was highest in the 2% phantom and lowest in the 6% phantom. This TE was biggest in the 2% phantom and smallest in the 6% phantom. After the maximum has been reached, the signal intensities decreased continuously. Furthermore, the TQ and SQ signal intensities as a function of TE were fitted by Equation 4.2 and 4.4, respectively, with RSME < 0.0001. Overall, both the TQ and the SQ signal progression with varying TE could be described with equations predicted by theory. The margin of error of the SQ signal intensity decreased with increasing TE in all three phantoms, whereby the changes were most noticeable in the 2% phantom. Contrary to this trend, the margin of error of the TQ signal intensity increased with increasing TE, most noticeably in the 4% and the 6% phantom.

The $T_{2\text{s,f}}^{*}$ obtained from fitting were inserted in Equation 4.3 to determine $\text{TE}_{\text{opt,exp}}(T_{2\text{s,f}}^{*})$. The experimentally determined optimal TEs to achieve the highest signal intensity were $\text{TE}_{\text{opt,exp}}^{2\%} = (17.1 \pm 1.9)$ ms, $\text{TE}_{\text{opt,exp}}^{4\%} = (13.5 \pm 0.9)$ ms, and $\text{TE}_{\text{opt,exp}}^{6\%} = (11.3 \pm 0.8)$ ms. The theoretically optimal TEs were estimated to be $\text{TE}_{\text{opt.theo}}^{2\%} = (18.5 \pm 2.3)$ ms, $\text{TE}_{\text{opt,theo}}^{4\%} = (12.1 \pm 1.1)$ ms, and $\text{TE}_{\text{opt,theo}}^{6\%} = (10.0 \pm 1.2)$ ms by inserting $T_{2\text{s,f}}$ from Table 4.5 in Equation 3.31. Quantitatively, the fitted $\text{TE}_{\text{opt,exp}}(T_{2\text{s,f}}^{*})$ matched the predicted $\text{TE}_{\text{opt,theo}}(T_{2\text{s,f}})$ within the margins of error in all phantoms.

Exemplary images and maps acquired with TE $= 1\,\text{ms}$ and TE $= 19\,\text{ms}$ are displayed in Figure 4.25. Overall, a small area with reduced signal was visible in the periphery of each phantom. In both SQ images, the 2% phantom had the highest value, and the 6% phantom had the lowest value. Each TQ image was scaled relative to the respective SQ image. The TQ(TE $= 1\,\text{ms}$) image had much lower signal intensity than the TQ(TE $= 19\,\text{ms}$) image. Accordingly, the $S_{\text{T/S}}(\text{TE} = 1\,\text{ms})$ map has much lower values than the $S_{\text{T/S}}(\text{TE} = 19\,\text{ms})$ map. In both $S_{\text{T/S}}$ maps, the value was highest in the 6% phantom and lowest in the 2% phantom. In the $T_{2\text{s}}$ and the $T_{2\text{f}}$ maps, the overall contrast among the phantoms as well as the values in each phantom were similar for both experiments. However, the value distribution within each phantom was more homogeneous in the $T_2(\text{TE} = 19\,\text{ms})$ maps than the $T_2(\text{TE} = 1\,\text{ms})$ maps. Both the $T_{2\text{s}}$ and the $T_{2\text{f}}$ values were highest in the 6% and lowest in the 2% phantom.

Varying Δt_{evo} and $t_{\text{evo,max}}$

In this part, the influences of the sampling time step Δt_{evo} and the maximum sampling time $t_{\text{evo,max}}$ on $T_{2\text{s,f}}$ and $S_{\text{T/S}}$ were investigated. The TE was fixed at TE $= 10\,\text{ms}$. Different combinations of Δt_{evo} and n_{pc} were set to compare experiments with identical Δt_{evo} and different $t_{\text{evo,max}}$ and vice versa. The fitting results of $T_{2\text{s,f}}$ in the phantoms with 2%, 4% and 6% agarose are summarized in Table 4.8. The fitting results of $S_{\text{T/S}}$ are summarized in Table 4.9.

The fitted $T_{2\text{s,f}}$ values were grouped for each phantom and plotted as a function of $t_{\text{evo,max}}$ in Figure 4.26. The $T_{2\text{s}}(t_{\text{evo,max}} \geq 39\,\text{ms})$ values were constant within the margin of error. Compared with them, the $T_{2\text{s}}(t_{\text{evo,max}} \leq 19\,\text{ms})$ values deviated strongly and were additionally associated with large margins of errors. Therefore these data points were excluded from linear fitting. Across all phantoms, the margins of error of $T_{2\text{s}}$ and $T_{2\text{f}}$ were smaller in data acquired with larger $t_{\text{evo,max}}$. The $T_{2\text{f}}$ values showed neglectible variance across different $t_{\text{evo,max}}$. Overall, the $T_{2\text{f}}$ values were not influenced by setting either $\Delta t_{\text{evo}} = 0.15\,\text{ms}$ or $\Delta t_{\text{evo}} = 0.30\,\text{ms}$ within the margin of error. However, Δt_{evo} did have an influence on $T_{2\mathrm{s}}$. In data acquired with $t_{\mathrm{evo,max}} \leq 39\,\mathrm{ms}$, the $T_{2\mathrm{s}}(\Delta t_{\mathrm{evo}} = 0.15\,\mathrm{ms})$ values were larger than the $T_{2\mathrm{s}}(\Delta t_{\mathrm{evo}} = 0.30\,\mathrm{ms})$ values. In data acquired with $t_{\mathrm{evo,max}} = 77\,\mathrm{ms}$, the $T_{2\mathrm{s}}$ values were in close agreement.

With the exception of the $T_{2\mathrm{s}}(t_{\mathrm{evo,max}} \leq 19\,\mathrm{ms})$ data points, the data points of each relaxation time component of each phantom were fitted by the linear fit function $T_{2\mathrm{s,f}} = m \cdot \mathrm{TE} + h$. The RSME was < 0.09, and the slope was $m < 0.06$ in all linear fits. The offset h was approximated as the fitted T_2 due to $|m| \ll 1$. The results were $h_{2\mathrm{s}}^{2\%} = (46.8 \pm 4.1)\,\mathrm{ms}$, $h_{2\mathrm{s}}^{4\%} = (41.1 \pm 2.7)\,\mathrm{ms}$, $h_{2\mathrm{s}}^{6\%} = (37.5 \pm 2.5)\,\mathrm{ms}$, $h_{2\mathrm{f}}^{2\%} = (9.9 \pm 0.8)\,\mathrm{ms}$, $h_{4\mathrm{f}}^{2\%} = (5.8 \pm 0.3)\,\mathrm{ms}$ and $h_{6\mathrm{f}}^{2\%} = (4.4 \pm 0.2)\,\mathrm{ms}$. The $h_{2\mathrm{f}}$ values were in agreement with those obtained from the TQ-TPPI fits (Table 4.4), whereas the $h_{2\mathrm{s}}$ values are larger by up to 29%.

Table 4.8: Fitted $T_{2\mathrm{f}}$ and $T_{2\mathrm{s}}$ and $S_{\mathrm{T/S}}$ in agarose phantoms with different combinations of the sampling time step Δt_{evo} and the maximum sampling time $t_{\mathrm{evo,max}}$ of the t_{evo}-FID.

agar. (%)	Δt_{evo} (ms)	$T_{2\mathrm{s}}$ (ms) with a $t_{\mathrm{evo,max}}$ (ms) of				
		10	19	39	77	153
2	0.15	36.0 ± 10.8	43.6 ± 5.8	48.7 ± 3.1	46.2 ± 0.8	–
	0.30	25.9 ± 10.2	38.6 ± 7.2	45.7 ± 3.8	47.7 ± 1.2	47.9 ± 0.6
4	0.15	34.8 ± 8.7	37.4 ± 2.0	44.6 ± 0.7	40.0 ± 0.2	–
	0.30	32.6 ± 14.9	33.0 ± 2.0	38.8 ± 0.7	41.2 ± 0.3	41.0 ± 0.2
6	0.15	34.4 ± 7.2	32.9 ± 3.0	40.8 ± 2.2	36.9 ± 0.7	–
	0.30	33.5 ± 14.9	28.5 ± 3.5	35.2 ± 2.7	37.6 ± 1.1	37.1 ± 0.8

agar. (%)	Δt_{evo} (ms)	$T_{2\mathrm{f}}$ (ms) with a $t_{\mathrm{evo,max}}$ (ms) of				
		10	19	39	77	153
2	0.15	10.5 ± 0.9	9.7 ± 0.4	10.3 ± 0.3	10.2 ± 0.2	–
	0.30	9.4 ± 1.6	9.2 ± 0.6	9.7 ± 0.4	10.4 ± 0.2	10.5 ± 0.2
4	0.15	6.1 ± 0.4	5.8 ± 0.1	5.9 ± 0.1	5.8 ± 0.1	–
	0.30	5.6 ± 0.6	5.5 ± 0.1	5.7 ± 0.1	5.9 ± 0.1	5.9 ± 0.1
6	0.15	4.6 ± 0.2	4.5 ± 0.2	4.6 ± 0.2	4.5 ± 0.2	–
	0.30	4.4 ± 0.4	4.2 ± 0.3	4.4 ± 0.3	4.6 ± 0.2	4.7 ± 0.2

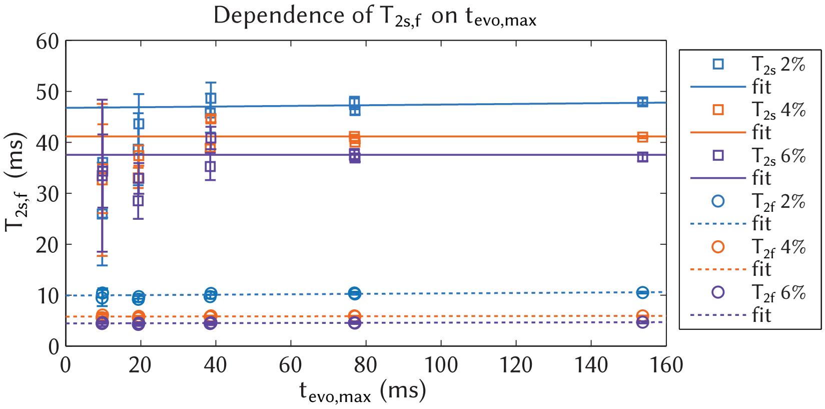

Figure 4.26: Dependence of fitted $T_{2\mathrm{s,f}}$ on $t_{\mathrm{evo,max}}$ and Δt_{evo}. The data points of each relaxation time component of each phantom were fitted by the linear fit function $T_{2\mathrm{s,f}} = m \cdot \mathrm{TE} + h$, whereby $T_{2\mathrm{s,f}}$ was approximated by the constant offset h if the slope m fulfills $|m| \ll 1$. The $T_{2\mathrm{s}}$ data points with $t_{\mathrm{evo,max}} \leq 19\,\mathrm{ms}$ were excluded from the fit due to their large margins of error. In comparison with the values from TQ-TPPI fits, the $T_{2\mathrm{f}}$ values were in agreement, while the $T_{2\mathrm{s}}$ values were larger by up to 29%.

The fitted $S_{\text{T/S}}$ ratios were grouped for each phantom and plotted as a function of $t_{\text{evo,max}}$ in Figure 4.27. The $S_{\text{T/S}}(t_{\text{evo,max}} \leq 19\,\text{ms})$ ratios deviated from $S_{\text{T/S}}(t_{\text{evo,max}} \geq 39\,\text{ms})$ ratios and were associated with large margins of error. On the other hand, the $S_{\text{T/S}}(t_{\text{evo,max}} \geq 39\,\text{ms})$ ratios showed little variance in all phantoms and were associated with smaller margins of errors. They were fitted by $S_{\text{T/S}} = m \cdot \text{TE} + h$. The RSME was < 0.02, and the slope was $m < 0.01$ in all linear fits. The offset h was approximated as the fitted $S_{\text{T/S}}$ due to $|m| \ll 1$. The results were $h^{2\%} = (16.5 \pm 1.3)\,\%$, $h^{4\%} = (28.2 \pm 4.1)\,\%$ and $h^{6\%} = (33.9 \pm 3.8)\,\%$. For each phantom, the fitted $h \approx S_{\text{S/T}}$ ratio lied between the $S_{\text{T/S}}$ ratios previously obtained in data acquired with $\text{TE} = 9\,\text{ms}$ and $\text{TE} = 11\,\text{ms}$ (Table 4.7).

Table 4.9: Fitted $S_{\text{T/S}}$ in agarose phantoms with different combinations of the sampling time step Δt_{evo} and the maximum sampling time $t_{\text{evo,max}}$ of the t_{evo}-FID.

agar. (%)	Δt_{evo} (ms)	$S_{\text{T/S}}$ (%) with a $t_{\text{evo,max}}$ (ms) of				
		10	19	39	77	153
2	0.15	19.7 ± 3.9	16.6 ± 2.5	16.1 ± 0.7	16.8 ± 0.3	–
	0.30	25.5 ± 3.4	18.6 ± 4.3	17.0 ± 1.0	16.3 ± 0.4	16.3 ± 0.3
4	0.15	33.2 ± 3.7	29.4 ± 0.8	26.9 ± 0.3	29.3 ± 0.2	–
	0.30	35.3 ± 7.1	35.6 ± 1.1	29.5 ± 0.4	28.3 ± 0.3	28.7 ± 0.2
6	0.15	37.8 ± 3.1	35.6 ± 3.7	32.7 ± 1.3	35.6 ± 1.0	–
	0.30	40.9 ± 6.8	38.7 ± 6.2	35.3 ± 2.3	34.4 ± 1.3	36.2 ± 1.2

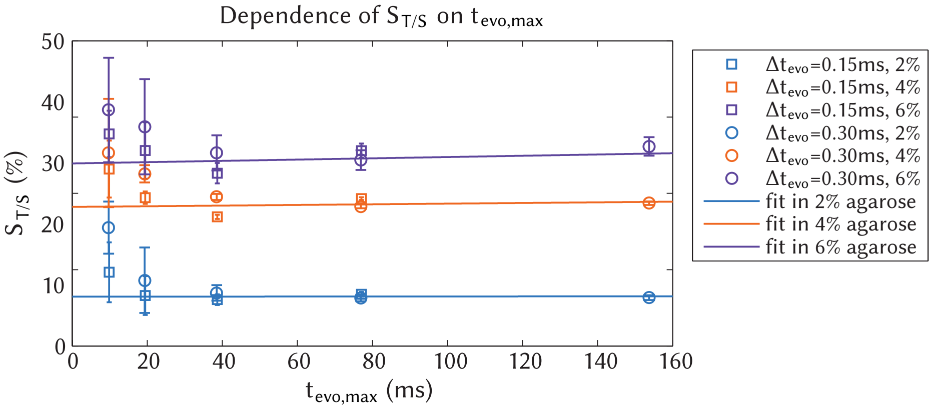

Figure 4.27: Dependence of fitted $S_{\text{T/S}}$ on $t_{\text{evo,max}}$ and Δt_{evo}. The data were fitted by the linear fit function $S_{\text{T/S}} = m \cdot \text{TE} + h$, whereby $S_{\text{T/S}}$ was approximated by the constant offset h if the slope m fulfills $|m| \ll 1$. The $S_{\text{T/S}}$ data points with $t_{\text{evo,max}} \leq 19\,\text{ms}$ were excluded from the linear fit due to their large margins of error. For each phantom, the fitted $h \approx S_{\text{S/T}}$ ratio lied between the $S_{\text{T/S}}$ ratios previously obtained in data acquired with $\text{TE} = 9\,\text{ms}$ and $\text{TE} = 11\,\text{ms}$.

The influence of varying Δt_{evo} or $t_{\text{evo,max}}$ on the MQ k-space, the MQ images and the fitted parameter maps was investigated.

Exemplary MQ k-space images of measurements with $t_{\text{evo,max}} = 10\,\text{ms}$ and $t_{\text{evo,max}} = 153\,\text{ms}$ are displayed in Figure 4.28. The sampling time step was fixed at $\Delta t_{\text{evo}} = 0.30\,\text{ms}$. The $\text{TQ}(t_{\text{evo,max}} = 153\,\text{ms})$ k-space had higher amplitude than the $\text{TQ}(t_{\text{evo,max}} = 10\,\text{ms})$ k-space. Moreoever, it contained distinctive signal patterns in the region of $t = 3-5\,\text{ms}$ towards the k-space periphery. This indicated that it contained information about the high frequency parts of the k-space and therefore would produce a TQ image with more distinguishable edges.

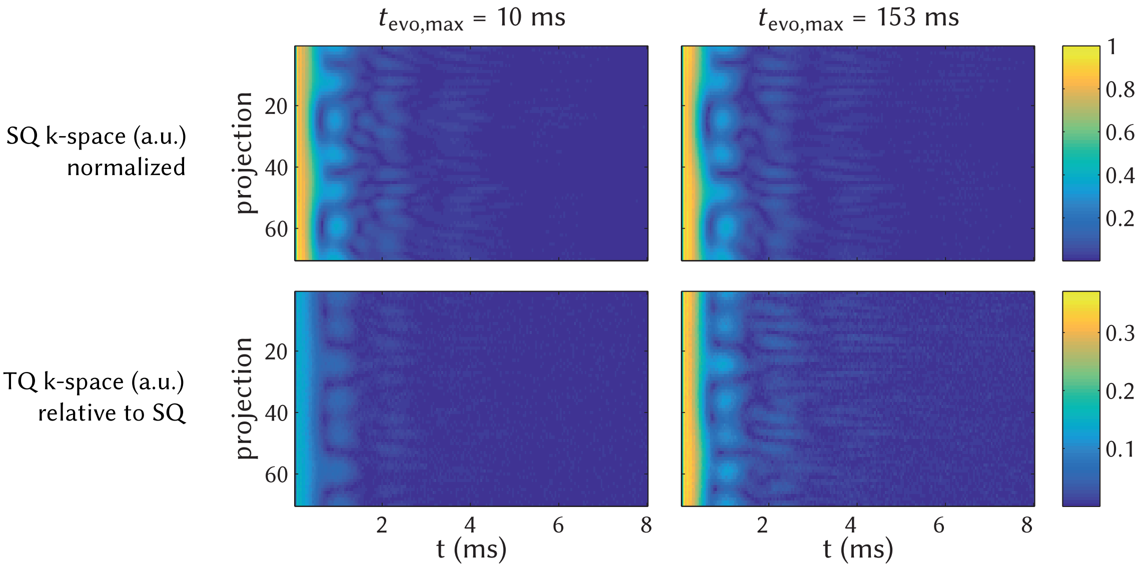

Figure 4.28: The TQ and SQ k-space from the measurements with $\Delta t_{\text{evo}} = 0.30\,\text{ms}$ $t_{\text{evo,max}} = 10$ and $153\,\text{ms}$. The absolute values are displayed, whereby the SQ k-space at f_{SQ} was normalized to itself, and the TQ k-space at f_{TQ} was normalized to the SQ k-space of the same measurement. The scaling in each row is identical. The center of the radial k-space is located at small values along the t-axis.

Exemplary images and maps acquired with $t_{\text{evo,max}} = 10\,\text{ms}$ and $t_{\text{evo,max}} = 153\,\text{ms}$ are displayed in Figure 4.29. Compared to the TQ($t_{\text{evo,max}} = 153\,\text{ms}$) image, the TQ($t_{\text{evo,max}} = 10\,\text{ms}$) image had lower signal intensities. In addition, the edges of the phantoms were less well defined. In both $S_{\text{T/S}}$ maps, the $S_{\text{T/S}}^{6\%}$ ratio was highest and the $S_{\text{T/S}}^{2\%}$ ratio was lowest. However, in each phantom, the ratio was higher in the $S_{\text{T/S}}(t_{\text{evo,max}} = 10\,\text{ms})$ map. The $T_{2\text{s}}(t_{\text{evo,max}} = 153\,\text{ms})$ map was mostly homogeneous within each phantom, with the $T_{2\text{s}}^{2\%}$ values being the highest and the $T_{2\text{s}}^{6\%}$ values being the lowest. In contrast, the $T_{2\text{s}}(t_{\text{evo,max}} = 10\,\text{ms})$ map was inhomogeneous and the three phantoms were indistinguishable. This discrepancy was not observed in the $T_{2\text{f}}$ maps. Both $T_{2\text{f}}$ maps showed similar values and degrees of homogeneity in each phantom.

To investigate the differences in the images and the margins of error associated with $T_{2\text{s}}$ and $S_{\text{T/S}}$ in measurements with small $t_{\text{evo,max}}$, the t_{evo}-FIDs of the measurement with $t_{\text{evo,max}} = 10\,\text{ms}$ are shown in Figure 4.30. At any t_{evo}, the signal intensity in the 6% phantom was lowest with the highest variation. This would contribute to higher fitting uncertainties overall. In all three phantoms, the t_{evo}-FID was not fully sampled with a $t_{\text{evo,max}}$ of $10\,\text{ms}$ only. Incomplete t_{evo}-FID sampling would contribute to a higher fitting uncertainty of especially the $S_{\text{T/S}}$ ratio in signal components with shorter relaxation times and therefore a longer $t_{\text{evo,opt}}$.

Exemplary MQ k-space images of measurements with $\Delta t_{\text{evo}} = 0.15\,\text{ms}$ and $\Delta t_{\text{evo}} = 0.30\,\text{ms}$ are displayed in Figure 4.31. The maximum t_{evo} sampling time was fixed at $t_{\text{evo,max}} = 77\,\text{ms}$. No qualitative differences in terms of signal distribution or noise behavior were visible when comparing the SQ and TQ k-space images of both measurements. Signal patterns were visible in the region of $t = 3 - 5\,\text{ms}$ in all k-space images.

Exemplary images and maps acquired with $\Delta t_{\text{evo}} = 0.15\,\text{ms}$ and $\Delta t_{\text{evo}} = 0.30\,\text{ms}$ are displayed in Figure 4.29. Qualitatively, the respective images and parameter maps of both measurements are in agreement. The background standard deviations in the SQ image acquired with acquired with $\Delta t_{\text{evo}} = 0.15\,\text{ms}$ and $\Delta t_{\text{evo}} = 0.30\,\text{ms}$ were 0.248 and 0.246, respectively. The background standard deviations in the TQ image acquired with acquired with $\Delta t_{\text{evo}} = 0.15\,\text{ms}$ and $\Delta t_{\text{evo}} = 0.30\,\text{ms}$ were 0.088 and 0.087, respectively.

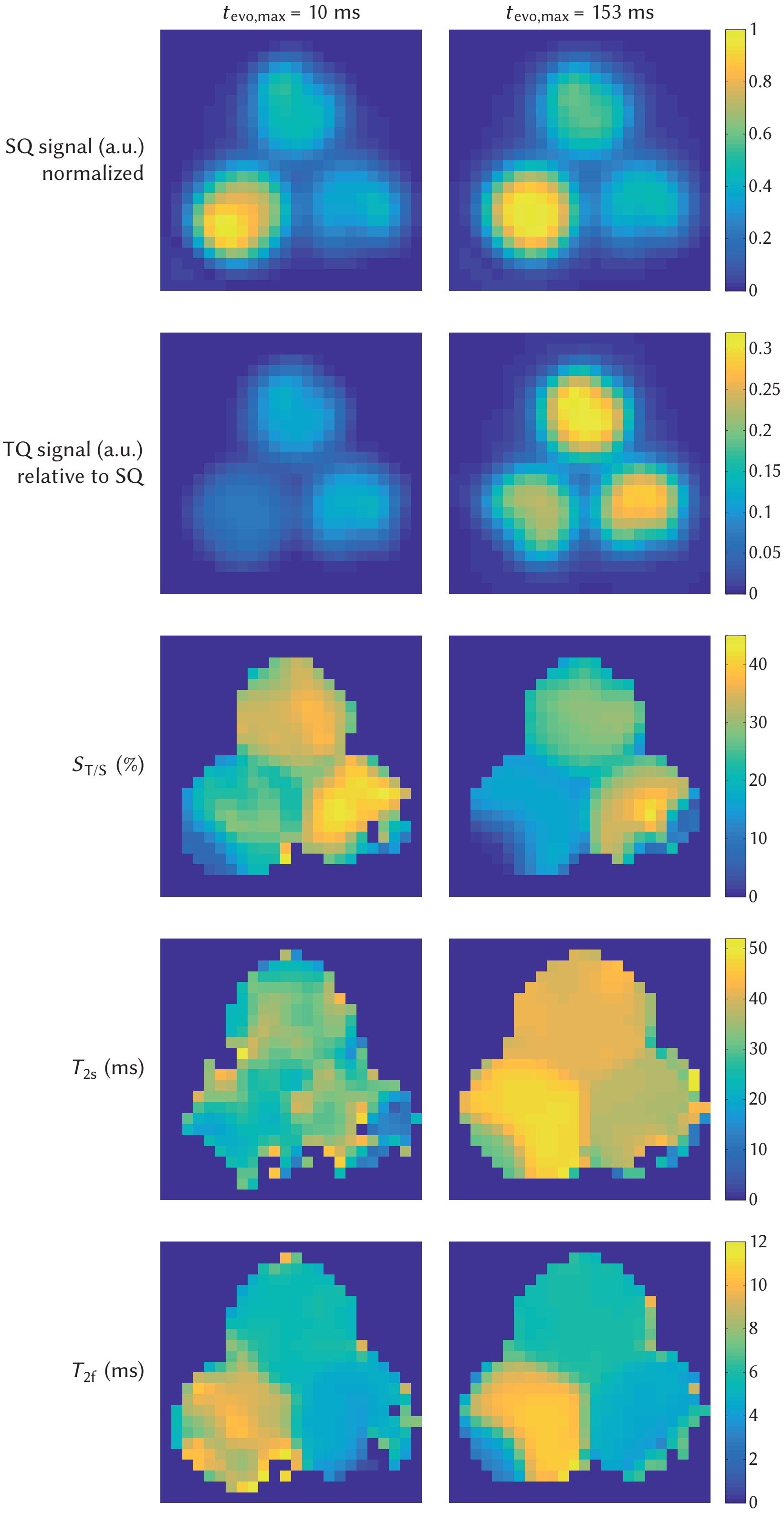
$t_{\text{evo,max}}$ = 10 ms
$t_{\text{evo,max}}$ = 153 ms
SQ signal (a.u.) normalized
TQ signal (a.u.) relative to SQ
$S_{\text{T/S}}$ (%)
T_{2s} (ms)
T_{2f} (ms)
1
0.8
0.6
0.4
0.2
0
0.3
0.25
0.2
0.15
0.1
0.05
0
40
30
20
10
0
50
40
30
20
10
0
12
10
8
6
4
2
0

Figure 4.29: Exemplary images and maps acquired with $t_{\text{evo,max}} = 10\,\text{ms}$ and $t_{\text{evo,max}} = 153\,\text{ms}$. The sampling time step was the same with fixed $\Delta t_{\text{evo}} = 0.30\,\text{ms}$. All images and maps have a FOV of $(72\,\text{mm})^2$ and a resolution of $(3\,\text{mm})^2$. Images of the same row are scaled identically. Comparing the maps from the measurement of $t_{\text{evo,max}} = 10\,\text{ms}$ with those of $t_{\text{evo,max}} = 153\,\text{ms}$, only the T_{2f} map showed largely the same results. The $S_{\text{T/S}}$ map had higher values, and the T_{2s} map made no visible distinction among the three phantoms.

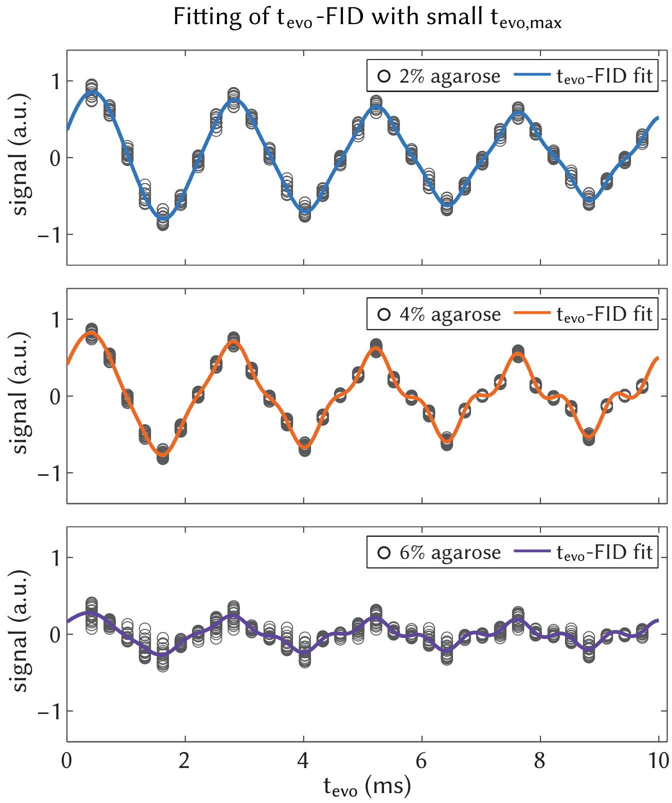

Figure 4.30: Fitting of the t_{evo}-FID with $t_{\text{evo,max}} = 10\,\text{ms}$ in different agarose concentrations with different $t_{\text{evo,opt}}$. The three subfigures contain the FIDs of voxels within each phantom. The data points of each phantom were fitted by Equation 3.24.

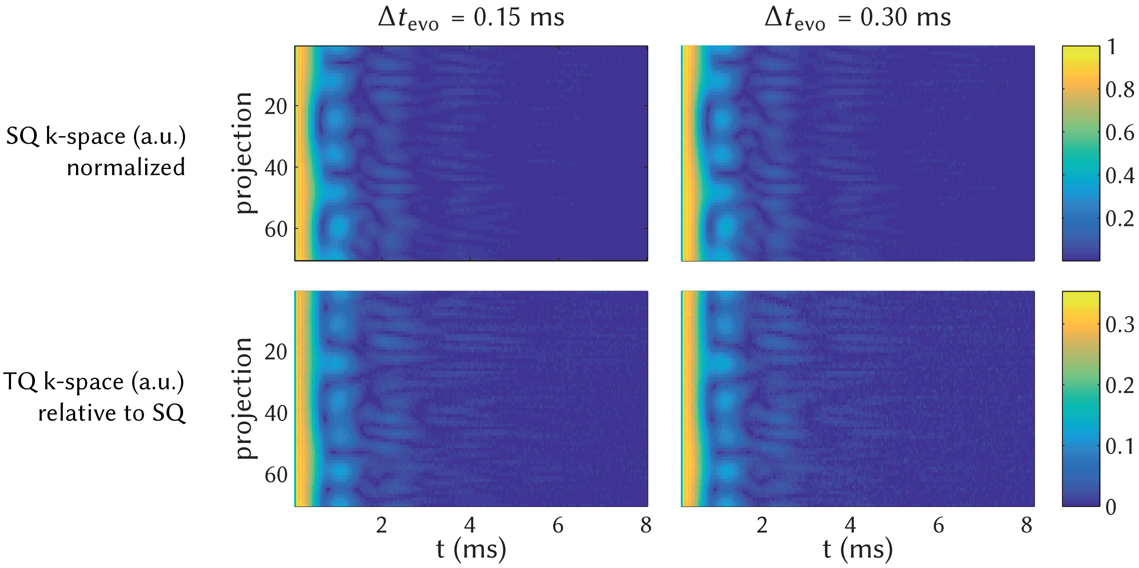

Figure 4.31: The TQ and SQ k-space from the measurements with $t_{\text{evo,max}} = 77\,\text{ms}$ and $\Delta t_{\text{evo}} = 0.15$ and $0.30\,\text{ms}$. The absolute values are displayed, whereby the SQ k-space at f_{SQ} was normalized to itself, and the TQ k-space at f_{TQ} was normalized to the SQ k-space of the same measurement. The scaling in each row is identical. The center of the radial k-space is located at small values along the t-axis.

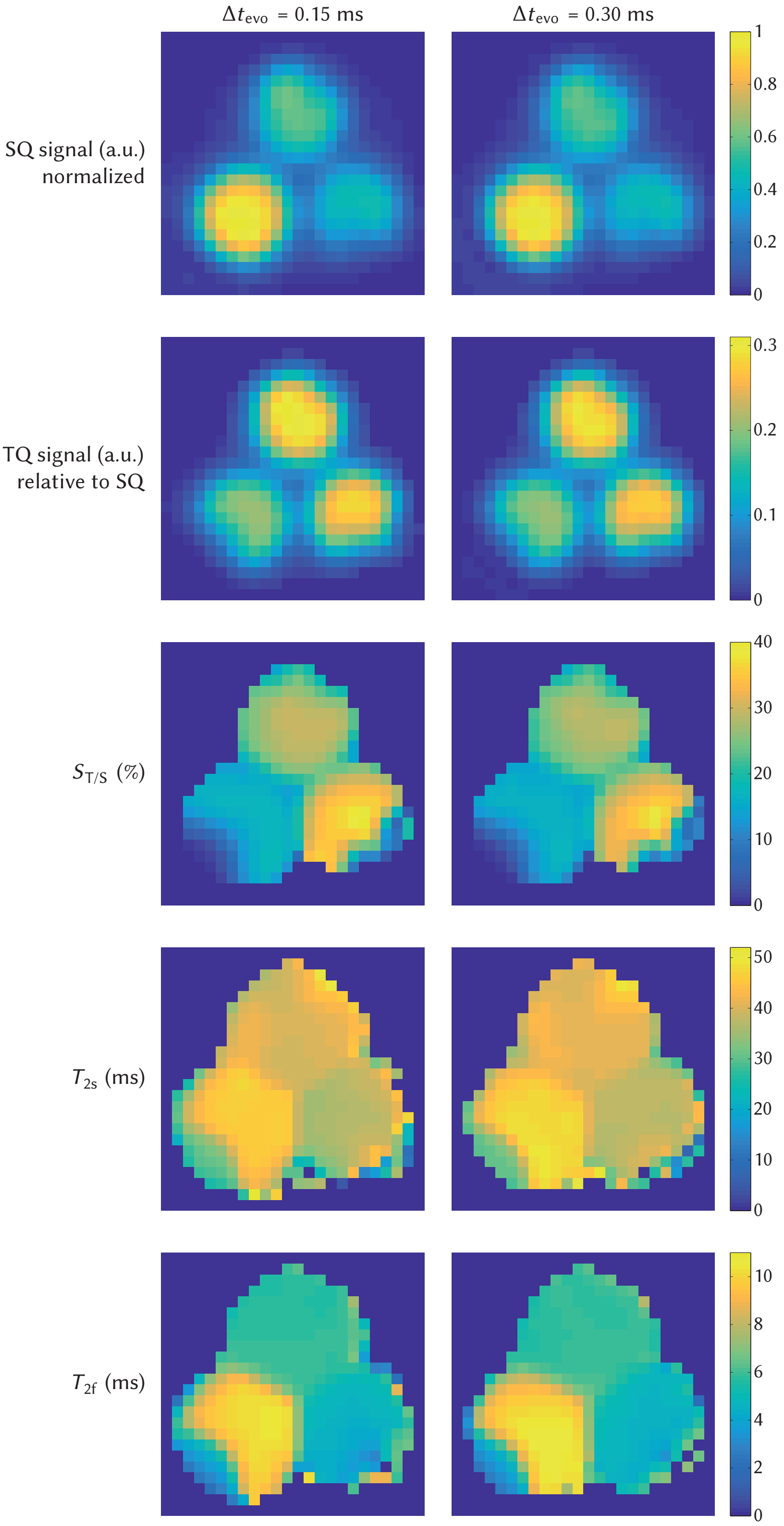
Δt_{evo} = 0.15 ms
Δt_{evo} = 0.30 ms
SQ signal (a.u.) normalized
TQ signal (a.u.) relative to SQ
$S_{\mathrm{T/S}}$ (%)
$T_{2\mathrm{s}}$ (ms)
$T_{2\mathrm{f}}$ (ms)
1
0.8
0.6
0.4
0.2
0
0.3
0.2
0.1
0
40
30
20
10
0
50
40
30
20
10
0
10
8
6
4
2
0

Figure 4.32: Exemplary images and maps acquired with $\Delta t_{\mathrm{evo}} = 0.15\,\mathrm{ms}$ and $\Delta t_{\mathrm{evo}} = 0.30\,\mathrm{ms}$. The sampling time was the same with fixed $t_{\mathrm{evo,max}} = 77\,\mathrm{ms}$. All images and maps have a FOV of $(72\,\mathrm{mm})^2$ and a resolution of $(3\,\mathrm{mm})^2$. The respective images and parameter maps of both measurements are in agreement.

4.3.3 Application in Rat Head

In this subsection, the results of the application of the TASTI sequence in rat head are shown. The first goal was to probe the feasibility of obtaining TQ and SQ images *in vivo*. Following this step, the second goal was to determine localized $S_{\mathrm{T/S}}$ ratios and $T_{\mathrm{2s,f}}$ values in rat head.

The SQ and TQ k-space images are displayed in Figure 4.33. In the SQ k-space image, the k-space center with high signal intensity was followed by distinctive patterns. The maximum signal intensity in the TQ image was approximately 20% that of the SQ image. Distinctive patterns further away from k-space center were not observed in the TQ image. This indicated that the TQ image would contain information on the general signal distribution. Yet it would not be able to distinguish structures to the same degree as the SQ image. Apart from the center of the TQ k-space, the higher frequency components were visibly noisy, which would translate to a noisy TQ image. To reduce the influence of k-space noise on the reconstructed TQ image, the k-space data at all f_{MQ} were filtered by a $\cos^2$ function, while accepting the trade-off of losing high frequency information in the SQ k-space.

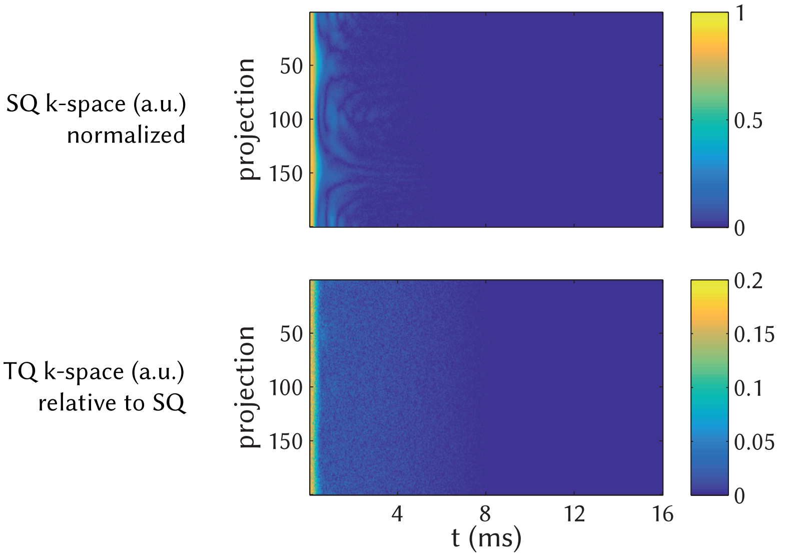

Figure 4.33: The TQ and SQ k-space images in absolute values. The k-space at all f_{MQ} were filtered by a $\cos^2$ function with factor 2 to reduce the influence of k-space noise on the TQ image. The SQ k-space at f_{SQ} was normalized to itself, and the TQ k-space at f_{TQ} was normalized to the SQ k-space.

The TASTI SQ and TQ images are shown in Figure 4.34. An anatomical ^{1}H image can be found in Figure 4.8. In the SQ image, the eyes were the most distinctive features with the highest signal intensity. The outline of the head was well separated from the reference phantoms to both sides. Both reference phantoms contained the $50\,\mathrm{mM}$ NaCl and $4\,\%$ agarose and were placed symmetrically in regard to the coil. Yet the $2\,\mathrm{ml}$ phantom to the right appeared much brighter than the $1\,\mathrm{ml}$ phantom to the left. In the TQ image, on the other hand, the reference phantoms could not be distinguished. The TQ signal distribution in the eyes appeared distorted, and it deviated from the expected round shape. Relative to the head tissue, the SQ signal in the eyes were much brighter than the TQ signal.

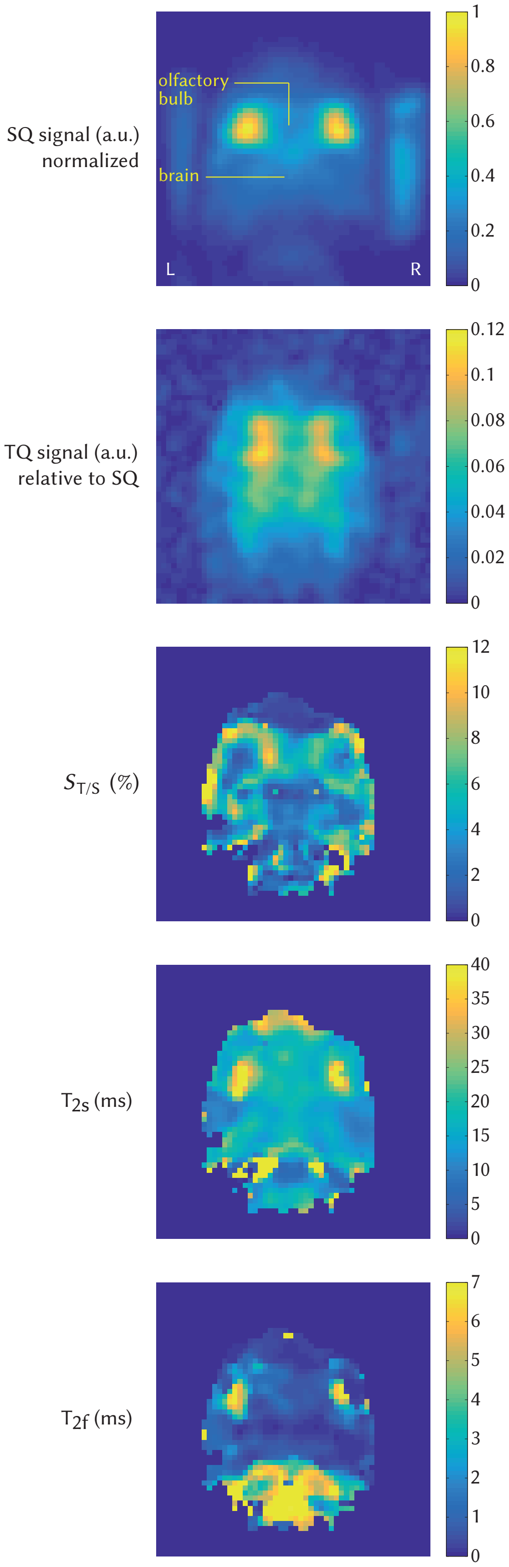
SQ signal (a.u.)
normalized
olfactory bulb
brain
L
R
1
0.8
0.6
0.4
0.2
0
TQ signal (a.u.)
relative to SQ
0.12
0.1
0.08
0.06
0.04
0.02
0
$S_{T/S}$ (%)
12
10
8
6
4
2
0
T_{2s} (ms)
40
35
30
25
20
15
10
5
0
T_{2f} (ms)
7
6
5
4
3
2
1
0

Figure 4.34: Pseudo 2D ^{23}Na TASTI images of rat head *in vivo* in the coronal view. All images and maps have a FOV of $(54\,\mathrm{mm})^2$ and a resolution of $(1\,\mathrm{mm})^2$. The SQ image was normalized to itself, while the TQ image was normalized to the SQ image. Thresholds were applied prior to fitting to exclude voxels below an SNR threshold. Voxel-wise fitting with Equation 3.24 yielded the b, $T_{2\mathrm{s}}$ and $T_{2\mathrm{f}}$ parameter maps.

Prior to fitting of the t_{evo}-FIDs of each voxel, thresholds were set based on the normalized SQ signal intensities and the TQ signal intensities relative to the SQ image. Signal intensities with SQ $\leq 10 \cdot \text{SNR}_{\text{SQ}}$ and TQ $\leq 10 \cdot \text{SNR}_{\text{TQ}}$ were not identified in the rat head of the respective image, and the t_{evo}-FIDs of these voxels were discarded. The remaining t_{evo}-FIDs constituted the image space of the entire head and were fitted voxel-wise by Equation 3.24. The parameters maps are shown in Figure 4.34.

In the uncorrected $S_{\text{T/S}}$ map, the ratio distribution in the olfactory bulb located between the eyes was relatively homogeneous. In the brain, the $S_{\text{T/S}}$ ratios were lower than those in the olfactory bulb and the cheek tissue to both sides. The eyes were visible as areas of very low $S_{\text{T/S}}$ ratios. Areas around the eyes, however, had very high $S_{\text{T/S}}$ ratios. In the $T_{2\text{s}}$ map, high values were found in the eyes. Patterns of relatively high $T_{2\text{s}}$ values were also visible in the olfactory bulb and the brain. Based on the symmetry of the patterns, the patterns could be attributed to regions with arterial blood. In the $T_{2\text{f}}$ map, the values appeared to be consistently low in the range of $0.5 - 1\,\text{ms}$ apart from the eyes and the region in the neck farther away from the sensitivity center of the coil. In all parameters maps, values farther away from the sensitivity center of the coil appeared inconsistent with values in neighboring tissue.

To obtain parameters in different regions of the head, the sums of the t_{evo}-FIDs in the entire head, the olfactory bulb, the brain and the eyes were each fitted by Equation 3.24. Additionally, the t_{evo}-FIDs of voxels in the eyes were fitted by Equation 3.23. The fitting results are listed in Table 4.10.

Therefore it was essential to correct the measured TASTI $S_{\text{T/S}}$ ratios, which was the ratio between the SQ signal amplitude $S_{\text{SQ}}(\text{TE})$ and the TQ signal amplitude $S_{\text{TQ}}(\text{TE})$, such that the ratios are independent of TE. To do so, the TASTI $S_{\text{T/S}}$ ratios were corrected with the TASTI $T_{2\text{s,f}}$. The measured $S_{\text{SQ}}(\text{TE})$ was referenced to the theoretical maximum SQ signal intensity $S_{\text{SQ}}(0)$, and the measured $S_{\text{TQ}}(\text{TE})$ was referenced to the theoretical maximum TQ signal intensity $S_{\text{TQ}}(\text{TE}_{\text{evo,opt}})$. The $S_{\text{T/S}}$ ratios were multiplied by the correction factor

$$\frac{S_{\text{TQ}}(\text{TE}_{\text{evo,opt}})}{S_{\text{TQ}}(\text{TE})} \cdot \frac{S_{\text{SQ}}(0)}{S_{\text{SQ}}(\text{TE})} \,. \tag{4.5}$$

The correction functions,

$$S_{\text{SQ}}(t) = (1-b) \cdot \exp\left(-\frac{t}{T_{2\text{f}}}\right) + b \cdot \exp\left(-\frac{t}{T_{2\text{s}}}\right) \text{ and} \tag{4.6}$$

$$S_{\text{TQ}}(t) = \exp\left(-\frac{t}{T_{2\text{f}}}\right) - \exp\left(-\frac{t}{T_{2\text{s}}}\right) \,, \tag{4.7}$$

used the parameters b and $T_{2\text{s,f}}$ obtained from the TASTI measurements (Table 4.6).

The corrected TASTI $S_{\text{T/S}}$ ratios were compared with the TQ-TPPI $S_{\text{T/S}}$ ratios. The TQ-TPPI $S_{\text{T/S}}$ ratios were the ratios between the maximum TQ signal and the maximum SQ signal. Thus they served as a reference point because they were independent of TE and t_{evo} due to the fact that both the t_{evo}- and the t-FIDs were fully sampled.

Analogous to the correction procedure detailed in Subsection 4.3.2, the TASTI $S_{\text{T/S}}$ ratio of each tissue was corrected with the measured b and $T_{2\text{s,f}}$ of the same tissue. The corrected TASTI $S_{\text{T/S}}$ ratios represented the ratio between the maximum TQ signal and the maximum SQ signal.

Table 4.10: Fitting results of the sum of the t_{evo}-FIDs in the entire head, the brain, the olfactory bulb and the eyes (RMSE< 0.038). The fraction of the fast relaxing component is given by b. The TQ-TPPI results in the head are listed for an easier comparison.

	b (%)	$T_{2\mathrm{f}}$ (ms)	$T_{2\mathrm{s}}$ (ms)	$S_{\mathrm{T/S}}$ (%)	cor. factor	cor. $S_{\mathrm{T/S}}$ (%)
head (TQ-TPPI)	55.5 ± 1.6	2.2 ± 0.2	27.7 ± 0.6	8.9 ± 0.5	–	–
head	34.6 ± 2.0	0.78 ± 0.44	15.9 ± 1.3	5.0 ± 1.8	1.73 ± 0.27	8.7 ± 3.5
brain	30.7 ± 2.2	1.03 ± 0.65	15.6 ± 1.5	3.3 ± 2.0	1.80 ± 0.41	5.9 ± 3.9
olfactory bulb	35.6 ± 1.9	0.68 ± 0.44	17.9 ± 1.5	5.1 ± 1.8	1.71 ± 0.25	8.7 ± 3.3
eyes (TQ & SQ)	65.4 ± 27.7	3.65 ± 2.70	34.7 ± 0.3	2.2 ± 3.5	3.60 ± 3.13	7.8 ± 14.2
eyes (SQ only)	–	–	22.1 ± 0.3	–	–	–

In the entire head and in the brain, the relaxation times $T_{2\mathrm{s,f}}$ and the fraction b of the fast relaxaing component were in agreement within the margin of error. Interestingly, their corrected $S_{\mathrm{T/S}}$ ratios were not in agreement, with $S_{\mathrm{T/S}}^{\mathrm{head}} = (1.5 \pm 1.1) \cdot S_{\mathrm{T/S}}^{\mathrm{brain}}$. In the eyes, the relaxation times are bigger than those in other regions. The $S_{\mathrm{T/S}}^{\mathrm{eye}}$ ratio was associated with very large margins of error. Mono-exponential fitting of the t_{evo}-FIDs in the eyes yielded the relaxation time $T_2 = (22.1 \pm 0.3)\,\mathrm{ms}$. All parameters in the olfactory bulb and the entire head were in agreement. Regions with $S_{\mathrm{T/S}}$ ratios higher than that of the entire head were not among the ones characterized in Table 4.10. Such regions were made up by areas surrounding the eyes and a few spots with no apparent correlation with anatomical features in the cheek tissue, as was visible in the $S_{\mathrm{T/S}}$ map.

Comparing the TASTI results in the head with the TQ-TPPI results (Table 4.5), the TASTI $T_{2\mathrm{s,f}}$ ($T_{2\mathrm{s}} = (15.9 \pm 1.3)\,\mathrm{ms}$ and $T_{2\mathrm{f}} = (0.78 \pm 0.44)\,\mathrm{ms}$) were lower than the TQ-TPPI values ($T_{2\mathrm{s}} = (27.7 \pm 0.6)\,\mathrm{ms}$ and $T_{2\mathrm{f}} = (2.2 \pm 0.2)\,\mathrm{ms}$). Deviations were also found in the parameter b. The fraction of the fast relaxing component determined with TQ-TPPI was $(55.5 \pm 1.6)\,\%$ and therefore close to the theoretical prediction of $60\,\%$. The value determined with TASTI was much lower with $(34.6 \pm 2.0)\,\%$. Despite the discrepancies in the values of $T_{2\mathrm{s,f}}$ and b, the corrected TASTI $S_{\mathrm{T/S}}^{\mathrm{head}} = (8.7 \pm 3.5)\,\%$ ratio in the entire head was in agreement with the TQTPPI $S_{\mathrm{T/S}}^{\mathrm{head}} = (8.9 \pm 0.5)\,\%$ ratio within the margin of error.

5 Discussion

This chapter discusses the findings from the three main parts of this dissertation. In the first part, the DA-R sequence was implemented for the first time at a preclinical $9.4\,\mathrm{T}$ Bruker MR scanner to the best of the Author's knowledge. Improvement in terms of SNR and image resolution were demonstrated in ^{35}Cl phantom studies. High resolution ^{23}Na and ^{35}Cl images were acquired in the bioreactor and in rat head and abdomen. Findings in this part have been previously presented in (Hu et al., 2017a) and (Hu et al., 2017b). In the second part, ^{23}Na and ^{35}Cl TQ-TPPI measurements determined relaxation parameters which additionally served as comparison with results acquired with the TASTI sequence. Results in rat head pointed to differences in the creation of the TQ signals involving Na^{+} and Cl^{-}. In the third part, the TASTI sequence was developed by combining the TQ-TPPI RF pulse and phase cycling scheme with the DA-R density-adapted readout gradients. In phantom experiments, the feasibility of the sequence was demonstrated and the influence of parameter settings was evaluated. Moreoever, the capability of producing a SQ image, a TQ image, a $S_{\mathrm{T/S}}$ map, a $T_{2\mathrm{s}}$ map and a $T_{2\mathrm{f}}$ map from the same dataset was shown. The TASTI sequence was finally applied to *in vivo* imaging of the rat head to quantify localized $S_{\mathrm{T/S}}$ and $T_{2\mathrm{s,f}}$ in the entire head, in the brain, in the olfactory bulb and in the eyes. Findings in this part have been previously presented in Hu et al. (2018a), Hu et al. (2018b) and Hu et al. (2018c).

5.1 DA-R

Sequence Validation in Phantom Studies

Low-gamma nuclei such as ^{35}Cl benefit from a ultrahigh magnetic field strength. The sensitivity gain is proportional to $\omega_0^{7/4}$ (Hoult and Richards, 1976). Bruker preclinical spectrometers are available at ultrahigh field of up to $21.1\,\mathrm{T}$ and allow for applications in animal models (Baier et al., 2014; Elabyad et al., 2014; Kirsch et al., 2010; Schepkin et al., 2006a,b, 2014; Schepkin, 2016; Wetterling et al., 2012, 2015) and studies on 3D cell cultures in a physiologically controlled environment (Gottwald et al., 2013, 2016; Hoesl et al., 2019; Neubauer et al., 2017). To discover the possibilities of preclinical imaging at $9.4\,\mathrm{T}$, the DA-R sequence was implemented in the Bruker scanner. The sequence was validated in ^{35}Cl phantom studies in two important features: its SNR gain through density-adapted k-space sampling, and its resolution capacity in comparison with the available Bruker UTE sequence. Furthermore, ^{23}Na and ^{35}Cl images of the bioreactor were acquired. They served as a proof-of-concept to acquire high-resolution images of two separate compartments, in which different physiological conditions could be configured. Finally, ^{23}Na and ^{35}Cl images were acquired in healthy rats. Previous studies have shown differences in the percentage increase of ^{23}Na and ^{35}Cl signal in rat glioma (Schepkin et al., 2014) and differences in the time point of signal increase in the infarcted region in a rat stroke model (Baier et al., 2014). ^{23}Na myocardial signals have been linked to tissue viability (Constantinides et al., 2001; Kim et al., 1999, 2000; Sandstede et al., 2004), yet cardiac ^{35}Cl studies have not been carried out. Therefore it was important to establish ^{23}Na and ^{35}Cl imaging protocols for rat head and rat torso.

Density-adapted k-space sampling yields a more homogeneous distribution of data points in k-space, which results in a favorable noise behavior. The degree of the homogeneity depends on the proportion of data sampled during density-adapted gradient. This proportion is given by $(t_{\mathrm{ro}} - t_0)/t_{\mathrm{ro}}$, which means that the shorter t_0, the higher is the degree of density-adaption. During t_0, the gradient is ramped up and remains constant before entering the density-adapted section. Thus, t_0 is limited by the gradient ramp time and the fact that the gradient cannot, in practice, immediately decrease after ramp-up. In clinical scanners, the limiting factors are gradient strength and slew rate, whereby the latter plays the more important role due to the risk of nerve stimulation. In the Bruker scanner, both gradient strength and the maximum slew rate are so high that neither is in theory a limiting factor of the hardware.

The SNR variation course with different t_0 (Figure 4.1), however, indicates that there might be a practical downward limitation of t_0 above the theoretical hardware limit. The maximum SNR increase was not achieved at $t_{0,\mathrm{min}} = 0.5\,\mathrm{ms}$ with a $0.26\,\mathrm{ms}$ long section of constant gradient. In all three phantoms, it was achieved at $t_0 = 0.7\,\mathrm{ms}$. This was likely due to a combination of two reasons. One, strong and rapidly changing currents in the gradient coil might cause additional noise, which negates the purpose of enhancing noise behavior with maximizing the density-adapted gradient section. Two, deviations in the k-space trajectory might have led to degradation in image quality. To investiage the possible deviations, the limitations posed by the ramp-up and the constant gradient section were looked into. The preset ramp-up time by other Bruker sequences of approximately $0.12\,\mathrm{ms}$ can be further undercut to approximately $0.06\,\mathrm{ms}$, a value determined by experience according to Bruker technicians. Moreoever, an immediate decrease of gradient strength can be hard-coded immediately after ramp-up. As a consequence, however, deviating k-space trajectories were measured in pratice. They were likely attributed to a mismatch between the set gradient list and the achieved gradient values, which has previously been reported in short yet strong diffusion gradients (Bertleff, 2018). This mismatch might lead to deviations in the k-space locations at which data points were acquired, resulting in image artifacts. To partially compensate for this mismatch, a timing delay of the k-space trajectories was added to the image reconstruction.

Therefore it is recommended to set t_0 reasonably high, if high-resolution ^{23}Na and ^{35}Cl images are acquired with comparable sequence parameters. The maximum gradient strength is anti-proportional to the voxel size and to γ (Equation 3.20). Th experiment series in Subsection 4.1.1 acquired ^{35}Cl images with a voxel size of $2\,\mathrm{mm}$. To obtain the maximum SNR in images with submillimeter resolution, $t_0 > 1\,\mathrm{ms}$ would be recommended, though the exact value is empirical.

A maximum SNR increase of $38\,\%$ in the $6\,\%$ phantom was obtained when density-adapted readout was used. It was in the range of the theoretical maximum of $34\,\%$ Nagel et al. (2009). As the SNR is proportional to the square root of the measurement time, $47\,\%$ measurement time can be saved to achieve the same SNR in the $6\,\%$ phantom if density-adapted gradients are used. The fact that the maximum increase was smallest in the $2\,\%$ phantom confirms the expectation. Compared to the conventional center-out k-space trajectory, density-adapted k-space trajectory samples data ahead of time. Therefore it is more beneficial in environment with shorter $T_{2\mathrm{f}}$. The $T_{2\mathrm{f}}/T_{2\mathrm{s}}$ ratios are 0.22 ± 0.01, 0.20 ± 0.02 and 0.16 ± 0.02 for the $2\,\%$, $4\,\%$ and $6\,\%$ phantom, respectively. Results confirm that SNR benefit is larger, the smaller the $T_{2\mathrm{f}}/T_{2\mathrm{s}}$ ratio is Konstandin et al. (2011).

In addition to the influence of density-adaption on SNR in agarose phantoms, the spatial resolution capacity of the Bruker UTE sequence and the DA-R sequence was evaluated in images of two resolution phantoms. The images of the two phantoms were inverted in a sense that in Phantom AG, the structures were surrounded by background filled with NaCl, and that in Phantom MM, the structures themselves were filled with NaCl. The fitted resolution in the DA-

R images was found to be 1.43 ± 0.04 and 1.62 ± 0.05 times the nominal voxel size in Phantom AG and Phantom MM, respectively. It indicates that the ability to resolve small structures was more superior if the background contained signal instead of the structures themselves. This was likely due to the fact that signals in Phantom AG with a filled background were higher than signals in Phantom MM with only the structures containing NaCl and therefore led to a higher image SNR. Given this construction difference, shimming was likely to have yielded better results in Phantom AG filled with NaCl. A more homogeneous B_0 is associated with larger T_2^* values, which causes less blurring at the border between the structure and the background.

Overall, the DA-R images had noticeably less noise, rarely contained bright noise spikes that could be mistaken for a small structure, and had much more distinctive transitions between signal and background. The enhancement in image quality can be attributed to two factors. First, the DA-R k-space data are more homogeneously distributed than the UTE k-space data. The advantage in noise behavior was also evident in Figure 4.1, when the DA-R sequence was compared to itself with different t_0. However, the UTE image still faired worse than the DA-R acquired with $t_0 = t_{\mathrm{ro}}$. This leads to the second reason, a possibly more superior reconstruction algorithim. The DA-R data interpolation uses a Kaiser Bessel convolution kernel with a window width of 4, which has been shown to produce SNR only marginally worse than the theoretically optimal, yet calculation time-intensive sinc convolution kernel Konstandin et al. (2011). Additionally, a Hamming filter was used to increase SNR and to suppress Gibbs ringing. Gibbs ringing can be seen in the UTE image in Figure 4.3, whereas it is not visible in the DA-R images. A comparison between two imaging methods with different reconstruction pipelines may thus seem unfair. However, our focus was to compare the overall image outcome of the newly implemented sequence with that of the existing method.

Apart from image quality, reduced measurement time through undersampling was the second major advantage. Undersampling can be achieved in radial direction by reducing the number of data points per projection, which does not save time. It can also be achieved in angular direction by reducing the number of projections, which saves time and is the undersampling conventionally referred to. Undersampling in either directions will cause aliasing artifacts in combination of outer rings and center-out stripes. The dominant effect is determined by whether the maximum distance between two neighboring k-space data points is bigger in radial or angular direction. This aliasing signal ring can be observed in the UTE images of Phantom AG at the border of the spherical cut-off. The UTE centor-our k-space projection acquires a fixed minimum number of sampling points along each trajectory, namely half of the matrix size. Due to the higher density in k-space center, aliasing rings appear if the object is close to filling up the entire FOV. In images acquired with DA-R, where the sampling points along each trajectory were higher than the minimum, aliasing rings were not visible. Undersampling with reduced number of projections would further decrease the radius of the aliasing ring in the UTE images. However, undersampling can be used in DA-R by up to $32\,\%$, corresponding to measurement time reduction of the same percentage, without significant reduction in image quality Nagel et al. (2009).

The measurement time could be further reduced depending on the geometry of the imaged object. The UTE reconstruction outputs a sphere, while the DA-R image is a cube, which is $6/\pi$ times the size of the sphere. The measurement time could be reduced by up to 65 % if the imaged object, which fills the entire FOV, was a cube instead of a sphere. Taking into acount the option of undersampling, the measurement time could be reduced by up to 76%.

Bioreactor

^{23}Na and ^{35}Cl pseudo 2D images of the bioreactor were acquired. ^{23}Na images with a voxel size of $0.15\,\mathrm{mm}$ and $0.40\,\mathrm{mm}$ were acquired in $67\,\mathrm{min}$ and $5\,\mathrm{min}$, respectively, with an an SNR of 39.9 ± 0.7 and 83.1 ± 0.9. The ^{35}Cl image with a voxel size of $0.80\,\mathrm{mm}$ and an SNR of 65.7 ± 0.5 was acquired in $60\,\mathrm{min}$. The image SNRs were used to test the hypothesis that the SNR ratio between two 2D images can be estimated with Equation 4.1, relying only on the ratio between the voxel size, the measurement and the Larmor frequency. If the hypothesis hold true, then the method can help to determine the trade-off between the voxel size and the imaging parameters when setting up an experiment. For instance, if a minimum voxel size is necessary, then an image can be quickly acquired with few averages. Based on the SNR of the image, the necessary number of averages to obtain images above a certain SNR threshold can be estimated.

Using the SNR of in the high resolution ^{23}Na image as the starting value, the estimated SNR in the low resolution ^{23}Na image was $(7.3 \pm 2.0)\,\%$ lower than the measured value, and the estimated SNR in the ^{35}Cl image was $(20.0 \pm 3.1)\,\%$ lower than the measured value. The discrepancy in the cross-nucleus estimation was considered reasonably low considering that the images were acquired with two different coils. The discrepancies are small enough for Equation 4.1 to be a valid tool to estimate sequence parameters based on previous results.

In all images, the two bioreactor chambers were distinguished. In future bioreactor models with densely sealed chambers, one side could serve as the reference chamber, while alternative physiological conditions could be established in the test chamber. The physiological conditions might differ in pH, oxygenation, ion concentration, blockage of membrane proteins, and cell type. Previous studies with altered conditions in both chambers have shown promising results (Hoesl et al., 2019; Neubauer, 2017). Cell vitality in the test chamber relative to the reference chamber can be assessed upon provocation or during controlled cell death. Especially interesting are comparisons between the changes in the ^{23}Na and the ^{35}Cl images. Both the degree and the timing of signal variation could be measured to reveal fundamental differences between the mechanisms of the physiological processes Na^+ and Cl^- are involved in.

As of now, the possibility of acquiring ^{23}Na images of the bioreactor in just $5\,\mathrm{min}$ can be used as a supporting tool in bioreactor experiments in general. The image offers information on the coil placement and the possible presence of air bubbles. If a sudden signal reduction is observed, possible causes such as the detachment of the coil or the influx of air bubbles can be assessed with an image. Without this tool, the entire bioreactor setup has to be taken out of the scanner. After bringing the setup back into the scanner, a lengthy adjustment pipeline of matching and tuning, frequency adjustment, shimming and RF pulse calibration is required, taking up to $15\,\mathrm{min}$. In spectrsocopy measurements sensitive to coil placement and shim, the measurement conditions before and after the readjustment cannot be regarded as identical.

Rat Head and Rat Torso

^{23}Na 3D images of rat head with a voxel size of $1\,\mathrm{mm}$ were acquired in $7\,\mathrm{min}$. Different brain regions were well distinguishable, with an average SNR of 33.3 ± 3.6 despite the very short measurement time. The ^{23}Na SNR ratio between the eyes and the brain was 2.04 ± 0.28. ^{35}Cl images of rat head with a voxel size of $1.5\,\mathrm{mm}$ were acquired in $50\,\mathrm{min}$. The only distinctive structures were the eyes and the brain, with an SNR of 24.4 ± 3.5 in the brain, respectively. The ^{35}Cl SNR ratio between the eyes and the brain was 1.20 ± 0.19 and therefore much lower than that found in the ^{23}Na images. The smaller ratio is possibly in part due to a smaller coil radius and therefore reduced ^{35}Cl signal in the eyes relative to the brain, the latter of which was placed in the center of the coil. An intrinsic lower chlorine concentration in the eyes relative to the brain compared with sodium can, however, not be excluded. To quantify sodium and chlorine concentrations, either a small birdcage customized to the rat head volume or an elaborate B_1 correction routine for surface coils would be required.

^{23}Na 3D images of rat torso with a voxel size of $1\,\mathrm{mm}$ were acquired in $29\,\mathrm{min}$. The cartilage was noticeable in five instances, and the resolution was good enough to clearly make out the layer of fat with low signal intensity between the skin and cartilages. The most striking feature is the myocardium with an SNR of 47.4 ± 2.8. Neglecting B_1 variance across the heart and considering the TSC of $80\,\mathrm{mM}$ in mammalian blood, the myocardium TSC was estimated to be $(54.4 \pm 5.6)\,\mathrm{mM}$ using the SNR ratio between the two tissues. This value is in agreement with the uncorrected myocardium TSC of $(54 \pm 4)\,\mathrm{mM}$ in human (Lott et al., 2019). Partial volumen correction and respiratory and cardiac motion gating were reported to have reduced the uncorrected value by $(34 \pm 1)\,\%$ and $(11 \pm 1)\,\%$, respectively (Lott et al., 2019). Motion-induced signal change of $5\,\%$ was measured in the absence of ECG-triggering in human Konstandin (2012). Both partial volume effects and motion artifacts, if uncorrected, would result in the high blood signal being mixed with or misinterpreted as the myocardium signal. Therefore, the real TSC in myocardium is most likely much lower.

^{35}Cl 3D images of rat torso with a voxel size of $1.5\,\mathrm{mm}$ were acquired in $119\,\mathrm{min}$. Despite the very long measurement time, only the extent of the heart was identified, without clear evidence of the myocardium. Overall, *in vivo* ^{23}Na images had excellent quality and achieved high SNR in tissues of interest within short measurement times. ^{35}Cl imaging, on the other hand, allowed for the distinction of gross structures only. In rat head, for instance, the total chlorine concentration was reported to be 1.9 times less than sodium (Schepkin et al., 2014). The low biological abundance is an additional hurdle in the attempt to obtain well defined structures in ^{35}Cl *in vivo* images. Nevertheless, ^{35}Cl imaging in rat brain in a stroke or tumor model seeking relative changes between diseased and contralateral tissue or between different time points after disease onset would be feasibile with the current setup. This is especially true as an addition alongside ^{23}Na imaging, as the physiological differences of Na^{+} and Cl^{-} allow both imaging results to be complimentary not only to ^{1}H imaging, but also to each other. Furthermore, the ^{23}Na head images were acquired with a time resolution of 7 min only, providing an excellent basis for imaging of rapidly progressing diseases such as stroke.

5.2 TQ-TPPI

Agarose Phantoms

In the first part of the experiments, TQ-TPPI spectra were acquired in phantoms with $134.75\,\mathrm{mM}$ NaCl and $0\,\%$, $2\,\%$, $4\,\%$ and $6\,\%$ agarose at both the ^{23}Na and the ^{35}Cl frequency. For each nucleus-phantom combination, the influence of TR/T_1 on $S_{\mathrm{T/S}}$ and $T_{2\mathrm{s,f}}$ was examined for a range of TR/T_1 ratios. In the $0\,\%$ phantom, an artifical ^{23}Na TQ peak was measured for TR/T_1 $\lesssim 3.5$, resulting in a non-zero $S_{\mathrm{T/S}}$ ratios. In the same TR range, reduced $S_{\mathrm{T/S}}$ ratios outside 2σ were observed in the $2\,\%$ phantom. The $T_{2\mathrm{s,f}}$ values, however, were unaffected by TR in the range of the experiments. In conclusion for the ^{23}Na TQ-TPPI measurements, setting TR in the range of TR/T_1 $\lesssim 3.5$ would result in artificial creation of TQ signals in acqueous medium. In the ^{35}Cl TQ-TPPI measurements, no conclusive influence of varying TR/T_1 ratios on $S_{\mathrm{T/S}}$ and $T_{2\mathrm{s,f}}$ were found.

The major limitation of this study was the fact that the TR/T_1 ratios did not cover a more extended range including smaller values. TR was limited downwards by the t-FID readout time, as only a fully sample t-FID would yield $S_{\mathrm{T/S}}$ as a ratio between all TQ and SQ signals. In the TASTI experiments, the readout time is much shorter, therefore allowing shorter TR values whose influence on $S_{\mathrm{T/S}}$ and $T_{\mathrm{2s,f}}$ remain to be investigated.

In the second part of the experiments, the TQ-TPPI $T_{\mathrm{2s,f}}$ and b (fraction of the fast relaxing component) of each nucleus-phantom combination were compared with those determined in spin echo experiments. The aim was to verify whether results obtained with both methods were in agreement and whether, consequently, TQ-TPPI measurements could substitute spin echo measurements in measuring T_2. The results summarized in Table 4.4 are conclusive. For almost all parameters b, T_{2s} and T_{2f}, the respective values determined with both methods were in agreement within the margin of error. Additionally, the confidence intervals were smaller for the TQ-TPPI values than for the spin echo values. Therefore, the TQ-TPPI method is as accurate as the spin echo method and, in addition, has a higher precision.

One interesting value that needs to be pointed out is the ^{35}Cl $S_{\mathrm{T/S}}$ in the $6\,\%$ phantom. Contrary to the ^{23}Na $S_{\mathrm{T/S}}$ ratios, which increased with increasing agarose concentration, the ^{35}Cl $S_{\mathrm{T/S}}$ ratio was lower in the $6\,\%$ than the $4\,\%$ phantom. This is observed alongside the fact that $T_{\mathrm{2s,f}}$ values were smaller in the $6\,\%$ than the $4\,\%$ phantom. One possible explanation is that with increasing agarose concentration, a fraction of quadrupolar interactions with an interaction time longer than TE because its interaction time was reduced to be shorter than TE. This signal fraction may have decayed during the RF pulse and therefore can no longer be detected optimally. This explanation can be supported by the sub-millisecond T_{2f} measured in the $6\,\%$ phantom.

Lecithin Phantoms

NaCl phantoms with added agarose are the most commonly used types of phantoms to emulate tissues with short bi-exponential transverse relaxation times. Recently, lecithin phantoms have been used to investigate the source of TQ signal creation (Hoesl et al., 2019). Liposomes contained in lecithin form a double-lipid membrane, similar to the cell membrane. The manufacturing process allowed Na^{+} and Cl^{-} ions to be on either side of or inside the double-lipid membrane. The aim was to investigate the potential differences in the ^{23}Na and ^{35}Cl TQ signal and relaxation times and to determine whether lecithin phantoms could be an alternative to agarose phantoms.

A conclusive ^{23}Na TQ peak was found in all cases, whereas a ^{35}Cl TQ peak was found only in the phantoms with the two highest lecithin concentrations. The ^{23}Na $S_{\mathrm{T/S}}$ ratios were in the same order as in agarose phantoms, while the two non-zero ^{35}Cl $S_{\mathrm{T/S}}$ ratios were both much smaller than ratios found in agarose phantoms. This discrepancy was seen in a positive light, as the ^{23}Na and ^{35}Cl $S_{\mathrm{T/S}}$ ratios *in vivo* might differ greatly inspite of similar $T_{\mathrm{2s,f}}$ values. This is a feature that agarose phantoms could not explore. The $T_{\mathrm{2s,f}}$ values in lecithin phantoms were overall in the same order as in agarose phantoms for both nuclei. However, the three out of four fractions of the fast relaxaing component in the^{23}Na results are in the range $70-80\,\%$, which is larger than the theoretical $60\,\%$. This possibly indicates the presence of multiple pools of Na^{+} ions with different relaxation characteristics, which may have been forcefully fitted with one averaged set of relaxation parameters.

This study was limited by the fact that the exact content of the locally obtained edible lecithin was unknown, as official regulations allowed substances below a certain quantity to not be declared in the ingredients. Future studies should use lecithin from designated manufactures instead to avoid this uncertainty. Furthermore the study did not investigate the stability of the phantoms. The edible substances might deteriorate over time, and the homogeneous state might separate into, for instance, a liquid and a solid layer within the phantom. In conclusion, lecithin phantoms have the potential to more accurately immitate *in vivo* $T_{2\mathrm{s,f}}$ and $S_{\mathrm{T/S}}$ values for both Na$^+$ and Cl$^-$ ions. However, more studies on the influence of chemical compositions on the MR properties and the stability of such phantoms are necessary before they could reliably substitute agarose phantoms.

Bioreactor

The possibility to detect ^{23}Na TQ signals of cells in the bioreactor has been demonstrated before (Hoesl et al., 2019; Neubauer et al., 2017). Compromised activity of the Na$^+$/K$^+$-ATPase under the unfluence of ouabain was directly observed in changes of the TQ signals. The aim of this study was to expand on that finding by investigating whether TQ signal from the quadrupolar interactions experienced by Cl$^-$ ions could be detected as well.

In ^{23}Na spectra, a $S_{\mathrm{T/S}}^{\mathrm{Na}}$ ratio of approximately $0.4\,\%$ could be repeatedly measured in the bioreactor. Interestingly, the $T_{2\mathrm{f}} = (0.2 \pm 0.1)\,\mathrm{ms}$ value was very small, while the $T_{2\mathrm{s}} = (64.0 \pm 0.2)\,\mathrm{ms}$ value was very high and in the range of saline. Additionally, the fraction $b = (22.2 \pm 2.8)\,\%$ was rather small. It indicates that the one-compartment fit model using one pair of $T_{2\mathrm{s,f}}$ values may not be appropriate for the bioreactor system (Burstein and Springer, 2019). A more realistic model would be to include two sets of SQ and TQ fitting terms, each set presumably being able to describe the relaxation parameters in the medium and in the cells. Based on the geometry of the cell cavity arrays, a total of $24\,\mu\mathrm{l}$ cell volume could be estimated, if two arrays with cavities of $300\,\mu\mathrm{m}$ in diameter were stacked in the bioreactor. This yields a cell volume fraction of $2.7\,\%$ in the square bioreactor. In light of this small cell volume fraction and the small $S_{\mathrm{T/S}}^{\mathrm{Na}}$ ratio, the approach to include two sets of fitting terms may result in over-fitting and is thus deemed more realistic, yet less practical. A more practical approach is to include one SQ fitting term to describe all available Na$^+$ ions and a separate TQ fitting term with independent relaxation times to describe Na$^+$ ions contributing to TQ signals.

Initial ^{35}Cl TQ-TPPI measurements on cells in the square bioreactor containing $0.9\,\mathrm{ml}$ liquid found no distinctive peak above noise level at the TQ peak position in repeated measurements on multiple occasions. Manual shimming was carried out in these experiments; automatic shimming was not possible due to the very low SNR. This may have led to loss of TQ signals as TQ signals are very sensitive to B_0 inhomogeneities (Matthies et al., 2010). Depending on the off-resonance, B_0 inhomogeneities cause phases to accumulate along different coherence pathways, leading to signal decrease or even cancellation. In biological tissues with a typical $t_{\mathrm{evo,opt}} = 5\,\mathrm{ms}$, an offset of merely $50\,\mathrm{Hz}$ could lead to destructive interference of the TQ signal (Tanase and Boada, 2005). Any offset apart from this value would also generally decrease the TQ signal strength.

To increase the overall available signal and therefore the likelihood of successful automatic shimming, one feasibility test was carried out on the round bioreactor containing $1.5\,\mathrm{ml}$ liquid. Here, automatic shimming was possible, though the signal amplitude observed in the shim procedure was only slightly above noise level, and the quality of the shim was up to debate. In this setup, a ^{35}Cl TQ peak with $S_{\mathrm{T/S}}^{\mathrm{Cl}} = (5.1 \pm 3.0)\,\%$ was detected. This value was higher than expected, especially since the $S_{\mathrm{T/S}}^{\mathrm{Cl}}$ ratio was many times lower than the $S_{\mathrm{T/S}}^{\mathrm{Na}}$ ratio *in vivo*.

In general, two factors affect the TQ signal strength. In our bioreactor experiments a hepatoma i.e. liver tumor cell line was used. Significantly reduced TQ signal has been measured in tumor (Fiege et al., 2013). Additionally, data were acquired with a flat surface coil. The RF flip angle was determined globally, which means that only a fraction of the applied B_1^+ was actually $90°$.

As the measured TQ signal is prorportional to $\sin^5$ of the flip angle if a 180° refocussing pulse is not applied after the first pulse. , it is very sensitive to B_1^+ inhomogeneities.

Experiments using the round bioreactor were terminated after the feasibility test due to the high risk of contamination of the entire bioreactor perfusion system. The contamination risk lay in the detachment of the bioreactor from the medium supply tubes in order to pass it between the control room and the scanner room. More evidence including control measurements is therefore essential to rule out other sources of TQ signal than the cells. As of now, the ^{35}Cl TQ signal found in the bioreactor must be treated with caution.

Rat Head

^{23}Na and ^{35}Cl TQ-TPPI spectra were acquired in rat head to uncover possible discrepancies in the TQ signal strength between both nuclei *in vivo*. In combination with the DA-R imaging results, the results were furthermore used to estimate the possibility of obtaining localized TQ-TPPI data *in vivo* using the TASTI method. The ^{23}Na spectrum was acquired under 7 min and yielded a conclusive TQ peak with $S_{\mathrm{T/S}}^{\mathrm{Na}} = (8.9 \pm 0.5)\,\%$. The relaxation times were $T_{2\mathrm{s}}^{\mathrm{Na}} = (27.7 \pm 0.6)\,\mathrm{ms}$ and $T_{2\mathrm{f}}^{\mathrm{Na}} = (2.2 \pm 0.2)\,\mathrm{ms}$. The fraction of the fast relaxing component was $b^{\mathrm{Na}} = (55.5 \pm 1.6)\,\%$, which is close to the theoretical prediction of 60 % for the satellite peak intensity undergoing quadrupolar interactions (Rooney and Springer, 1991). The fraction of quadrupolar interactions on the measurable time scale of a few ms was much lower. This fraction is reflected in the $S_{\mathrm{T/S}}$ ratio. It indicates that *in vivo*, interactions between the electric-quadrupole moment of the nucleus and the electric field gradients of the surrounding molecules have different interaction strength and are therefore on a range of different time scales. While the entirety of such interactions are expressed in $T_{2\mathrm{f}}$, only those on the time scale of a few ms may contribute to TQ signals. The time scale with the most TQ signal contributions was measured to be in the range of $5-7\,\mathrm{ms}$ in mammal head (Fiege et al., 2013; Fleysher et al., 2013; Hancu et al., 1999; Mirkes et al., 2016; Schepkin et al., 2017; Tsang et al., 2012). The interpreation of the descrepancy between b and $S_{\mathrm{T/S}}$ is in agreement with previous interpretation by Schepkin et al. (2017). Interactions between Na$^+$ ions and the electric field gradients of negatively charged macromolecules, mainly proteins, are on a longer time scale, if the charged molecules are larger and thus have a smaller tumbling rate.

This train of thought can be applied to interpret the ^{35}Cl *in vivo* results. The ^{35}Cl spectrum was acquired in less than 15 min and yielded a TQ peak just above noise level with $S_{\mathrm{T/S}}^{\mathrm{Cl}} = (1.0 \pm 0.5)\,\%$. This $S_{\mathrm{T/S}}^{\mathrm{Cl}}$ ratio was roughly 8.9 times lower than the $S_{\mathrm{T/S}}^{\mathrm{Na}}$ ratio. The fraction of the fast relaxing component was $b^{\mathrm{Cl}} = (22.6 \pm 0.8)\,\%$ and therefore about 2.5 times lower than the corresponding ^{23}Na value. On the other hand, the relaxation times of $T_{2\mathrm{s}}^{\mathrm{Cl}} = (30.0 \pm 5.8)\,\mathrm{ms}$ and $T_{2\mathrm{f}}^{\mathrm{Cl}} = (1.1 \pm 0.4)\,\mathrm{ms}$ were in the same range as ^{23}Na. The results indicate that even though Cl$^-$ ions experience quadrupolar interactions with positively charged chemical groups within macormolecules, the majority of such interactions may be with small ions and thus not be on a time scale of a few ms. The Cl$^-$ ions are predominantly in the extracellular space, which contains far fewer proteins than the intracellular space. Therefore, the result confirms the expectated lower ^{35}Cl TQ signals *in vivo*.

This interpretation can be supported by looking into the intra- and extracellular ionic composition in mammals, which is illustrated in Figure 5.1. The total amount of positive and negative charge in the intra- and extracellular fluid is shown. This amount is calculated by multiplying the concentration and the charge of a certain charged ion or molecule. Note that the graph shows molecules with a net charge only; macromolecules may have charged chemical groups yet remain uncharged in sum. In the intracellular space, positive ions such as K$^+$ and Na$^+$

ions interact with abundant negatively charged interaction sites within macromolecules. These macromolecules are in part manufactured inside the cell and are included in the categories 'proteins' and 'organic phosphates and acids' in the graph. The interaction sites include carboxylic groups, phosphate groups in small metabolites and DNA, and hydroxyl groups (Andersen, 2013; Schepkin et al., 2017). Cl$^-$ ions, on the other hand, are abundant in the extracellular space and mostly encounter positively charged K$^+$and Na$^+$ ions with extremely high tumbling rates, resulting in quadrupolar interactions on a time scale not detectable as TQ signals. They have fewer opportunities to undergo quadrupolar interactions with positively charged (groups within) macromolecules, simply because the protein concentration in the extracellular space is much lower. Moreoever, the majority of Mg^{2+} ions is bound to ATP, ribosomes and other macromolecules and metabolites (Milo and Phillips, 2015), which may provide positively charged interaction sites for the Cl$^-$ ions, though this hypothesis needs further investigation.

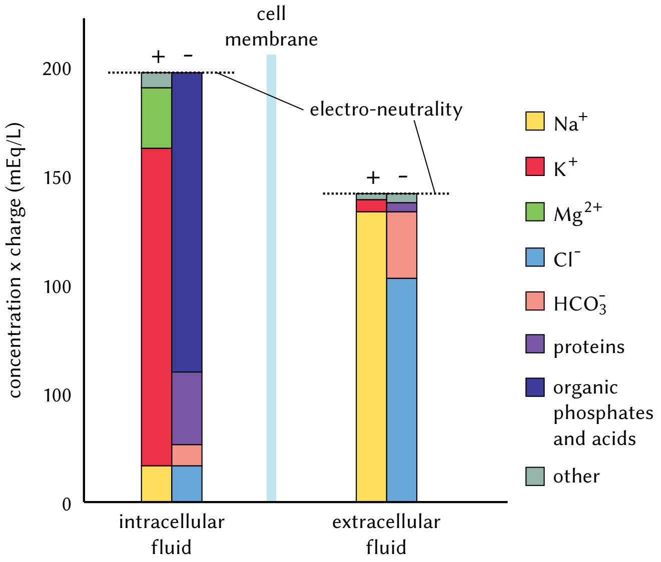

Figure 5.1: Compositions of ions and charged molecules in intra- and extracellular space in mammals. The y-axis is given in the concentration of an ion or molecule multiplied by its charge. Within the intra- and the extracellular compartment, the sum of either the positive or negative charge is almost equal (electro-neutrality). Only a small surplus of the total charge contributes to the membrane potential. (Adapted from Andersen (2013))

5.3 TASTI

Sequence Development and Considerations for Applications in Rat Head

A method to simultaneously acquire SQ and TQ images using TPPI was developed. It combines the TQ-TPPI RF pulse and phase cycling scheme with the DA-R readout gradients. In phantom experiments, the feasibility of the sequence was demonstrated and the influence of parameter settings was evaluated.

Experiments on $50\,\mathrm{ml}$ phantoms containing $134.75\,\mathrm{mM}$ NaCl and 2, 4 and $6\,\%$ agarose were conducted. In the first measurement series, TE was varied in the range of $1-19\,\mathrm{ms}$. The choice of TE had no significant influence on either $T_{2\mathrm{s}}$ or $T_{2\mathrm{f}}$ in all phantoms. The TASTI $T_{2\mathrm{f}}$ values were in agreement with the TQ-TPPI $T_{2\mathrm{f}}$ values within the margin of error. However, the TASTI $T_{2\mathrm{s}}$ values were significantly higher by up to $36\,\%$. We suspect that phantom water content may have evaporated in the time span of a year after the TASTI experiments, causing a decrease in relaxation times measured in the TQ-TPPI experiments. Contrary to $T_{2\mathrm{s,f}}$, the $S_{\mathrm{T/S}}$ ratio was found to be highly dependent on TE, pointing to the necessity of correction for relaxation effects *in vivo*. Variation of the TQ and SQ signal intensities over the range of TE could be described by equations predicted by theory. In the second measurement series, the influence of $t_{\mathrm{evo,max}}$ and Δt_{evo} was examined. Fitting of partially sampled t_{evo}-FIDs resulted in reduced accuracy and precision associated with the $S_{\mathrm{T/S}}$ ratio. Moreoever, the $T_{2\mathrm{s}}$ map of the measurement with the smallest $t_{\mathrm{evo,max}}$ was not able to differentiate among the three phantoms. It is therefore recommended to sample a sufficiently large range of t_{evo} that includes $t_{\mathrm{evo,opt}}$ for a given medium. Differences in image qualities and fitted parameters were not found by varying Δt_{evo}.

The phantom studies includes several limitations. One, the agarose phantoms may not be able to exactly predict the TQ signal behavior *in vivo*. In order to obtain results that can be directly compared to results *in vivo*, phantoms with matching relaxation properties are required. Two, the TASTI phantom experiments were carried out with the ^{1}H/^{23}Na volume coil, while the TQ-TPPI phantom data were acquired with the saddle coil. Possible descrepancies in relaxation properties determined with both coils were not examined. Three, the sampling step Δt_{evo} was set to two values only. On top of that, the difference between them was small, and none was the Δt_{evo} actually chosen for the *in vivo* measurements. For a better comparison, phantom experiments with the exact sequence parameters as *in vivo* shall be carried out on phantoms with matching relaxation characteristics.

In addition to phantom experiments, a discussion concerning the imaging modes is essential. The TASTI sequence was programmed to be able to acquire 3D or pseudo 2D images; it was not programmed to acquire true 2D images. All TASTI experiments were conducted in pseudo 2D mode inspite of the possibility of acquiring 3D images. In the following the trade-off between the 3D and pseudo 2D modes as well as between the 2D and pseudo 2D modes are discussed.

In an ideal scenario where signal is abundant and measurement is not an issue, 3D images always prevail. Consider acquiring an isotropic 3D image with the Nyquist number of projections. The measurement is N-times as long as a (pseudo) 2D measurement with the same in-plane resolution, whereby N is the number of voxels per dimension. To acquire the *in vivo* rat head image with an in-plane voxel dimension of 54×54 in 3D, for example, would increase the scan time from $71\,\mathrm{min}$ to approximately 64 hours. Moreover, the reduced voxel size requires more signal averaging, a factor for additional increase in scan time that needs to be accounted for. Therefore, pseudo 2D image acquisition was preferred to allow for reasonable scan time.

The alternative to the pseudo 2D readout is the “true” 2D readout. To select a 2D slice, slice selection gradient runs simultaneously to a sinc pulse. Sinc pulses, however, do not fulfill the hard pulse condition. Their duration, depending on the coil design and the load, is typically in the range of $1-2\,\mathrm{ms}$, which contrasts the typical length of $0.1\,\mathrm{ms}$ of a block pulse. The slice selection gradient needs to be rewound for about half the length of the sinc-pulse afterwards, thereby extending the time between the sinc-pulse and the next sequence element. Furthermore, dephasing during the RF pulse could not be neglected in case of such a long RF pulse (Tanase and Boada, 2005). The transformation of $\hat{T}_{lm}$ under a hard pulse as illustrated in Figure 2.5 is also not given. For detailed discussion on the violation of the hard pulse condition refer to (van der Maarel, 2003a). Observable TQ signal fractions may deter from the designated coherence pathway and not be detected after the observation pulse. In addition, the question of which $90°$ pulse to choose as the slice selection pulse needs to be addressed. It is assumed that the observation pulse may be the most suitable candidate for the slice selection pulse. In this case, the violation of the hard pulse condition is during the last RF pulse, affecting only the transformations $\hat{T}_{3\pm3} \rightarrow \hat{T}_{3-1}$ and $\hat{T}_{1\pm1} \rightarrow \hat{T}_{1-1}$ (Figure 3.14).

The acquisition of pseudo 2D images has its drawbacks and limitations. While homogeneous phantoms in cylindrical containers can be measured in the homogeneous excitation region in the birdcage coil without major concern, issues arise when acquiring pseudo 2D images of tissues *in vivo* in two aspects.

(1) TASTI images in rat head were acquired using the ^{23}Na saddle coil with a inhomogeneous B_1 profile. The TQ signal S_{TQ} is very sentitive to B_1^+ (Hancu et al., 1999). It depends on the flip angles θ_{1-3} of the three pulses such that

$$S_{\mathrm{TQ}} \propto \sin\theta_1 \sin^2\theta_2 \sin^2\theta_3 \ , \tag{5.1}$$

if a $180°$ refocussing pulse is not applied after the first pulse. The maximum TQ signal is obtained if $\theta_1 = \theta_2 = \theta_3 = 90°$. A deviation of the flip angle by $30°$ would lead to a loss of approximately 50% of the maximum TQ signal. The double flip angle method (Insko and Bolinger, 1993) and the phase-sensitive method (Morrell, 2008) can be applied to acquire B_1^+ maps. The B_1^+ map can then be used as input for Equation 5.1, with which the influence of B_1^+ inhomogeneities on the TQ signal can be correted for. The B_1^- inhomogeneities can be corrected using the reciprocity principle.

(2) If the readout gradient is set to zero in any direction, heterogeneous tissue signals of various organs along this direction are summed up indiscriminately. To investigate whether pseudo 2D TASTI images along any of the three directions may differentiate the brain, pseudo 2D DA-R images in the rat head were consulted. They revealed that in a transverse slice the signals of the eyes overlapped with signals from the brain. In the sagittal slice, an overlap was found with signals from the cheek tissue to either side of the brain. In the coronal slice, signals from the skin and tissue overlapped with signals from the brain. However, this contribution was much smaller than the contribution from the cheek tissue in the sagittal slice. Additionally, signals from the region below the brain might contribute as well. 3D ^{23}Na DA-R images in rat as shown in Figure 4.10 revealed that the sensitivity region of the coil extends maximum $35\,\mathrm{mm}$ in depth, though this number depends on many factors including coil loading. This depth extends beyond the sum of the skull thickness and the superior-inferior brain thickness of approximately $10\,\mathrm{mm}$ (Gefen et al., 2003). Therefore head tissue below the brain most likely contributes to signals in the brain in the coronal view. However, it lies farther away from the sensitivity center of the coil, in which the RF flip angles are reduced. The contribution may be very small, though the exact amount needs to be determined in additional reference studies. As of now, the contribution from signals in the brain may be assumed to be predominant in the ROI of the brain.

Application in Rat Head

The possibility to acquire a SQ image, a TQ image, a $S_{\mathrm{T/S}}$ map, a $T_{2\mathrm{s}}$ map and a $T_{2\mathrm{f}}$ map from one dataset in one measurement *in vivo* was demonstrated. Localized $S_{\mathrm{T/S}}$ ratios and $T_{2\mathrm{s,f}}$ values were determined in the entire head, in the brain, in the olfactory bulb and in the eyes. Based on the results from phantom experiments, an optimal TE to obtain the maximum TQ signal in rat head should be used. However, given the very low in vivo SNR and a sodium concentration of only $(45 \pm 5)\,\mathrm{mM}$ in rat brain (Christensen et al., 1996), a TE of $1\,\mathrm{ms}$ was chosen in favor of a higher overall signal.

The TASTI $S_{\mathrm{T/S}}^{\mathrm{head}}$ ratio was in agreement with the TQ-TPPI $S_{\mathrm{T/S}}^{\mathrm{head}}$ ratio. It follows that, given the application of the relaxation time correction, the TASTI method can be used to determine the $S_{\mathrm{T/S}}$ ratio in rat head *in vivo*. Even though the ratio in the entire head was confirmed with the TQ-TPPI ratio, it cannot be directly followed that the TASTI $S_{\mathrm{T/S}}$ ratio in any voxel is necessarily truthful. This should be kept in mind when discussing the local $S_{\mathrm{T/S}}$ ratios as well as parameters derived therefrom.

Another observation was that the relaxation times $T_{2\mathrm{s,f}}$ and the fraction b of the fast relaxaing component in the entire head and in the brain were in agreement within the margin of error. Yet, their corrected $S_{\mathrm{T/S}}$ ratios were not in agreement, with the $S_{\mathrm{T/S}}^{\mathrm{head}}$ higher than the $S_{\mathrm{T/S}}^{\mathrm{brain}}$ by $50\,\%$. This result is especially interesting as it highlights the differences between the underlying mechanisms responsible for the bi-exponential T_2 relaxation and for the creating of detectable TQ signal with correlation times in the range of ms. It underlines the fact that fast bi-exponential T_2 relaxation is a necessary yet not sufficient prerequisite for the detection of TQ signals. The bi-exponential T_2 relaxation is a result of the nuclear spin of $3/2$, whose theory predicts such behavior. On the other hand, TQ signals arise due to the very transient interactions between the charged spin-$3/2$ nuclei and the oppositely charged interaction sites within macromolecules. It follows that compared with the head average, there may be fewer such interaction sites in the brain with interaction time in the order of ms. However, influence on the $S_{\mathrm{T/S}}$ ratio by other physiological parameters such as the Na$^+$ concentration cannot be excluded.

The measured $S_{\mathrm{T/S}}$ ratios are the ratios between the total TQ signal $\mathrm{TQ}_{\mathrm{total}}$ and the total SQ signal $\mathrm{SQ}_{\mathrm{total}}$. This ratio can be further broken down into the ratio betwen the intracellular TQ signal TQ_i and the intracellular SQ signal SQ_i, and between the extracellular TQ signal TQ_e and the extracellular SQ signal SQ_e. Moreoever, the ratios between TQ_i and $\mathrm{SQ}_{\mathrm{total}}$ as well as between TQ_e and $\mathrm{SQ}_{\mathrm{total}}$ can be calculated. To do so, the relations $\mathrm{SQ}_i/\mathrm{SQ}_e$ and $\mathrm{TQ}_i/\mathrm{TQ}_e$ are established. The calculation steps are detailed in the following.

1. The assumption made in the earlier days of ^{23}Na NMR on the MR invisibility of certain Na$^+$ ions in biological tissues was overturned, and as of now there is no evidence suggesting that there are Na$^+$ ions not detectable by the NMR signal (Burstein and Springer, 2019; Hu et al., 2019; Thulborn, 2018). Therefore, the total SQ signal $\mathrm{SQ}_{\mathrm{total}}$ comprises the intra- and extracellular contributions such that $\mathrm{SQ}_{\mathrm{total}} = \mathrm{SQ}_i + \mathrm{SQ}_e$. Furthermore, the SQ signal is proportional to the sodium content in the respective compartment. The ratio between the intra- and the extracellular sodium content under physiological conditions can be calculated as follows (Schepkin et al., 1998): The intra- and extracellular sodium concentrations are $\sim 15\,\mathrm{mM}$ and $\sim 140\,\mathrm{mM}$, respectively. The intra- and extracellular volume fractions, on the other hand, are $85\,\%$ and $15\,\%$, respectively. Therefore, the intra- and extracellular sodium contents, as in absolute amounts, are $37.8\,\%$ and $62.2\,\%$ of the total sodium content, respectively. It yields
$$\frac{\mathrm{SQ}_i}{\mathrm{SQ}_e} = \frac{0.378}{0.622} = 0.608\ . \tag{5.2}$$

2. The $\mathrm{TQ}_{\mathrm{total}}$ comprises the intra- and extracellular contributions such that $\mathrm{TQ}_{\mathrm{total}} = \mathrm{TQ}_i + \mathrm{TQ}_e$ due to non-averaged quadrupolar interactions inside and outside the cells (Jelicks and Gupta, 1993; Rooney and Springer, 1991; Schepkin et al., 1996). The possibility to differentiate between the intra- and extracellular TQ signal contribution using TQ spectroscopy has been demonstrated independently by many groups. In detail, the ratio $\mathrm{TQ}_i/\mathrm{TQ}_e$ between the intra- and extracellular TQ signal was calculated in perfused rat hearts (Dizon et al., 1996; Jelicks and Gupta, 1993; Schepkin et al., 1996, 1998), in the perfused mouse heart (Eykyn et al., 2015), in the *in situ* rat liver (Seshan et al., 1997), in rat brain tumor (Winter and Bansal, 2001) and in suspesions of human red blood cells (Knubovets et al., 1998). The contribution of the extracellular TQ signal to the total TQ signal was found to

be in the range of $40 - 70\,\%$. The lower and the upper limits of

$$\frac{\mathrm{TQ}_i}{\mathrm{TQ}_e} = \frac{0.3}{0.7} \text{ and } \frac{\mathrm{TQ}_i}{\mathrm{TQ}_e} = \frac{0.6}{0.4}\,, \tag{5.3}$$

respectively, were used for the estimation.

3. From 1. and 2. it follows that the measured $S_{\mathrm{T/S}}$ ratio can be broken down into

$$S_{\mathrm{T/S}} = \frac{\mathrm{TQ}_{\mathrm{total}}}{\mathrm{SQ}_{\mathrm{total}}} = \frac{\mathrm{TQ}_i + \mathrm{TQ}_e}{\mathrm{SQ}_i + \mathrm{SQ}_e}\,. \tag{5.4}$$

4. By substituting TQ_e and SQ_e with TQ_i and TQ_i in Equation 5.4, respectively, the ratio $\mathrm{TQ}_i/\mathrm{SQ}_i$ can be calculated. And with analogous substitution, the ratio $\mathrm{TQ}_e/\mathrm{SQ}_e$ can be calculated. The ratios $\mathrm{TQ}_i/\mathrm{SQ}_i$ and $\mathrm{TQ}_e/\mathrm{SQ}_e$ indicate the percentage of Na^+ ions contributing to TQ signal relative to the total Na^+ content in either intra- or extracellular compartment. Not breaking down the $\mathrm{SQ}_{\mathrm{total}}$ into SQ_i and SQ_e, the ratios $\mathrm{TQ}_i/\mathrm{SQ}_{\mathrm{total}}$ and $\mathrm{TQ}_e/\mathrm{SQ}_{\mathrm{total}}$ are obtained.

The calculations were carried out for the entire head and the brain with inputs from Table 4.10, and the results are listed in Table 5.1. The olfactory bulb was omitted to shift the focus to the entire head and the brain. The corresponding organ in human is, relative to the rest of the brain, much less developed than in rat and offered no transferable medical value.

Table 5.1: Ratios between the between the intracellular TQ signal TQ_i and the intracellular SQ signal SQ_i, between the extracellular TQ signal TQ_e and the extracellular SQ signal SQ_e, between the intracellular TQ signal TQ_i and the total SQ signal $\mathrm{SQ}_{\mathrm{total}}$, as well as between the extracellular TQ_e and the total SQ signal $\mathrm{SQ}_{\mathrm{total}}$. All ratios are given in %. The estimation range is a consequence of the $\mathrm{TQ}_i/\mathrm{TQ}_e$ range from literature given in Equation 5.3.

	$\mathrm{TQ}_{\mathrm{total}}/\mathrm{SQ}_{\mathrm{total}}$	$\mathrm{TQ}_i/\mathrm{SQ}_i$	$\mathrm{TQ}_e/\mathrm{SQ}_e$	$\mathrm{TQ}_i/\mathrm{SQ}_{\mathrm{total}}$	$\mathrm{TQ}_e/\mathrm{SQ}_{\mathrm{total}}$
head	8.7 ± 3.5	$\mathbf{7.2}$ to 3.6	$\mathbf{5.6}$ to 7.7	$\mathbf{5.2}$ to 2.6	$\mathbf{3.5}$ to 6.1
brain	5.9 ± 3.9	$\mathbf{4.9}$ to 2.4	$\mathbf{3.8}$ to 6.6	$\mathbf{3.5}$ to 2.4	$\mathbf{1.8}$ to 4.2

The ratio between $\mathrm{TQ}_i/\mathrm{SQ}_i$ *and* $\mathrm{TQ}_e/\mathrm{SQ}_e$ has been interpreted by literature as a measure of whether TQ signal is intracellular-sensitive. For instance, if $\mathrm{TQ}_i/\mathrm{SQ}_i = \mathrm{TQ}_e/\mathrm{SQ}_e$, then Na^+ ions contributes to the same amount of TQ signals relative to the total pool of Na^+ within either compartment. Equally if $\mathrm{TQ}_i/\mathrm{SQ}_i > \mathrm{TQ}_e/\mathrm{SQ}_e$, the TQ signal can be interpreted as intracellular-sensitive. Our study is limited in the sense that it makes no prediction about this interpretation and currently relies on $\mathrm{TQ}_i/\mathrm{TQ}_e$ ratios from literature to estimate $\mathrm{TQ}_i/\mathrm{SQ}_i$ and $\mathrm{TQ}_e/\mathrm{SQ}_e$. Therefore in line with the calculation method suggested above, the interpretation of the TQ signal being more sensitive in either compartment solely relies on Equations 5.2 and 5.3. The ratio between $\mathrm{TQ}_i/\mathrm{SQ}_i$ and $\mathrm{TQ}_e/\mathrm{SQ}_e$ falls in the range of $0.5 - 1.3$ and may reflect on the diversity of the macromolecular composition and ion content in different cell types. To more accurately estimate the ratios in Table 5.1, it is therefore essential to perform additional experiments to determine the ratios in Equations 5.2 and 5.3 in rat brain.

Among the studies that have made estimations for $\mathrm{TQ}_i/\mathrm{TQ}_e$, the study by Winter and Bansal (2001) on rat brain tumor cells with a extracellular contribution of $40\,\%$ might be closest in representing healthy brain cells. The calculated ratios using this value are marked in bold in Table 5.1. Under this assumption, ratio between $\mathrm{TQ}_i/\mathrm{SQ}_i$ and $\mathrm{TQ}_e/\mathrm{SQ}_e$ is estimated to be 1.3. Care must be taken though, as TQ signal has been shown to decrease in turmor by Fiege et al. (2013) due to the effect of a more acqueous intracellular compartment with reduced macromolecular concentration overshadowing the increase in intracellular sodium content.

This calculation method is limited by its assumptions. The first assumption in Equation 5.2 is based on a fixed intra- and extracellular sodium concentration and volume fraction. Both the concentration and volume fractions depend on the cell type and especially the pathological state. If an animal model with a certain disease is used and the TASTI method is applied, then the quantification of the ratios in diseased and healthy tissues will require two sets of concentration and volume fractions. This is problematic for two reasons. One, the factions might depend on the disease progression. Two, using different fractions will introduce *a priori* bias to the results in the way that the investigators will detect what they intended to find.

The second assumption in Equation 5.3 is based on the intra- to extracellular TQ signal fractions determined by previous studies. Using these fractions introduce bias in the same way as using the fixed intra- and extracellular sodium concentration and volume fraction. Additionally, the available fractions were determined predominantly in perfused rat hearts. The intra- and extracellular physiological environment of cardiac myocytes are different from those of cells in the brain, which in themselves comprise a variety of cells with different properties.

Comparison with Existing TQ Imaging Methods

Early efforts of TQ NMR were partially driven by the prospect of becoming an intracellular-sensitive and shift reagent-free method (Dizon et al., 1996; Schepkin et al., 1996, 1998). The intracellular-sensitivity of the TQ signal is motivated as follows. The extracellular Na^+ content (not concentration, see Equation 5.2) is high, yet there are few proteins in the extracellular space. The intracellular space has a relatively speaking lower Na^+ content and yet an abundance of proteins and therefore quadrupolar interaction sites. If the extracellular molecular and ion composition is kept constant, i.e. in perfused organs, then changes in the ^{23}Na TQ signal can be attributed to changes of the intracellular TQ signal. In diseased tissue, the TQ signal strength may be different due to changes in the molecular composition and ion content. Therefore, changes on the most fundamental level of a disease may be detected as changes in the strength and the correlation times of the localized ^{23}Na TQ signals (Griffey et al., 1990).

In general, all TQ imaging methods suffer from inherently low SNR and low spatial resolutions. If conventional TQ filtering is applied, then the a 6-step RF phase cycling scheme is used. This means that to acquire a TQ image with otherwise identical sequence parameters as a SQ image, the measurement time is multiplied by 6. In clinical settings, high SAR as a result of three consecutive RF pulses is highly problematic. To reduce SAR, the TR needs to be further extended, thereby further increasing the measurement time.

Existing TQ imaging methods include TQ filters extended with Cartesian sampling (Fleysher et al., 2013; Petracca et al., 2016b), twisted projection sampling (Borthakur et al., 1999; Hancu et al., 1999; LaVerde et al., 2007; Tsang et al., 2012), and spiral sampling (Mirkes et al., 2016). These methods will be referred to as TQ filtered imaging. TQ filters do not separate between the SQ and the TQ signal, therefore it is crucial that the SQ signal contributions undergo coherence pathways that lead to their cancellation. Any coherence different from TQ coherence that has not been filtered out will be misinterpreted as TQ signals. Moreoever, TQ imaging methods with TQ filters are especially sensitive to B_0 off-resonances and B_1^+ inhomogeneities (Matthies et al., 2010; Mirkes et al., 2016; Tanase and Boada, 2005). Any loss of the intrisincally low TQ signal can be detrimental. Several methods have been proposed to correct for B_0 off-resonances by extending the 6-step phase cycle to a 12/24-step phase cycle, thought with only a small or no SNR gain (Fleysher et al., 2010; Matthies et al., 2010; Tanase and Boada, 2005).

Additionally, *in vivo* relaxation times are required to calculate the fixed $t_{\text{evo,opt}}$. As *in vivo* T_2 mapping is very time consuming, literature is generally consulted instead, which can be a source of error. The contrast between different organs in the TQ image therefore depends on t_{evo}. Most importantly, the causes for TQ signal changes in a certain tissue cannot be unambiguously attributed to changes in relaxation times or changes regarding the quadrupolar interaction sites. For instance, an increase in relaxation times will yield a smaller $t_{\text{evo,opt}}$ of the tissue, which will result in either an increase or decrease of the measured TQ signal depending on the value of the fixed sequence parameter $t_{\text{evo,opt}}$.

A recently proposed TQ imaging method termed SISTINA was developed by (Fiege et al., 2013) with the aim to simultaneously acquire SQ and TQ images. This sequence follows a similar aim to the TASTI sequence and will be discussed in more detail. SISTINA acquires multiple TQ images with Cartesian sampling at different TE after the third RF pulse. In addition, it incoorporates a UTE readout with subsequent gradient rewinding after the first RF pulse. As such, SISTINA is able to acquire one SQ and several TQ images. The name of the sequence includes the description 'simultaneous'. However, this is up to debate as the the acquisition of the SQ image preceeds that of the TQ images, albeit within the same TR. The conditions under which SQ and TQ images are acquired are not identical. Moreoever, the SQ and TQ images were sampled with different k-space trajectories. Therefore any quantitative referencing of the TQ image(s) to the SQ image must be treated with care. The SISTINA sequence uses a 2×6-step phase cycling and therefore requires double the measurement time of a TQ filtering imaging sequence using the 6-step phase cycling. The investigators used the SQ image to calculate a TSC map. It is not clear whether a separate SQ image acqusition combined with a 6-step phase cycling TQ imaging sequence might yield similar results while saving time.

The TASTI method developed in this thesis addresses the majority of the above mentioned limitations faced by TQ filtered imaging and SISTINA. In addition to the improvement in the general limitations of TQ imaging, the TASTI method offers multiple novel features. The improvements and new possibilities are:

1. The TASTI sequence acquires SQ and TQ signals simultaneously after the last RF pulse and separates them by frequency. The low intrinsic TQ signal is therefore superimposed by the much higher SQ signal, allowing for better distinction between TQ signals and noise.
2. The SQ and TQ images are acquired under identical conditions with the same k-space trajectories and gridding algorithms. It facilitates quantitative comparisons between both images. With the appropriate setup (see limitations in the list below), a TSC map can be calculated from the SQ image.
3. In addition to SQ and TQ images, $T_{2\text{s}}$, $T_{2\text{f}}$ and $S_{\text{T/S}}$ parameter maps are acquired in the same measurement session and based on the same data set using the TASTI sequence. Each voxel is described by one t_{evo}-FID that contains information about the SQ and TQ signal intensities and relaxation properties. So far, no other sequence has demonstrated the ability to obtain these images and parameter maps in one measurement.
4. The $S_{\text{T/S}}$ ratios in different tissues can be corrected for relaxation effects based on $T_{2\text{s,f}}$ determined in the same tissue. Under certain assumptions, the $S_{\text{T/S}}$ ratio can be used to estimate (i) the ratio between the TQ and SQ signal in the intracellular space, (ii) the ratio between the TQ and SQ signal in the extracellular space, (iii) the ratio between the intracellular TQ signal and the total SQ signal, and (iv) the ratio between the extracellular TQ signal and the total SQ signal.

Limitations of the TASTI imaging setup in the current state as well as possible areas for improvement are:

1. The major limitation factor is the prolonged measurement time due to the minimum of 1×8-step phase cycling. The prolonged measurement time makes the acquisition of high resolution *in vivo* 3D images in any reasonable time frame impossible. This results in pseudo 2D imaging to be the more viable option currently. The interpretation of pseudo 2D images and parameter maps is, however, based on many assumptations and therefore sources of error.
2. A B_0 and B_1^+ correction pipeline does not exist yet despite the dire need in light of the saddle coil setup. The currently available ^{23}Na volume coil would be a huge improvement to B_0 off-resonances. However it is not matched to the geometry and load of the rat and cannot be used for TQ imaging due to the low sensitivity. A transmit-and-receive-only setup in which RF signals are sent with a volume coil and received with a separate surface coil may increase SNR gain and bring about improvement regarding the B_0 and B_1^+ inhomogeneities.

6 Conclusion and Outlook

Currently, ^{23}Na NMR methods aim at uncovering an unambiguous link between the physiological role of Na^{+} ions in diseases and the translation of the accompanying metabolic changes on a microscopic level to macroscopically detectable physical signals. The major approaches to accomplish this goal include:

1. TQ spectra and images are acquired with the goal of relating quadrupolar interaction properties of Na^{+} to changes in the molecular composition.
2. The total sodium content is quantified in SQ imaging with the goal to obtain gold-standard biomarkers in clinical diagnosis.
3. The relaxation times $T_{2\mathrm{s}}$ and $T_{2\mathrm{f}}$ are mapped to organs of interest with the goal of relating changes of these values in diseases to variation in the metabolic compositions on a cellular level.
4. Quantitative measures such as concentration are separated into intra- and extracellular equivalents with the goal of direct monitoring of the physiologically and medically more relevant intracellular space.

The **major goal** of this thesis was to develop an MR method that combines the perspectives and goals of the four major approaches. This method was named the TASTI sequence, short for **t**riple- **a**nd **s**ingle-quantum **T**PPI **i**maging. By combining the TQ-TPPI RF pulse scheme and the DA-R imaging module, the sequence aims at acquiring SQ and TQ images as well as $T_{2\mathrm{s,f}}$ and $S_{\mathrm{T/S}}$ maps under identical conditions in one single measurement. This goal is achieved by simultaneously acquiring a 3D dataset in which the SQ image and the TQ image are separated in the MQ frequency domain. In the same dataset an FID composed of SQ and TQ relaxation contributions is assigned to each image voxel. From this FID the relaxation times $T_{2\mathrm{s,f}}$ and the ratio $S_{\mathrm{T/S}}$ between the TQ and the SQ signal can be computed for voxel-wise mapping. Based on additional assumptions, the $S_{\mathrm{T/S}}$ ratio can be used to estimate the separate ratios reflecting the quadrupolar interaction affinity in the intra- and extracellular space. The sequence has been verified in phantom studies and applied to *in vivo* rat head imaging at a $9.4\,\mathrm{T}$ preclinical MR scanner.

In other words, the following possibilities have been achieved with the TASTI sequence (in reference to the list above):

1. The TQ image is acquired simultaneously and under identical conditions to the SQ image. The signal acquisition therefore benefits immensely from the additional SQ signals. This feature is an answer to the hurdle faced by conventional TQ imaging, which acquires only the intrinsically low TQ signals. Furthermore, it has unlocked the possibility to map the relative strength between the TQ and the SQ signals by fitting $S_{\mathrm{T/S}}$. No other established method has previously demonstrated this feature.
2. Though not demonstrated explicitly within the current experimental setup, the SQ image can be used to quantify TSC with additional reference phantoms and, depending on the coil, B_0 and B_1 corrections. The additional procedures are well documented in literature and are thus not expected to encounter major issues.

3. $T_{2\mathrm{s}}$ and $T_{2\mathrm{f}}$ values can be calculated for individual voxels. Therefore, mapping is accomplished within the same measurement and does not require an additional localized spin echo measurement, which is on its own a very time-consuming task. Local changes in relaxation times and the fraction b of the fast relaxing component can indicate changes in the molecular composition. For instance, a decrease in b may indicate that the environment has become more acqueous, i.e. due to cell swelling, while a decrease in $T_{2\mathrm{f}}$ may indicate an increase in the availability of quadrupolar interaction sites. These changes can be additionally compared with possible changes of $S_{\mathrm{T/S}}$. For instance if a decrease in b is not accompanied with an increase in $S_{\mathrm{T/S}}$, then it may offer insight into the composition of the additional quadrupolar interaction sites. They are likely to consist of charged ions instead of charged macromolecules, as only the latter will give rise to TQ signals. The possibility of $T_{2\mathrm{s,f}}$ mapping in combination with the other outputs enables further investigation of these indications.
4. Under assumptions about the distribution of the total sodium content and the distribution of the TQ signal fractions in the intra- and extracellular space, the $S_{\mathrm{T/S}}$ quantified in individual organs can be used to estimate the TQ signal strength relative to the available Na^{+} in either space. This feature can lay the foundation to motivate spectroscopic studies of the intracellular TQ signal fraction in more diverse cell types.

Given the possibilities shown above, the TASTI sequence was sucsessfully applied to rat head *in vivo*. Its applicability in rat brain with low total sodium content was demonstrated. The $T_{2\mathrm{s,f}}$ and $S_{\mathrm{T/S}}$ parameter maps revealed local differences matching the expected value distribution in different head regions. Furthermore, a localized relaxation-corrected ratio of $S_{\mathrm{T/S}}^{\mathrm{brain}} = (5.9 \pm 3.9)\,\%$ was determined for the first time in rat brain. Based on this result, separate ratios between the TQ and SQ signal fractions were estimated in the intra- and extracellular space.

In addition to the cation Na^{+}, MR experiments on the anion Cl^{-} have also been carried out with the goal to illuminate physiological changes from a differently poled perspective. With each ion involved in different, yet equally vital tasks on the cellular level, their roles in biological processes are best understood in combination. Therefore, the **minor goal** of this thesis was to evaluate the feasibilities of $^{35}\mathrm{Cl}$ imaging and TQ spectroscopy alongside $^{23}\mathrm{Na}$ imaging and TQ spectroscopy.

Two steps were undertaken. In the first step, the DA-R imaging sequence was implemented at a preclinical scanner. The DA-R sequence has previously proven its superiority in terms of SNR and image quality over radial sequences with constant imaging gradients. $^{35}\mathrm{Cl}$ imaging in agarose phantoms achieved an SNR gain of up to $38\,\%$, if the k-space was sampled with density-adapted gradients. This translates to a $47\,\%$ measurement time reduction if the same SNR is to be achieved with constant readout gradients. Furthermore, $^{35}\mathrm{Cl}$ imaging in resolution phantoms demonstrated superior image quality, noise behavior and higher capability to resolve smaller structures compared with the standard radial imaging sequence provided by the vendor. Furthermore, it was free of undersampling aliasing and Gibbs ringing, both of which negatively affected the quality of the images acquired with the standard radial sequence. If undersampling is applied to an object of the appropriate geometry, the DA-R sequence can save measurement time by up to 76%. Images in the bioreactor showed that both compartments were well distinguished, allowing for future studies using one compartment as the control and the other as the test chamber. In high SNR $^{23}\mathrm{Na}$ images acquired in short measurement times in rat head and rat torso, different parts of the brain, different tissues inside the eyes, cartilage, skin and myocardium were distinctive. $^{35}\mathrm{Cl}$ images required longer measurement times and had lower SNR. Nevertheless they allowed the distinction of the eyes, the brain and the heart.

In the second step, $^{23}\mathrm{Na}$ and $^{35}\mathrm{Cl}$ TQ-TPPI spectra were acquired in phantoms, the bioreactor and rat head. In agarose phantoms, a $S_{\mathrm{T/S}}$ in a similar range was measured at both the ^{23}Na and the ^{35}Cl frequencies. Due to the small fraction of the cells of $2.7\,\%$relative to the bioreactor volume, the ratio of $S_{\mathrm{T/S}}^{\mathrm{Na}} = (0.4 \pm 0.1)\,\%$ was measured. The measured $S_{\mathrm{T/S}}^{\mathrm{Cl}} = (5.1 \pm 3.0)\,\%$ was unexpectedly higher than the ^{23}Na ratio, therefore it needs further experiments to confirm. A disinctive TQ peak of $S_{\mathrm{T/S}}^{\mathrm{Na}} = (8.9 \pm 0.5)\,\%$ was measured in rat head, whereas it was 8.9 times lower in the ^{35}Cl measurement with $S_{\mathrm{T/S}}^{\mathrm{Cl}} = (1.0 \pm 0.5)\,\%$. This discrepancy *in vivo* is explained by the fact that Na^{+} ions can interact with an abundance of negatively charged quadrupolar interaction sites in macromolecules, resulting in TQ signals with an interaction time in the detectable range of a few ms. On ther other hand, Cl^{-} ions are abundant in the extracellular space, where proteins are few. Therefore, they have fewer positively charged interaction sites, resulting in less TQ signal.

The DA-R and TQ-TPPI results confirm the difficulties of *in vivo* ^{35}Cl NMR experiments in comparison to ^{23}Na. Nevertheless, ^{35}Cl imaging allows for the distinction of important anatomical features despite its lower spatial resolution. The ^{35}Cl TQ signal was small yet significant. Therefore, adding ^{35}Cl imaging and spectroscopy to ^{23}Na studies would offer an alternative perspective on the intricate physiological processes in healthy and diseased tissues.

In conclusion, a DA-R imaging sequence with excellent image quality and superior measurement time efficiency was implemented at a preclinical scanner, thereby paving the road to future ^{23}Na and ^{35}Cl studies in animal models. Such studies can be accompanied by global TQ-TPPI spectroscopy, which can detect changes in the quadrupolar interactions of both Na^{+} and Cl^{-} ions, reflecting on the molecular and ionic compositions on a cellular level. The advantages of DA-R and TQ-TPPI were combined to create the TASTI sequence. It acquires SQ and TQ images as well as $T_{\mathrm{2s,f}}$ and $S_{\mathrm{T/S}}$ maps under identical condition in one single measurement. With its ability to analyze local changes in ion content, relaxation time and TQ signal, the TASTI sequence has the potential to become the one tool to combine all major approaches to address ^{23}Na NMR.

Bibliography

Alvarez-Leefmans, F. J. (2012). *Chapter 15 - Intracellular Chloride Regulation*, pages 221–259. Academic Press, San Diego.

An, H., Ford, A. L., Eldeniz, C., Chen, Y., Vo, K. D., Zhu, H., Powers, W. J., Lin, W., and Lee, J.-M. (2016). Reperfusion beyond 6 hours reduces infarct probability in moderately ischemic brain tissue. *Stroke*, 47(1):99–105.

Andersen, O. S. (2013). *Cellular Electrolyte Metabolism*, pages 580–587. Springer New York, New York, NY.

Andrasko, J. (1974). Nonexponential relaxation of 23na+ in agarose gels. *Journal of Magnetic Resonance (1969)*, 16(3):502–504.

Baier, S., Kraemer, P., Grudzenski, S., Fatar, M., Kirsch, S., and Schad, L. R. (2014). Chlorine and sodium chemical shift imaging during acute stroke in a rat model at 9.4 tesla. *Magnetic Resonance Materials in Physics, Biology and Medicine*, 27(1):71–79.

Bain, A. D. (1980). A superspin analysis of two-dimensional ft nmr experiments. *Journal of Magnetic Resonance (1969)*, 39(2):335–342.

Bain, A. D. (1984). Coherence levels and coherence pathways in nmr. a simple way to design phase cycling procedures. *Journal of Magnetic Resonance (1969)*, 56(3):418–427.

Bain, A. D. and Martin, J. S. (1978a). Ft nmr of nonequilibrium states of complex spin systems. i. a lionville space description. *Journal of Magnetic Resonance (1969)*, 29(1):125–135.

Bain, A. D. and Martin, J. S. (1978b). Ft nmr of nonequilibrium states of complex spin systems. ii. weakly coupled systems. *Journal of Magnetic Resonance (1969)*, 29(1):137–150.

Bartha, R., Megyesi, J., and Watling, C. (2008). Low-grade glioma: correlation of short echo time 1h-mr spectroscopy with 23na mr imaging. *American Journal of Neuroradiology*, 29(3):464–470.

Bertleff, M. (2018). *Characterization of microstructures with diffusion MRI: pore imaging implementation at preclinical 9.4T and robust IVIM-Kurtosis evaluation at clinical 3T and 7T systems.* Thesis.

Bloch, F. (1953). The principle of nuclear induction. *Science*, 118:425–430.

Boada, F. E., Qian, Y., Nemoto, E., Jovin, T., Jungreis, C., Jones, S., Weimer, J., and Lee, V. (2012). Sodium mri and the assessment of irreversible tissue damage during hyper-acute stroke. *Translational stroke research*, 3(2):236–245.

Bodenhausen, G. (2011). Reflections of pathways: a short perspective on 'selection of coherence transfer pathways in nmr pulse experiments'. *J Magn Reson*, 213(2):295–7.

Bodenhausen, G., Kogler, H., and Ernst, R. R. (1984). Selection of coherence-transfer pathways in nmr pulse experiments. *Journal of Magnetic Resonance (1969)*, 58(3):370–388.

Bodenhausen, G., Vold, R. L., and Vold, R. R. (1980). Multiple quantum spin-echo spectroscopy. *Journal of Magnetic Resonance*, 37(1):93–106.

Borthakur, A., Hancu, I., Boada, F. E., Shen, G. X., Shapiro, E. M., and Reddy, R. (1999). In vivo triple quantum filtered twisted projection sodium mri of human articular cartilage. *Journal of Magnetic Resonance*, 141(2):286–290.

Bowden, G. J., Hutchison, W. D., and Khachan, J. (1986). Tensor operator formalism for multiple-quantum nmr. 2. spins 32, 2, and 52 and general i. *Journal of Magnetic Resonance (1969)*, 67(3):415–437.

Burstein, D. and Springer, C. S., J. (2019). Sodium mri revisited. *Magn Reson Med*, 82(2):521–524.

Christensen, J. D., BarrÃšre, B. J., Boada, F. E., Vevea, J. M., and Thulborn, K. R. (1996). Quantitative tissue sodium concentration mapping of normal rat brain. *Magnetic Resonance in Medicine*, 36(1):83–89.

Constantinides, C. D., Kraitchman, D., O'Brien, K., Boada, F., Gillen, J., and Bottomley, P. A. (2001). Noninvasive quantification of total sodium concentrations in acute reperfused myocardial infarction using 23na mri. *Magnetic Resonance in Medicine*, 46(6):1144–1151.

Damadian, R. (1971). Tumor detection by nuclear magnetic resonance. *Science*, 171(3976):1151–1153.

Davids, M., Zoellner, F. G., Ruttorf, M., Nees, F., Flor, H., Schumann, G., and Schad, L. R. (2014). Fully-automated quality assurance in multi-center studies using mri phantom measurements. *Magnetic Resonance Imaging*, 32(6):771–780.

De Graaf, R. A. (2007). *In Vivo NMR Spectroscopy: Principles and Techniques*. John Wiley & Sons, 2 edition.

Dizon, J. M., Tauskela, J. S., Wise, D., Burkhoff, D., Cannon, P. J., and Katz, J. (1996). Evaluation of triple-quantum-filtered 23na nmr in monitoring of intracellular na content in the perfused rat heart: Comparison of intra- and extracellular transverse relaxation and spectral amplitudes. *Magnetic Resonance in Medicine*, 35(3):336–345.

Drobny, G., Pines, A., Sinton, S., Weitekamp, D. P., and Wemmer, D. (1978). Fourier transform multiple quantum nuclear magnetic resonance. *Faraday Symposia of the Chemical Society*, 13(0):49–55.

Dubbers, D. and Stoeckmann, H.-J. (2013). *Quantum Physics: The Bottom-Up Approach: From the Simple Two-Level System to Irreducible Representations*. Springer.

Eisele, P., Konstandin, S., Griebe, M., Szabo, K., Wolf, M. E., Alonso, A., Ebert, A., Serwane, J., Rossmanith, C., and Hennerici, M. G. (2016). Heterogeneity of acute multiple sclerosis lesions on sodium (23na) mri. *Multiple Sclerosis Journal*, 22(8):1040–1047.

Eisele, P., Konstandin, S., Szabo, K., Ebert, A., Rossmanith, C., Paschke, N., Kerschensteiner, M., Platten, M., Schoenberg, S. O., Schad, L. R., and Gass, A. (2019). Temporal evolution of acute multiple sclerosis lesions on serial sodium (23na) mri. *Multiple Sclerosis and Related Disorders*, 29:48–54.

Elabyad, I. A., Kalayciyan, R., Shanbhag, N. C., and Schad, L. R. (2014). First in vivo potassium-39 (39k) mri at 9.4 t using conventional copper radio frequency surface coil cooled to 77 k. *IEEE Trans Biomed Eng*, 61(2):334–45.

Engstroem, S., Joensson, B., and Impey, R. W. (1984). Molecular dynamic simulation of quadrupole relaxation of atomic ions in aqueous solution. *The Journal of Chemical Physics*, 80(11):5481–5486.

Ernst, R. R., Bodenhausen, G., and Wokaun, A. (1987). *Principles of Nuclear Magnetic Resonance in One And Two Dimensions*. Clarendon Press.

Eykyn, T. R., Aksentijevic, D., Aughton, K. L., Southworth, R., Fuller, W., and Shattock, M. J. (2015). Multiple quantum filtered (23)na nmr in the langendorff perfused mouse heart: Ratio of triple/double quantum filtered signals correlates with [na]i. *J Mol Cell Cardiol*, 86:95–101.

Fiege, D. P., Romanzetti, S., Mirkes, C. C., Brenner, D., and Shah, N. J. (2013). Simultaneous single-quantum and triple-quantum-filtered mri of 23na (sistina). *Magn Reson Med*, 69(6):1691–6.

Fleysher, L., Oesingmann, N., Brown, R., Sodickson, D. K., Wiggins, G. C., and Inglese, M. (2013). Noninvasive quantification of intracellular sodium in human brain using ultrahigh-field mri. *NMR Biomed*, 26(1):9–19.

Fleysher, L., Oesingmann, N., and Inglese, M. (2010). B(0) inhomogeneity-insensitive triple-quantum-filtered sodium imaging using a 12-step phase-cycling scheme. *NMR Biomed*, 23(10):1191–8.

Gefen, A., Gefen, N., Zhu, Q., Raghupathi, R., and Margulies, S. S. (2003). Age-dependent changes in material properties of the brain and braincase of the rat. *J Neurotrauma*, 20(11):1163–77.

Gerlach, W. and Stern, O. (1924). Ueber die richtungsquantelung im magnetfeld. *Annalen der Physik*, 379(16):673–699.

Gottwald, E., Kleintschek, T., Giselbrecht, S., Truckenmuller, R., Altmann, B., Worgull, M., Dopfert, J., Schad, L., and Heilmann, M. (2013). Characterization of a chip-based bioreactor for three-dimensional cell cultivation via magnetic resonance imaging. *Z Med Phys*, 23(2):102–10.

Gottwald, E., Neubauer, A., and Schad, L. (2016). *Assessment of Cellular and Organ Function and Dysfunction using Direct and Derived MRI Methodologies*, book section 2. InTech.

Griffey, R. H., Griffey, B. V., and Matwiyoff, N. A. (1990). Triple-quantum-coherence-filtered imaging of sodium ions in vivo at 4.7 tesla. *Magnetic Resonance in Medicine*, 13(2):305–313.

Guermazi, A., Alizai, H., Crema, M. D., Trattnig, S., Regatte, R. R., and Roemer, F. W. (2015). Compositional mri techniques for evaluation of cartilage degeneration in osteoarthritis. *Osteoarthritis Cartilage*, 23(10):1639–53.

Haacke, E. M., Brown, R. W., Thompson, M. R., and Venkatesan, R. (1999). *Magnetic Resonance Imaging: Physical Principles and Sequence Design*. John Wiley & Sons.

Hancu, I., Boada, F. E., and Shen, G. X. (1999). Three-dimensional triple-quantum-filtered 23na imaging of in vivo human brain. *Magnetic Resonance in Medicine: An Official Journal of the International Society for Magnetic Resonance in Medicine*, 42(6):1146–1154.

Harris, R. K., Becker, E. D., Cabral de Menezes, S. M., Goodfellow, R., and Granger, P. (2002). Nmr nomenclature: nuclear spin properties and conventions for chemical shifts. iupac recommendations 2001. international union of pure and applied chemistry. physical chemistry division. commission on molecular structure and spectroscopy. *Magnetic Resonance in Chemistry*, 40(7):489–505.

Hartzell, H. C. (2010). *Chapter 1 - Chloride Channels: An Historical Perspective*, pages 1–15. Academic Press, San Diego.

Hoesl, M. A. U., Kleimaier, D., Hu, R., Malzacher, M., Nies, C., Gottwald, E., and Schad, L. R. (2019). 23na triple-quantum signal of in vitro human liver cells, liposomes, and nanoparticles: Cell viability assessment vs. separation of intra- and extracellular signal. *J Magn Reson Imaging*, 50(2):435–444.

Hoult, D. I. and Richards, R. E. (1976). The signal-to-noise ratio of the nuclear magnetic resonance experiment. *Journal of Magnetic Resonance (1969)*, 24(1):71–85.

Hu, R., Kleimaier, D., Malzacher, M., Hoesl, M. A. U., Paschke, N. K., and Schad, L. R. (2019). X-nuclei imaging: Current state, technical challenges, and future directions. *J Magn Reson Imaging*.

Hu, R., Malzacher, M., Davids, M., Neubauer, A., Konstandin, S., and Schad, L. (2017a). Spatial resolution analysis comparing density-adapted and conventional projection reconstruction in chlorine-35 at 9.4 t. *Proc. Intl. Soc. Mag. Reson. Med.*

Hu, R., Malzacher, M., Hoesl, M. A. U., Kleimaier, D., and Schad, L. (2018a). Optimizing simultaneously acquired single- and triple-quantum imaging with time proportional phase increment for 23na and 35cl. *Proc. Intl. Soc. Mag. Reson. Med.*

Hu, R., Malzacher, M., Hoesl, M. A. U., Kleimaier, D., and Schad, L. (2018b). Simultaneously acquired 23na single- and triple-quantum imaging in rat in vivo at 9.4 t. *Proc. Intl. Soc. Mag. Reson. Med.*

Hu, R., Malzacher, M., Hoesl, M. A. U., Kleimaier, D., and Schad, L. (2018c). Simultaneously acquired single- and triple-quantum spectroscopic imaging with density-adapted projection reconstruction and time proportional phase increment. *Proc. Intl. Soc. Mag. Reson. Med.*

Hu, R., Neubauer, A., Malzacher, M., Konstandin, S., and Schad, L. (2017b). Density-adapted k-space sampling technique for fast relaxaing chlorine-35 nuclei at 9.4 t. *Proc. Intl. Soc. Mag. Reson. Med.*

Hubbard, P. S. (1970). Nonexponential nuclear magnetic relaxation by quadrupole interactions. *The Journal of Chemical Physics*, 53(3):985–987.

Insko, E. K. and Bolinger, L. (1993). Mapping of the radiofrequency field. *Journal of Magnetic Resonance, Series A*, 103(1):82–85.

Jaccard, G., Wimperis, S., and Bodenhausen, G. (1986). Multiple-quantum nmr spectroscopy of s=3/2 spins in isotropic phase: A new probe for multiexponential relaxation. *The Journal of Chemical Physics*, 85(11):6282–6293.

Jelicks, L. A. and Gupta, R. K. (1993). On the extracellular contribution to multiple quantum filtered23na nmr of perfused rat heart. *Magnetic Resonance in Medicine*, 29(1):130–133.

Kim, R. J., Hillenbrand, H. B., and Judd, R. M. (2000). Evaluation of myocardial viability by mri. *Herz*, 25(4):417–430.

Kim, R. J., Judd, R. M., Chen, E.-L., Fieno, D. S., Parrish, T. B., and Lima, J. A. C. (1999). Relationship of elevated 23na magnetic resonance image intensity to infarct size after acute reperfused myocardial infarction. *Circulation*, 100(2):185–192.

Kirsch, S., Augath, M., Seiffge, D., Schilling, L., and Schad, L. R. (2010). In vivo chlorine-35, sodium-23 and proton magnetic resonance imaging of the rat brain. *NMR Biomed*, 23(6):592–600.

Knubovets, T., Shinar, H., and Navon, G. (1998). Quantification of the contribution of extracellular sodium to 23na multiple-quantum-filtered nmr spectra of suspensions of human red blood cells. *J Magn Reson*, 131(1):92–6.

Konstandin, S. (2012). *Development of 2D Radial Techniques for Sodium MRI with Application to Abdominal Imaging at 3 Tesla*. Thesis.

Konstandin, S., Nagel, A. M., Heiler, P. M., and Schad, L. R. (2011). Two-dimensional radial acquisition technique with density adaption in sodium mri. *Magn Reson Med*, 65(4):1090–6.

Lauterber, P. C. (1974). Image formation by induced local interactions : examples employing nuclear magnetic resonance. *Nature*, 246:469.

LaVerde, G., Nemoto, E., Jungreis, C. A., Tanase, C., and Boada, F. E. (2007). Serial triple quantum sodium mri during non-human primate focal brain ischemia. *Magn Reson Med*, 57(1):201–5.

Lesperance, L. M., Gray, M. L., and Burstein, D. (1992). Determination of fixed charge density in cartilage using nuclear magnetic resonance. *Journal of Orthopaedic Research*, 10(1):1–13.

Levitt, M. H. (2008). *Spin Dynamics: Basics of Nuclear Magnetic Resonance*. John Wiley & Sons, 2 edition.

Liao, J.-R., Pauly, J. M., Brosnan, T. J., and Pelc, N. J. (1997). Reduction of motion artifacts in cine mri using variable-density spiral trajectories. *Magnetic Resonance in Medicine*, 37(4):569–575.

Lott, J., Platt, T., Niesporek, S. C., Paech, D., G. R. Behl, N., Niendorf, T., Bachert, P., Ladd, M. E., and Nagel, A. M. (2019). Corrections of myocardial tissue sodium concentration measurements in human cardiac 23na mri at 7 tesla. *Magnetic Resonance in Medicine*, 82(1):159–173.

Madelin, G., Kline, R., Walvick, R., and Regatte, R. R. (2014). A method for estimating intracellular sodium concentration and extracellular volume fraction in brain in vivo using sodium magnetic resonance imaging. *Sci Rep*, 4:4763.

Madelin, G. and Regatte, R. R. (2013). Biomedical applications of sodium mri in vivo. *J Magn Reson Imaging*, 38(3):511–29.

Malzacher, M., Hu, R., Chacon-Caldera, J., and Schad, L. R. (2018). Reducing signal-to-noise ratio degradation due to coil coupling in a receiver array for 35cl mri at 9.4 t: A comparison of matching and decoupling strategies. *Concepts in Magnetic Resonance Part B: Magnetic Resonance Engineering*, 48(2):e21383.

Matthies, C. (2010). *Ueber den Einfluss von Inhomogenitaeten im Grundmagnetfeld auf die Tripelquantengefilterte Natrium-MR-Spektroskopie und -Bildgebung*. Thesis.

Matthies, C., Nagel, A. M., Schad, L. R., and Bachert, P. (2010). Reduction of b0 inhomogeneity effects in triple-quantum-filtered sodium imaging. *J Magn Reson*, 202(2):239–44.

Milo, R. and Phillips, R. (2015). *Cell Biology by the Numbers*. Garland Science.

Mirkes, C., Shajan, G., Bause, J., Buckenmaier, K., Hoffmann, J., and Scheffler, K. (2016). Triple-quantum-filtered sodium imaging at 9.4 tesla. *Magn Reson Med*, 75(3):1278–89.

Monoi, H. (1985). Nuclear magnetic resonance of 23na ions interacting with the gramicidin channel. *Biophysical Journal*, 48(4):643–662.

Morrell, G. R. (2008). A phase-sensitive method of flip angle mapping. *Magnetic Resonance in Medicine*, 60(4):889–894.

Mueller, N., Bodenhausen, G., and Ernst, R. R. (1987). Relaxation-induced violations of coherence transfer selection rules in nuclear magnetic resonance. *Journal of Magnetic Resonance (1969)*, 75(2):297–334.

Nagel, A. M. (2009). *Natrium-Magnetresonanztomographie: Entwicklung einer 3D radialen Messtechnik mit optimierter k-Raum-Abtastdichte und hoher SNR-Effizienz*. Thesis.

Nagel, A. M., Laun, F. B., Weber, M. A., Matthies, C., Semmler, W., and Schad, L. R. (2009). Sodium mri using a density-adapted 3d radial acquisition technique. *Magn Reson Med*, 62(6):1565–73.

Nagel, A. M., Lehmann-Horn, F., Weber, M.-A., Jurkat-Rott, K., Wolf, M. B., Radbruch, A., Umathum, R., and Semmler, W. (2014). In vivo 35cl mr imaging in humans: a feasibility study. *Radiology*, 271(2):585–595.

Navon, G. (1993). Complete elimination of the extracellular23na nmr signal in triple quantum filtered spectra of rat hearts in the presence of shift reagents. *Magnetic Resonance in Medicine*, 30(4):503–506.

Neubauer, A. (2017). *Modellierung und Validierung ionischer Regulationsprozesse in Nervenzellen mittels X-Kern-Magnetresonanztomographie*. Thesis.

Neubauer, A., Nies, C., Schepkin, V. D., Hu, R., Malzacher, M., Chacon-Caldera, J., Thiele, D., Gottwald, E., and Schad, L. R. (2017). Tracking protein function with sodium multi quantum spectroscopy in a 3d-tissue culture based on microcavity arrays. *Sci Rep*, 7(1):3943.

Niesporek, S. C., Umathum, R., Fiedler, T. M., Bachert, P., Ladd, M. E., and Nagel, A. M. (2017). Improved t2* determination in 23na, 35cl, and 17o mri using iterative partial volume correction based on 1h mri segmentation. *Magnetic Resonance Materials in Physics, Biology and Medicine*, 30(6):519–536.

Nyquist, H. (1928). Certain topics in telegraph transmission theory. *Transactions of the American Institute of Electrical Engineers*, 47(2):617–644.

Ouwerkerk, R., Bleich, K. B., Gillen, J. S., Pomper, M. G., and Bottomley, P. A. (2003). Tissue sodium concentration in human brain tumors as measured with 23na mr imaging. *Radiology*, 227(2):529–537.

Pekar, J. and Leigh, J. S. (1986). Detection of biexponential relaxation in sodium-23 facilitated by double-quantum filtering. *Journal of Magnetic Resonance (1969)*, 69(3):582–584.

Petracca, M., Fleysher, L., Oesingmann, N., and Inglese, M. (2016a). Sodium mri of multiple sclerosis. *NMR Biomed*, 29(2):153–61.

Petracca, M., Vancea, R. O., Fleysher, L., Jonkman, L. E., Oesingmann, N., and Inglese, M. (2016b). Brain intra- and extracellular sodium concentration in multiple sclerosis: a 7 t mri study. *Brain*, 139(3):795–806.

Purcell, E. M., Torrey, H. C., and Pound, R. V. (1946). Resonance absorption by nuclear magnetic moments in a solid. *Physical Review*, 69(1-2):37–38.

Pyper, N. C. (1971). Theory of symmetry in nuclear magnetic relaxation including applications to high resolution n.m.r. line shapes. *Molecular Physics*, 21(1):1–33.

Rabi, I. I., Zacharias, J. R., Millman, S., and Kusch, P. (1938). A new method of measuring nuclear magnetic moment. *Physical Review*, 53(4):318–318.

Rakhmanov, E., Saff, E. B., and Zhou, Y. M. (1994). Minimal discrete energy on the sphere. *Mathematical Research Letters*, 1:647–662.

Reiser, M. F., Semmler, W., and Hricak, H. (2007). *Magnetic Resonance Tomography*. Springer.

Rooney, W. D. and Springer, C. S. (1991). A comprehensive approach to the analysis and interpretation of the resonances of spins 3/2 from living systems. *NMR Biomed*, 4(5):209–226.

Sandstede, J. J., Hillenbrand, H., Beer, M., Pabst, T., Butter, F., Machann, W., Bauer, W., Hahn, D., and Neubauer, S. (2004). Time course of 23na signal intensity after myocardial infarction in humans. *Magn Reson Med*, 52(3):545–51.

Schepkin, V. D. (2016). Sodium mri of glioma in animal models at ultrahigh magnetic fields. *NMR Biomed*, 29(2):175–186.

Schepkin, V. D., Chenevert, T. L., Kuszpit, K., Lee, K. C., Meyer, C. R., Johnson, T. D., Rehemtulla, A., and Ross, B. D. (2006a). Sodium and proton diffusion mri as biomarkers for early therapeutic response in subcutaneous tumors. *Magn Reson Imaging*, 24(3):273–8.

Schepkin, V. D., Choy, I. O., and Budinger, T. F. (1996). Sodium alterations in isolated rat heart during cardioplegic arrest. *J Appl Physiol (1985)*, 81(6):2696–702.

Schepkin, V. D., Choy, I. O., Budinger, T. F., Obayashi, D. Y., Taylor, S. E., Decampli, W. M., Amartur, S. C., and Young, J. N. (1998). Sodium tqf nmr and intracellular sodium in isolated crystalloid perfused rat heart. *Magnetic Resonance in Medicine*, 39(4):557–563.

Schepkin, V. D., Elumalai, M., Kitchen, J. A., Qian, C., Gor'kov, P. L., and Brey, W. W. (2014). In vivo chlorine and sodium mri of rat brain at 21.1 t. *Magnetic Resonance Materials in Physics, Biology and Medicine*, 27(1):63–70.

Schepkin, V. D., Lee, K. C., Kuszpit, K., Muthuswami, M., Johnson, T. D., Chenevert, T. L., Rehemtulla, A., and Ross, B. D. (2006b). Proton and sodium mri assessment of emerging tumor chemotherapeutic resistance. *NMR Biomed*, 19(8):1035–42.

Schepkin, V. D., Neubauer, A., Nagel, A. M., and Budinger, T. F. (2017). Comparison of potassium and sodium binding in vivo and in agarose samples using tqtppi pulse sequence. *J Magn Reson*, 277:162–168.

Seo, Y., Murakami, M., Suzuki, E., Watari, H., and Nagayama, K. (1990). Nmr characteristics of intracellular k in the rat salivary gland: A 39k nmr study using double-quantum filtering. *Biochemistry*, 29(3):599–603.

Seshan, V., Sherry, A. D., and Bansal, N. (1997). Evaluation of triple quantum-filtered 23na nmr spectroscopy in the in situ rat liver. *Magnetic Resonance in Medicine*, 38(5):821–827.

Shah, N. J., Worthoff, W. A., and Langen, K. J. (2016). Imaging of sodium in the brain: a brief review. *NMR Biomed*, 29(2):162–74.

Stein, W. D. and Litman, T. (2015). *Chapter 1 - Structural Basis of Movement Across Cell Membranes*, pages 1–36. Elsevier, London.

Tanase, C. and Boada, F. E. (2005). Triple-quantum-filtered imaging of sodium in presence of b0 inhomogeneities. *J Magn Reson*, 174(2):270–8.

Thulborn, K. R. (2018). Quantitative sodium mr imaging: A review of its evolving role in medicine. *Neuroimage*, 168:250–268.

Tsang, A., Stobbe, R. W., and Beaulieu, C. (2012). Triple-quantum-filtered sodium imaging of the human brain at 4.7 t. *Magnetic Resonance in Medicine*, 67(6):1633–1643.

van der Maarel, J. R. (2003a). Thermal relaxation and coherence dynamics of spin 3/2. ii. strong radio-frequency field. *Concepts in Magnetic Resonance Part A*, 19A(2):117–133.

van der Maarel, J. R. C. (2003b). Thermal relaxation and coherence dynamics of spin 3/2. i. static and fluctuating quadrupolar interactions in the multipole basis. *Concepts in Magnetic Resonance*, 19A(2):97–116.

Wang, C., McArdle, E., Fenty, M., Witschey, W., Elliott, M., Sochor, M., Reddy, R., and Borthakur, A. (2010). Validation of sodium magnetic resonance imaging of intervertebral disc. *Spine*, 35(5):505–510.

Weber, M.-A., Nagel, A. M., Marschar, A. M., Glemser, P., Jurkat-Rott, K., Wolf, M. B., Ladd, M. E., Schlemmer, H.-P., Kauczor, H.-U., and Lehmann-Horn, F. (2016). 7-t 35cl and 23na mr imaging for detection of mutation-dependent alterations in muscular edema and fat fraction with sodium and chloride concentrations in muscular periodic paralyses. *Radiology*, 280(3):848–859.

Wetterling, F., Ansar, S., and Handwerker, E. (2012). Sodium-23 magnetic resonance imaging during and after transient cerebral ischemia: multinuclear stroke protocols for double-tuned (23)na/(1)h resonator systems. *Phys Med Biol*, 57(21):6929–46.

Wetterling, F., Gallagher, L., Mullin, J., Holmes, W. M., McCabe, C., Macrae, I. M., and Fagan, A. J. (2015). Sodium-23 magnetic resonance imaging has potential for improving penumbra detection but not for estimating stroke onset time. *J Cereb Blood Flow Metab*, 35(1):103–10.

Wimperis, S., Cole, P., and Styles, P. (1992). Triple-quantum-filtration nmr imaging of 200 mm sodium at 1.9 tesla. *Journal of Magnetic Resonance (1969)*, 98(3):628–636.

Wimperis, S. and Wood, B. (1991). Triple-quantum sodium imaging. *Journal of Magnetic Resonance (1969)*, 95(2):428–436.

Winter, P. M. and Bansal, N. (2001). Triple-quantum-filtered (23)na nmr spectroscopy of subcutaneously implanted 9l gliosarcoma in the rat in the presence of tmdotp(5-1). *J Magn Reson*, 152(1):70–8.

Wokaun, A. and Ernst, R. R. (1977). Selective excitation and detection in multilevel spin systems: Application of single transition operators. *The Journal of Chemical Physics*, 67(4):1752–1758.

Worthoff, W. A., Shymanskaya, A., and Shah, N. J. (2018). Relaxometry and quantification in simultaneously acquired single and triple quantum filtered sodium mri. *Magn Reson Med*.

List of Abbreviations

BW	bandwidth
DA-R	density-adapted radial imaging
DQ	double-quantum
TE	echo time
t_{evo}	evolution time
Δt_{evo}	evolution time step
$T_{2\mathrm{f}}$	fast component of the transverse relaxation time
FOV	field-of-view
FID	free inducation decay
t-FID	free inducation decayin the time domain after the last pulse
t_{evo}-FID	free inducation decayin the evolution time domain after the first pulse
TI	inversion time
T_1	longitudinal relaxation time
MQ	multiple-quantum
MTF	modulation transfer function
n_{ps}	number of phase steps pairs
n_{pc}	number of phase cycles
$S_{\mathrm{T/S}}$	ratio between single- and triple-quantum signal
t_{ro}	readout duration
TR	repetition time
t_{sc}	scan time of an experiment
SISTINA	simultaneous single-quantum and triple-quantum-filtered MRI of ^{23}Na
SQ	single-quantum
$T_{2\mathrm{s}}$	slow component of the transverse relaxation time
SAR	specific absorption rate
TPPI	time-proportional phase incrementation
TSC	tissue sodium concentration
TQ	triple-quantum
TASTI	triple- and single-quantum TPPI imaging
TQ-TPPI	triple-quantum spectroscopy with time-proportional phase incrementation
UTE	ultra-short echo time

List of Publications

Peer-Reviewed Journal Articles

- Hu, R., Kleimaier, D., Malzacher, M., Hoesl, M., Paschke, N. K., and Schad, L. R. (2019). X-nuclei imaging: Current state, technical challenges, and future directions. J Magn Reson Imaging. https://doi.org/10.1002/jmri.26780.
- Hoesl, M., Kleimaier, D., Hu, R., Malzacher, M., Nies, C., Gowald, E., and Schad, L. R. (2019). 23Na triple-quantum signal of in vitro human liver cells, liposomes, and nanoparticles: Cell viability assessment vs. separation of intra- and extracellular signal. J Magn Reson Imaging, 50(2):435–444.
- M. Malzacher, R. Hu, J. Chacon-Caldera and L. Schad. Reducing signal-to-noise ratio degradation due to coil coupling in a receiver array for 35Cl MRI at 9.4 Tesla: A comparison of matching and decoupling strategies. (2018) Concept Magn Reson B: Magnetic Resonance Engineering, 48(2):e21383.
- A. Neubauer, C. Nies, V. Schepkin, R. Hu, M. Malzacher, J. Chacón-Caldera, D. Thiele, E. Gottwald and L. Schad. (2017) Tracking protein function with sodium multi quantum spectroscopy in a 3D-tissue culture based on microcavity arrays. Sci. Rep., 7 (1), p.3943.

Conference Contributions

- R. Hu, M. Malzacher, M. Hoesl, D. Kleimaier and L. Schad. Simultaneously Acquired Single- and Triple-Quantum Spectroscopic Imaging with Density-Adapted Projection Reconstruction and Time Proportional Phase Increment. (2018) Proc. Int. Soc. Magn. Reson. Med., Paris, France, 26, p.3866.
- M. Hoesl, D. Kleimaier, R. Hu, M. Malzacher, E. Gottwald, C. Nies and L. Schad. Can sodium triple-quantum signal separate extra- and intracellular signals? – investigation on HEP G2 liver cells, liposomes and nanoparticles. (2018) Proc. Int. Soc. Magn. Reson. Med., Paris, France, 26, p.3875.
- M. Hoesl, D. Kleimaier, M. Malzacher, R. Hu and L. Schad. Voxel localization for sodium NMR triple-quantum signal; sequence design and test in agarose phantoms and in-vivo rat. (2018) Proc. Int. Soc. Magn. Reson. Med., Paris, France, 26, p.3874.
- R. Hu, A. Neubauer, M. Malzacher, S. Konstandin and L. Schad. Density-Adapted K-Space Sampling Technique for Fast Relaxing Chlorine-35 Nuclei at 9.4 T. (2017) Proc. Int. Soc. Magn. Reson. Med., Honolulu, HI, USA, 25, p.2949.
- R. Hu, M. Malzacher, M. Davids, A. Neubauer, S. Konstandin and L. Schad. Spatial Resolution Analysis Comparing Density-Adapted and Conventional Projection Reconstruction in Chlorine-35 MRI at 9.4 T. (2017) Proc. Int. Soc. Magn. Reson. Med., Honolulu, HI, USA, 25, p.5219.

- M. Malzacher, R. Hu, J. Chacon-Caldera, A. Neubauer and L. Schad. A 35Cl ToRo Resonator System for Preclinical MRI/MRS at 9.4T. (2017) Proc. Int. Soc. Magn. Reson., Honolulu, HI, USA, 25, p.5622.
- A. Neubauer, M. Malzacher, V. Schepkin, J. Chacon-Caldera, R. Hu, E. Gottwald, C. Nies, D. Thiele and L. Schad. Investigation of Strophanthin Induced Na-/K-ATPase Blockage by Means of 23Na Multi Quantum Spectroscopy in a High Density Cell Culture on Chip. (2017) Proc. Int. Soc. Magn. Reson. Med., Honolulu. HI. USA, 25, p.5630.
- R. Hu, A. Neubauer, J. Chacón-Caldera, J. Uranga Solchaga, C. Schuch, T. Gläser, C. Nies, E. Gottwald, S. Giselbrecht and L. Schad. In Vitro Oxygen-17 NMR Spectroscopy of Cellular Metabolism at Ultra High Field. (2016) Proc. Intl. Soc. Mag. Reson. Med., Singapur, Singapur, 24, p.3963.
- R. Hu, S. Konstandin and L. Schad. Fast Sodium MRI of the Human Brain Using a Balanced Steady-State Free Precession Sequence. (2915) Proc. Int. Soc. Magn. Reson. Med., Toronto, Canada, 23, p.2373.

List of Figures

2.1 Scaled nuclear Zeeman effect at $B_0 = 9.4\,\mathrm{T}$ illustrated for the ^{1}H, the ^{23}Na and the ^{35}Cl nucleus. Th energy levels of the ^{23}Na and the ^{35}Cl nucleus are equidistant. 4

2.2 Types of spin interactions according to the nature (electric or magnetic) and the source of field (external and internal). Electric interactions are experienced by nuclei with $I > 1/2$ only, while all NMR-compatible nuclei are subject to magnetic interactions. 11

2.3 Summary of the nuclear spin Hamiltonians with their relative magnitudes for solids and isotropic liquids (adapted from Levitt (2008)). Electric-quadrupole coupling is only present for nuclei with $I > \frac{1}{2}$. It is marked by an dashed outline. . . 14

2.4 **A** Single-, DQ and TQ coherences illustrated as transitions between energy levels. **B** Density matrix elements. The real diagonal elements are the populations of the four quantum states. The complex off-diagonal elements are superpositions of two quantum states and per definition coherences. 17

2.5 Transformation of the spherical tensors $\hat{T}_{lm}$ in an isotropic environment with zero-average EFG. The rank might change upon the application of an hard RF pulse, whereas the order might change during relaxation. The even- and odd-rank tensors are decoupled in an isotropic environment, so that rank-two coherences cannot be created via relaxation. 20

2.6 Basic RF pulse scheme to excite MQ coherences. TQ, DQ and SQ coherence pathways with matching time stamps are shown below. 24

3.1 $9.4\,\mathrm{T}$ preclinical MR system by Bruker. Animal beds that can be heated with adjustable temperature are availabe. After the laser adjustment, the experimental setup is driven into the iso-center by a mechanical belt. 30

3.2 **A** ^{23}Na surface coil **B** ^{23}Na saddle coil **C** ^{1}H and ^{23}Na double-resonant volume coil (Bruker) 30

3.3 **A** ^{35}Cl surface coil **B** ^{35}Cl saddle coil **C** ^{35}Cl volume coil (Malzacher et al., 2018) 30

3.4 **A** Resolution phantom MH with its blueprint. White circles and black background indicate that the holes are filled with NaCl. **B** Resolution phantom AG with its ^{1}H MR image. Black circles and white background within the boundary of the cylindrical phantom indicate that the phantom is filled with NaCl while the rods are solid. 32

3.5 **A** Drawing of liposomes formed by lecithin solved in acqueous solution. Liposomes emulate cells as both share the feature of a lipid bilayer. **B** Lecithin phantoms with 2, 4, 10 and $20\,\%$ lecithin and $154\,\mathrm{mM}$ NaCl. Phantoms with a higher percentage of lecithin have a darker color. 32

3.6 Fluorescence images of a microcavity array **A** from above and **B** in cross section (images courtesy of Cordula Nies). **C** Square bioreactor filled with isoproyl alcohol. **D** Round bioreactor filled with medium. 33

3.7 **A** Diagram and **B** photograph of the bioreactor setup. The scanner room is separated from the control room via a wall with a small hole to pass through the bioreactor and the medium tubes. 34

3.8 **A** Aeriel view of the flow system. In future models with densely sealed left and right compartments, either side could be operated independently through its inlets and outlets in bottom ('b') and top ('t') position. **B** Cross section of the flow system. In perfusion mode, the bottom inlets and the top outlets are open. This is the life-sustaining operation mode. In the superfusion modes, medium flows either entirely above or beneath the chip (yellow bar). 34

3.9 **A** The animal bed including the attached reference vials, the front teeth hold, and the isoflurane inlet. **B** Rat placed onto the bed with indication of the brain and the heart. **C** Setup for head measurement with ^{23}Na saddle coil. 35

3.10 Example of a flip angle calibration fit. 36

3.11 Example of structure paths in Resolution Phantom MH. 37

3.12 **A** UTE sequence diagram with a trapezoid gradient. **B** DA-R sequence diagram with a density-adapted gradient. The maximum gradient strength is G_0. After the ramp-up, the gradient is initially constant. The density-adapted part starts at t_0. 38

3.13 **A** Radial k-space spokes represented by arrows ($N_{\text{proj}} = 200$) **B** Connected path reached by the end points k_{max} of the spokes ($N_{\text{proj}} = 1000$) 40

3.14 TQ-TPPI sequence diagram with coherence pathways. 41

3.15 TQ-TPPI phase steps and phase cycles. 42

3.16 Exemplary k-space trajectories for DA$_{\text{max}}$ and DA$_{\text{min}}$ with a readout time of 8 ms. The trajectory with a higher percentage of density-adapted readout has a lower sampling density at k-space center and reaches a given point in k-space along the trajectory faster. To reach $0.5k_{\text{max}}$ in this example, the trajectory with DA$_{\text{min}}$ takes approximately 3.5-fold the readout time as that with DA$_{\text{max}}$. 45

4.1 Percentage SNR increase in DA-R images acquired with different t_0 and thus varying degrees of density-adaption. The nominal resolution was 2 mm with a FOV of $(64\,\text{mm})^2$. 53

4.2 ^{35}Cl resolution phantom analysis with phantom AG and a nominal voxel size of 0.33 mm. Gray values in the bar plots were reversed for this phantom. In **A** and **B** the same FOV with the same number of spokes were sampled. The high noise level of **A** was also reflected in the higher standard deviation of the MTF points. The GV along the structure paths shown in the bar plots in **A** also failed to clearly reveal the distribution of the structures, while those in **B** contained repetitive patterns of signal in- and decrease for all except the smallest structure size. 55

4.3 ^{35}Cl resolution phantom analysis with phantom AG and a nominal voxel size of 0.49 mm. Gray values in the bar plots were reversed for this phantom. In **A** and **B** the same FOV with the same number of spokes were sampled. In **A** fine ringing artefacts were visible in the center; gross ringing was found at the edge of the circular image. The image of the minimalist FOV chosen in **C** had comparable image quality and fitted spatial resolution as the image in **B**. 56

4.4 ^{35}Cl resolution phantom analysis with phantom MM and a nominal voxel size of $0.33\,\mathrm{mm}$. Gray values in the bar plots in **A** are overlayed by noise, whereas the distinction between peaks and valleys were clear in **B**. Despite the fact that fitting was not applicable due to low dispersion of the MTF values, the higher peak-valley gray value differences in **B** was nevertheless an indicator for a better spatial resolution capacity. 57

4.5 ^{35}Cl resolution phantom analysis with phantom MM and a nominal voxel size of $0.49\,\mathrm{mm}$. In **A** and **B** the same FOV with the same number of spokes were sampled. Uncorrelated signal spikes due to the high noise level in **A** artificially increased the peak-valley signal differences especially for smaller structures. Imaging objects not compliying with the circular image edge of UTE benefited from the cubical FOV of DA-R in terms of drastically reduced measurement time. Comparable spatial resolutions in **B** and **C** were obtained through fitting of the MTF. 58

4.6 Normalized pseudo 2D ^{23}Na DA-R images of the square bioreactor in the coronal view with a FOV of $(28\,\mathrm{mm})^2$ and the corresponding line plots. The high resolution image and the low resolution image have an isotropic nominal voxel of $0.15\,\mathrm{mm}$ and $0.40\,\mathrm{mm}$, respectively. The positions of the line plots are indicated by the dashed lines across the images. 59

4.7 Normalized pseudo 2D ^{35}Cl DA-R image of the square bioreactor in the coronal view and the corresponding line plot. The image was normalized to its own maximum. The image has a FOV of $(32\,\mathrm{mm})^2$ and an isotropic nominal voxel of $0.8\,\mathrm{mm}$. The position of the line plot is indicated by the dashed lines across the image. 60

4.8 3D *in vivo* ^{23}Na DA-R images of the rat head in prone position acquired in 7 minutes. The coronal slice in the top row is closer to the surface coil. Each image is normalized to its own maximum. The images have a FOV of $(64\,\mathrm{mm})^2$. The ^{1}H and the ^{23}Na images have an isotropic nominal voxel of $0.25\,\mathrm{mm}$ and $1\,\mathrm{mm}$, respectively. 61

4.9 3D *in vivo* ^{23}Na DA-R image of the rat head in prone position acquired in 50 minutes. One coronal slice is shown containing the same anatomical features as the first slice of the ^{23}Na image is shown. The ^{35}Cl image is normalized to its own maximum and has a FOV of $(60\,\mathrm{mm})^2$. The ^{1}H and the ^{35}Cl image have an isotropic nominal voxel of $0.25\,\mathrm{mm}$ and $1.5\,\mathrm{mm}$, respectively. 62

4.10 3D *in vivo* ^{23}Na DA-R images of the rat torso in supine position acquired in 29 minutes. One transverse, one sagittal and one coronal slice with a FOV of $(64\,\mathrm{mm})^2$ are shown. The locations of the other slices are indicated by dashed lines, and the coil position is indicated by the dotted line. Each image was normalized to its own maximum. The ^{1}H and the ^{23}Na images have an isotropic nominal voxel of $0.25\,\mathrm{mm}$ and $1\,\mathrm{mm}$, respectively. In the sagittal ^{1}H image, the anterior and the posterior direction are labeled with “A” and “P”, respectively. 64

4.11 3D *in vivo* ^{35}Cl DA-R images of the rat torso in supine positiosn acquired in 1 hour and 59 minutes. One transverse, one sagittal and one coronal slice with a FOV of $(63\,\mathrm{mm})^2$ are shown. The slice locations of the other two slices are indicated by dashed lines, and the coil position is indicated by the dotted line. Each image was normalized to its own maximum. The ^{1}H and the ^{35}Cl images have an isotropic nominal voxel of $0.25\,\mathrm{mm}$ and $1.5\,\mathrm{mm}$, respectively. In the sagittal ^{1}H image, the anterior and the posterior direction are labeled with “A” and “P”, respectively. . . 65

4.12 Fitted TQ-TPPI ^{23}Na t_{evo}-FIDs and the corresponding TQ-TPPI spectra along the acquired with maximum TR. The fit function was $f_{\text{SQDQTQ}}(t_{\text{evo}}) = g_{\text{S}}^{\text{bi}}(t_{\text{evo}}) + g_{\text{D}}(t_{\text{evo}}) + g_{\text{T}}(t_{\text{evo}}) + c$ unless the TQ component was absent, in which case the fit function was $f_{\text{S}}(t_{\text{evo}}) = g_{\text{S}}^{\text{mono}}(t_{\text{evo}}) + c$. 68

4.13 Fitted TQ-TPPI ^{35}Cl t_{evo}-FIDs and the corresponding TQ-TPPI spectra acquired with maximum TR. The fit function was $f_{\text{SQDQTQ}}(t_{\text{evo}}) = g_{\text{S}}^{\text{bi}}(t_{\text{evo}}) + g_{\text{D}}(t_{\text{evo}}) + g_{\text{T}}(t_{\text{evo}}) + c$ unless the TQ component was absent, in which case the fit function was $f_{\text{S}}(t_{\text{evo}}) = g_{\text{S}}^{\text{mono}}(t_{\text{evo}}) + c$. 69

4.14 **A** ^{23}Na (in blue) and ^{35}Cl (in green) $S_{\text{T/S}}$ ratios plotted against TR/T_1. The $S_{\text{T/S}}^{\text{Na}}$ratios were constant in the range of $\text{TR}/T_1 \gtrsim 3.5$. The $S_{\text{T/S}}^{\text{Cl}}$ ratios were constant for all TR/T_1 in the 0% phantom. In the $> 0\%$ phantoms, the $S_{\text{T/S}}^{\text{Cl}}$ ratios fluctuated around a constant value. **B** ^{23}Na (in blue) and ^{35}Cl (in green) T_2 plotted against TR/T_1. In some cases, the confidence interval was too small to be discerned. 70

4.15 Fitted ^{23}Na TQ-TPPI spectra of lecithin phantoms with the fit function $f_{\text{SDT}}(t_{\text{evo}}) = g_{\text{S}}^{\text{bi}}(t_{\text{evo}}) + g_{\text{T}}(t_{\text{evo}}) + c$. In all four phantoms, a TQ peak was present, whereby its amplitude increases with increasing lecithin concentration. 71

4.16 Fitted ^{35}Cl TQ-TPPI spectra of lecithin phantoms with the fit function $f_{\text{SDT}}(t_{\text{evo}}) = g_{\text{S}}^{\text{bi}}(t_{\text{evo}}) + g_{\text{T}}(t_{\text{evo}}) + c$. A zoomed view of the TQ peak is displayed in the left column. A TQ peak was present only in the phantoms with 10% and 20% lecithin. 72

4.17 Fitted ^{23}Na and ^{35}Cl TQ-TPPI spectra of cells in the bioreactor. The ^{23}Na spectrum of the square bioreactor showed a TQ peak with $S_{\text{T/S}}^{\text{Na,square}} = (0.4 \pm 0.1)\%$. In the same setup, a ^{35}Cl TQ peak was not measured. The ^{35}Cl spectrum of the round bioreactor showed a TQ peak with $S_{\text{T/S}}^{\text{Cl,round}} = (5.1 \pm 3.0)\%$. 73

4.18 Fitted ^{23}Na and ^{35}Cl TQ-TPPI spectra of rat head *in vivo* with zoom on the TQ peak. The ^{23}Na TQ peak was very prominent, whereas the ^{35}Cl TQ peak was barely above noise level. 74

4.19 TASTI sequence diagram. The RF pulse scheme and the density-adapted readout gradient were adopted from the TQ-TPPI and the DA-R sequence, respectively. TE was the time between the observation pulse and the readout gradients, which marks the beginning of signal acquisition. TR was defined as the time between the observation pulse and the next excitation pulse. This way, the time for signal decay after the observation pulse was constant in all phase steps with varying t_{evo}. 75

4.20 TASTI sequence loop hierarchy. First, the n_{av} loop averages the t-FIDs. Second, the $\varphi \pm 90°$ loop suppresses DQ signal contributions with opposite phase from two subsequent acquisitions. Third, the $n_{\text{ps}} \cdot n_{\text{pc}}$ loop acquires the t_{evo}-FID in $n_{\text{ps}} \cdot n_{\text{pc}}$ steps in total. Last, the n_{proj} loop records the k-space along different radial projections. Loops in which the acquired signals were added contain a plus sign. 76

4.21 TASTI reconstruction pipeline. Fourier transform of the raw data along the t_{evo}-axis yielded a 3D matrix in which 2D radial k-space planes were aligned along the f_{MQ}-axis. Fourier transform of the k-space gridded onto a Cartesian grid yielded a 3D matrix with MQ images ligned up along the f_{MQ}-axis. To fit each voxel along the t_{evo}-domain, Fourier transform was performed along the f_{MQ}-axis. The t_{evo}-FIDs were fitted to obtain parameter maps such as the $T_{2\text{f}}$ map, the $T_{2\text{s}}$ map and the $S_{\text{T/S}}$. 77

4.22 Dependence of fitted $T_{2\mathrm{s,f}}$ on TE. The data points of each relaxation time component of each phantom was fitted by the linear fit function $T_{2\mathrm{s,f}} = m \cdot \mathrm{TE} + h$, whereby the constant offset h is approximately $T_{2\mathrm{s,f}}$ if the slope m fulfills $|m| \ll 1$. In comparison with values from TQ-TPPI fits, the $T_{2\mathrm{f}}$ values are in agreement, while the $T_{2\mathrm{s}}$ values are larger by up to 36%. 79

4.23 Dependence of fitted $S_{\mathrm{T/S}}$ on TE. The choice of TE in TASTI influences $S_{\mathrm{T/S}}$ The percentage increase was highest in the 2% phantom and lowest in the 6% phantom. 80

4.24 **a** The TQ signal intensities in each phantom obtained from TQ images acquired with different TEs, fitted by $S_{\mathrm{TQ}} = a\left(\mathrm{e}^{-\mathrm{TE}/T_{2\mathrm{f}}^*} - \mathrm{e}^{-\mathrm{TE}/T_{2\mathrm{s}}^*}\right) + h$. **b** The SQ signal intensities in each phantom obtained from SQ images acquired with different TEs, fitted by $S_{\mathrm{SQ}} = b \cdot \mathrm{e}^{-\mathrm{TE}/T_{2\mathrm{f}}^*} + (1-b) \cdot \mathrm{e}^{-\mathrm{TE}/T_{2\mathrm{s}}^*} + h$. 80

4.25 Exemplary images and maps acquired with $\mathrm{TE} = 1\,\mathrm{ms}$ and $\mathrm{TE} = 19\,\mathrm{ms}$. Images of the same row are scaled identically. All images and maps have a FOV of $(72\,\mathrm{mm})^2$ and a resolution of $(3\,\mathrm{mm})^2$. The phantoms have different relaxation properties and a different ratio between the TQ and the SQ component. These physical properties are reflected in the TQ image, the SQ image, the $S_{\mathrm{T/S}}$ map, the $T_{2\mathrm{s}}$ map and the $T_{2\mathrm{f}}$ map. Additionally, the relative TQ signal intensity, the absolute SQ signal intensity and the $S_{\mathrm{T/S}}$ ratios differ in the images acquired with different TEs. The relaxation times in all three phantoms are, however, largely the same regardless of TE. 81

4.26 Dependence of fitted $T_{2\mathrm{s,f}}$ on $t_{\mathrm{evo,max}}$ and Δt_{evo}. The data points of each relaxation time component of each phantom were fitted by the linear fit function $T_{2\mathrm{s,f}} = m \cdot \mathrm{TE} + h$, whereby $T_{2\mathrm{s,f}}$ was approximated by the constant offset h if the slope m fulfills $|m| \ll 1$. The $T_{2\mathrm{s}}$ data points with $t_{\mathrm{evo,max}} \leq 19\,\mathrm{ms}$ were excluded from the fit due to their large margins of error. In comparison with the values from TQ-TPPI fits, the $T_{2\mathrm{f}}$ values were in agreement, while the $T_{2\mathrm{s}}$ values were larger by up to 29%. 83

4.27 Dependence of fitted $S_{\mathrm{T/S}}$ on $t_{\mathrm{evo,max}}$ and Δt_{evo}. The data were fitted by the linear fit function $S_{\mathrm{T/S}} = m \cdot \mathrm{TE} + h$, whereby $S_{\mathrm{T/S}}$ was approximated by the constant offset h if the slope m fulfills $|m| \ll 1$. The $S_{\mathrm{T/S}}$ data points with $t_{\mathrm{evo,max}} \leq 19\,\mathrm{ms}$ were excluded from the linear fit due to their large margins of error. For each phantom, the fitted $h \approx S_{\mathrm{S/T}}$ ratio lied between the $S_{\mathrm{T/S}}$ ratios previously obtained in data acquired with $\mathrm{TE} = 9\,\mathrm{ms}$ and $\mathrm{TE} = 11\,\mathrm{ms}$. 84

4.28 The TQ and SQ k-space from the measurements with $\Delta t_{\mathrm{evo}} = 0.30\,\mathrm{ms}$ $t_{\mathrm{evo,max}} = 10$ and $153\,\mathrm{ms}$. The absolute values are displayed, whereby the SQ k-space at f_{SQ} was normalized to itself, and the TQ k-space at f_{TQ} was normalized to the SQ k-space of the same measurement. The scaling in each row is identical. The center of the radial k-space is located at small values along the t-axis. 85

4.29 Exemplary images and maps acquired with $t_{\mathrm{evo,max}} = 10\,\mathrm{ms}$ and $t_{\mathrm{evo,max}} = 153\,\mathrm{ms}$. The sampling time step was the same with fixed $\Delta t_{\mathrm{evo}} = 0.30\,\mathrm{ms}$. All images and maps have a FOV of $(72\,\mathrm{mm})^2$ and a resolution of $(3\,\mathrm{mm})^2$. Images of the same row are scaled identically. Comparing the maps from the measurement of $t_{\mathrm{evo,max}} = 10\,\mathrm{ms}$ with those of $t_{\mathrm{evo,max}} = 153\,\mathrm{ms}$, only the $T_{2\mathrm{f}}$ map showed largely the same results. The $S_{\mathrm{T/S}}$ map had higher values, and the $T_{2\mathrm{s}}$ map made no visible distinction among the three phantoms. 86

4.30 Fitting of the t_{evo}-FID with $t_{\mathrm{evo,max}} = 10\,\mathrm{ms}$ in different agarose concentrations with different $t_{\mathrm{evo,opt}}$. The three subfigures contain the FIDs of voxels within each phantom. The data points of each phantom were fitted by Equation 3.24. 87

4.31 The TQ and SQ k-space from the measurements with $t_{\text{evo,max}} = 77\,\text{ms}$ and $\Delta t_{\text{evo}} = 0.15$ and $0.30\,\text{ms}$. The absolute values are displayed, whereby the SQ k-space at f_{SQ} was normalized to itself, and the TQ k-space at f_{TQ} was normalized to the SQ k-space of the same measurement. The scaling in each row is identical. The center of the radial k-space is located at small values along the t-axis. 87

4.32 Exemplary images and maps acquired with $\Delta t_{\text{evo}} = 0.15\,\text{ms}$ and $\Delta t_{\text{evo}} = 0.30\,\text{ms}$. The sampling time was the same with fixed $t_{\text{evo,max}} = 77\,\text{ms}$. All images and maps have a FOV of $(72\,\text{mm})^2$ and a resolution of $(3\,\text{mm})^2$. The respective images and parameter maps of both measurements are in agreement. 88

4.33 The TQ and SQ k-space images in absolute values. The k-space at all f_{MQ} were filtered by a $\cos^2$ function with factor 2 to reduce the influence of k-space noise on the TQ image. The SQ k-space at f_{SQ} was normalized to itself, and the TQ k-space at f_{TQ} was normalized to the SQ k-space. 89

4.34 Pseudo 2D ^{23}Na TASTI images of rat head *in vivo* in the coronal view. All images and maps have a FOV of $(54\,\text{mm})^2$ and a resolution of $(1\,\text{mm})^2$. The SQ image was normalized to itself, while the TQ image was normalized to the SQ image. Thresholds were applied prior to fitting to exclude voxels below an SNR threshold. Voxel-wise fitting with Equation 3.24 yielded the b, $T_{2\text{s}}$ and $T_{2\text{f}}$ parameter maps. 90

5.1 Compositions of ions and charged molecules in intra- and extracellular space in mammals. The y-axis is given in the concentration of an ion or molecule multiplied by its charge. Within the intra- and the extracellular compartment, the sum of either the positive or negative charge is almost equal (electro-neutrality). Only a small surplus of the total charge contributes to the membrane potential. (Adapted from Andersen (2013)) 101

List of Tables

2.1 A selection of nuclei with their corresponding nuclear spin I, gyromagnetic ratio $\frac{\gamma}{2\pi}$, isotope abundance c, the physical NMR sensitivity S_{phy} relative to ^{1}H and the Larmor frequency ω_0 at 9.4 T (Harris et al., 2002). 9
2.2 Basis operators using the symmetric and antisymmetric combinations of the irreducible tensor operators van der Maarel (2003a). 18

3.1 Phases of each phase step of the SQ, DQ and TQ coherence within one phase cycle using TPPI with DQ suppression. 44
3.2 3D DA-R sequence parameters to investigate SNR improvement through density-adaption. The flip angle was $\alpha = 90°$ and no spoiling was used. 45
3.3 Parameters of the DA-R sequence and the UTE sequence. Identical parameters for all series are: $t_{\text{ro}} = 8\,\text{ms}$, $n_{\text{av}} = 8$, $\alpha = 90°$, TE $= 306\,\mu\text{s}$ and TR $= 80\,\text{ms}$. . . 46
3.4 Pseudo 2D DA-R sequence parameters used to acquire ^{23}Na and ^{35}Cl images of the square bioreactor. Spoilers were not used, and the flip angle was $\alpha = 90°$. . . 46
3.5 3D DA-R sequence parameters used to acquire ^{23}Na and ^{35}Cl images of the rat brain and the rat heart. Spoilers were used to lower TR. Global *in vivo* T_1 measurements were done to esimate the optimal flip angle. The bandwidth was $25\,\text{kHz}$ and identical for all measurements. 47
3.6 Inversion recovery sequence parameters to measure T_1 in agarose phantoms. . . 48
3.7 Spin echo sequence parameters to measure T_2 in agarose phantoms. 48
3.9 ^{23}Na and ^{35}Cl TQ-TPPI sequence parameters of agarose phantom experiments to investigate the effect of TR length on the qualitative and quantitative behavior of the TQ-TPPI spectrum. The scan time t_{sc} was in the range of $2 - 5\,\text{min}$ and $4 - 16\,\text{min}$ for ^{23}Na and ^{35}Cl experiments, respectively. 48
3.10 TQ-TPPI sequence parameters of lecithin phantom experiments to examine the difference in ^{23}Na and ^{35}Cl $S_{\text{T/S}}$ ratios. 49
3.11 ^{23}Na and ^{35}Cl TQ-TPPI sequence parameters of bioreactor experiments to probe the feasibility of acquiring TQ signal *in vitro*. 49
3.12 ^{23}Na and ^{35}Cl TQ-TPPI sequence parameters of measurements on the rat brain to investigate the difference in TQ/SQ signal ratio between ^{23}Na and ^{35}Cl *in vivo*. 50
3.13 TASTI sequence parameters in ^{23}Na agarose phantom studies. In the first set of measurements, TE was varied. In the second set of measurements, different combinations of Δt_{evo} and n_{pc} were set. The identical parameters for all measurements are: $n_{\text{proj}} = 70$, BW $= 25\,\text{kHz}$, $t_{\text{ro}} = 8\,\text{ms}$ and $n_{\text{ps}} = 8$. 50
3.14 TASTI sequence parameters to acquire pseudo 2D ^{23}Na images in rat head. . . . 51

4.1 SNR values in different organs and tissues in rat head (upper section) and rat torso (lower section) extracted from ^{23}Na and ^{35}Cl *in vivo* images. 66
4.2 Signal ratios between organ regions in the column and those in the top row in ^{23}Na rat head, ^{35}Cl rat head and ^{23}Na rat torso images. 66

4.3 ^{23}Na and ^{35}Cl inversion recovery T_1 fitting results with the fit function $S_{T_1}(\mathrm{TI}) = \mathrm{abs}\left[a \cdot \left(1 - b \cdot \mathrm{e}^{-\mathrm{TI}/T_1}\right)\right]$ for agarose phantoms with $0, 2, 4$ and $6\,\%$ agarose and $134.75\,\mathrm{mM}$ NaCl. The RMSE was < 0.014 overall. 67

4.4 Summary of ^{23}Na and ^{35}Cl T_2 values in agarose phantoms with $0, 2, 4$ and $6\,\%$ agarose and $134.75\,\mathrm{mM}$ NaCl. The TQ-TPPI results of each nucleus-phantom combination were from the respective measurement at maximum TR. The fraction of the fast component is given by b. The spin echo T_2 were determined with the fit functions $S_{T_2}^{\mathrm{mono}}(\mathrm{TE}) = a{\cdot}\mathrm{e}^{-\mathrm{TE}/T_2}{+}c$ and $S_{T_2}^{\mathrm{bi}}(\mathrm{TE}) = a{\cdot}\left(b \cdot \mathrm{e}^{-\mathrm{TE}/T_{2\mathrm{f}}} + (1-b)\mathrm{e}^{-\mathrm{TE}/T_{2\mathrm{s}}}\right) + c$, with the overall RMSE < 0.019. 71

4.5 Summary of ^{23}Na and ^{35}Cl TQ-TPPI fitting results in phantoms, rat head *in vivo* and cells in the bioreactor *in vitro*. The fraction of the fast relaxing component is given by b. 74

4.6 Fitted $T_{2\mathrm{s}}$ and $T_{2\mathrm{f}}$ in phantoms with graphical presentation in Figure 4.22. 78

4.7 Fitted $S_{\mathrm{T/S}}$ in phantoms with graphical presentation in Figure 4.23. 79

4.8 Fitted $T_{2\mathrm{f}}$ and $T_{2\mathrm{s}}$ and $S_{\mathrm{T/S}}$ in agarose phantoms with different combinations of the sampling time step Δt_{evo} and the maximum sampling time $t_{\mathrm{evo,max}}$ of the t_{evo}-FID. 83

4.9 Fitted $S_{\mathrm{T/S}}$ in agarose phantoms with different combinations of the sampling time step Δt_{evo} and the maximum sampling time $t_{\mathrm{evo,max}}$ of the t_{evo}-FID. 84

4.10 Fitting results of the sum of the t_{evo}-FIDs in the entire head, the brain, the olfactory bulb and the eyes (RMSE$<$ 0.038). The fraction of the fast relaxing component is given by b. The TQ-TPPI results in the head are listed for an easier comparison. 92

5.1 Ratios between the between the intracellular TQ signal TQ_i and the intracellular SQ signal SQ_i, between the extracellular TQ signal TQ_e and the extracellular SQ signal SQ_e, between the intracellular TQ signal TQ_i and the total SQ signal $\mathrm{SQ}_{\mathrm{total}}$, as well as between the extracellular TQ_e and the total SQ signal $\mathrm{SQ}_{\mathrm{total}}$. All ratios are given in %. The estimation range is a consequence of the $\mathrm{TQ}_i/\mathrm{TQ}_e$ range from literature given in Equation 5.3. 105

Declaration

This thesis is the result of my independent investigation under supervision. Where my work is indebted to the work or ideas of others, for example from the literature or the internet, I have acknowledged this within the thesis.

I declare that this study has not already been accepted for any other degree, nor is it currently being submitted in candidature for any other degree.

I am aware that a false declaration could have legal implications.

Mannheim, November 25th 2019 ______________________________

Ruomin Hu